

INFORMATION TO USERS

This manuscript has been reproduced from the microfilm master. UMI films the text directly from the original or copy submitted. Thus, some thesis and dissertation copies are in typewriter face, while others may be from any type of computer printer.

The quality of this reproduction is dependent upon the quality of the copy submitted. Broken or indistinct print, colored or poor quality illustrations and photographs, print bleedthrough, substandard margins, and improper alignment can adversely affect reproduction.

In the unlikely event that the author did not send UMI a complete manuscript and there are missing pages, these will be noted. Also, if unauthorized copyright material had to be removed, a note will indicate the deletion.

Oversize materials (e.g., maps, drawings, charts) are reproduced by sectioning the original, beginning at the upper left-hand corner and continuing from left to right in equal sections with small overlaps. Each original is also photographed in one exposure and is included in reduced form at the back of the book.

Photographs included in the original manuscript have been reproduced xerographically in this copy. Higher quality 6" x 9" black and white photographic prints are available for any photographs or illustrations appearing in this copy for an additional charge. Contact UMI directly to order.

UMI

A Bell & Howell Information Company
300 North Zeeb Road, Ann Arbor MI 48106-1346 USA
313/761-4700 800/521-0600

Spatial and Temporal Variations of Basal Conditions
Beneath Glaciers and Ice Sheets
Inferred From Radio Echo-Sounding Measurements

by

Anthony M. Gades

A dissertation submitted in partial fulfillment of
the requirements for the degree of

Doctor of Philosophy

University of Washington

1998

Approved by Charles F. Raymond
(Chairperson of Supervisory Committee)

Program Authorized
to Offer Degree GEOPHYSICS

Date 10 June, 1998

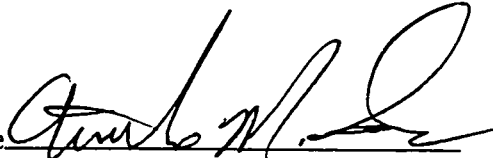
UMI Number: 9836169

UMI Microform 9836169
Copyright 1998, by UMI Company. All rights reserved.

**This microform edition is protected against unauthorized
copying under Title 17, United States Code.**

UMI
300 North Zeeb Road
Ann Arbor, MI 48103

In presenting this dissertation in partial fulfillment of the requirements for the Doctoral degree at the University of Washington, I agree that the Library shall make its copies freely available for inspection. I further agree that extensive copying of this dissertation is allowable only for scholarly purposes, consistent with "fair use" as prescribed in the U.S. Copyright Law. Requests for copying or reproduction of this dissertation may be referred to University Microfilms, 1490 Eisenhower Place, P.O. Box 975, Ann Arbor, MI 48106, to whom the author has granted "the right to reproduce and sell (a) copies of the manuscript in microform and/or (b) printed copies of the manuscript made from microform."

Signature 

Date 10 June, 98

University of Washington

Abstract

Spatial and Temporal Variations of Basal Conditions
Beneath Glaciers and Ice Sheets
Inferred From Radio Echo-Sounding Measurements

by Anthony M. Gades

Chairperson of Supervisory Committee: Professor
Charles F. Raymond
Geophysics Program

The basal structure of Black Rapids Glacier, Alaska and Siple Dome, West Antarctica were studied using new radio echo-sounding (RES) methods and analysis techniques. Development of these methods was motivated by the need to make rapid large-scale non-invasive observations of sub-ice systems. RES data from each study site are analyzed to identify and isolate the portion of the data associated with the reflection from the bed by using a calibration determined from principal component analysis of the ice-internal reflectors/scatterers. Reflectivity models are developed to calculate the dielectric structures responsible for the measured reflections and to infer the range of physical conditions responsible for those structures. Repeated RES measurements on Black Rapids Glacier were made during the time of annual spring speedup which is associated with changes in meltwater input. These measurements show that the subglacial structure near the center of the subglacial valley did not change significantly during the period of observation, but allow for some changes toward the glacier margin. Together with other geophysical measurements, these re-

sults show that the observed speedup of the glacier was probably not driven locally by changes in the subglacial system at the center of the glacier, but from changes toward the sides and/or down glacier. The absence of glacier-wide changes in basal conditions in the presence of glacier-wide changes in glacier speed suggests that large-scale glacier motion may be affected or even controlled by localized changes in sensitive regions of the glacier bed. RES profiles across Siple Dome and onto adjacent paleo-ice streams are used to reveal information about their history and current basal conditions. The pattern of reflective layering in the ice is used to positively identify the location of paleo-ice stream margins and the depth of buried crevasses is used to estimate the time since shutdown of these ice streams. The pattern of reflected power from the bed is used to show that the bed under Siple Dome must be either one of ice frozen to smooth bedrock or to a thin (< 1 m) frozen till, and the bed under the paleo-ice streams are either underlain by a thawed or frozen till layer > 1 m thick. The absence of a thick till beneath Siple Dome is consistent with its apparent stability as an inter-ice stream ridge in the past and suggests that it may remain as a stable limiter of ice stream width in the future. Together these results reveal much about both the potential and the limitations of RES for investigating basal conditions in polar and temperate ice masses.

TABLE OF CONTENTS

List of Figures	vii
List of Tables	xi
Chapter 1: Introduction: Investigating Sub-Glacial Structures	1
1.1 Motivation and Goals	2
1.1.1 Black Rapids Glacier, Alaska	2
1.1.2 Siple Dome, Antarctica	3
1.2 Development of New Field Methods	3
1.3 Organization	4
1.4 Overview	5
Chapter 2: Radio Echo-Sounding Instrumentation	7
2.1 Summary	7
2.2 General Description of Ground-Based Radio Echo-Sounding	7
2.3 MKI and MKII Mono-Pulse Transmitters	13
2.4 Receivers Characteristics	13
Chapter 3: Radio Echo-Sounding Background and Theory	16
3.1 Summary	16
3.2 Introduction	16
3.3 Model of Radio Wave Propagation	18
3.4 Transmission and Reflection of Electromagnetic Waves	22

3.4.1	The three-layer reflectivity model	23
3.5	Equivalent Layer Theory	25
3.5.1	Mixtures of Materials	27
3.5.2	Heterogeneous Surfaces	29
3.5.3	Effective Conductivity Models and Measurements	31
3.6	Summary	32
Chapter 4:	The Topography and Hydraulic Potential of Black	
	Rapids Glacier, Alaska	33
4.1	Summary	33
4.2	Introduction	33
4.3	Methods	34
4.4	Results	40
4.4.1	Surface and Bedrock Topography	40
4.4.2	The Subglacial Hydraulic Potential	41
4.5	Summary	46
Chapter 5:	Radio Echo-Sounding Investigation of Basal Properties,	
	Black Rapids Glacier, Alaska I: Measurements and Data	
	Analysis	48
5.1	Summary	48
5.2	Introduction	49
5.3	Black Rapids Glacier Site Description	50
5.4	Repeated Radio Echo-Sounding Measurements at Fixed Locations . .	53
5.4.1	Methods and Data	53
5.4.2	Time Variation of Returned Power	54
5.4.3	Correction for Variations in Transmitted Energy	60

5.4.4	The Residual Bed Reflection Power	63
5.4.5	Error Analysis of Method	65
5.4.6	Bed Reflection Phase	69
5.5	Repeated RES Profiles	76
5.5.1	Methods	76
5.5.2	Determination of Bed Reflection Power	77
5.5.3	The Residual Bed Reflection Power	78
5.6	Summary and Conclusions	79
 Chapter 6: Radio Echo-Sounding Investigation of Basal Properties, Black Rapids Glacier, Alaska II: Inferred Subglacial Structure		 83
6.1	Summary	83
6.2	Introduction	84
6.3	Expected Changes in Subglacial Hydrological Systems	84
6.3.1	General Descriptions of Subglacial Hydrology	84
6.3.2	Expected Seasonal Evolution	86
6.3.3	General Categories of Subglacial System Change	87
6.4	Constraints on Basal Property Changes from Repeated RES Measure- ments	88
6.4.1	Reference Calculations of Reflectivity and Phase	89
6.4.2	Implications RES Fixed Site Measurements	92
6.4.3	Implications of Repeated RES Profiles	94
6.5	Synthesis of RES Results with Other Observations	101
6.5.1	Comparison of RES with Seismic Measurements	101
6.5.2	Importance of Glacier Margins	103
6.5.3	Longitudinal Coupling	107

6.5.4	Comparison With Expected Seasonal Evolution	109
6.6	Summary and Conclusions	109
Chapter 7: Radio Echo-Sounding Investigation of Basal Properties, Siple Dome West Antarctica		112
7.1	Abstract	112
7.2	Introduction	114
7.3	Siple Dome Site Description	115
7.4	Radio Echo-Sounding Data	117
7.4.1	Removal of Instrumentation Effects	119
7.4.2	Selection of Basal Reflection	119
7.4.3	Calculation of Power	121
7.4.4	Correction for Ice Thickness Variation	122
7.4.5	Correction for Frequency Differences	124
7.5	The Residual Bed Reflection Power of Siple Dome	125
7.6	Discussion	126
7.6.1	Buried Stratigraphy Across the "Siple Ice Stream" Margin . .	126
7.6.2	Bed Reflection Power Variations Across the Siple Ice Stream Margin	130
7.6.3	Inferred Basal Composition of Siple Dome	131
7.6.4	Inferred Basal Composition of Siple Ice Stream	131
7.6.5	Pattern of Reflected Power Variation	135
7.6.6	Basal Reflection Power Variations: Duck's Foot	136
7.7	Conclusions	137
Chapter 8: Summary and Conclusions		139
8.1	Black Rapids Glacier, Alaska	139

8.2	Siple Dome, Antarctica	143
8.3	The Potential and Limitations of Radio Echo-Sounding	145
Bibliography		147
Appendix A: Electromagnetic Waves in Dielectric Media.		159
A.1	Electromagnetic Waves in Non-Conducting Media	159
A.1.1	Maxwell's Equations in Free-Space	159
A.1.2	Maxwell's Equations in Non-Conducting Matter	160
A.1.3	Plane Waves in Free Space	160
A.1.4	Reflection and Transmission Coefficients I: 2-layer, Non-Conducting Media	161
A.1.5	Two-Layer, Non-Conducting, Oblique incidence, <i>p</i> Polarization	163
A.1.6	Two-Layer, Non-Conducting, Oblique incidence, <i>s</i> Polarization	163
A.1.7	Three-layer, Non-Conducting, Oblique Incidence, <i>s</i> Polarization	164
A.2	Electromagnetic Waves in Conducting Media	165
A.2.1	Maxwell's Equations in Conducting Media	165
A.2.2	Three-layer, Conducting, Oblique Incidence	168
Appendix B: Principal Component Analysis		173
B.1	Principal Component Analysis in 2-D	173
B.2	Principal Component Analysis in M-Dimensions	176
B.3	Application of PCA to Repeated RES Measurements	178
Appendix C: Survey Measurements, Black Rapids Glacier, AK		180
Appendix D: Weather Observations, Black Rapids Glacier, AK		184

Appendix E: Marginal Lake Drainage Events	187
Appendix F: Diffusion of Water in Till Layers	189
Appendix G: Calculation of Radio Wave Propagation Velocity at Siple Dome.	191

LIST OF FIGURES

2.1	Wavelength of electromagnetic waves in ice, water and rock for frequencies 1:50 MHz	8
2.2	Schematic diagram of UW RES system.	9
2.3	The mean RES record from Black Rapids Glacier, AK Km-16U site. .	11
2.4	A-scope to Z-scope diagram.	12
3.1	Reflectivity for 5 MHz wave impinging on a water layer.	24
3.2	Contours of constant reflectivity and phase (radians) for a water layer	25
3.3	Effective dielectric for a till layer.	28
3.4	Effective dielectric for a rough surface.	30
4.1	Outline of Black Rapids Glacier, AK.	36
4.2	Black Rapids Glacier, 5 MHz Km-14 transverse profile, 3 June, 1993.	37
4.3	Black Rapids Glacier, 5 MHz Km-16 transverse profile, 10 June, 1993.	38
4.4	Black Rapids Glacier, 5 MHz Km-18 transverse profile, 23 May, 1993.	39
4.5	25 meter interval contour map of surface elevations on BRG.	42
4.6	100 meter interval contour map of ice thickness of BRG.	43
4.7	100 meter interval contour map of BRG bedrock elevation.	44
4.8	Calculated ice thickness minus the gridded values.	45
4.9	1 bar interval contour map of BRG hydraulic potential.	47
5.1	Black Rapids Glacier and its relation to Alaska (inset panel).	51
5.2	Black Rapids Glacier measurement record summary.	52

5.3	Upper Km-16 fixed site data z-scope image.	55
5.4	Km-14 fixed site data z-scope image.	56
5.5	Bed reflection pulse from a typical RES waveform.	58
5.6	Km-16U RES fixed site normalized BRP and IRP	59
5.7	Km-14 RES fixed site normalized BRP and IRP	60
5.8	Km-14, Km-16U residual bed reflection power.	64
5.9	20 ns fractional uncertainty, M , and the fraction of total variance explained	68
5.10	10 ns fractional uncertainty, M , and the fraction of total variance explained	69
5.11	Km-16U RES fixed site mean bed reflection and representative sinusoid.	71
5.12	Km-14 and Km-16U RES fixed site zeroth lag correlation of bed reflection pulse.	72
5.13	Power spectral density of average waveform from Km-16U.	73
5.14	Sinusoid of 2.2 MHz with phase shift of zero and $\pi/4$ radians	74
5.15	Variation of zeroth-lag correlation with phase shift.	75
5.16	Phase spectra of mean and least correlated record.	76
5.17	BRP_R along profiles Km-18, Km-16, and Km-14.	80
6.1	Hard Bed: Reflectivity and phase contour for 2 MHz.	90
6.2	Hard Bed: Contours of reflectivity for 5 MHz.	91
6.3	Soft Bed: Contours of reflectivity and phase for 2 MHz.	92
6.4	Soft Bed: Contours of reflectivity for 5 MHz.	93
6.5	Hard Bed: Reflectivity and phase contour for 2 MHz.	94
6.6	Summary of RES measurements along profiles.	96
6.7	The hydraulic potential of Black Rapids Glacier.	105

6.8	The overburden pressure divided by subglacial water pressure for Km-16 cross section of BRG.	106
6.9	Horizontal strain between Km-14, Km-15, Km-16.	108
7.1	Map view of the Siple Coast Region of West Antarctica.	116
7.2	AVHRR satellite image of Siple Dome showing ice streams C and D.	117
7.3	RES profile across Siple Dome.	118
7.4	The bed reflection from a typical RES record from Siple Dome.	120
7.5	Relative power levels of bed reflection power and internal reflection power.	123
7.6	BRP vs. travel time relation.	124
7.7	The corrected BRP.	126
7.8	RES profile across Siple Ice Stream Margin.	127
7.9	RES profile across the ice stream C margin.	128
7.10	Contours of constant reflectivity for a till layer.	133
A.1	Schematic diagram of 3-layer reflectivity model.	164
A.2	Schematic diagram of 3-layer reflectivity model.	169
B.1	Data plotted on measured axis	174
B.2	Data plotted with principal components	175
B.3	Data plotted with principal components	176
B.4	Example record and the first three principal components.	177
B.5	Fraction of total variance accounted for by the first ten principal components	179
C.1	Summary of twice-daily survey measurements from Km-15.5	182
C.2	Transverse velocity profile at Km-16.	183

D.1	Summary of hourly weather observations	185
D.2	Ablation as measured near the Km-15 survey site.	186
F.1	Characteristic depth for a range of hydraulic diffusivities	190

LIST OF TABLES

3.1	Factors which affect received power.	20
3.2	Dielectric permittivities and conductivities from <i>Jiracek</i> (1967), and CRC Handbook of Chemistry and Physics. Reflectivities, dB loss ($-10 \log_{10}(\mathcal{R})$) and skin depths calculated using the reflectivity model.	26
3.3	Calculations of \mathcal{R} for 5 MHz wave incident on composite basal layer of infinite thickness with given porosity ϕ , water conductivity σ_w and bulk dielectric permittivity $\bar{\epsilon}$	32

ACKNOWLEDGMENTS

I am incredibly indebted to my advisor Charlie Raymond for his many ideas, inspirations, for assistance in field projects, and for encouragement in finishing this dissertation.

I wish to thank Howard Conway for the countless discussions we have had on all kinds of topics while in locations varying from Alaska to a tunnel we drilled at the base of a glacier in the Dry Valleys, Antarctica. These discussions and encouragement have been of critical importance to my completion of this degree.

I thank my office and 7th floor mates and especially Ed Waddington and Al Rasmussen for the many valuable discussions on a wide variety of issues over the past several years.

I acknowledge and thank Bruce Weertman, John Chin, Bob Benedict and Dave Morse for each of their contributions to the University of Washington radio echosounding system which we have developed.

The Black Rapids Glacier portion of this dissertation would not have been possible without our collaborators at the University of Alaska, Fairbanks. I thank them for their planning and assistance in the field, particularly Keith Echelmeyer, Will Harrison, Matt Nolan, Chris Larsen, and Jeanette DeMallie.

I thank Bob Jacobel of St. Olaf College, for giving me my first opportunity to get started in the field of Glaciology.

I thank my parents for their encouragement and their unquestioning faith that I have always been doing something useful in my years of formal education.

Finally, I thank Nadine Nereson for many things, including patient proof-reading, assistance, and support. Since beginning undergraduate Physics and Math studies together many years ago, it has been an amazing path that has led us to where we are now. I am grateful for both the path and its destination.

This work was primarily supported by NSF grant numbers DPP 91-22540, OPP 95-30827, OPP 93-16807

Chapter 1

INTRODUCTION: INVESTIGATING SUB-GLACIAL STRUCTURES

Though subglacial basal properties are known to play an important role in the motion of ice masses, their precise role is not well-understood. Direct investigations of the relationship between basal properties and ice motion are difficult because of the inaccessibility of the glacier bed. Previous investigations of basal properties have primarily been done by either (i) direct measurements through boreholes drilled in the ice (e.g., *Engelhardt and Kamb, 1997; Hubbard et al., 1995*), (ii) measurements from sampling glacial discharge in pro-glacial streams (e.g., *Raymond et al., 1995*) (iii) investigations of exposed basal materials in recently deglaciated regions (e.g., *Walder and Hallet, 1979*), or (iv) measurements of seismic reflections (e.g., *Blankenship et al., 1986, 1987b*). These techniques have provided much of what is known about the connection between basal properties and ice motion. However, because these techniques lack either spatial coverage (boreholes), spatial resolution (stream measurements) or temporal resolution (investigations of deglaciated regions, seismic studies), we are strongly motivated to explore additional methods.

In this dissertation, I present studies which use new remote sensing and data analysis techniques based on radio echo-sounding (RES) to investigate spatial and/or temporal variations in basal properties. In the primary study, on Black Rapids Glacier, Alaska, data collection and analysis techniques are developed in order to gain better understanding of the temporal and spatial variations in hydraulic conditions respon-

sible for the observed seasonal variations in glacier surface speed. In another study I apply these techniques to two relict margins of formerly active ice streams on the flanks of Siple Dome, West Antarctica in order to understand the spatial variation in basal properties that define these margins.

1.1 Motivation and Goals

1.1.1 Black Rapids Glacier, Alaska

Black Rapids Glacier (BRG), Alaska, provides an opportunity to study how basal hydrology and glacier motion are related. Observations by the University of Alaska, Fairbanks (UAF) over the last decade have shown that the glacier speeds up in late spring and slows down during the summer. The primary environmental change occurring during this period is the amount of melt water, and it is clear that this spring speedup is a result of changing sub-glacial hydraulic conditions associated with the introduction of meltwater. Since this speedup occurs at a predictable time each year, it provides a good opportunity to study concurrent spatial and temporal variations in hydraulic conditions. As part of a collaborative project with UAF, we made extensive measurements during the time of the speedup in spring, 1993.

We have used RES to investigate the temporal and spatial variations in hydraulic conditions of BRG during the spring speedup of 1993. A set of three transverse RES profiles and one longitudinal profile was repeated every few days starting before and continuing through the spring speedup, giving us measurements with both spatial and temporal resolution. RES records were also collected hourly or half-hourly at two fixed locations positioned over the deepest portion of the underlying bedrock. From these measurements, we have a large, high-quality digital data set that contains information about spatial and temporal changes in the reflectivity of the glacier base which can be used to constrain the structure of the hydrological system of Black Rapids Glacier.

1.1.2 Siple Dome, Antarctica

Relict ice stream margins on the flanks of Siple Dome, West Antarctica provide an opportunity to study the basal structure of polar ice stream margins using RES. Ice streams in West Antarctica move at velocities of two to nearly three orders of magnitude greater than the surrounding ice sheet. Seismic experiments conducted on ice stream B, detected a water-saturated basal till layer a few meters thick (*Blankenship et al.*, 1987b), and more recent direct evidence from drilling supports this conclusion (*Engelhardt et al.*, 1990b). It is also known that the presence of fast-flowing ice streams is not necessarily a permanent condition and that ice streams can shut down in a relatively short period of time (*Retzlaff and Bentley*, 1993). I was involved in recent radio echo-sounding traverses across the margin of a formerly active ice stream (*Jacobel et al.*, 1996) that show a large change in bed reflection characteristics across the margin. These results provide a means to study the spatial variations in basal properties responsible for the differing reflection characteristics and the controls on streaming motion.

1.2 Development of New Field Methods

Previous techniques to determine basal properties of glaciers have primarily involved measurements from boreholes drilled in the ice, and measurements of glacial discharge properties in pro-glacial streams. These techniques have provided much of what is known about the connection between hydraulic conditions and glacial motion. However, these techniques lack either spatial coverage (boreholes) or spatial resolution (stream measurements). A measurement technique that addresses these problems is needed, and for this purpose, I have used the remote sensing technique of radio echo-sounding (RES).

RES has long been the primary tool for mapping ice thickness and internal ice structure (e.g., *Paren and Robin*, 1975; *Weertman*, 1993). It is portable, accurate,

and efficient, so that large scale ice mapping is possible. It is also effective for distinguishing internal water bodies in temperate glaciers (e.g., *Walford and Kennett, 1989*), and for detecting certain basal properties such as bed roughness (e.g., *Berry, 1972, 1973*), or the presence of liquid water (e.g., *Oswald, 1975*).

RES is limited by the fact that the transmitted signal travels to and from the reflection of interest through one or several media layers; during this time the signal of interest may be altered. To reliably interpret RES data we need to first identify and account for these alterations in order to separate the portion of the signal that is of interest for studying the bed. Much of the work presented in this dissertation is dedicated to developing techniques to identify and extract the portion of the data that is associated with basal properties. In temperate environments, we find that the RES data are dominated by changing meltwater abundance at the ice surface. This has forced me to develop a method of calibration using persistent internal reflectors to measure and remove the effects of varying surface conditions. The considerations associated with this work have also proven useful in the analysis of RES data from polar settings, where instead of varying surface properties, potentially varying properties within the ice column need to be considered.

1.3 Organization

I begin in Chapter 2 by describing the general properties of the RES instrumentation and the specific details of the equipment used for the investigations described in subsequent chapters. In Chapter 3 I briefly review the physics of electro-magnetic wave propagation and arrive at a three-layer reflectivity model following *Born and Wolf (1980)*. To this model I add the capability of calculating the effective dielectric properties of layers with mixed components by using effective dielectric permittivity and effective conductivity models. This composite model is used in subsequent chapters to invert measured reflectivity changes for changes in physical structure. In Chap-

ter 4 I determine the surface and bedrock topography of the region of Black Rapids Glacier from RES measurements, surveying measurements, and topography maps. From these measurements, I calculate the subglacial hydraulic potential. Chapter 5 describes the RES measurements made on Black Rapids Glacier during spring 1993 and the subsequent analysis done to reduce the data to a time series of reflectivity changes associated with changes of basal properties. In Chapter 6 I apply reflectivity modeling to the results determined in the previous chapter and place constraints on the physical changes that occurred at the bed of the glacier during the observation period. These results are compared with other studies.

Chapter 7 discusses RES measurements made across the two stagnant stream margins of Siple Dome, Antarctica. In this chapter we place constraints on the timing of shut-down, and investigate the current basal structure spanning these margins to infer what conditions must have been while they were active.

To promote the continuity of this dissertation, some of the development that is necessary for completeness is included in appendices rather than within the chapters.

1.4 Overview

In these chapters I develop the data analysis methods necessary to reduce the large quantity of information recorded in RES measurements that relate only to basal reflectivity properties. I develop and describe reflectivity models which I then use to convert the RES basal reflectivity measurements to information about the physical properties of the basal interface or layer. I use these methods and models to deduce information about the temporal and spatial variability of basal properties through the spring melt season on Black Rapids Glacier, Alaska and conclude that basal properties locally near the center of the glacier are not altered significantly during the spring speedup, but that changes may occur toward the margins of the glacier. I conclude that the absence of glacier-wide changes in basal conditions in the presence of glacier-

wide changes in speed suggests that large-scale glacier motion may be affected or even controlled by localized changes in sensitive small-scale regions of the glacier bed. In addition to applying these RES methods to the temperate setting of Black Rapids Glacier, I also apply the methods and models in a polar setting at Siple Dome, West Antarctica to infer the spatial variability of basal structure across an inter-ice stream ridge onto paleo-ice streams. From these measurements I conclude that Siple Dome is underlain by either solid bedrock or at most a thin (< 1 m) till layer and that liquid water or a frozen till layer (> 1 m) is likely to be present under the paleo-ice stream.

Chapter 2

RADIO ECHO-SOUNDING INSTRUMENTATION

2.1 Summary

This chapter describes the University of Washington ground-based radio echo-sounding (RES) system used to collect data discussed in subsequent chapters. The two transmitters (MKI and MKII) and oscilloscope-based receivers (Tektronix models 222, 2432/2440, TDS410 and Fluke model 97) are briefly described.

2.2 General Description of Ground-Based Radio Echo-Sounding

The University of Washington radio echo-sounding (*RES*) system is an improved version of the basic system design described by *Watts and Wright* (1981). The mono-pulse transmitter consists of two high-voltage storage capacitors which discharge through high-speed switches to produce short (~ 20 ns) stepped voltage pulses. Each pulse travels the length of the resistively-loaded dipole antenna and radiates a broad band of frequencies. The center frequency of the band is determined primarily by the length of the transmitting antenna. The antennae are approximately critically damped to prevent ringing. Resistive loading per unit length is determined according to Equation 2.1 after *Wu and King* (1965):

$$R(x) = \frac{\Psi}{h - x} \quad (2.1)$$

where x is the distance from the feed point, Ψ is the loading constant in ohms, h is the antenna half-length in meters. All antennae are weighted at 1 m intervals with $\Psi = 400 \Omega$.

The UW system is typically operated at frequencies 1-20 MHz, corresponding to a range of wavelengths in ice and rock of about 100-10 m, and in water of about 1-10 m (Figure 2.1). The receiver for this system uses the same type antenna as the transmitter. The received reflection amplitude versus time is recorded by a high-speed digital oscilloscope. The digital oscilloscope allows for stacking of successive measurements to reduce environmental noise and minimize the effects of any slight variations in transmitted signal. Stacked time series of received amplitudes (waveforms) are then down-loaded to a PC controller and stored to disk. Our system also contains a pressure transducer which records the atmospheric pressure with each record. This pressure record is used to interpolate the surface elevation variation between known elevation points when correcting the RES profile.

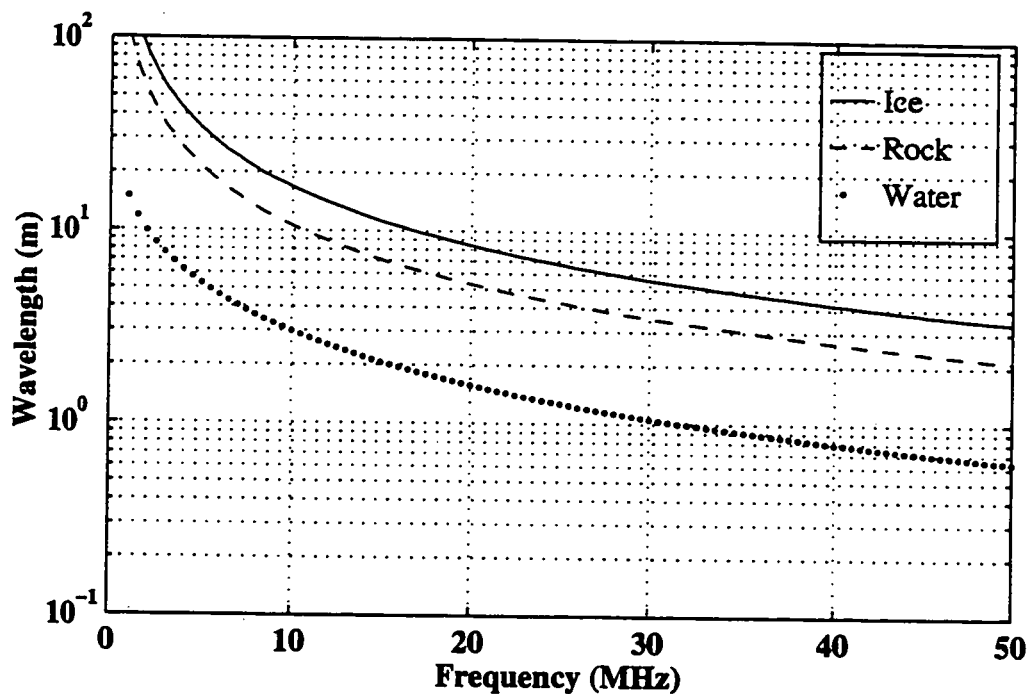


Figure 2.1: Wavelength of electromagnetic waves in ice, water, and rock for frequencies 1:50 MHz.

When profiling with this system on large glaciers or ice sheets, the transmitter

and receiver travel on separate sleds attached by a rope and separated by a distance of 20-100 m (Fig. 2.2). The antennae are arranged in the endfire parallel configuration (*Watts and Wright, 1981*) to minimize the coupling between the antennae (and the resulting distortion to the received signal) as well as for convenience while traveling. The forward section of each of the two dipole antennae is attached to the towing line and the rear sections are allowed to trail behind the sleds. A bike wheel with magnets attached to several spokes activates a stationary magnetic reed switch attached to the fork. This switch is attached to the PC controller, and signals the distance intervals to download and store a stacked waveform accumulated in a digital oscilloscope.

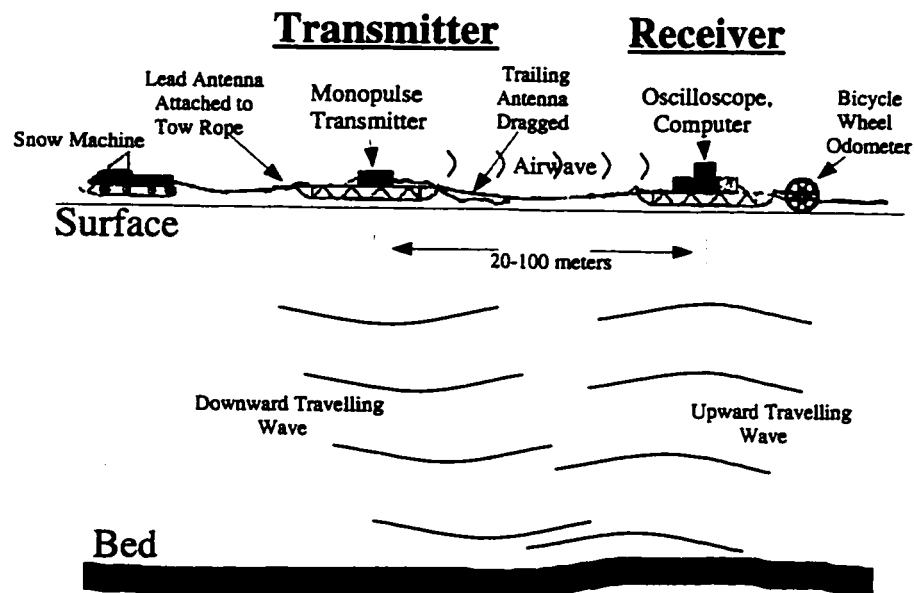


Figure 2.2: Schematic diagram of UW RES system showing the arrangement of the transmitter/receiver in profiling mode. The diagram is not drawn to scale.

The transmitter produces a voltage step on the resistively loaded dipole antenna that interacts with the dielectric interface formed by the snow-air surface. The resulting radiation pattern transmitted into the sub-surface is complex and difficult to predict (*Walford et al., 1986*). The radio wave energy returning back from the ice to the receiving antenna is similarly complex. Once the energy enters the ice, it

is affected by absorption (due to conductive losses), scattering, geometrical spreading, (*Smith and Evans, 1972*) and partial reflections from electrical inhomogeneities (*Paren and Robin, 1975*). Some of the scattered or reflected energy is returned toward the surface to the receiving antenna. Some of the remaining energy is transmitted downward and later reflected by deeper inhomogeneities. Because of the significant dielectric contrast between the ice and underlying rock, the bottom of a glacier tends to be a strong reflector. When liquid water is present at the bed an even stronger dielectric contrast exists and a correspondingly greater reflection can occur. Thus, variations in the thickness and conductivity of a water layer at the bed of a glacier produces variations in reflection strength (Chapter 3). It is this relationship that potentially allows the use of RES to map out the configuration of sub-glacial waters. High electrical conductivity of pore water at the bed of temperate glaciers leads to high attenuation, so that energy penetrating the bed is rapidly attenuated. Modeling the reflectivity of the basal layer is discussed in Chapter 3.

Some energy, depending on the near-surface structure, propagates along the surface directly from the transmitting to receiving antenna as a direct wave. The arrival of this wave is used to trigger the recording of the reflection signals, and is used to mark the beginning of the RES record.

A typical RES record (Fig. 2.3) is a time series of voltage samples characterized by a pre-trigger interval which records the background noise level, the high initial amplitude from the direct-wave (0-1.5 μ s), energy returning from interior reflectors, the bed reflection, and finally energy from more distant, off-axis locations in the interior or bed. The duration of the direct-wave obscures returns from the zone immediately beneath the surface as can be seen in Figure 2.3. Thus, the propagation path and the corresponding record can be considered in terms of three zones: surface, interior and bed (Fig. 2.3). The properties of the surface affect returns from the interior, while properties of both the surface and interior affect returns from the bed. The contribution from these sources needs to be considered when interpreting

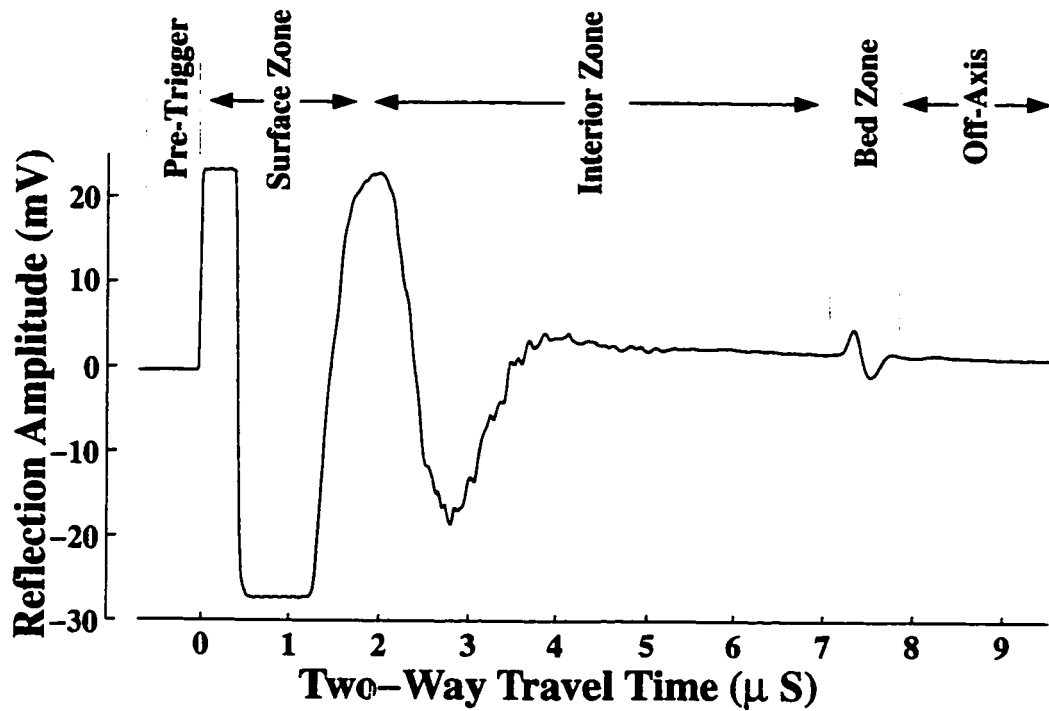


Figure 2.3: The mean RES record from Black Rapids Glacier, AK (Km-16U fixed site). Plotted as received voltage versus time and its schematic relation to pre-trigger, surface, interior bed, and off-axis zones.

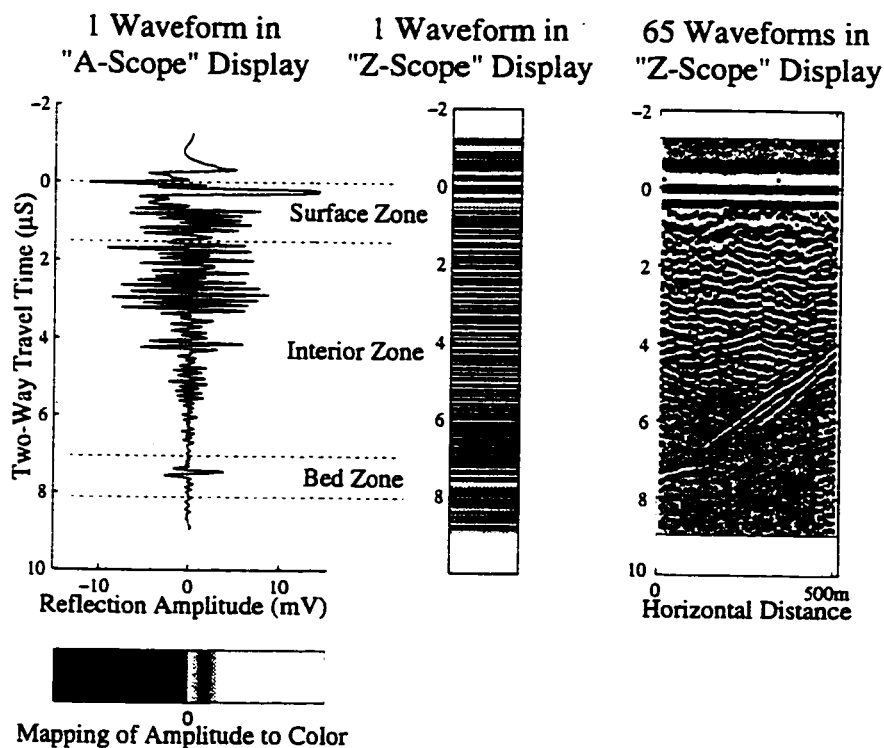


Figure 2.4: A single time series of reflection amplitudes (waveform) is shown at left in *A-scope*. Beneath the *A-scope* waveform is shown the gray scale color mapping used to produce the pixel array shown at center. At right, the result of this process is displayed - the *Z-scope* image for a series of 65 waveforms of a profile from Black Rapids Glacier, AK.

reflection changes at the bed. If not, changes in the upper zones which affect the bed reflection could be erroneously attributed to physical changes at the bed. In theory it is possible to predict the returned signal time-series with knowledge of the transmitter/receiver characteristics, the electrical properties of the ice and bed geometry (e.g., *Walford et al.*, 1986). In this study insufficient knowledge of the RES system or ice properties prohibits using this approach.

For display purposes, it is common to convert these time series of reflection amplitudes (*A-scope*) to a single pixel array (*Z-scope*). The (gray-scale) color of the pixels are related to the amplitude. This is shown in figure 2.4.

2.3 MKI and MKII Mono-Pulse Transmitters

The first version of the UW mono-pulse transmitter (which I refer to as the MKI transmitter) was designed by UW electrical engineer John Chin and built by Bruce Weertman (*Weertman et al.*, 1990). A detailed description of the MKI transmitter can be found in *Weertman* (1993). This transmitter operates with 12V DC input and the output is a ± 1 kV, 20 ns pulse. The transmitter was designed to produce a pulse with stable amplitude and shape. This is important for effective stacking of returned signals. This transmitter was also designed to be stable over a range of power input and ambient temperatures. A more powerful version of this transmitter was designed by John Chin in 1994. David Morse was responsible for laying out the board design as well as tuning the finished transmitters. Nadine Nereson and I were primarily responsible for the assembly of the MKII transmitters. This version (MKII) produces a ± 2 kV, 15 ns pulse that is even more stable than the MKI version.

2.4 Receivers Characteristics

The receiver for the UW RES system uses a digital oscilloscope to record the amplitude as a function of travel time. Several oscilloscopes were used for the experiments described in subsequent chapters. All oscilloscopes are connected to a personal computer which controls the data gathering and stores the data to disk. All data gathered with these various systems have, out of necessity, differing raw data streams. To deal with this diverse data stream I designed filters to convert each data type into a common header-less binary format which I could then read with a suite of Matlab data processing routines which I developed. These filters and this suite of analysis routines forms the basis of the current University of Washington RES system and has been extensively used by other students.

The receiver for the RES profiling system at Black Rapids Glacier, in 1993 used

either a Tektronix 2432 or 2440 100 MHz digital oscilloscope¹ powered by a portable 110 V AC generator. Data (waveforms) from these oscilloscopes are 1024 samples in length, and were generally recorded at 10 ns per sample. These oscilloscopes can stack up to 256 measurements at a rate of ~ 12 per second. Attempts were made to profile at a traverse rate so that each record contained the full number of averages. This oscilloscope was also used at the Km-16L fixed location RES site on Black Rapids Glacier, where batteries charged by a solar panel and a 12 V DC-110 V AC inverter were used for power. Data collection software for the Tek 2432 profiling system used for RES profiling on Black Rapids glacier is described in detail in *Weertman* (1993). I modified that software for the fixed site operation.

The RES profiling system used at Siple Dome used a Tektronix TDS410 100 MHz oscilloscope. This oscilloscope is similar in design to the Tektronix 2432, but allows up to 10,000 measurements to be stacked at a rate of ~ 85 per second. Data recorded with this oscilloscope were 2500 samples in length at 10 ns per sample. This oscilloscope requires 110 V AC power which is supplied by a portable generator. I developed a new operating system for use with this system.

A Tektronix 222 10 MHz digital oscilloscope was used at the Km-16U fixed location RES site on Black Rapids Glacier. Data were 512 samples in length and were collected at 20 ns per sample. This oscilloscope requires 12 V DC input and was powered by batteries maintained by solar panels. The internal stacking capacity of this oscilloscope is limited to only 4 measurements. Further averaging is accomplished by transferring several of these 4-measurement stacked waveforms to the controlling computer and stacking them within the computer. Each of the recorded waveforms from the Km-16U fixed site is an average of 32 transferred waveforms and is therefore the average of 128 measurements. I wrote software for the Tek 222 for use in sta-

¹ Note that the frequencies listed for the oscilloscopes refer only to their maximum real-time capacity, all of the digital oscilloscopes used are able to gather data at higher frequencies by assuming a repetitive waveform.

tionary operation as well as for profiling. This system has been used successfully in many locations including the North Cascades and several locations in the Antarctic.

A Fluke 97 50 MHz digital oscilloscope was used at the Km-14 fixed location RES site on the Black Rapids Glacier. The data collected were 512 samples in length and at 20 ns per sample. Each of the recorded waveforms consisted of 256 measurements averaged within the oscilloscope. Power was supplied by 12 V batteries maintained by solar panels. Specifications for this oscilloscope list a 50 MHz recording capability, but in reality the triggering is only capable of a lower frequency (<10 MHz, B. Narod, pers. comm.). The result is that the oscilloscope, while averaging, triggers at slightly variable locations at the onset of the waveform thereby reducing the amplitude of the returned signals, and does so in a way that is not necessarily consistent for each measurement. Much of the data collected with this receiver therefore contained high noise levels and was ultimately not used. I wrote software for this system for fixed location monitoring.

Chapter 3

RADIO ECHO-SOUNDING BACKGROUND AND THEORY

3.1 Summary

In this chapter, the use of radio echo-sounding (RES) to determine thickness and internal structure of ice masses is reviewed including the basic theory of radio wave propagation in layered dielectric media, reflection from three-layer structures, dielectric mixing models and reflection from heterogeneous surfaces. I develop an integrated reflectivity model that can be used to investigate contrasts in reflectivity at the ice base from RES measurements and to calculate the constraints on the physical properties which produce these reflectivity contrasts.

3.2 Introduction

Early RES investigations focused on ice in polar environments. This work was aided by the fact that cold polar ice is more transparent to radio wave propagation than temperate ice. These studies relied primarily on airborne instruments, and concentrated on the determination of ice thickness and mapping of large portions of the subglacial topography of the Antarctic continent. The Antarctic data were compiled by *Drewry* (1983). Mapping of the Greenland summit region using airborne RES was similarly done in the 1980's (e.g., *Hodge et al.*, 1990).

Uses of RES beyond the determination of ice thickness were quickly recognized in the early 1970's, and at that time regular use of RES on temperate glaciers began. *Smith and Evans* (1972) discuss the absorption and scattering of electromagnetic

waves by ice and water inclusions. *Watts and England* (1976) carried this discussion further to show that frequencies less than 5MHz would be required to reliably use RES to determine ice thickness on temperate glaciers. Because RES records of this time were photographs of an oscilloscope screen, they contained only approximate information about power returns. However, it was recognized that information about the basal layer contained in these reflection strength records could be used to infer contrasts in basal properties. Other work focussed on the use of RES to infer the statistical properties of basal roughness (e.g., *Berry*, 1972, 1973, 1975).

The existence of large subglacial lakes in a region near Vostok station in East Antarctica was suggested by *Oswald and Robin* (1973). On the basis of surface topography, reflection strength, and inferred roughness, *Oswald* (1975) confirmed this suggestion. *Neal* (1976) described a method for recording the bed reflection power with the specific goal of distinguishing regions of contrasting bed roughness and/or reflectivity.

Many subsequent RES studies on temperate glaciers have revealed the presence of structures such as internal reflecting horizons, varying basal properties, and internal water bodies. *Jacobel and Raymond* (1984) observed changes in the reflection properties of an englacial cavity on Variegated Glacier, Alaska, and interpreted those changes in terms of flow of water to and from the cavity. *Walford et al.* (1986) used RES to arrive at statistical measures of bedrock properties as well as the distribution and size of englacial reflectors (water bodies). *Jones* (1987) used repeated RES measurements at a fixed site on Trapridge Glacier, Yukon Territory to study englacial and subglacial temporal variations in reflectivity. *Walford and Kennett* (1989) conducted a synthetic-aperture RES experiment on Storglaciären, Sweden. They found identifiable targets within their small study area and suggested that they were water-filled cavities. *Jacobel and Anderson* (1987) used RES to detect water-filled cavities on the Variegated Glacier, Alaska.

In the studies presented in this dissertation, RES measurements were made to

determine temporal and/or spatial variations in subglacial structure. These measurements of reflected amplitude and phase must be analyzed to determine subglacial structures responsible for the returned signal. In this chapter I develop a three-layer reflectivity model which will be used to infer the physical structures responsible for the measurements of returned amplitude and phase.

3.3 Model of Radio Wave Propagation

In order to infer physical structures from RES data, we must first be able to predict the measured returned signal from a distribution of electrical properties in the ice and at the glacier bed and a known transmitted pulse.

Surface-based RES systems radiate short pulses of energy from a transmitting antenna located on the ice or snow surface. For a given pulse amplitude and duration, the amount of energy transmitted into the ice and the amount of returned energy depends on properties of the antennae, the ice surface, the internal ice, and the basal interface.

After a pulse is generated on the transmitting antennae, some energy enters the ice subsurface and monotonically decreases in amplitude as a result of both geometric spreading and attenuation (due to ice conductivity). When the energy encounters a layer of electrical inhomogeneity, some energy is reflected back to the surface where it is detected by the receiving antenna, and some energy is transmitted downward. When the energy encounters bodies of electrical inhomogeneity, some energy is reflected incoherently and is scattered. The amount of energy lost to scattering depends on the size and number of the scattering bodies. When the energy reaches the basal interface, some energy is reflected back up to the receiving antenna, and the rest is attenuated after a short propagation distance into the bed. The amount and character of the bed reflection depends on the dielectric structure of the basal interface.

The factors which affect power received by the RES system are summarized in

Table 3.1.

We can reduce all of these to 4 factors:

- Focusing parameter F
- Surface/antenna parameter G - accounts for the instrumentation characteristics, and antenna coupling with the ice surface.
- Attenuation/loss parameters L - the product of all of the loss parameters associated with path length(see below). This is a function of ice conductivity and thickness and includes geometric spreading.
- Bed/basal layer reflectivity parameter R .

I begin with a simplified model and assume a flat homogeneous ice mass situated on flat horizontal substrate and further assume that we can neglect polarization losses and scattering (or at least that they will be constant for a particular experiment). In this case, the returned power can be approximately expressed by a modified form of the *radar equation* (after *Bogorodsky et al.*, 1985):

$$P_r = \frac{P_t}{(4\pi)^2(2H)^2} G^2 F \lambda^2 \frac{1}{L} \quad (3.1)$$

where P_r and P_t are the received and transmitted power, H is the path length, G is the transmitting antenna gain, F is the gain from the focusing effect, L are losses, and λ is the wavelength of the wave. The losses L include L_a the attenuation loss from the two-way travel through the ice, the loss associated with the bed reflection L_R , and the loss due to the transmission downward and upward through the ice surface L_{Td} and L_{Tu} . L_a is an exponential function of depth due to the conductivity of the ice and a consequence of the loss of energy due to joule heating of the ice, as well as the distribution of scattering bodies within the ice. L_{Td} is a function of the dipole antenna interaction with the dielectric interface and L_{Tu} is the loss due to the

Table 3.1: Factors which affect the amount of power received from the bed.

Geometrical Spreading	Loss	A function of travel distance from source.
Absorption	Loss	Primarily a function of ice conductivity, which in turn depends on temperature and chemistry distribution of the ice.
Internal Reflections	Loss	A function of the number and type of internal ice interfaces.
Bed Reflectivity	Loss	A function of basal layer composition and geometry.
Geometrical Focusing	Gain or Loss	A function of reflector geometry, and a result of the fact that the radio wave is transmitted not as a narrow beam but over some angle.
Scattering	Loss	A function of number, size, and type of scattering bodies in the ice.
Antenna Coupling and Gain		A function of surface properties, antenna properties and antenna orientation.
Radio Wave Polarization	Loss	A function of antenna orientation relative to the returned signal. Should be constant given an antenna spacing, orientation.

downward reflection at the ice surface from the dielectric contrast between ice and air. The total loss is then the product of these loss terms,

$$L = L_a L_{Td} L_{Tu} L_R. \quad (3.2)$$

Given the power transmitted, a particular ice structure, and knowledge of the instrumental parameters, we can in principal predict the power returned to the receiver.

For the studies on the Black Rapids Glacier, repeated RES measurements at a given location are used to look for temporal changes in returned energy. We examine the ratio of the power received (P_{r,t_1,t_2}) for repeated measurements at t_1 and t_2 :

$$P_{r,t_1,t_2} = \frac{P_r(t_1)}{P_r(t_2)} = \frac{\frac{P_{t_1}}{(4\pi)^2(2h)^2} G_{t_1}^2 F_{t_1} \lambda^2 \frac{1}{L_{t_1}}}{\frac{P_{t_2}}{(4\pi)^2(2h)^2} G_{t_2}^2 F_{t_2} \lambda^2 \frac{1}{L_{t_2}}} = \frac{L_{t_2}}{L_{t_1}} = \frac{L_{a,t_2} L_{Td,t_2} L_{Tu,t_2} L_{R,t_2}}{L_{a,t_1} L_{Td,t_1} L_{Tu,t_1} L_{R,t_1}} \quad (3.3)$$

Further simplifications can be made by eliminating the factors which we assume to be constant with time.

For repeated measurements at a fixed location with the same instrumentation, the focusing effect F , the path length H and the wavelength λ should be constant in time. If we assume that the ice properties are constant, we can eliminate L_a . If the ice surface properties are assumed constant, then L_{Td} and L_{Tu} will be constant as will the antenna gain factor G .

Thus, if we consider the idealized situation where the equipment, antenna, ice surface, and internal ice properties are constant with time, only a change in bed reflectivity (expressed as the loss term L_R) will result in a change in returned energy. This idealized situation is not what is observed in practice. Other loss terms can vary and may obscure the changes in L_R that are of interest to the study of varying conditions at the glacier bed. It is necessary to correct for variations in these other loss terms. After making these corrections, changes in physical properties of the basal interface and the resulting change in reflectivity of the glacier bed (L_R) are responsible for any observed changes in reflected power.

3.4 *Transmission and Reflection of Electromagnetic Waves*

Once a variation in basal reflectivity has been established from analysis of the RES data, we then have a time series of $L_{R_{t_2}}/L_{R_{t_1}}$. A reflectivity model is necessary to examine the variations in physical properties responsible for the time variation in basal reflectivity. To this end, it is appropriate to review the physics of the propagation and reflection of electromagnetic waves in dielectric media. I will review the derivations of the reflection coefficients for a two and three layer laterally homogeneous dielectric model. The properties of more complex layers such as rough surfaces and/or layers of mixed composition will be mapped onto equivalent homogeneous layers and then calculations will be done with the derived three-layer model. These scenarios encompass the range of expected physical models of the basal layer of a glacier, and will be used to interpret repeat RES measurement data in subsequent Chapters.

The model for the bed reflectivity which I use is a plane parallel, absorbing film situated between two half-spaces of dielectric media. Allowing for conductivity only in the middle layer allows considerable simplification of the derivation. In this model the upper layer is the ice, the middle represents the basal layer, and the bottom represents the underlying bedrock. This model follows an optical model given by (*Born and Wolf*, 1980), and allows an adequate representation of several likely characteristics of the bed reflection. The top layer is characterized by a dielectric constant ϵ_1 (non-conducting layer). The middle layer is characterized by its thickness h , and the real (ϵ_2) and imaginary (represented by the corresponding conductivity σ) parts of the permittivity. This allows for the modeling of a large range of likely basal conditions. The bottom layer is characterized by a real dielectric constant ϵ_3 (non-conductive) and is assumed to be infinite in depth. The infinite depth accounts for the reasonable assumption that no energy is reflected back to the surface from within the bedrock because of high attenuation (skin depths for radio waves of frequency 1-20MHz in most bedrock types are typically less than a single wavelength). Although I do not

explore this possibility, it may be reasonable to assume that a very highly reflective bottom layer (such as would be the case if it were conductive) could be represented by a larger real part of the permittivity ϵ_3 . However, in subsequent Chapters I assume that layer three is non-conducting bedrock. This model calculates the amplitude and phase of the reflected wave for an incident wave of specified amplitude, phase and frequency.

To arrive at this model, I first calculate the reflections produced in two and three-layer non-conducting configuration, and then extend these results to include conductivity in the intermediate layer by introducing a complex index of refraction in that layer. I include the derivations in Appendix A for completeness although they may be found, with varying notation, in a variety electricity and magnetism texts. The resulting equations for the three-layer model are included below.

3.4.1 The three-layer reflectivity model

The quantities ρ_{ij} , ϕ_{ij} , χ_{ij} , τ_{ij} , η , are derived in Appendix A. From these, the transmission (t) and reflection (r) coefficients can be evaluated:

$$r = \rho e^{i\delta_r} = \frac{\rho_{12} e^{i\phi_{12}} + \rho_{23} e^{-2v_2\eta} e^{i(\phi_{23} + 2u_2\eta)}}{1 + \rho_{12}\rho_{23} e^{-2v_2\eta} e^{i(\phi_{12} + \phi_{23} + 2u_2\eta)}} \quad (3.4)$$

$$t = \tau e^{i\delta_t} = \frac{\tau_{12}\tau_{23} e^{v_2\eta} e^{i(\chi_{12} + \chi_{23} + u_2\eta)}}{1 + \rho_{12}\rho_{23} e^{-2v_2\eta} e^{i(\phi_{12} + \phi_{23} + 2u_2\eta)}} \quad (3.5)$$

From (3.4) the reflectivity \mathcal{R} (commonly referred to as the *power reflection coefficient*) \mathcal{R} , and phase of the reflected wave δ_r are:

$$\mathcal{R} = |r|^2 = \frac{\rho_{12}^2 e^{2v_2\eta} + \rho_{23}^2 e^{-2v_2\eta} + 2\rho_{12}\rho_{23} \cos[\phi_{23} - \phi_{12} + 2u_2\eta]}{e^{2v_2\eta} + \phi_{12}^2 \phi_{23}^2 e^{-2v_2\eta} + 2\rho_{12}\rho_{23} \cos[\phi_{12} + \phi_{23} + 2u_2\eta]}, \quad (3.6)$$

$$\tan \delta_r = \frac{\rho_{23}(1 - \rho_{12}^2) \sin(2u_2\eta + \phi_{23}) + \rho_{12}[e^{2v_2\eta} - \rho_{23}^2 e^{-2v_2\eta}] \sin \phi_{12}}{\rho_{23}(1 - \rho_{12}^2) \cos(2u_2\eta + \phi_{23}) + \rho_{12}[e^{2v_2\eta} + \rho_{23}^2 e^{-2v_2\eta}] \cos \phi_{12}} \quad (3.7)$$

From equations 3.6-3.7 and the appropriate ρ and ϕ (Appendix A) we can calculate the reflection power and phase from a layer of known thickness (h), conductivity

(σ) and permittivity (ϵ_2). These relations hold for both polarizations of the electric vector when the appropriate ρ and ϕ are used (Appendix A). Figure 3.1 displays the reflectivity of a water layer between ice and rock as a function of layer thickness. From these curves, we can see that \mathcal{R} varies with both layer conductivity and thickness. With varying layer thickness, one can also see the maxima and minima associated with the constructive and destructive interaction of the impinging wave with the outgoing portion of the wave. A maximum is achieved when the layer thickness is equal to odd quarter wavelengths of the wave in the medium. The wavelength of the electromagnetic wave depends on the conductivity of the layer.

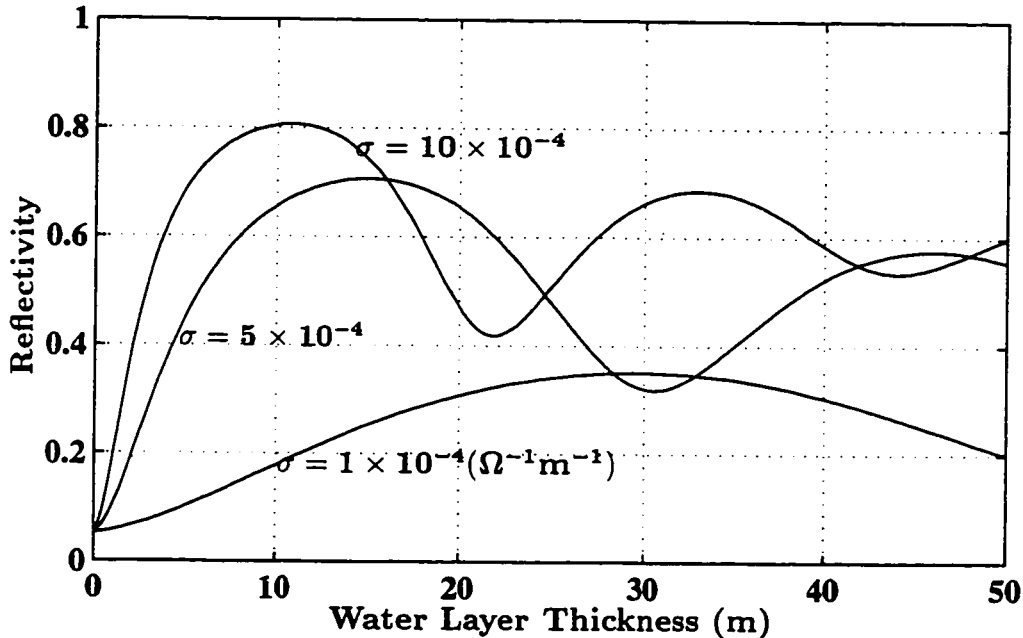


Figure 3.1: Reflectivity for 5 MHz wave impinging on a water layer (layer 2) of given thickness and conductivity situated between ice ($\epsilon_1 = 3.17$) and rock ($\epsilon_3 = 8$). The oscillations in reflectivity are associated with quarter-wavelength interference between incident and reflected wave. The wavelength is shorter for layers of higher conductivity. Note that when layer thickness goes to zero, the reflectivity approaches that for an interface between ϵ_1 and ϵ_3 .

Figure 3.2 gives the contours of constant reflectivity \mathcal{R} and reflected phase angle δ ,

for a water layer between rock and ice. This result clearly demonstrates that changes in either thickness or conductivity of the layer will result in changes in reflectivity and/or phase.

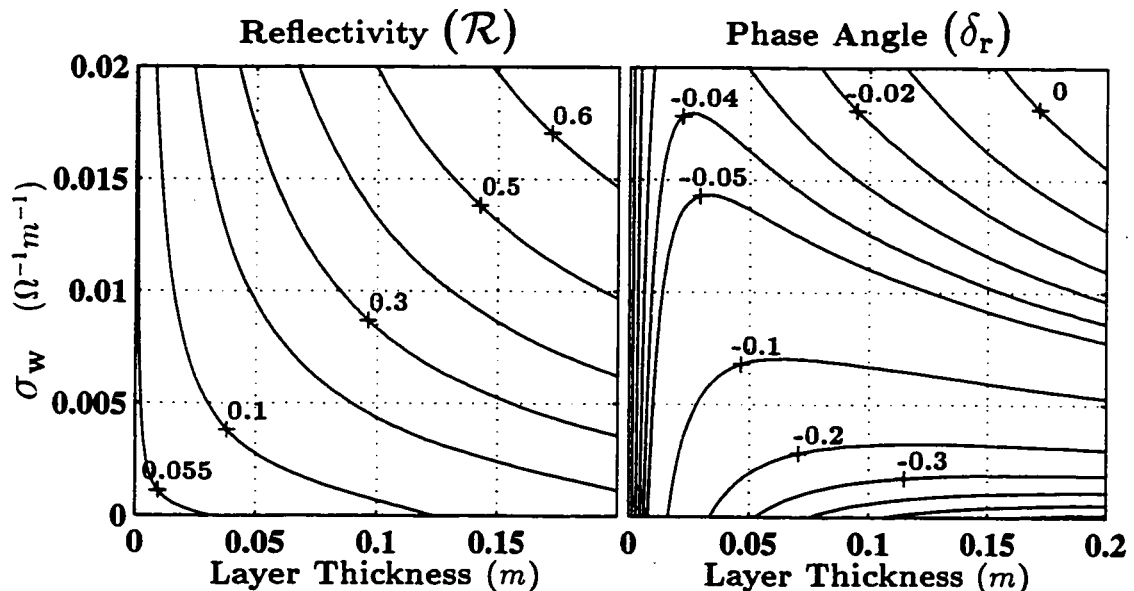


Figure 3.2: Contours of constant reflectivity and phase (radians) for a water layer of given thickness and conductivity situated between ice ($\epsilon_1 = 3.17$) and rock ($\epsilon_3 = 8$).

For reference, Table 3.2 lists the reflection properties, for the interface between pure polar ice and several materials, calculated using the model listed above. In these calculations, I allow the conducting intermediate layer to be infinitely thick (making it essentially a two-layer model). Bed reflections measured with calibrated RES systems have been found to be $\mathcal{R} \sim 0.05$, which is consistent with a non-conducting layer with $\epsilon_{rock} \sim 8$ (e.g., Taylor Dome, West Antarctica, pers. comm. D. Morse, 1997).

3.5 Equivalent Layer Theory

The model developed in the previous section is of limited use because it calculates reflectivity and phase for a homogeneous layer. To extend this model to encompass a

Table 3.2: Dielectric permittivities and conductivities from *Jiracek* (1967), and CRC Handbook of Chemistry and Physics. Reflectivities, dB loss ($-10 \log_{10}(\mathcal{R})$) and skin depths calculated using the reflectivity model.

Reflectivity, Reflection Loss, and Skin Depth for 2, 5MHz at a Boundary Between Pure Ice and Given Materials					
Material	σ_{∞} ($\Omega^{-1}\text{m}^{-1}$)	ϵ_{∞}	\mathcal{R} 2-5MHz	dB Loss 2-5MHz	D_{skin} (m) 2-5MHz
Polar Ice	10×10^{-6}	3.17	0.00-0.00	0-0	300-300
Freshwater	5×10^{-3}	88	0.65-0.55	1.9-2.6	5.5-4.0
Salt Water (35ppt, -2 °C)	3	88	0.98-0.97	0.08-0.13	0.2-0.1
Sea Ice (-5 °C)	1.1×10^{-3}	3.4	0.37-0.21	4.3-6.8	11-7.0
Rocky Land	2×10^{-3}	10	0.49-0.33	3.1-4.8	8.1-5.4
Gravel	3×10^{-3}	3.2	0.55-0.39	2.6-4.1	6.5-4.1
Quartz	10^{-4}	4.3	0.04-0.01	14-20	45-37
Granite	10^{-4}	8	0.08-0.06	11-12	53-48
Sandstone	10^{-5}	10	0.08-0.08	11-11	530-470
Silver	6×10^7	1	1.0-1.0	0.0-0.0	0.0-0.0
Synthetic Permafrosts (-35 °C)					
Tap Water in					
Coarse Sand	8.3×10^{-4}	4.5	0.32-0.17	4.9-7.7	13-8.4
Wet Sand, Clay	7.7×10^{-3}	5	0.69-0.55	1.6-2.6	4.0-2.6
Brown Soil	5.0×10^{-3}	4.4	0.63-0.48	2.0-3.2	5.0-3.2
High-Fe Clay	1.5×10^{-2}	7	0.77-0.66	1.1-1.8	2.9-1.8
High-Al Clay	1.6×10^{-2}	3.3	0.77-0.66	1.1-1.8	2.8-1.8
Limey Mud	7.2×10^{-3}	3.6	0.68-0.54	1.7-2.7	4.2-2.7
Silica Mud	7.4×10^{-3}	1	0.68-0.55	1.7-2.6	4.1-2.6

more complicated layer geometry, a common approach is to represent it by an equivalent layer. We can then use the equivalent layer in the three-layer model outlined above (e.g., *Hunderi*, 1980). The equivalent medium approach is appropriate when the dimensions of the inhomogeneities and all correlation lengths in the heterogeneous material are much smaller than the wavelength of the radiation. This is an appropriate approximation for the case of RES on temperate glaciers, where the wavelength in the present studies was $\sim 35 - 85m$ (5-2MHz), while the length scales of subglacial and englacial heterogeneities are expected to be on the order of 10^0 meters (e.g., *Hooke et al.*, 1990; *Kamb*, 1987). In this case, the reflectivity characteristics of a layer may be described in terms of its thickness and an effective dielectric constant $\bar{\epsilon}$.

In the following subsections, I review some methods for calculating equivalent layers. First I review models for determining an effective dielectric constant for mixed dielectric materials. Second, I review methods for determining an effective dielectric constant for heterogeneous rough surfaces, and finally I discuss a model for determining the effective conductivity of a till layer.

3.5.1 Mixtures of Materials

Two methods for predicting the effective dielectric permittivity of mixtures $\bar{\epsilon}$ are listed by *Glen and Paren* (1975), and are among those reviewed by *van Beek* (1967). Both of these methods assume that one material (with permittivity ϵ) is uniformly dispersed in a second material (with permittivity ϵ_m). One relation is known as Böttcher's mixing equation:

$$\frac{\bar{\epsilon} - \epsilon_m}{3\bar{\epsilon}} = \frac{V_2(\epsilon - \epsilon_m)}{\epsilon + 2\bar{\epsilon}}$$

$$\bar{\epsilon} = \frac{-b + \sqrt{b^2 + 8\epsilon\epsilon_m}}{4}, \quad \text{where } b = \epsilon - 2\epsilon_m - 3V_2(\epsilon - \epsilon_m) \quad (3.8)$$

and V_2 is the volume fraction of included material. The other relation is called Looyenga's equation:

$$\bar{\epsilon}^{1/3} = V_2\epsilon^{1/3} + (1 - V_2)\epsilon_m^{1/3}$$

$$\bar{\epsilon} = (V_2(\epsilon^{1/3} - \epsilon_m^{1/3}) + \epsilon_m^{1/3})^3 \quad (3.9)$$

Considering the case of a till layer mixture of rock ($\epsilon_m = 8$) interspersed with water ($\epsilon = 88$), we see that these two methods differ only slightly (Figure 3.3), and both relations apparently agree with experiments over a large range of included materials (Glen and Paren, 1975). I use Looyenga's equation (Equation 3.9) in subsequent calculations.

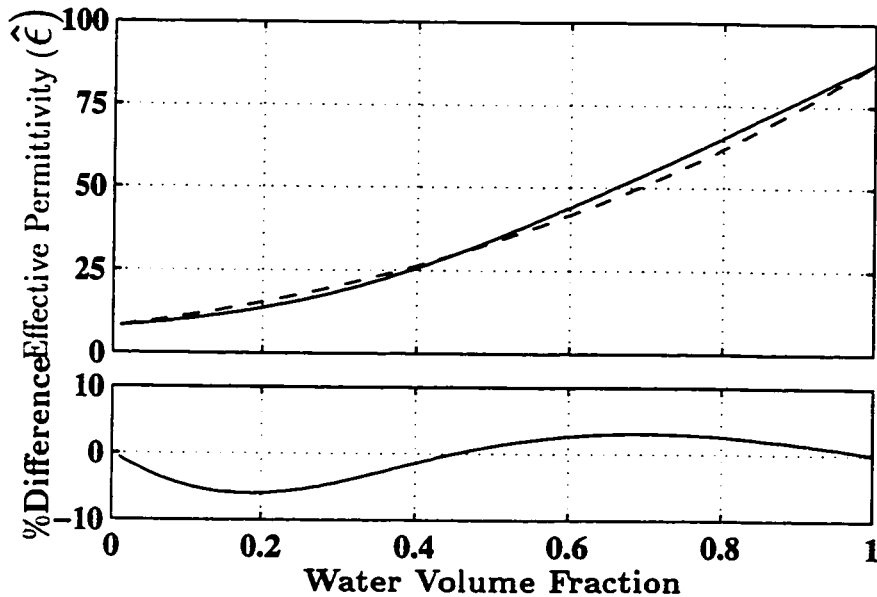


Figure 3.3: Upper panel shows the effective dielectric permittivity for a layer of rock ($\epsilon_{rock} = 8$), and a given volume fraction of water ($\epsilon_{water} = 88$), calculated using the methods of Looyenga (solid line) and Böttcher (dashed line). The lower panel shows that the difference between the two methods is less than 5%.

The dielectric permittivity of a dry glacier bed should be $7 < \epsilon < 11$ (the values given for solid limestone and basalt respectively). While conductivities should be on the order of 10^{-8} S m^{-1} . Most measurements of frozen ground indicate $4 < \bar{\epsilon} < 7$ and conductivities less than 10^{-3} S m^{-1} (e.g., Jones, 1987, and references therein). Arcone and Delaney (1982) list the dielectric permittivity of ice-rich gravel as $\bar{\epsilon} = 5.1$. Using equation 3.9, with $\epsilon_{ice} = 3.2$ and $\epsilon_{rock} = 8$, this quoted value corresponds to a porosity

of $\sim 40\%$. *Hoekstra and Delaney* (1974) found that the relation between $\bar{\epsilon}$ and water content is insensitive to the rock material.

3.5.2 Heterogeneous Surfaces

Several authors have represented the optical properties of a heterogeneous surface by a smooth homogeneous film with effective properties. Although in some instances the results are not quantitatively correct, they demonstrate the essential qualitative correctness of this kind of approach for calculating the effective properties of a heterogeneous surface (*Hunderi*, 1980). *Chan and Marton* (1974a), provide a method for approximating the effective dielectric properties of a heterogeneous surface by an equivalent layer. The relations for the effective dielectric constants for the heterogeneous surface for \mathbf{E} parallel and to the surface (TE) and for \mathbf{E} perpendicular (TM) are:

$$\frac{\bar{\epsilon}_{TM} - 1}{\bar{\epsilon}_{TM} + (4\pi - a)/a} = q \frac{\epsilon - 1}{\epsilon + (4\pi - a)/a}, \quad (3.10)$$

$$\frac{\bar{\epsilon}_{TE} - 1}{\bar{\epsilon}_{TE} + a/(2\pi - a)} = q \frac{\epsilon - 1}{\epsilon + a/(2\pi - a)}, \quad (3.11)$$

where q (ranges from 0:1) gives a qualitative description of the degree of roughness of the surface (as q approaches 1, the smoother the surface and the closer q is related to the fractional surface coverage), $\bar{\epsilon}$ is the effective dielectric constant, and a is a value relating to the arrangement of the surface roughness features. If $a = \frac{4}{3}\pi$, and $\bar{\epsilon}_{TE} = \bar{\epsilon}_{TM}$ the relations collapse to $\bar{\epsilon}_{TE} = \bar{\epsilon}_{TM}$. If $a > \frac{4}{3}\pi$ it indicates that the particles are oriented to give a stronger dipole moment for the TE polarization (\mathbf{E} parallel to surface), if $a < \frac{4}{3}\pi$ a stronger dipole moment for the TM polarization (\mathbf{E} perpendicular to surface). Thus, the rough surface is represented by a smooth homogeneous surface film having effective optical properties. The authors demonstrate experimentally that this rough surface model works well for interpreting reflection measurements (*Chan and Marton*, 1974b).

In practice, we can not measure the polarization of the transmitted or reflected electric field with our mono-pulse radio echo-sounding system, which prohibits a quantitative application of this theory. We can however, make qualitative estimates of the variation of effective dielectric permittivity for a range of parameters. We first assume that $a = \frac{4}{3}\pi$ so that the values for both TM and TE polarizations are equal. We can then approximate the variation of the effective permittivity using either Equation 3.11 or 3.10. Assuming that q is directly related to the fractional surface coverage, Figure 3.4 shows the variation of the effective permittivity with q . Though this is a considerable simplification of the theory since we are neglecting the effect of the electric field polarization as well as the importance of dipole characteristics of the roughness features a , one can estimate the variation of the effective dielectric permittivity for a given fractional coverage - though, as pointed out by the authors, the values for small q are not valid.

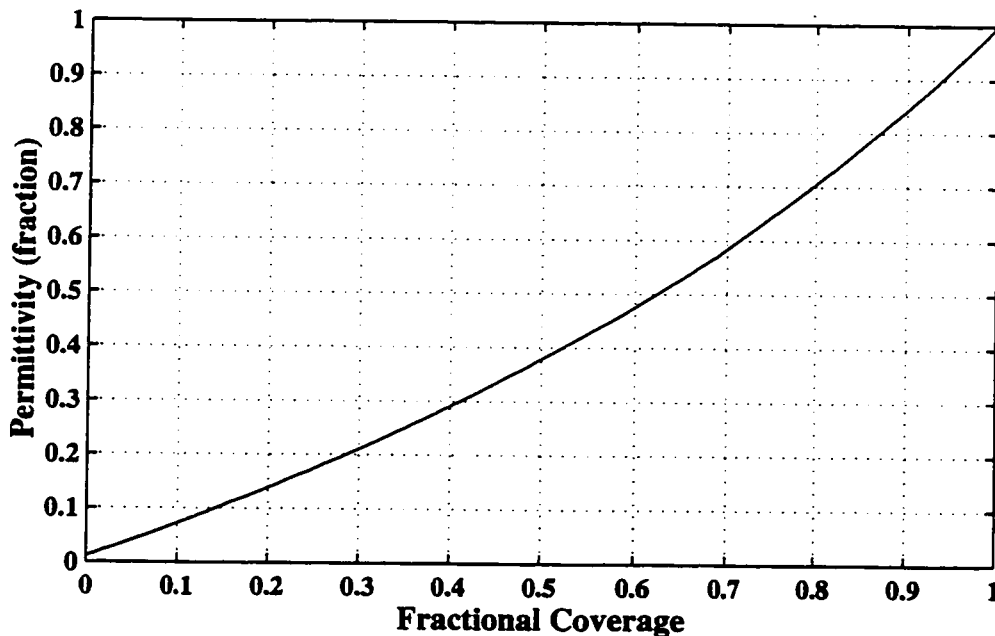


Figure 3.4: The effective dielectric permittivity for a range of fractional surface coverage from 0 to 1 (total coverage). The effective permittivity is plotted as the fraction of the permittivity for the covering material.

3.5.3 Effective Conductivity Models and Measurements

Keller and Frischknecht (1966) give an empirical relationship for the bulk conductivity of subglacial debris of weakly cemented rocks with porosity between 25% and 45%:

$$\frac{1}{\bar{\sigma}} = \frac{0.88}{\sigma_w} \phi^{-1.37} \quad (3.12)$$

where $\bar{\sigma}$ is the bulk conductivity, σ_w is the conductivity of the water in the pores, and ϕ is the porosity.

The conductivity of subglacial water σ_w has been measured in several locations either by means of sampling water through boreholes or in outflow streams. *Collins* (1981) found, during a year-long study of the outflow at the terminus of Gornergletscher, Switzerland, a maximum conductivity of $1.2 \times 10^{-2} \text{ S m}^{-1}$. *Keller and Frischknecht* (1966) mention that *in situ* measurements of pore-water conductivities are generally greater than $1 \times 10^{-2} \text{ S m}^{-1}$ for sandstones or $1 \times 10^{-1} \text{ S m}^{-1}$ for siltstone. *Jones* (1987) measured surface water conductivity on the Trapridge Glacier at $2.8 \times 10^{-3} \text{ S m}^{-1}$ and ground water from the surrounding areas up to $6.5 \times 10^{-2} \text{ S m}^{-1}$. *Raymond et al.* (1995) measured several properties of the glacial outflow from Black Rapids Glacier and Fels Glaciers between late May and early September in 1989. For Black Rapids the average water conductivity was $\sim 3 \times 10^{-3} \text{ S m}^{-1}$ with a maximum $\sim 8 \times 10^{-3} \text{ S m}^{-1}$. For Fels Glacier outflow, the average and maximum conductivities, during approximately the same period in 1987, were $\sim 1 \times 10^{-2} \text{ S m}^{-1}$ and $\sim 1.5 \times 10^{-2} \text{ S m}^{-1}$ (*Raymond et al.*, 1995). In May 1997 the conductivity of subglacial waters sample from boreholes at Black Rapids Glacier was $\sim 3 \times 10^{-3} \text{ S m}^{-1}$ (Ian Willis, pers. comm.), consistent with values measured in the outflow stream.

These measurements indicate that the conductivity of subglacial water ranges from $\sim 10^{-3} - 10^{-2} \text{ S m}^{-1}$. Table 3.3 lists the reflectivity between ice and a half space of till, calculated using the reflectivity model, the effective conductivity model (Equation 3.12) and the effective dielectric permittivity (Equation 3.9) for the likely

Table 3.3: Calculations of \mathcal{R} for 5 MHz wave incident on composite basal layer of infinite thickness with given porosity ϕ , water conductivity σ_w and bulk dielectric permittivity $\bar{\epsilon}$.

Bed Reflectivity, Reflection Loss, for 5 MHz					
ϕ	$\sigma_{\text{water}}(\text{S m}^{-1})$	$\bar{\epsilon}$	$\bar{\sigma}(\text{S m}^{-1})$	\mathcal{R}	dB Loss
0.20	3×10^{-3}	15.4	3.8×10^{-4}	0.17	-7.7
0.20	12×10^{-3}	15.4	1.5×10^{-3}	0.30	-5.2
0.40	3×10^{-3}	26.4	9.7×10^{-4}	0.29	-5.4
0.40	12×10^{-3}	26.4	3.9×10^{-3}	0.46	-3.4

range of porosity ϕ 20-40%, (e.g., *Boulton and Hindmarsh*, 1987) and the measured range of water conductivity σ_{water} . This demonstrates that the reflectivity of a thick porous till layer increases with increasing porosity (because of the resulting increase in dielectric permittivity) and increasing pore-water conductivity. The results will vary if thin layers (relative to the wavelength used to investigate the layer) underlain by a substrate are considered because of the interaction between reflected waves from each of the two interfaces.

3.6 Summary

An integrated three layer reflectivity model can be formed using the three-layer model (*Born and Wolf*, 1980) together with Looyenga's dielectric mixing model, an effective conductivity model (*Keller and Frischknecht*, 1966), and an effective layer model for heterogeneous surfaces (*Chan and Marton*, 1974a). This model can be used to investigate the reflectivity for layers of glaciological interest such as thin water films or saturated porous tills. This model allows limits to be placed on the physical changes that give rise to measured changes in radio wave power reflected from the bed.

Chapter 4

THE TOPOGRAPHY AND HYDRAULIC POTENTIAL OF BLACK RAPIDS GLACIER, ALASKA

4.1 Summary

The surface and bed topography of Black Rapids Glacier was determined using a combination of radio echo-sounding (RES) measurements, global positioning satellite (GPS) surveying, and United States Geological Survey (USGS) topographic maps. From these data, contour maps of bedrock and surface topography and the hydraulic potential are calculated. It is found that the hydraulic potential favors the development of a single drainage system at the deepest point of the subglacial valley.

4.2 Introduction

The drainage system of a glacier is affected by the distribution of the subglacial hydraulic potential over the bed. Calculation of this potential requires knowledge of ice thickness and surface topography.

The subglacial hydraulic potential Φ (in Pascals) can be estimated according to *Shreve* (1972),

$$\Phi = \rho_{water} * g * B + \rho_{ice} * g * (H - B). \quad (4.1)$$

where $\rho_{water}=1000 \text{ kg m}^{-3}$ and $\rho_{ice} = 917 \text{ kg m}^{-3}$ are the densities of water and ice, $g = 9.8 \text{ m s}^{-2}$ is the acceleration of gravity, H and B are the surface and bed elevation measured in meters above sea level.

Given maps of the ice surface elevation and ice thickness distribution, it is possible

to calculate Φ and predict the route of subglacial drainage beneath a glacier. For example, *Richards et al.* (1996) used RES ice thickness data and surveys of surface topography to calculate the subglacial hydraulic potential for Haut Glacier d'Arolla, Valais, Switzerland. The results predicted that two distinct drainage channels should be present in the lower reaches of this glacier. Subsequent borehole drilling (*Sharp et al.*, 1993), and dye tracing (*Nienow et al.*, 1996) established that the predictions were accurate. This example demonstrates the possible use of this calculation in predicting the pattern of the subglacial hydrological system of a glacier.

The surface topography of Black Rapids Glacier, Alaska (BRG) has been established by photogrammetric methods and is available from USGS maps. However, knowledge of the ice thickness distribution of this glacier was limited to a few tens of RES spot measurements taken at various locations along the glacier length (*Heinrichs et al.*, 1995), which was insufficient to establish a detailed map of subglacial hydraulic potential.

In this chapter, I outline the measurement and analysis methods used to calculate the subglacial hydraulic potential of Black Rapids Glacier (BRG) from new RES data, and show that the probable drainage system configuration predicted by theory is a simple single system centered in the deepest part of the subglacial valley.

4.3 Methods

At the start of the 1993 BRG field season, the UW MKI RES profiling system (see chapter 2) was used to map the ice thickness distribution of a section of the glacier. Transverse profiles with ~ 15.7 m record spacing were made at distances of 6.5, 8, 10, 11, 12, 13, 14, 15, 16, 17, 18, and 20 km from the glacier head. These profiles span as much of the glacier width as was navigable with the snow-machines and were on average ~ 2 km long. A longitudinal profile connected the centers of the transverse profiles. Figure 4.1 displays the locations of these profiles within the outline of the

glacier. Locations of the profiles were determined by kinematic GPS surveying¹. The glacier outline was estimated from USGS maps².

The ice thickness distribution was determined from the RES profiles using a series of data analysis techniques. The RES data for each profile were first bandpass filtered to remove environmental and system noise. The data were then migrated using maximum convexity technique (*Robinson and Treitel, 1980*)³ and using a wave propagation speed of $168 \pm 2 \text{ m } \mu\text{s}^{-1}$ in ice (e.g., *Glen and Paren, 1975; Bogorodsky et al., 1985*). Ice thickness was determined as the delay time to the arrival of the maximum value of the positive-going (arrives first) half of the bed reflection pulse. Uncertainty in the ice thickness determination arises from uncertainty in the wave speed ($\sim 0.5\%$) and uncertainty in selecting the migrated bed reflection ($0.15 \mu\text{s} \sim 15 \text{ m}$). Transverse profiles from Km-14 (Fig. 4.2), Km-16 (Fig. 4.3), and Km-18 (Fig. 4.4) are displayed below to show the data together with the ice thickness calculated by migration of RES profiles. These three profiles are referenced in later chapters because they were repeated several times over the course of the field season to detect changes in the reflection characteristics of the bed.

Surface topography was determined primarily from kinematic GPS surveying. These data were supplemented by the pressure transducer record from the RES pro-

¹ The GPS surveying was done primarily by Keith Echelmeyer of UAF, and the reduction of those data by Jeanette DeMallie of UAF using the 1927 North American Datum.

² USGS 1966, 1:63,350 *Mt. Hayes B-6, Quadrangle* and *Mt Hayes C-5, Alaska* were used to digitize the location and elevation of the Black Rapids Glacier outline. These maps were constructed using horizontal datum: 1927 North American Datum, and vertical datum: 1929 Sea Level Datum (subsequently named National Geodetic Vertical Datum 1929).

³ Migration is a technique used to correct for the fact that in RES, energy is transmitted as a wavefront over a large solid angle rather than in a narrow beam. Because of this, a particular reflection is constrained in space to an ellipse, rather than to a distance directly below the instrument. Migration of these data approximately corrects for this ambiguity, and allows for the actual ice thickness to be determined.

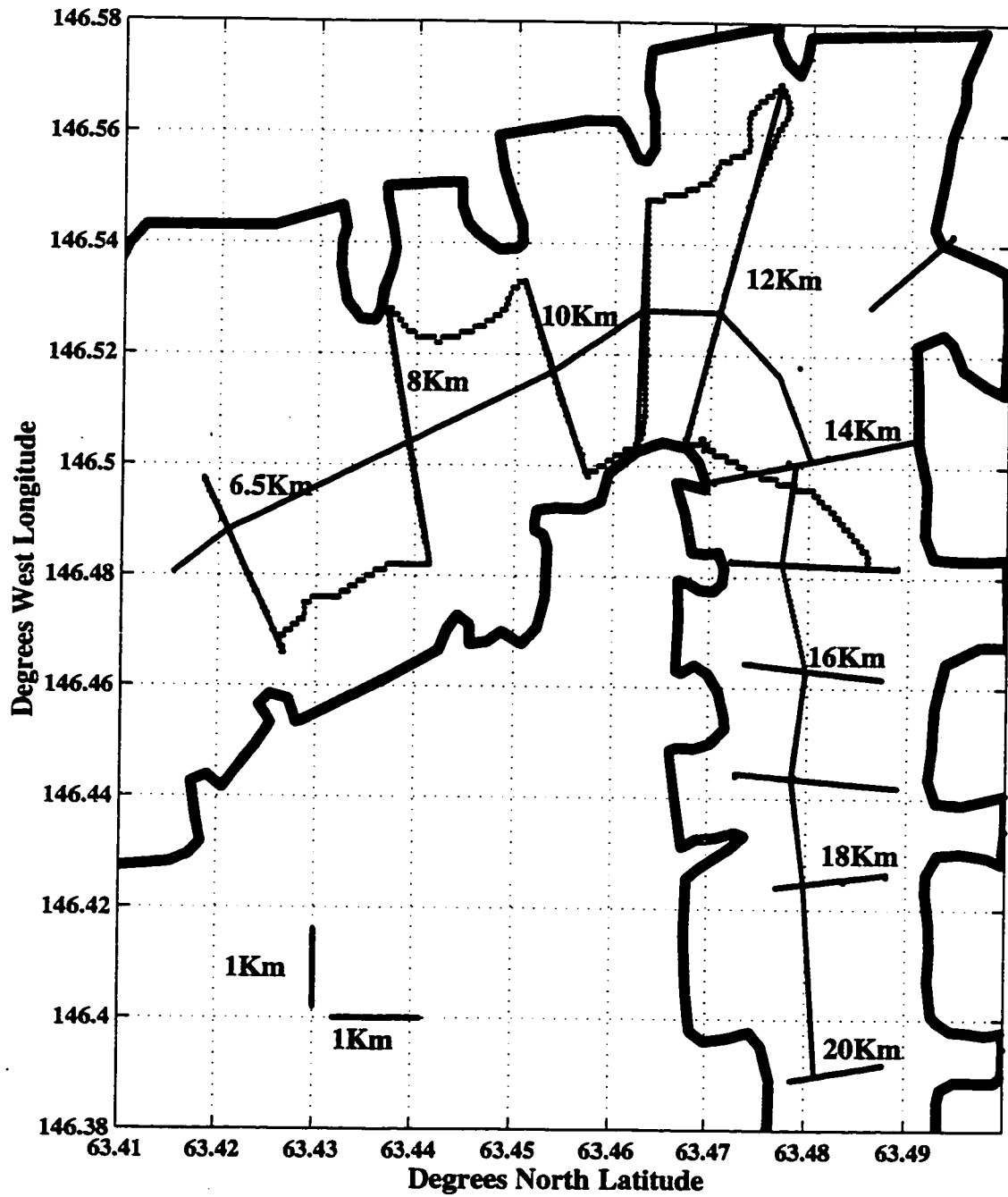


Figure 4.1: The outline of Black Rapids Glacier, AK, showing RES traverse lines (straight solid thin line segments) and GPS kinematic survey paths (all thin line segments).

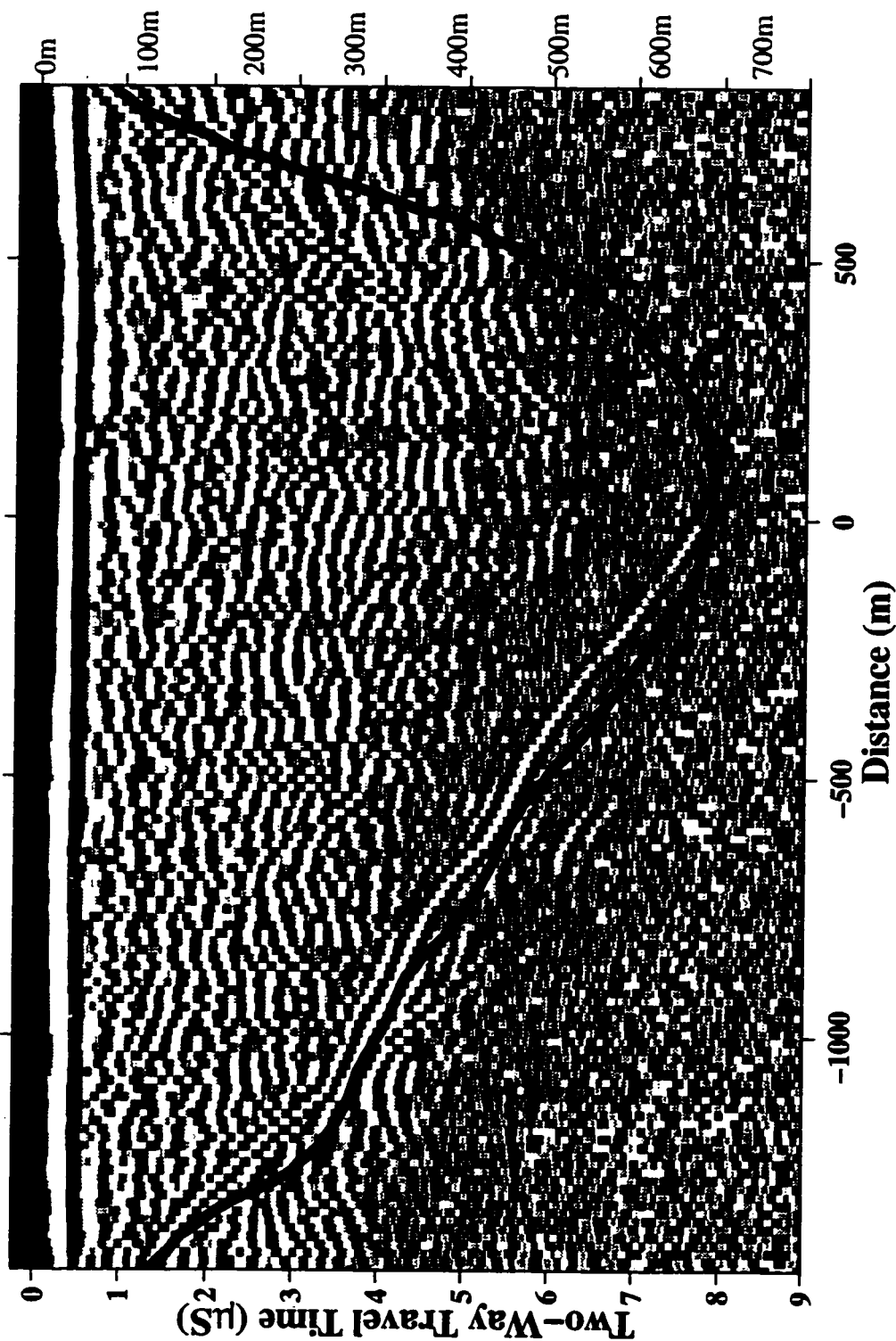


Figure 4.2: Black Rapids Glacier, 5 MHz Km-14 transverse profile, 3 June, 1993. Surface elevation is corrected using the pressure record. The left vertical axis is the two-way travel time, and the right vertical axis gives an approximate depth scale. The migrated depth, shown as a heavy black line, has uncertainty of $\pm(0.5\%+15 \text{ m})$. View is down-flow and North is approximately to the left. Vertical exaggeration $\sim 1.88 : 1$.

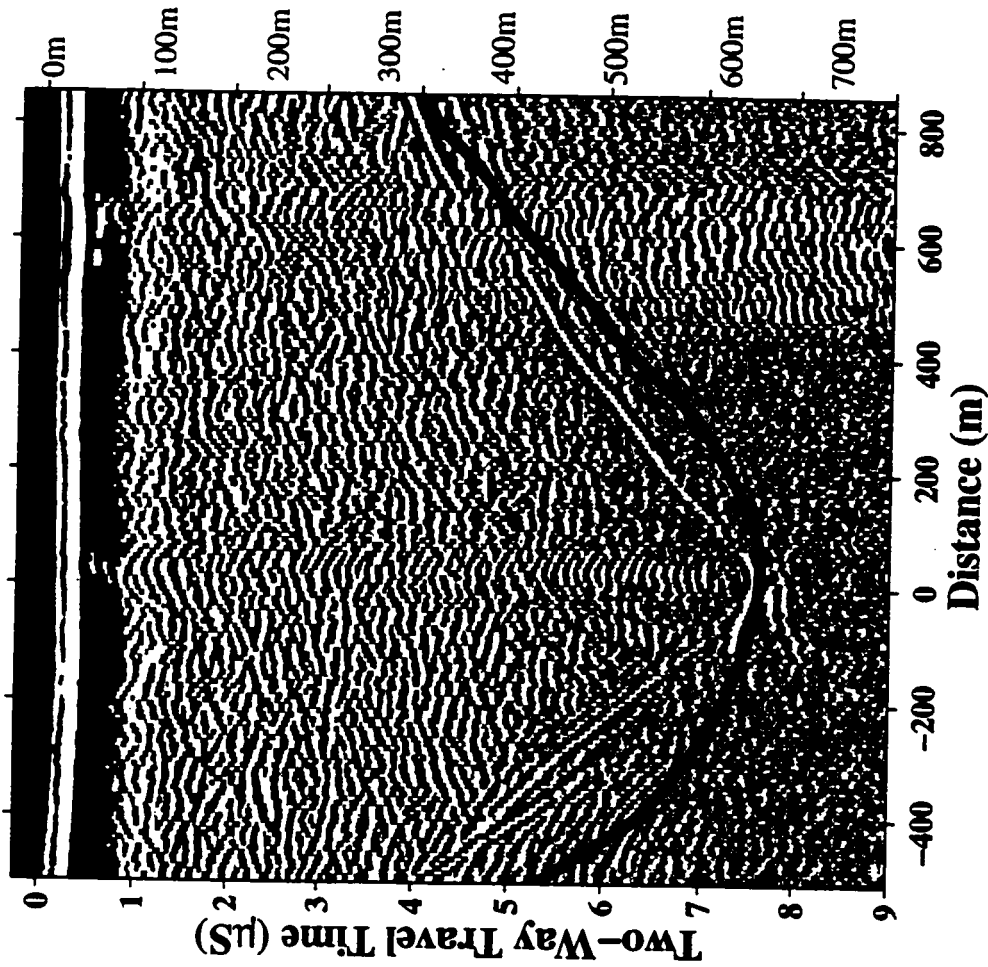


Figure 4.3: Black Rapids Glacier, 5 MHz Km-16 transverse profile, 10 June, 1993. Surface elevation is corrected using the pressure record. The left vertical axis is the two-way travel time measured in the data, and the right vertical axis gives an approximate depth scale. The migrated ice thickness, shown as a heavy black line, has certainty of $\pm(0.5\%+15\text{ m})$. View is down-flow and north is approximately to the left. Vertical exaggeration $\sim 1.88 : 1$.

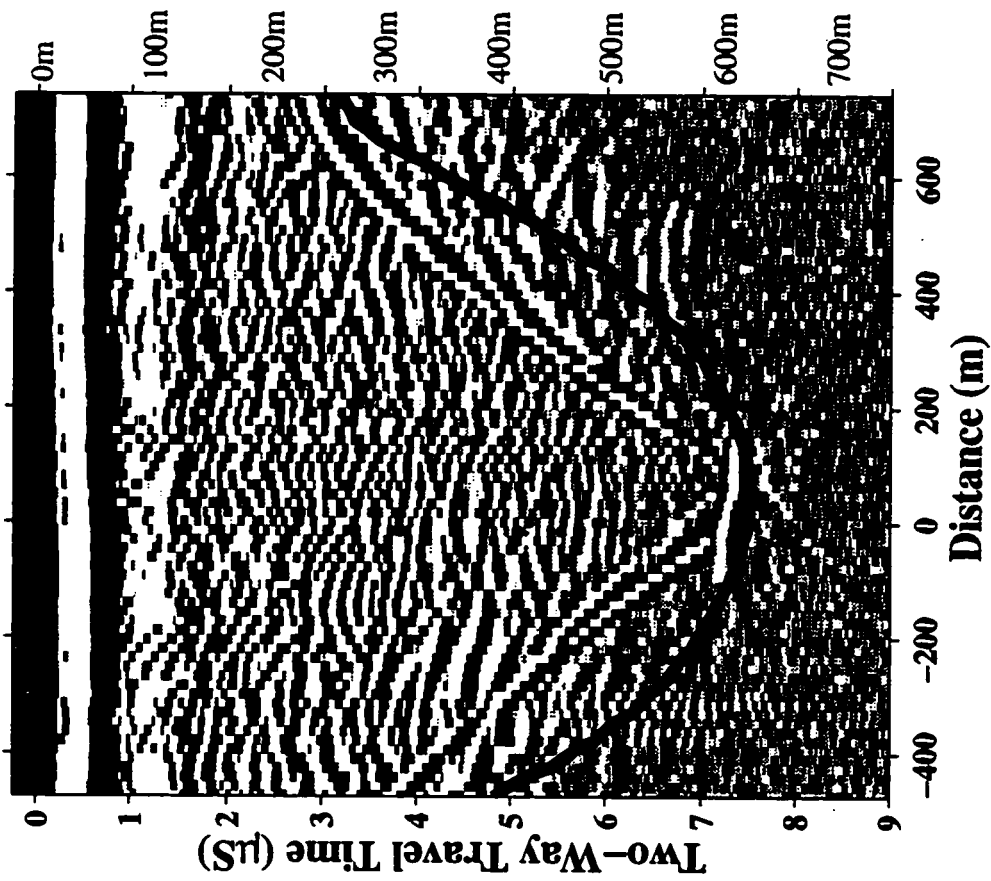


Figure 4.4: Black Rapids Glacier, 5 MHz Km-18 transverse profile, 23 May, 1993. Surface elevation is corrected using the pressure record. The left vertical axis is the two-way travel time, and the right vertical axis gives an approximate depth scale. The migrated ice thickness, shown as a heavy black line, has uncertainty of $\pm(0.5\%+15 \text{ m})$. View is down-flow and north is approximately to the left. Vertical exaggeration $\sim 1.88 : 1$.

files, which was used to interpolate the surface topography between known GPS locations. Elevations of the digitized glacier outline were also used to determine the surface elevations. The latitude and longitude of each record within the profile was determined by interpolating between known GPS-located points using the odometer from the RES system.

To display the results of this analysis, I use latitude/longitude (NAD 1927) as my coordinate system rather than the local coordinate system used by *Heinrichs et al.* (1995, 1996) because of ambiguities in relating that system to latitude/longitude (Jeanette DeMallie, 1994 pers. comm.). For display purposes, I scale the axes appropriately to account for the differing distance represented by a degree of latitude and longitude. At 63 deg latitude, 1km is approximately 1.404×10^{-2} degrees longitude, and 8.903×10^{-3} deg latitude.

4.4 Results

4.4.1 Surface and Bedrock Topography

The *Generic Mapping Tool* (GMT) package (*Wessel and Smith, 1995*) was used to interpolate the surface elevation (Fig. 4.5) and ice thickness (Fig. 4.6) data to 2 second longitude by 20 second latitude grids. MATLAB⁴ contouring routines were used for displaying the gridded data. Ice thickness data are dense (spacing ~ 15 m) along the transverse RES profiles but are sparse (spacing ~ 1000 m) along the direction of ice flow. The grid size is chosen to account for this disparity in data density in the two directions. Along the lower portion of the surveyed section (from Km-14 down to Km-20), ice thickness information is more dense in the north-south direction (along the cross profiles) and less dense in the east west direction (Fig. 4.1). An optimal grid for this section would be more dense in the north-south direction and

⁴ MATLAB is a registered trademark of The MathWorks, Inc., 24 Prime Park Way, Natick, MA 01760, 508-647-7000.

less dense in the east-west direction. The opposite is true for the upper portion of the glacier because the flow direction (and hence the orientation of greater data density) is approximately at a right angle to the lower section. The grid spacing (2 seconds longitude by 20 second latitude) was chosen to optimize the results for the lower section of the surveyed region (Km-12:20) because it is the location of concentrated studies by USGS, UAF, and UW investigators.

A side effect of this grid spacing is that the contours in the upper portion of the glacier are less accurate near the edges of the glacier. No ice thickness data were obtained on the many tributary glaciers. Thus, the surface and bed topography are not accurate in those regions. Finally, the Susitna glacier flows approximately westward from a divide approximately 3 km west of Km-14 (Fig. 4.1), and is not included in these data which results in the ice thickness in the northwest corner of these maps being artificially shallow. These regions have been masked out in the figures. Bedrock elevation (Fig. 4.7) was calculated as the difference between the surface elevation and ice thickness.

As a check of consistency after gridding the data, I compare the original migrated RES depth data with the gridded depth data. Figure 4.8 displays the residual (input data minus the gridded data) and shows that discrepancies are generally less than 10 m for the Km-14, 16 and 18 profiles, indicating the gridding process did not introduce significant errors. Some difference (≤ 8 m) may be caused by co-registration problems, the gridded data were not always at the same latitude/longitude locations as the original data.

4.4.2 The Subglacial Hydraulic Potential

We now calculate the subglacial hydraulic potential using Equation 4.1. Results are shown in Figure 4.9. Water flow is predicted to be routed preferentially in the direction opposite maximum potential gradient. Because the subglacial valley walls are steep (Fig. 4.7) and the ice surface is relatively flat (Fig. 4.5), the lowest potential

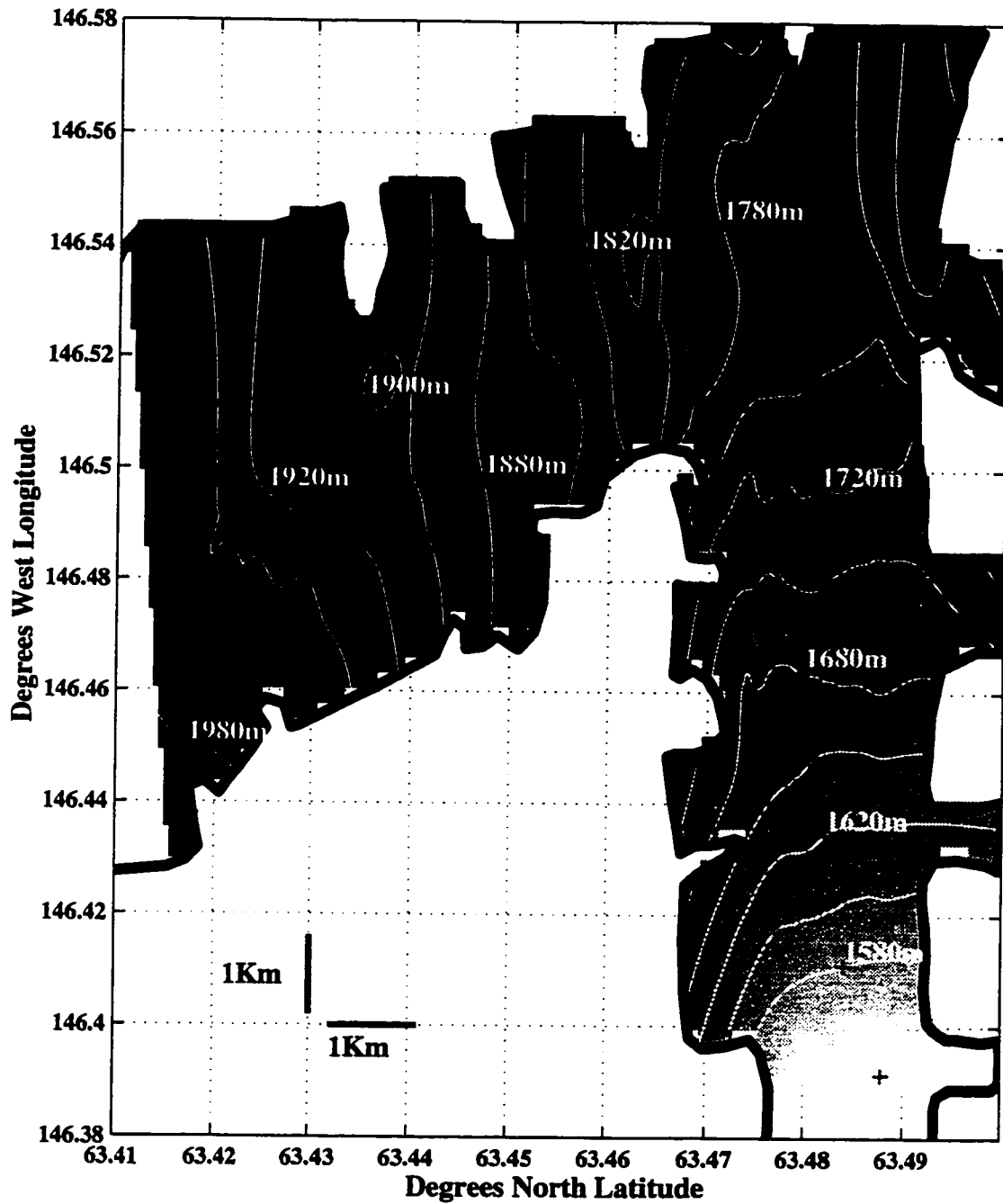


Figure 4.5: 25 meter interval contour map of surface elevations on BRG. Surface elevations are in meters above NGVD 1929. Data are from RES and GPS traverses shown in figure 4.1.

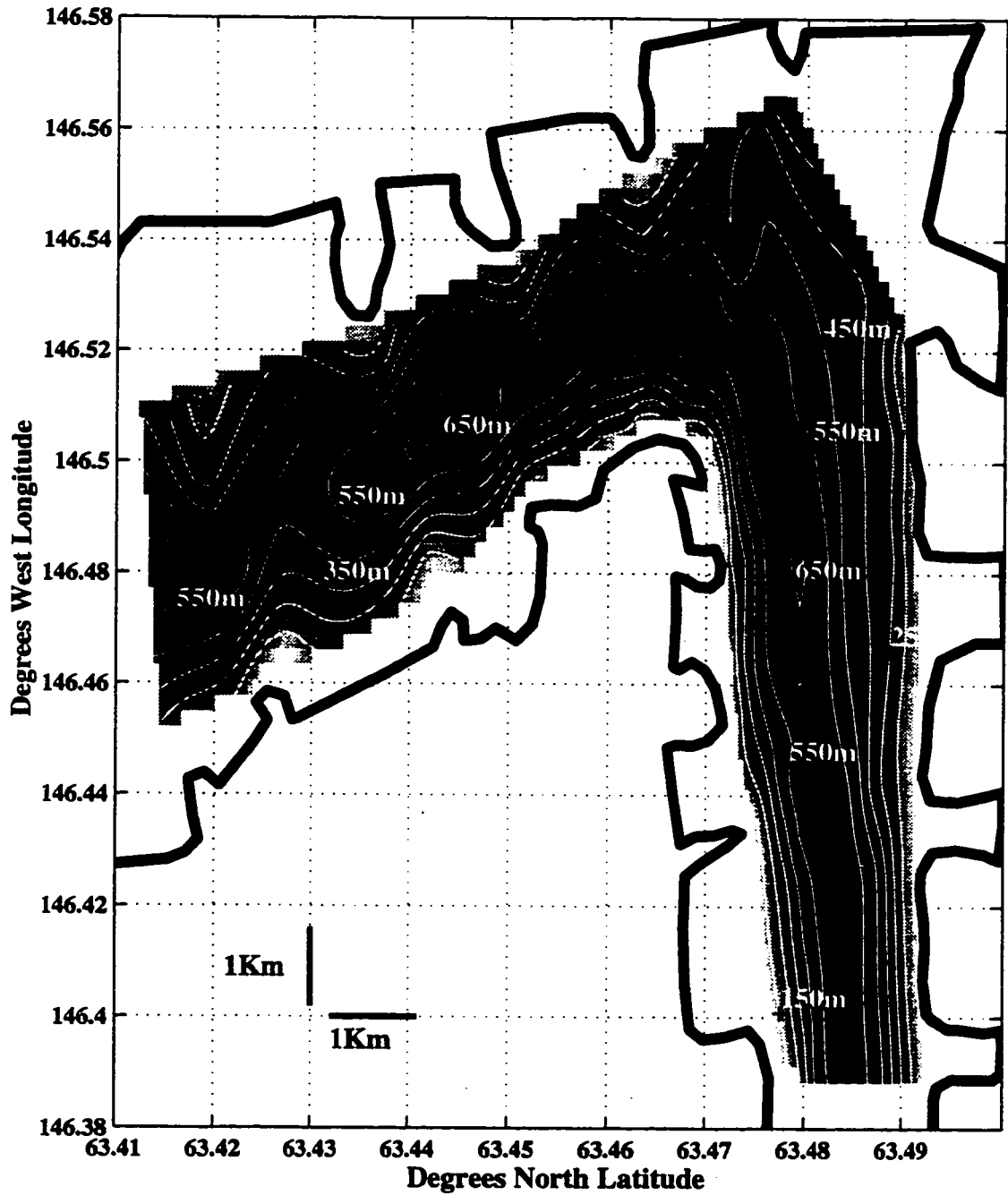


Figure 4.6: 100 meter interval contour map of ice thickness of BRG. Data are from RES traverses shown in figure 4.1.

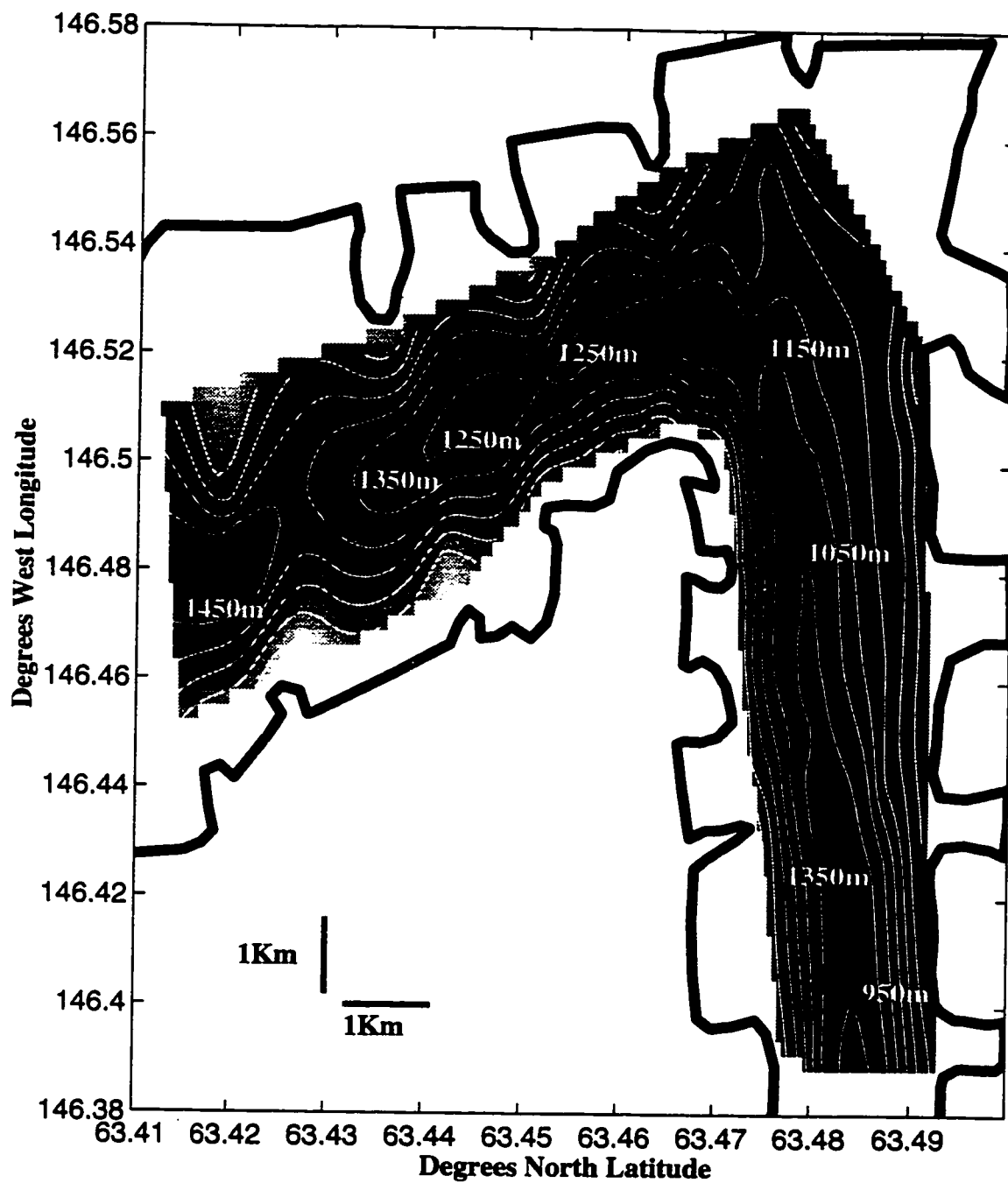


Figure 4.7: 100 meter interval contour map of BRG bedrock elevation. Surface elevations are in meters above NGVD 1929. Data are from RES and GPS traverses shown in figure 4.1.

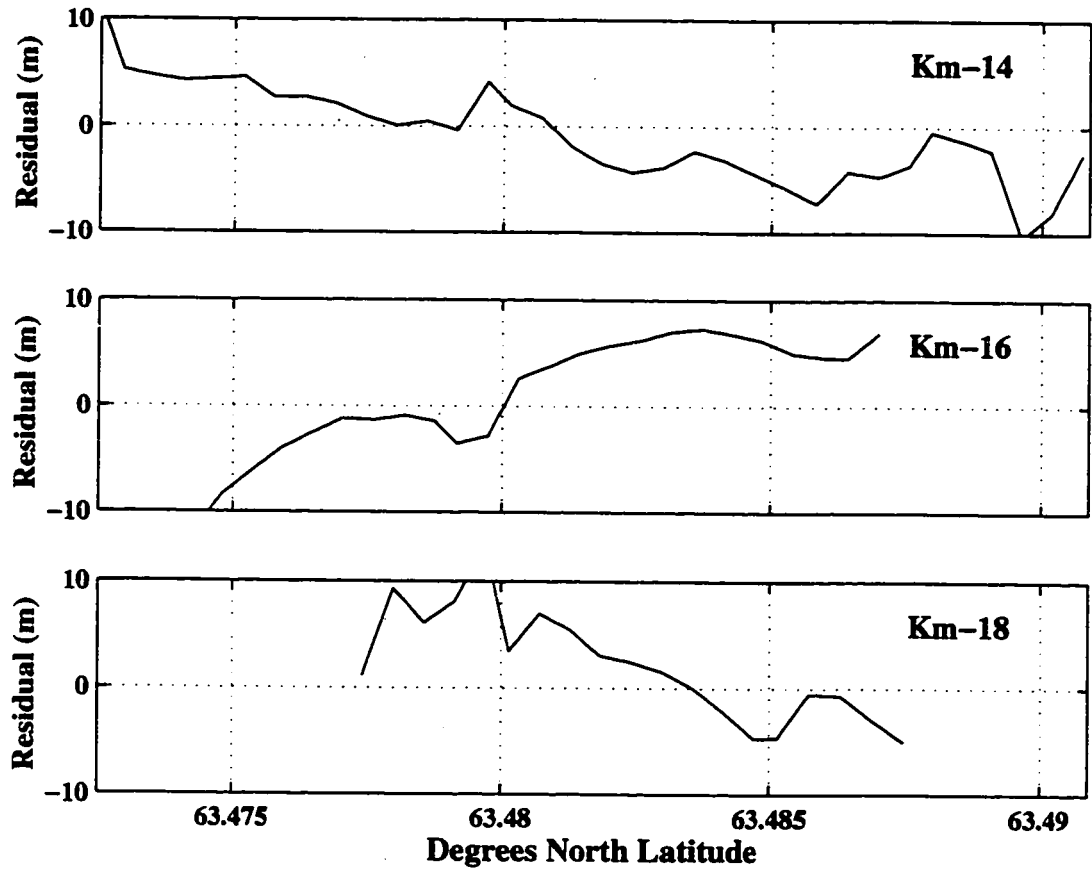


Figure 4.8: Residual calculated by subtracting the gridded ice thickness along the Km-14, Km-16 and Km-18 profiles from the migrated RES depths. If the gridding process introduced no artifacts, residuals would be ≤ 8 m.

in the cross sections is at the lowest point in the bed elevation. Thus, there will be a tendency for a single drainage channel along the bedrock trough in the lower section of this map (Km10-20).

Much of the meltwater input to Black Rapids Glacier originates from the tributary glaciers and from snow melt from the surrounding valley walls. Meltwater entering the subglacial system from the margins will be routed to the center of the sub-glacial valley. Meltwater originating on the glacier surface should also be directed toward the center of the subglacial valley. Given this expectation, one may expect the largest changes in subglacial structure to occur near the center of the subglacial valley during times of increasing water flux.

4.5 Summary

The subglacial hydraulic potential of Black Rapids Glacier, Alaska was determined by combining surface topography (from USGS maps and GPS surveying) and ice thickness distribution (from migrated RES measurements). The result (Figure 4.9) predicts that any meltwater which enters the subglacial system will be preferentially routed toward the center of the glacier, and that flow should occur in a single channel centered in the deepest portion of the bedrock trough. The implications of the subglacial potential in the region from Km-10 to Km-20 are discussed in Chapter 6.

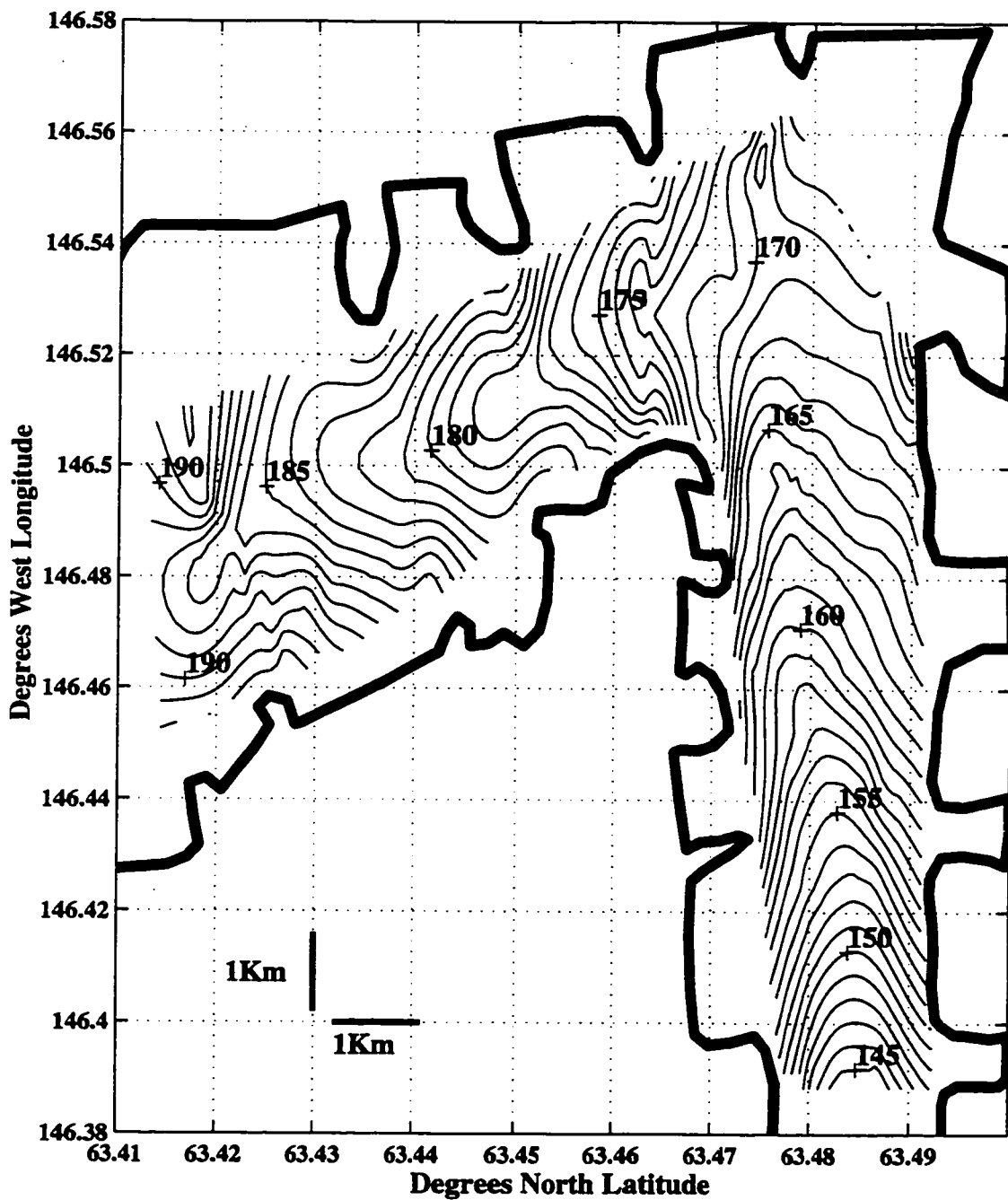


Figure 4.9: 1 bar interval contour map of subglacial hydraulic potential of Black Rapids Glacier, Alaska calculated using the calculated bed (Fig. 4.7) and surface elevations (Fig. 4.5).

Chapter 5

RADIO ECHO-SOUNDING INVESTIGATION OF BASAL PROPERTIES, BLACK RAPIDS GLACIER, ALASKA I: MEASUREMENTS AND DATA ANALYSIS

5.1 Summary

Surface-based radio echo-sounding (RES) data were collected from mid-May to mid-July, 1993 on Black Rapids Glacier, Alaska spanning the time of an annually-observed spring glacier motion speedup. The speedup is likely associated with onset of the melt season and the rapid introduction of large quantities of meltwater into the low-capacity subglacial hydrological system which developed during the previous winter. Repeated RES measurements were used to detect spatial and temporal variations in the bed reflection characteristics in an attempt to interpret changes in the subglacial hydrological system. Interpretation of the measurements requires accounting for the effect of varying transmission of energy through the ice surface (likely due to varying surface conditions). RES measurements were made at fixed locations on the glacier situated over the deepest part of the subglacial valley at high time resolution (half-hour or hour intervals). The bed reflection power and reflected phase show very little change throughout the period of measurements. RES measurements were also made along fixed surface tracks on the glacier and were repeated at 3 to 4 day intervals to provide a high spatial resolution record. Results from those measurements confirmed there was little change in the bed reflection power at the center of the valley, but showed some changes at locations toward the glacier margin.

5.2 Introduction

It is widely believed that hydraulic conditions at the base of a glacier exert strong control on its sliding motion (e.g., *Paterson*, 1994; *Willis*, 1995). Examples of hydraulic influence are the fast motion of polar ice-streams (e.g., *Alley et al.*, 1987), the surging of glaciers (e.g., *Kamb et al.*, 1985), and the seasonal variations in the speed of temperate glaciers (e.g., *Iken et al.*, 1983). Understanding the relationship between basal hydraulic conditions and motion of ice masses is important to understanding glacier dynamics (e.g., *Raymond and Harrison*, 1988).

Though subglacial water is known to play an important role in the motion of many temperate glaciers, the details of this role are not well-known. Direct investigations of the relationship between basal water and glacier motion are difficult because of the inaccessibility of the glacier bed. Previous investigations to determine basal conditions have primarily involved direct measurements through boreholes drilled in the ice (e.g., *Hubbard et al.*, 1995), or indirect measurements by sampling glacial discharge in pro-glacial streams (e.g., *Raymond et al.*, 1995). Additional information has come from investigations of exposed basal materials in recently deglaciated regions (e.g., *Walder and Hallet*, 1979). These techniques have provided much of what is known about the connection between hydraulic conditions and glacial motion. However, because these techniques lack either spatial coverage (boreholes), spatial resolution (stream measurements) or temporal resolution (investigations of deglaciated regions), we are strongly motivated to explore additional methods. For this purpose we have used radio echo-sounding (*RES*).

RES allows rapid coverage of large spatial regions of the bed, can provide high time-resolution measurements, and provides a non-invasive method of study. RES has been successfully used in the past to detect water in glaciers (e.g., *Jacobel and Raymond*, 1984; *Walford and Kennett*, 1989), and to examine the sub-ice bedrock conditions (e.g., *Oswald*, 1975). Our plan was to use RES techniques to monitor

changing subglacial hydrological conditions. The sensitivity of RES reflected power and phase to an expected range of basal water layer thicknesses and conductivities (Chapter 3) suggests that RES should be useful for monitoring changes at the bed. It is only relatively recently that technological advances allow the collection of large quantities of high-quality digital data for such a study.

We performed a series of repeated surface-based RES measurements to study the influence of subglacial hydrology on the flow of Black Rapids Glacier, AK (*BRG*), as part of a collaborative project with the University of Alaska Fairbanks. Repeated measurements of reflected power and phase were made at two fixed locations at the center of the glacier and along three transverse profile lines spanning the time of an annually-observed spring speedup. The intent of these repeated RES measurements was to establish a remote sensing technique to investigate the changes in configuration of the subglacial drainage system structure from winter to spring, and to investigate how these changes may cause the observed seasonal velocity variations.

Changes in the RES reflection from the bed may be caused not only by changes in the electrical properties of the bed, but also by changes in the ice column or ice surface. This chapter describes the RES measurements and data analysis methods used to identify and isolate the changes in returned signal due to changes in the basal interface from those due to other effects. The measurements show that: (1) the reflected power and the phase remained nearly constant at the center of the glacier during the period of measurement and (2) some changes in reflected power did occur toward the glacier margin. The physical interpretation of these findings is discussed in the next chapter.

5.3 Black Rapids Glacier Site Description

Black Rapids Glacier (Figure 5.1) is approximately 40 km long, about 2.3 km wide, has an average surface slope of 2.3° (*Heinrichs et al.*, 1996) and is situated over a

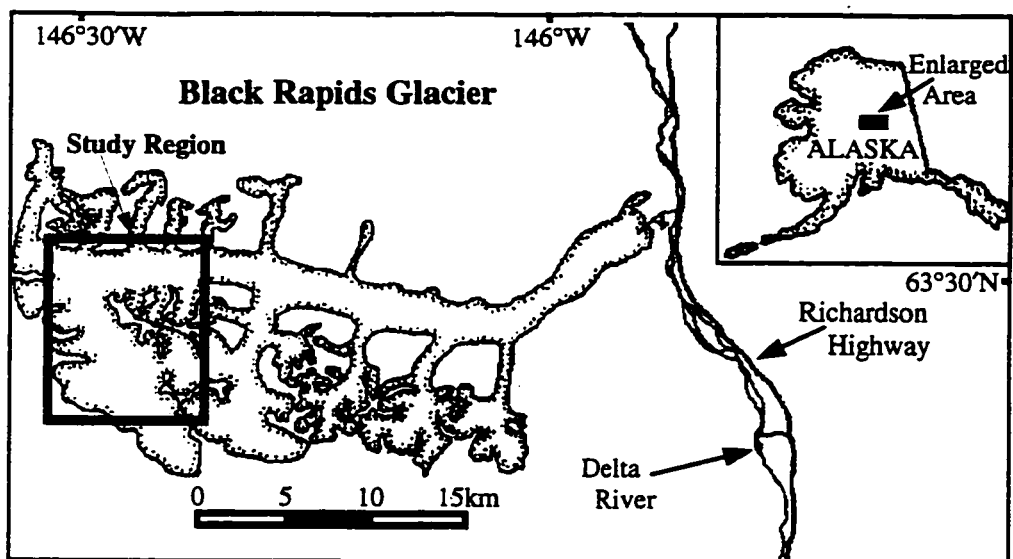


Figure 5.1: Black Rapids Glacier and its relation to Alaska (inset panel). The primary study region is shown by the heavy-lined box.

generally U-shaped subglacial valley of maximum depth of about 700 m (Chapter 4). BRG is a temperate (*Harrison et al.*, 1973), surge-type glacier which last surged in 1936-7 (*Post*, 1960). Our study region was centered 14-18 km from the head of the glacier (Chapter 4, Figure 4.1). This region of the glacier was chosen because past UAF photogrammetric velocity measurements show that it experiences a large spring speedup. The largest speedup occurs further down-glacier near 20 km (*Heinrichs et al.*, 1995). The spring speedup occurs annually and is thought to be caused by the rapid introduction of water into the subglacial hydrological system when the snow begins to melt. This feature is common to many temperate glaciers (e.g. *Willis*, 1995). The broad trend of increased velocity for the period of several weeks observed in 1993 (Figure 5.2, bottom panel) is typical of other years in which velocity has been measured. Peak velocities during this time ($\sim 1 \text{ m d}^{-1}$) are associated with drainage of lakes at the glacier margin. By contrast, ice motion is approximately constant and $\sim 0.18 \text{ m d}^{-1}$ for the remainder of the year.

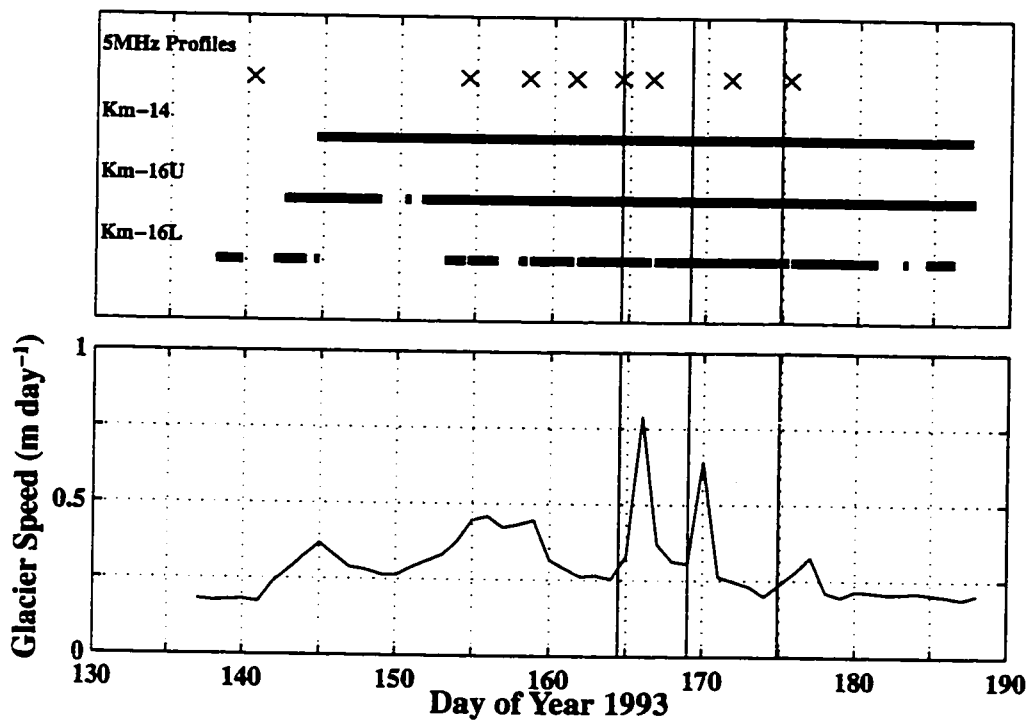


Figure 5.2: Black Rapids Glacier measurement record (top panel), and daily average glacier speed at Km-15 (bottom panel). Vertical lines show the approximate onsets of marginal lake drainages discussed in appendix E.

5.4 Repeated Radio Echo-Sounding Measurements at Fixed Locations

5.4.1 Methods and Data

To look for changes in basal power reflection characteristics at fixed locations, MK-I RES transmitter-receiver pairs (Chapter 2) were placed at two sites on the glacier. These fixed location RES measurement systems or *fixed sites* were automated by Campbell CR-10 dataloggers to collect waveforms at fixed time intervals (generally once or twice hourly). All transmitter and receiver systems were powered by battery banks maintained by solar panels. During the field season, the instruments were visited once or twice daily to down-load the data, to check the antennae conditions, and to ensure that battery power was maintained at a constant level.

Locations are described as distances from the glacier head, and are shown in Chapter 4, Figure 4.1. One RES fixed site was located 200 m down glacier from the Km-16 line ($63.48^\circ N$, $146.464^\circ W$). This site consisted of a single transmitter and two receivers, one located 80 m up glacier (Km-16U) and the other 80 m down glacier (Km-16L) from the transmitter. The site was located over the deepest part of the subglacial valley. The receiver at Km-16U used a Tektronix 222 oscilloscope and the Km-16L receiver used a Tektronix 2432/2440 oscilloscope. These instruments are described in Chapter 2. The depth of the Km-16 fixed site was 620 m (assuming propagation velocity $C_{ice} = 166 \text{ m } \mu\text{s}^{-1}$). The second RES fixed site used a MKI transmitter and receiver based on a Fluke 97 oscilloscope (Chapter 2). This site was located on the Km-14 line, and was also positioned over the deepest location in the subglacial valley (635 m). All RES fixed site systems used ~ 2 MHz center frequency weighted dipole antennae and no pre-amplifiers.

The Km-14 and Km-16U RES fixed site systems acquired waveforms at half-hour intervals, and the Km-16L system ran hourly. The clocks of the systems at Km-14 and Km-16 were offset by 5 minutes to avoid the possibility of interference between systems. Figure 5.2 (upper panel) displays the times during which the measurements

were made, as well as the daily average glacier speed during this time. Records from the upper Km-16 receiver (Km-16U) were more complete and were cleaner than records from the lower Km-16 receiver (Km-16L). Since there are no apparent differences in the records of both receivers, I use the more complete data from the upper receiver. Figure 5.3 shows data from this upper receiver. The Km-14 RES fixed site data are shown in Figure 5.4.

The emphasis of the data analysis which follows is to detect *changes* in the power and phase of the bed reflection. These are of interest because they can be used to reveal the nature of the physical changes, if any, occurring at the basal interface.

5.4.2 Time Variation of Returned Power

Several qualitative features are immediately evident in the raw data from Km-16U (Figure 5.3). The timing of the bed reflection at $\sim 7.5 \mu s$, does not change during the period of observation. In addition to the bed reflection, several other persistent reflections appear as horizontal lines throughout the record. Near the surface, a quasi-sinusoidal variation with period 24 hours can be seen. This signal is discussed in subsequent sections and is likely caused by variations in liquid water content in the snow surrounding the RES antenna. Apparently the varying water content alters the coupling of the antenna to the dielectric interface formed by the ice/air and thereby alters the amount of energy transmitted into the ice sub-surface. The varying water content also alters the amount of DC induction in the receiving antenna as well as its rate of decay.

Similar features can be seen in the Km-14 data (Figure 5.4). The bed reflection is at $\sim 7.5 \mu s$, several persistent reflectors can be seen between $5 - 7.5 \mu s$, and reflectors down to $4 - 5 \mu s$ show a quasi-sinusoidal variation with period 24 hours - somewhat deeper than at Km-16U. The difference in the depth of this sinusoidal variation is probably due to the differing coupling of the input signal to the different oscilloscopes used at each site.

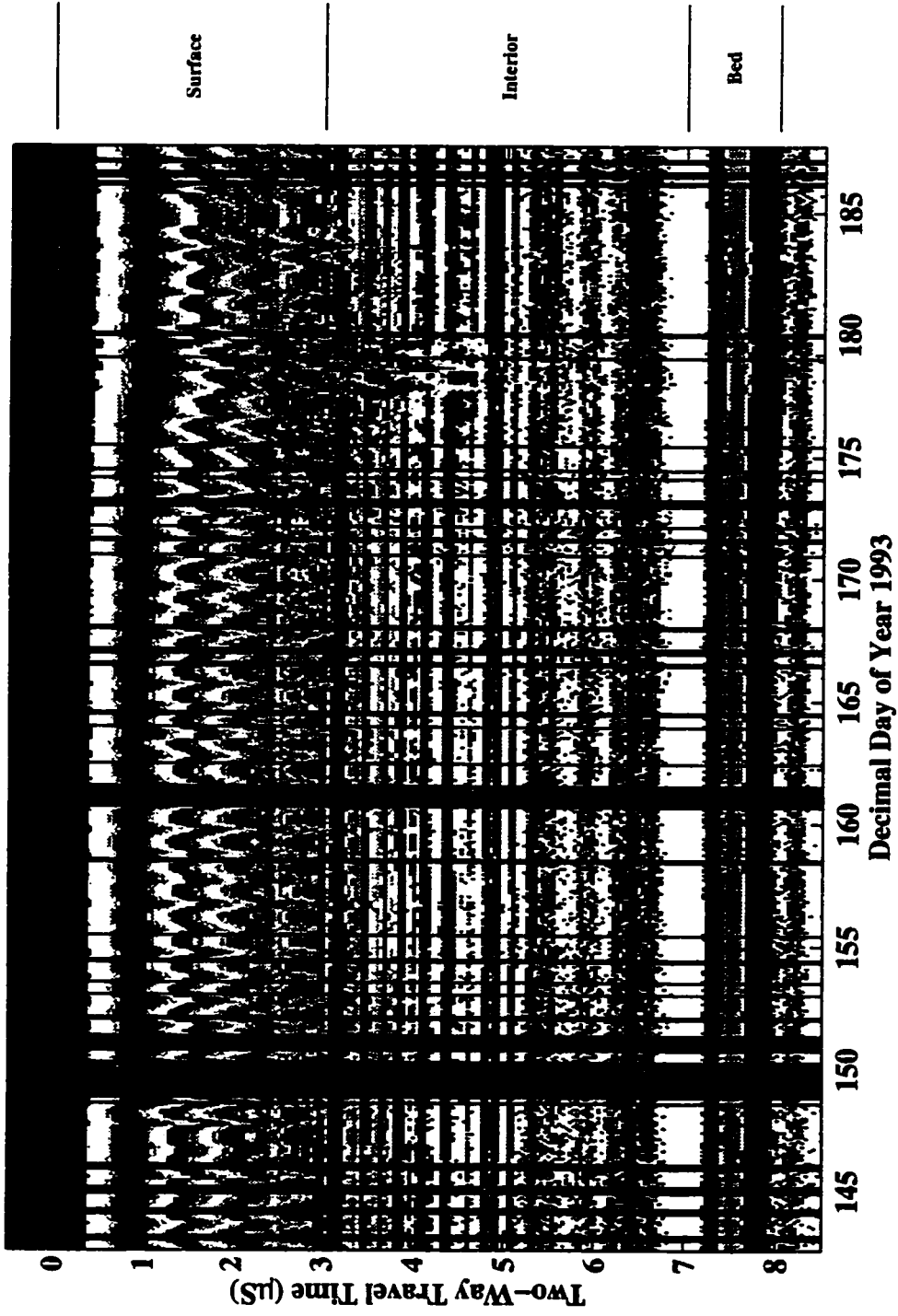


Figure 5.3: Upper Km-16 fixed site data z-scope image. The vertical axis is reflection delay time, and the horizontal axis is the time of observation. Color intensity along the vertical axis is related to the amplitude of the returned signal. Missing data are indicated by vertical black bands. The divisions into surface, interior, and bed regions are labeled along the right vertical axis.

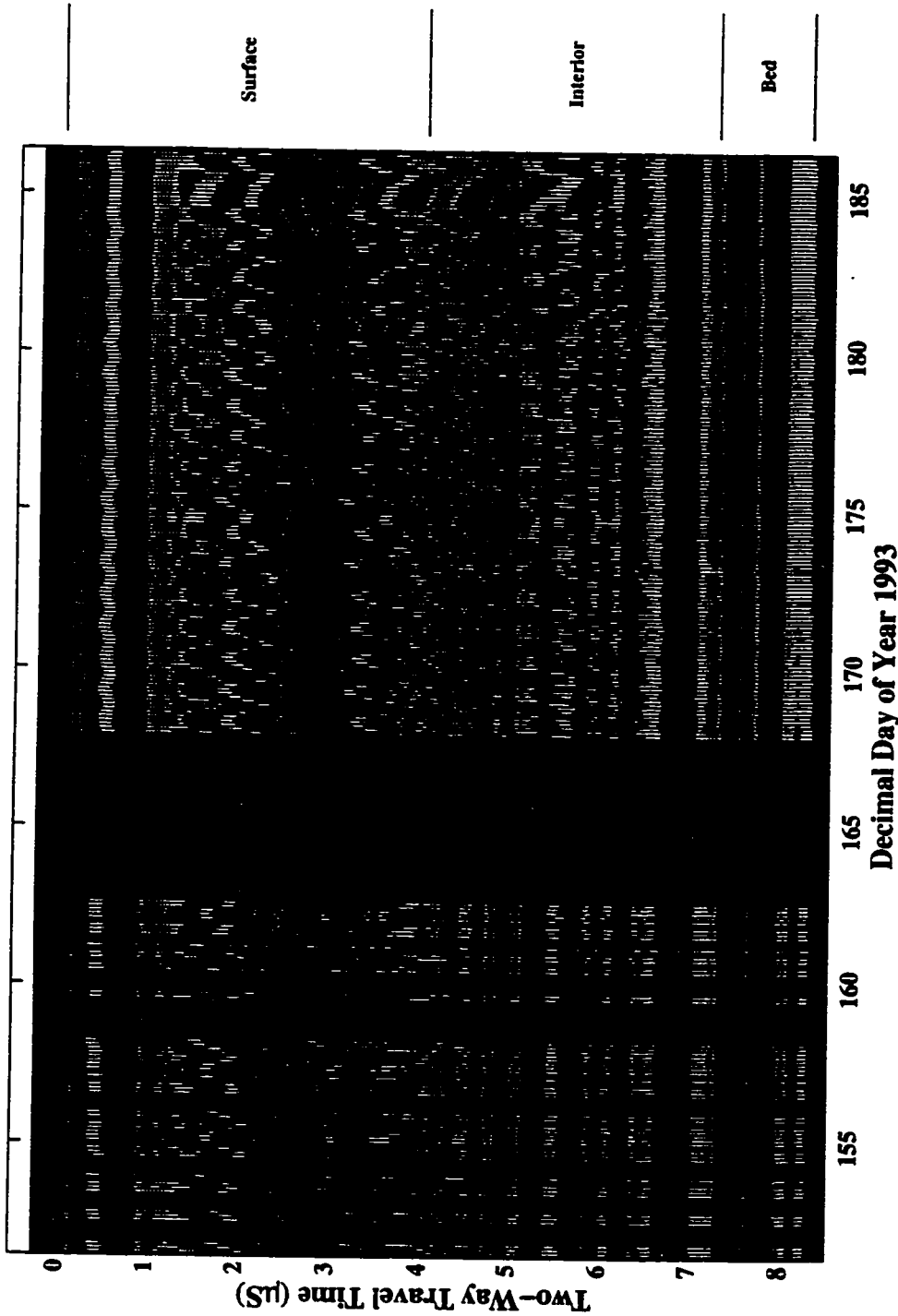


Figure 5.4: Km-14 fixed site data z-scope image. Data have been reduced to hourly measurements. The vertical axis is reflection delay time, and the horizontal axis is the time of observation. Color intensity along the vertical axis is related to the amplitude of the returned signal. Black vertical bands indicate gaps in the record. The divisions into surface, interior, and bed regions are labeled along the right vertical axis.

Calculation of Returned Power

To make quantitative evaluations of reflected power from any layer, I define the returned power P from within time window $t_1:t_2$ as one-half the sum-of-squared amplitudes (A_i) divided by the number of samples in the window:

$$P \equiv \frac{1}{2(t_2 - t_1 + 1)} \sum_{i=t_1}^{t_2} A_i^2. \quad (5.1)$$

This definition is consistent with the definition of the energy of a monochromatic sinusoidal wave train, which is simply half the amplitude squared and integrated over a full period. Normalizing by the number of samples allows a comparison of the power without distorting the results by the width of the window.

To determine the amount of power reflected from the bed, the window of time over which power calculations are made is defined as time length T centered on the reflected pulse (Figure 5.5). For each record the bed reflection power is calculated over a window using Equation 5.1. I refer to this quantity as the measured bed reflection power (*BRP*).

The effect of diurnal variation in the amount of energy transmitted on the *BRP* (calculated according to Equation 5.1) can be clearly seen for Km-16 fixed site in Figure 5.6 (upper curve). The effect is about constant from the beginning of the record until day 175. Peak amplitudes occur when the maximum amount of water is present in the snow pack. After day 175, the amplitude of the diurnal effect increases until day 178, when it abruptly decreases back to its approximate former level (Figure 5.6, upper curve). The gradual increase coincided with the formation of a slush swamp about 0.5 m deep in the region around and under the equipment. The abrupt decrease in amplitude on day 179 coincides with the release of a slush flow which rapidly drained the water from this region. Thereafter, the RES equipment was positioned on bare ice. A similar pattern can be seen in the Km-14 data (Figure 5.7 upper curve).

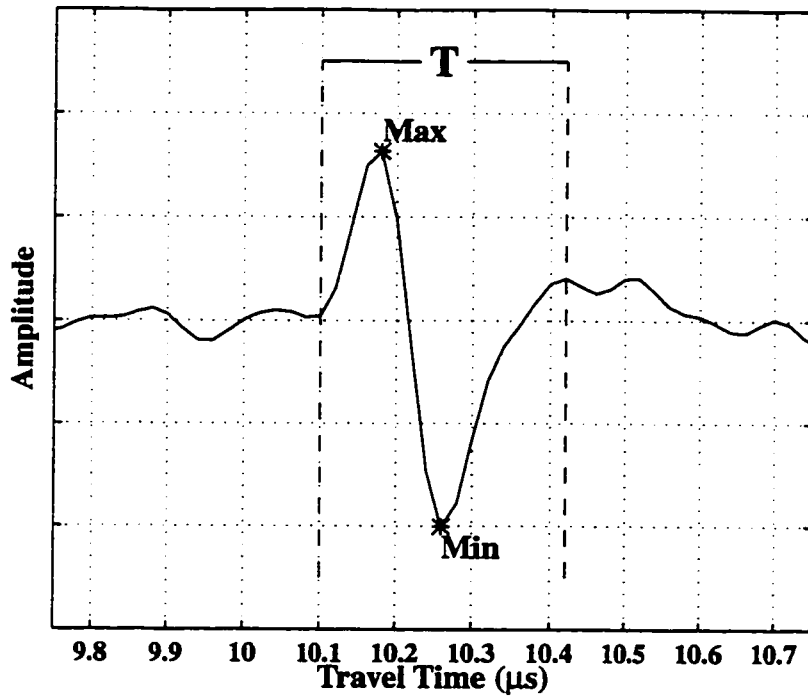


Figure 5.5: The bed reflection pulse from a typical RES waveform plotted as returned amplitude vs two-way travel time. The travel time and amplitude of the maximum and minimum are labeled, and the period of the pulse T is shown as the window of time between the dashed vertical lines.

We conclude that the observed diurnal variation in the data is likely caused by variations in the surface conditions. These variations affect the amount of energy entering the ice sub-surface and therefore the amount of energy returned from within the ice. To test this hypothesis, I calculate the power returning from reflectors/scatterers within the ice using Equation 5.1 over a time window starting just after extent of the direct wave and ending just before the bed reflection window (3 to 7 μs). This is the internal reflection power (IRP). For comparison, BRP and IRP are normalized by the relation: $(\text{value}/\text{mean}) - 1$. The normalized BRP and IRP for Km-16 are shown in Figure 5.6, and for Km-14 in Figure 5.7. A linear regression shows that BRP and IRP at Km-16 are highly (positively) correlated ($r^2=0.90$, $N=1700$). For Km-14, the correlation between BRP and IRP is similarly high ($r^2=0.84$, $N=640$). The high degree

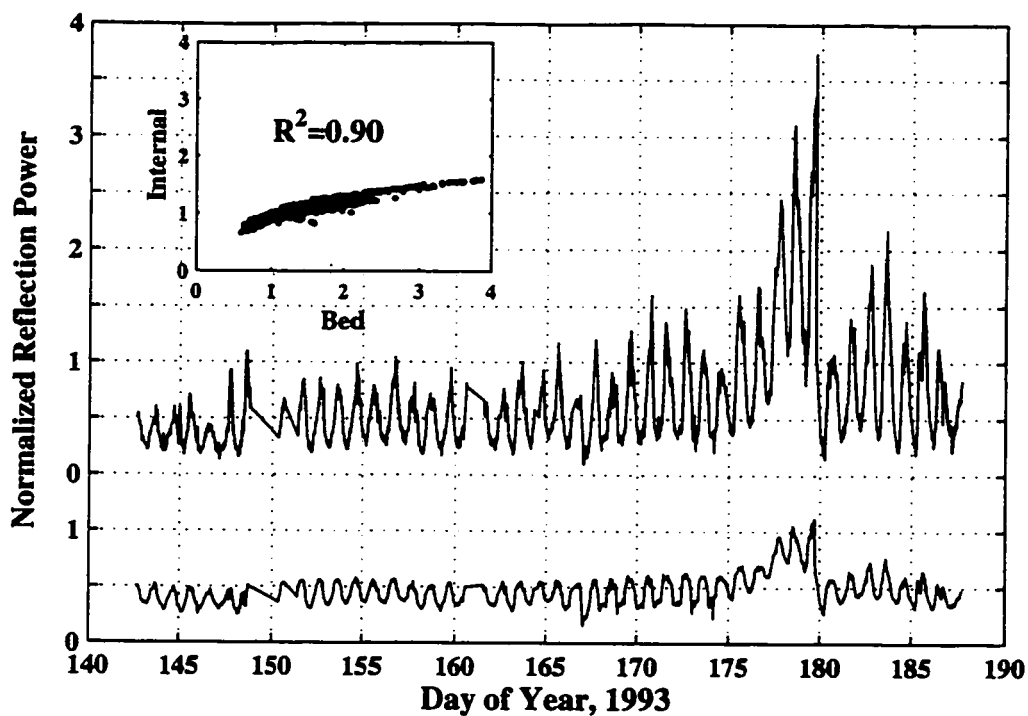


Figure 5.6: Upper Km-16 RES fixed site normalized reflection power from bed (upper curve) and internal regions (lower curve) of repeated spot measurements showing a high degree of correlation (inset plot).

of positive correlation between IRP and BRP demonstrates that they vary primarily in the same manner. For both the BRP and IRP to increase (decrease) at the same time requires (by conservation of energy) that the total amount of energy entering the ice sub-surface increase (decrease). Therefore, most of the temporal variability in returned power from the bed appears to arise from variations in energy transmitted into the ice which is likely due to the thinning and wetting of the surface snow. However, we do not rule out the possibility that the variation in transmitted energy may be due to additional factors.

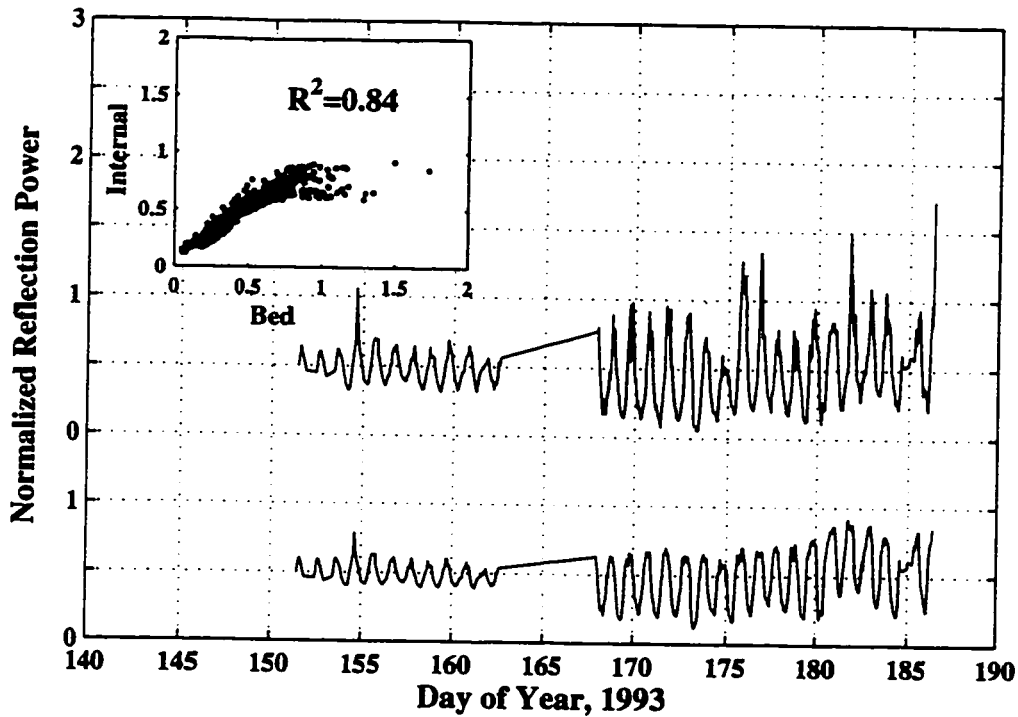


Figure 5.7: Km-14 RES fixed site normalized reflection power from bed (upper curve) and internal regions (lower curve) of repeated spot measurements showing a high degree of correlation (inset plot).

5.4.3 Correction for Variations in Transmitted Energy

Because the amount of energy transmitted into the ice sub-surface varied during the measurement period, the BRP measured at the fixed sites the data cannot be interpreted for variations in basal conditions without further analysis. The following steps are taken to reduce the effects of variations in transmitted energy on the data and to reveal the variations in BRP associated with variations of basal properties. Though we assume that this variation is caused by varying surface water, these steps do not in any way rely on understanding the specific mechanism for the variation of transmitted energy.

To remove the effect of varying transmitted energy, the RES records are first filtered using a zero-phase forward and reverse digital filter (chosen to minimize altering

phase) with a 1:10 MHz, 4th order Butterworth bandpass filter (chosen to minimize distortion of the amplitude of frequencies within the pass-band) to reduce the low frequency noise (artifact of the system configuration) and high frequency noise (environmental sources). The noise level remaining after filtering is then calculated from the pre-trigger portion of each waveform (Chapter 2, Figure 2.3). The noise level is used as part of the error analysis of the final results, and is also used to eliminate records with levels which exceed a pre-determined threshold. The bed reflection time is calculated as the delay time between the first arrival of the direct wave and the arrival of the first peak of the bed reflection; a value which can be uniquely determined. The reflection time is determined using an automated picking routine, and the bed reflection power is then calculated using Equation 5.1 over a window of time T shown in Figure 5.5.

A measure of the variation in energy transmitted into the ice is obtained by identifying the reflections from stable features within the ice using the multivariate analysis technique of principal component analysis (PCA). The assumption underlying the use of this measure is that some of the internal reflectors/scatterers do not vary with time. The RES records from fixed sites give some justification for this assumption because they show that the timing and form of internal reflections is remarkably stable (Figures 5.3, 5.4), indicating that many returns are produced by persistent englacial structures. The strongest of these reflectors/scatterers are likely to be water filled cavities (e.g., *Jacobel and Anderson, 1987*), and if these cavities are beneath the range of water table fluctuation, they should always remain water filled; their reflecting/scattering effects would be time independent. These stable reflectors/scatterers should yield a constant signal in the returns from the interior zone. I use PCA to quantify the constant interior signal and use the changes in amplitude of that persistent signal as a reference to calibrate and remove the effect of varying energy transmission from the bed reflection.

Application of Principal Component Analysis to RES Data

PCA is a technique that identifies the portion of a data set which accounts for most of the variance of that data. This is accomplished by forming a basis for the data space using linear combinations of the data such that the normalized basis functions (principal components) are chosen to sequentially maximize the variance represented. This technique allows one to quantitatively identify and extract the portions of the data that are common to the entire data set, leaving the portions that are time-varying. The PCA method is described in appendix B.

I define the interior portion to start just after the direct wave and to end just before bed reflection at each site. Using PCA, I identify the portion of the reflection signal in this internal region that is constant with time; the first principal component (a normalized vector \mathbf{E}_1 which points in the direction of maximum variance of the data). The projection (dot product) of the i^{th} record onto \mathbf{E}_1 is C_{1i} , and defines the amplitude of the first principal component present in the i^{th} measurement. Since \mathbf{E}_1 is determined for the interior portion of the record, the amplitude C_{1i} represents the amount of energy which is returned from the interior for the i^{th} measurement. I assume that this quantity C_{1i} is proportional to the energy that is transmitted into the ice. This method does not rely on the assumption that all of the reflectors within the ice have constant reflection properties because the reflectors whose properties vary with time, and which consequently return varying signatures, will not account for much of the total variance of the data set and their signal will therefore not be included in the first principal component.

Once the principal component \mathbf{E}_1 of the interior portion of the data and the amplitude of that component present in each measurement C_{1i} are determined, I subtract the portion of the measured BRP that is linearly related to the C_{1i} to produce the residual bed reflection power (BRP_R). This relation (dropping the subscripts) is

given by:

$$BRP_R = BRP - (A + BC_1), \quad (5.2)$$

where A, B are coefficients determined by the best (least squares) linear fit between the C_1 and BRP (the measured bed reflection power). The variations in returned power from the bed that remain (BRP_R) are not due to power transmission variations, but are presumably due to variations in the physical conditions at the base of the glacier.

5.4.4 *The Residual Bed Reflection Power*

The effects of varying energy transmission are removed from the Km-16U BRP data by calculating the first principal component of the interior reflections from 3 to 7 μ s and removing the linear relationship between the variation of the amplitude of the first principal component and the variation of the BRP to produce BRP_R (Equation 5.2). In these data, the first principal component accounts for 76% of the total variance of the data, indicating that most of the returned signal from the interior is due to persistent features. Figure 5.8 (lower panel) displays the resulting BRP_R plotted as a percentage difference from the mean value. The linear least squares best fit to the BRP_R shows that the overall trend of decline in amplitude $\sim 3.2\%$ with RMS error of 4% over the measurement period, indicating that the data only allow a slight decrease in the BRP_R at the Km-16U site during the measurement period.

The effects of varying energy transmission are removed from the Km-14 BRP using the principal component of interior reflections from 5 to 7 μ s using Equation 5.2. The first principal component accounts for 69% of the total variance of the data - slightly less than for the Km-16 site, but still indicating that most of the returned signal from the interior is due to persistent features. Figure 5.8 (upper panel) displays the BRP_R plotted as a percent difference from the mean value. The linear least squares best fit to the BRP_R shows a decline in amplitude of 2.2% with RMS error of 5% over the

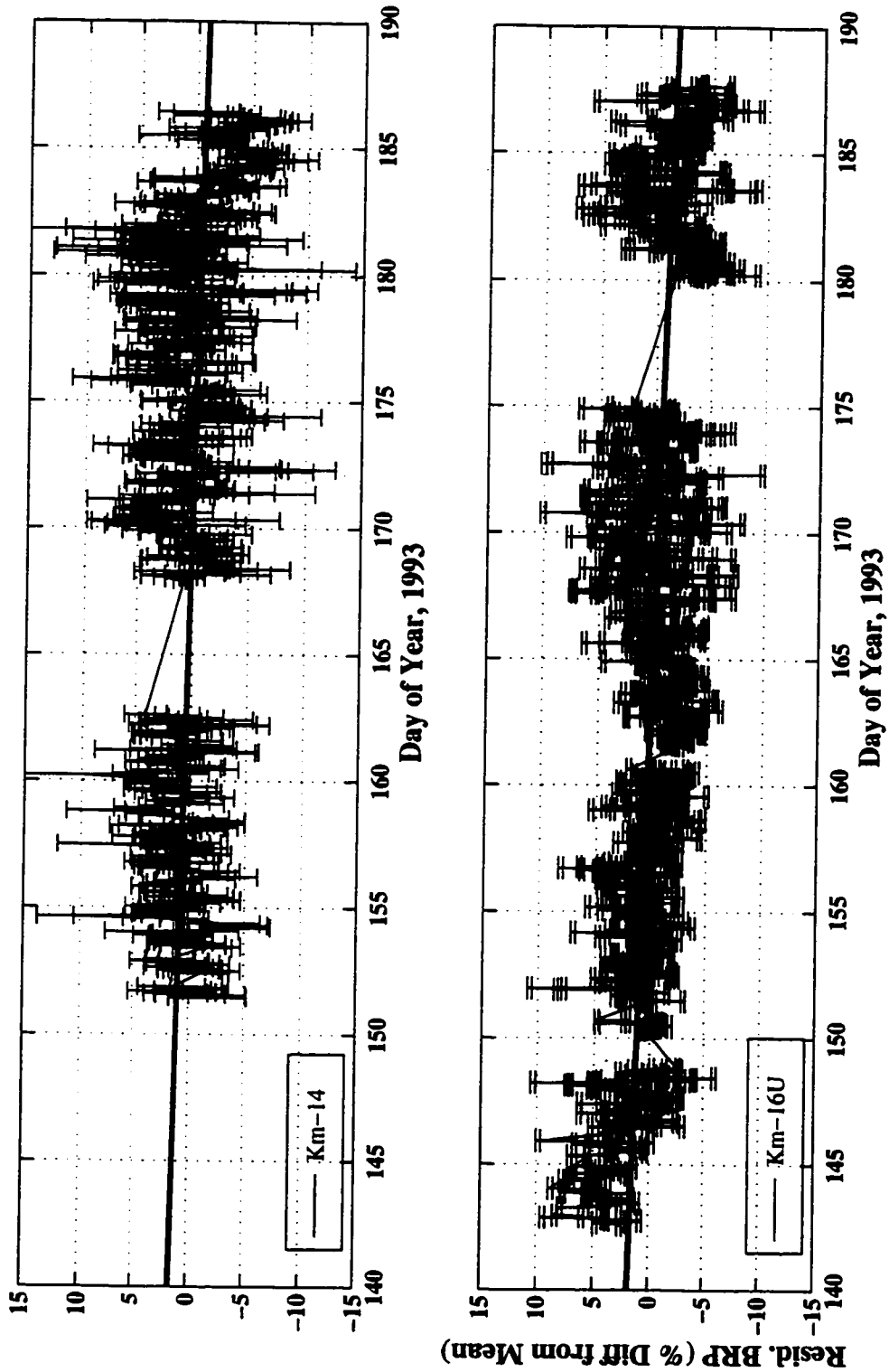


Figure 5.8: Km-14 (upper panel) and Km-16U (lower panel) residual bed reflection power (BRP_R) corrected for varying energy transmission effects. Values and uncertainties (calculated as described below) are plotted as a percentage difference from the mean value.

measurement period, indicating that the data only allow for a slight decrease in the BRP_R at the Km-14 site during the measurement period

5.4.5 Error Analysis of Method

The uncertainties in the BRP_R are determined from the contributions of the instrumentation error determined from noise level in the pre-trigger data, the error from the PCA method determined from the fraction of the total data variance accounted for by the first principal component and the number of data points within the interior portion, and the error in removing the linear relationship between the principal component of the interior region and the BRP to produce the BRP_R .

To estimate uncertainty in this application of PCA to RES repeated measurement data, two things must be determined: 1) how the fractional uncertainty in the C_1 , (δC_1) varies with data noise level, and 2) how δC_1 , for a given noise level, varies with N the number of data points used in the analysis (i.e., the number of data points that compose the "interior" region of the waveform that is used as a *calibrator*).

Determining δC_1

The standard technique for estimating the uncertainty in an application of principal component analysis, is to do a series of tests with known data and added noise (e.g., *Dillon and Goldstein, 1984*). I use this approach and begin by creating a "perfect" data set of repeated measurements by starting with a representative waveform (the mean waveform from Km-16 fixed site) and then copying it N times. To this perfect data, I add randomly generated uniformly distributed white noise of a known amplitude. Calculations with both uniformly distributed white noise and white noise with a Gaussian distribution yielded results that differ by less than $\sim 2\%$. Since the background noise recorded in the data pre-trigger from the RES fixed site data shows that the noise is closer to a Gaussian distribution, I use the calculations done with

that noise distribution.

The "noisy" data, obtained by adding the Gaussian noise to the representative waveform, are then processed as with the repeated measurement data. Principal component analysis is done to calculate \mathbf{E}_1 (the first principal component) and C_{1i} (the coefficient of measurement i obtained by projecting the measurement onto \mathbf{E}_1 - this is the "amplitude" of \mathbf{E}_1 in measurement i). If no noise were added to the data, the following conditions hold: \mathbf{E}_1 would be the original waveform, C_{1i} would be the same for all the M measurements (since they are simply copies of the original waveform); the standard deviation of the C_{1i} would be zero; and the fraction of the variance accounted for by \mathbf{E}_1 would be 1. With noise, the C_{1i} are not precisely the same. I calculate the mean and standard deviation of the C_{1i} , and the fraction of total variance accounted for by \mathbf{E}_1 . I repeat this process 10 times at a particular noise level. The mean of the statistics for the noise level is recorded. The noise level is incremented and the process repeated. This is done for increasingly large noise levels (relative to signal levels), until the fraction of the total variance accounted for by \mathbf{E}_1 (which I call V_1) is small relative to that obtained in the results from the actual analysis of RES data. This yields δC_1 as a function of noise level for a given number of samples M .

Determining δC_1 for Different M and Sample Rates

The repeated RES measurements at various locations contain differing lengths (M) of "interior record", and one may reasonably expect that the greater M , the lower the uncertainty introduced by the PCA method. Thus, I need to calculate the effect of varying record length. To do so, I repeat the steps above (to look for variations of δC_1 with noise level) for several values of M corresponding to different ranges of the "interior" region.

For each value of M , we can relate δC_1 to the added noise level and we can relate V_1 (the fraction of total data variance explained by \mathbf{E}_1) to the added noise level. We

can therefore directly relate V_1 to δC_1 which is equivalent to directly relating δC_1 to the noise level because the variance due to noise is just $1 - V_1$. For the purposes of determining δC_1 , any variance not accounted for by E_1 is noise.

Thus, given the length of the interior region M , and the fraction of the total variance accounted for by E_1 (V_1), I can compute uncertainty in the amplitude of the principal component: δC_1

Since the RES receivers that were used collected data at two different sampling rates, I also repeat this analysis for data of each rate. The relations for δC_1 the differing M are distinct for both sampling rates. The relationship between δC_1 and V_1 for each M is well described by a cubic fit.

Figure 5.9 displays the curves resulting from this analysis for the 20 ns sampling rate used with the Fluke 97 and Tektronix 222 oscilloscopes. Figure 5.10 displays the curves resulting from this analysis for the 10 ns sampling rate used with the Tektronix 2432/2440 oscilloscopes (Chapter 2).

Results of the Error Analysis

Thus, to calculate the uncertainty in the residual bed reflection power (BRP_R) as determined by the PCA of RES data, I must determine the contributions of:

- Measurement Error (δBRP): The uncertainty in the measured bed reflection power due to the error determined by the inherent limitations of the equipment and the background noise level measured in the pre-trigger portion of the record.
- Error from PCA Method (δC_1): The uncertainty in the removal of varying energy transmission from the measured BRP using PCA, determined from M , V_1 , and the sample rate.

Once the error contributions are determined I calculate the uncertainty in the residual bed reflection power δBRP_R . The expression for calculating BRP_R is given

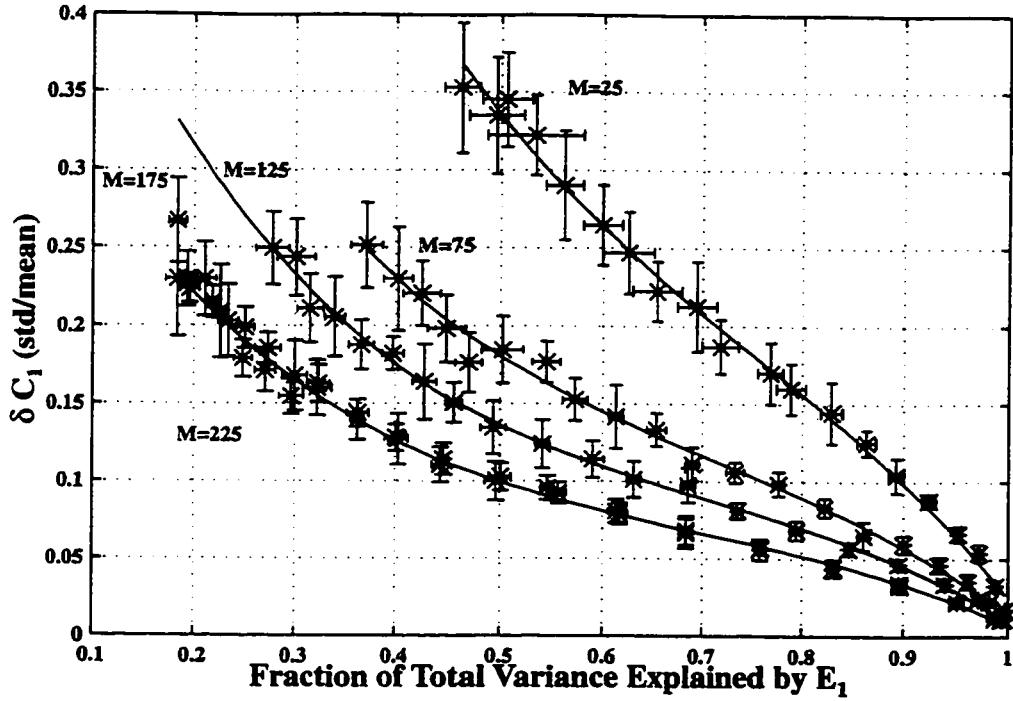


Figure 5.9: Results of error analysis for 20 ns per sample data giving the relationship between fractional uncertainty δC_1 , M , and V_1 the fraction of total variance explained by E_1 .

by Equation 5.2, where again A, B are determined by the best (least squares) linear fit between C_1 and BRP . The expression for the uncertainty in the residual bed reflection power (δBRP_R) is given by:

$$\delta BRP_R = \delta BRP + \delta(A + BC_1), \quad (5.3)$$

$$= \delta BRP + \frac{d(A + BC_1)}{dC_1} \delta C_1 \quad (5.4)$$

$$\delta BRP_R = \delta BRP + |B| \delta C_1 \quad (5.5)$$

Hence, the uncertainty in the residual bed reflection power calculated using the principal component analysis-based method of identifying internal calibrators is given by Equation 5.5. This error can be determined using the δC_1 for the noise level in the data and the sampling rate (determined above) and by knowing the instrumental uncertainty in the measurement of the BRP (δBRP).

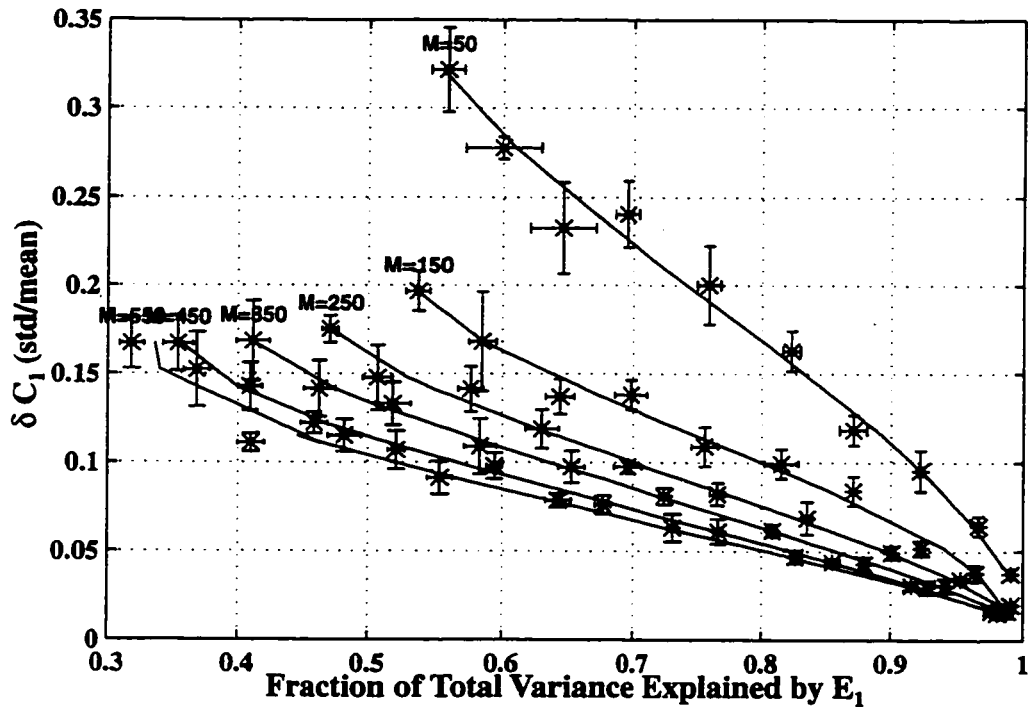


Figure 5.10: Results of analysis error analysis for 10 ns per sample data giving the relationship between fractional uncertainty δC_1 , M , V_1 and the fraction of total variance explained by E_1 .

5.4.6 Bed Reflection Phase

In addition to changes in the reflected power, changes in reflected phase may contain information about the physical conditions at the bed. If the basal interface can be idealized as a flat hard bed in which the ice over-lies a half-space of bedrock (no intermediate layer), the reflected wave will always be either exactly in phase (if the bedrock wave speed exceeds the speed in ice), or exactly out of phase (if the bedrock wave speed is less than the speed in ice). A more complex reflected phase will result if there is a basal layer separating the ice from the underlying bedrock. The total reflected wave will be the sum of the reflected wave from the ice/layer interface and the (attenuated) reflected wave from the layer/bedrock interface. At each interface, if the velocity of the second medium is greater (lesser) than the velocity of the first, the

reflected phase will be in (out) of phase with the incident wave. Therefore, either the development of a layer, or a change in existing layer thickness will produce a change in reflected phase. Changes in dielectric structure (conductivity or permittivity) of a layer will also produce a change in reflected phase even if the layer thickness does not change because such a variation will alter the wave speed and therefore the wavelength within the layer. The variation of reflected phase with layer properties is illustrated in Chapter 3, Figure 3.2.

RES systems that directly record the returned phase, generally do so by transmitting a pulse of high frequency radio waves several periods long (e.g., *Walford and Harper*, 1981) locked in phase to a continuously running oscillator of the same high frequency. The phase of a returned signal packet can then be directly recorded relative to the oscillator. Mono-pulse RES systems, such as the system we use (Chapter 2), do not record information about the returned phase with respect to some suitable reference signal. Therefore, with mono-pulse RES systems, the absolute phase of the returned signal is not known. Further, because the transmitted and returned signal of a mono-pulse system is broadband, the returned phase cannot be precisely defined.

Repeated RES measurements at fixed locations, while they do not permit the absolute determination of the returned phase, do allow the detection of changes in phase if we assume that both the ice thickness and radio wave speed remain constant. Under these assumptions, we can use the average returned pulse as the reference signal against which we measure phase change. We make this measurement in two steps. First we determine the correlation of returned pulse shape and then second, relate the level of correlation to changes in phase.

Variation of Bed Reflection Pulse Shape

To detect changes in pulse shape of the bed reflection, I calculate the zeroth lag correlation of the bed reflection pulse relative to the mean reflection pulse where the bed reflection is defined as the time window centered on the returned pulse (Figure 5.11,

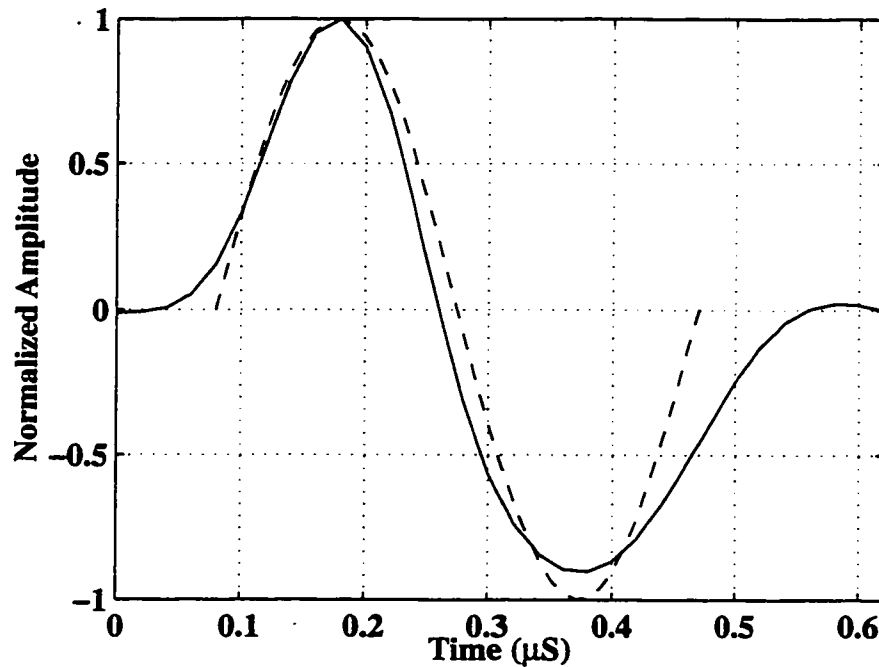


Figure 5.11: Km-16U RES fixed site mean bed reflection pulse (solid line), and the ~ 2.2 MHz sinusoid (dashed line) used to model the pulse for determining the relationship between pulse shape and phase shift.

solid line). The results of this correlation for the Km-16U site are given in Figure 5.12 (lower panel) and for Km-14 in Figure 5.12 (upper panel). The extremely high degree of correlation (~ 0.99) indicates that the shape of the reflected pulse was nearly constant at both sites over the measurement period.

Because the correlation is calculated over precisely the same delay time window (relative to the transmitted pulse) for each measurement we can immediately conclude two things: 1) the delay time of the bed reflection remained very nearly constant over the period of measurement indicating that the ice thickness as well as the wave speed did not change, and 2) the phase of the returned pulse remained nearly constant over the observation period. In the next section I quantify this second result.

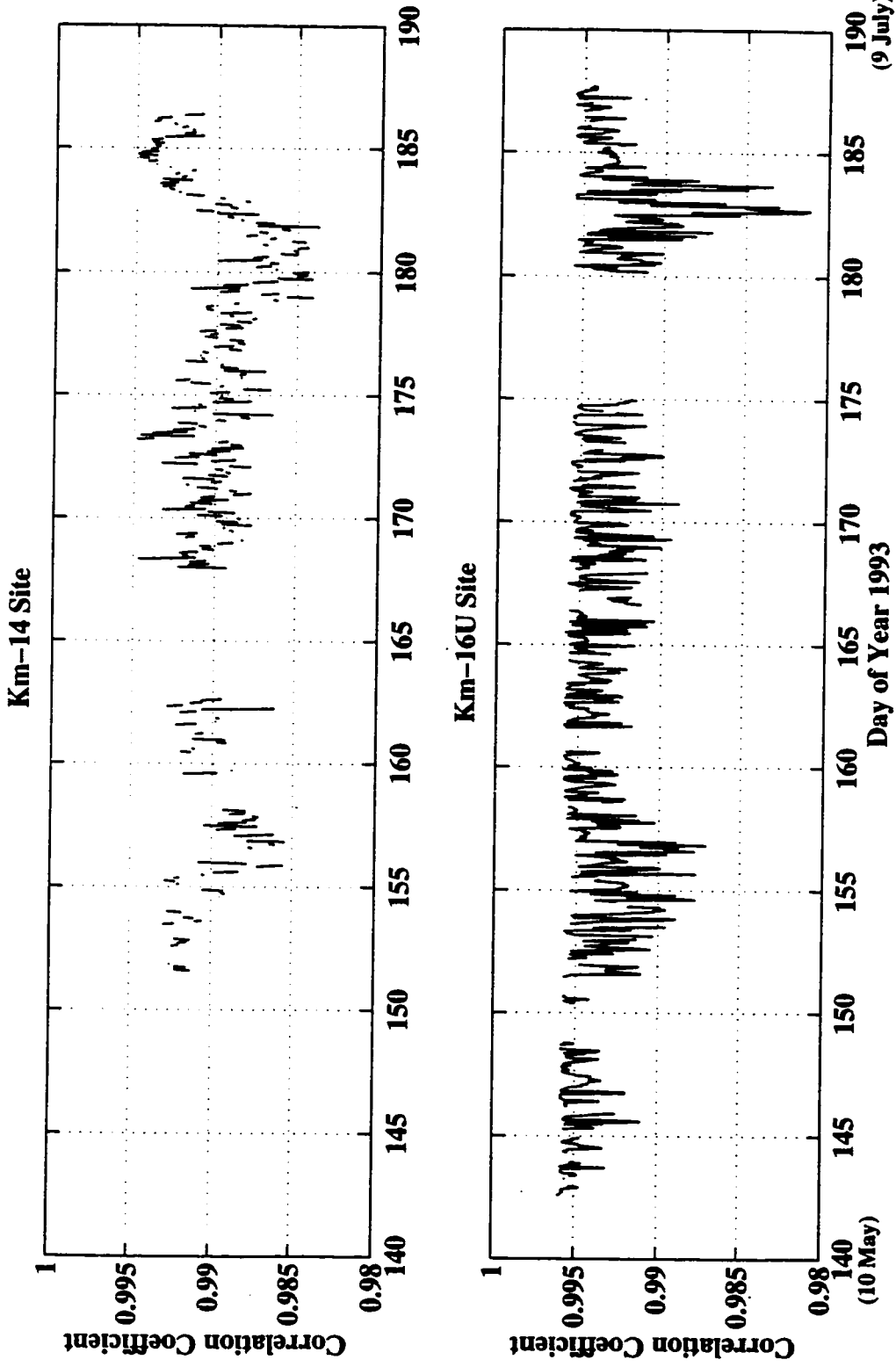


Figure 5.12: Km-14 (upper panel) and Km-16U (lower panel) RES fixed site zeroth lag correlation of bed reflection pulse with the mean pulse for hourly measurements. The high degree of correlation shows that the shape and therefore the phase of the pulse changed very little during the measurement period.

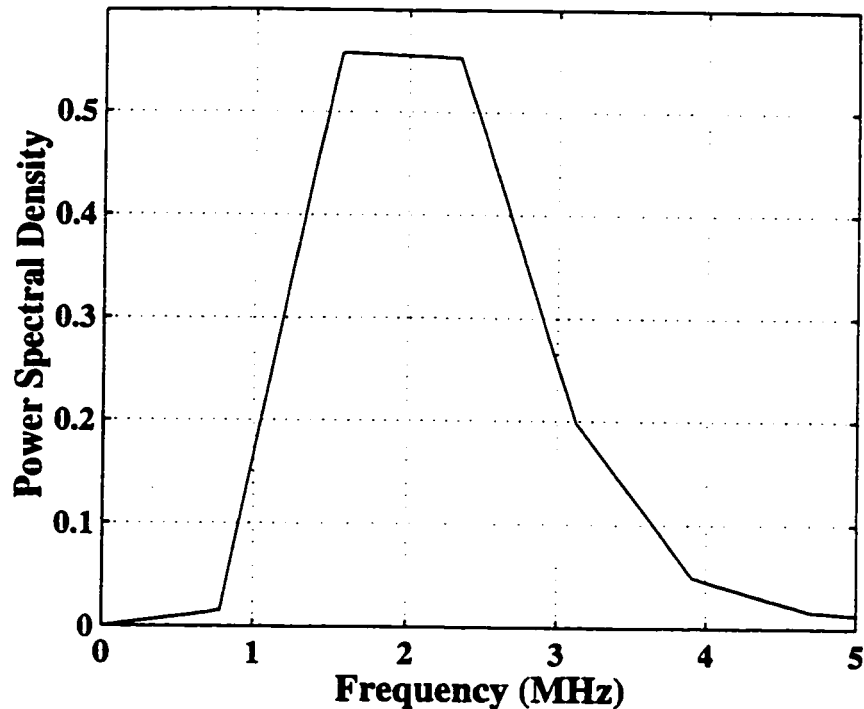


Figure 5.13: Power spectral density of the bed reflection pulse (Figure 5.11, solid line) from the average record at the Km-16U fixed site. This shows that the broad-band returned signal is heavily dominated by the center frequency of ~ 2.2 MHz.

Sensitivity of Correlation to Phase Change

It is important to estimate the constraint on possible changes in phase placed by the high degree of correlation of the return pulse. To do so requires knowing how the correlation varies with phase. To calculate this estimate, I make a reasonable mathematical representation of the returned pulse.

I begin by calculating the power spectral density of the bed reflection pulse from the Km-16U fixed site (Figure 5.13). This shows that the broad-band returned signal is heavily dominated by the center frequency of ~ 2.2 MHz. Thus, I represent the actual returned pulse by one period of a sinusoid with the measured center frequency. Figure 5.11 (dashed curve) shows that the 2.2 MHz sine wave makes a good approximation of the actual returned pulse.

From the original sinusoid, I construct a sequence of sinusoids with incremental phase shifts (Figure 5.14) and calculate the zeroth-lag correlation. From this we can arrive at an empirical relationship of correlation coefficient as a function of phase shift. The results from this analysis (Figure 5.15) show that a correlation coefficient of ~ 0.99 constrains possible phase changes to within ~ 0.06 radians. I note that this analysis neglects the contribution of noise and/or varying timing of the return pulse which both reduce the correlation, so the result shown in Figure 5.15 is only precisely valid if any deviation from perfect correlation is due entirely to phase shifts. Therefore this estimate places an upper bound on the amount of possible phase shift allowed for a given correlation value. From these data, we can then conclude that the returned phase of the bed reflection at Km-14 and Km-16U (correlation ~ 0.99) varied less than ~ 0.06 radians.

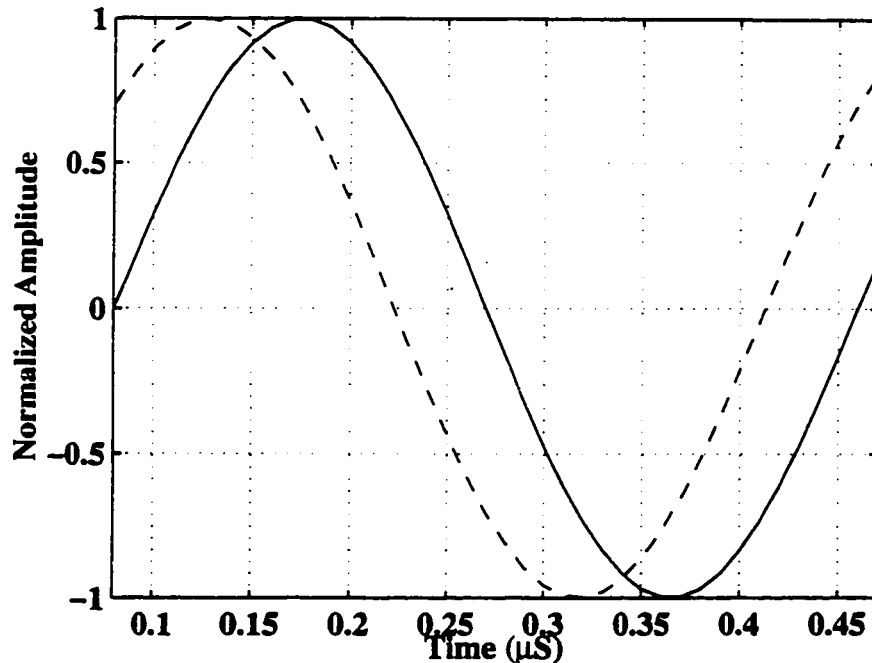


Figure 5.14: Sinusoid of 2.2 MHz with phase shift of zero (solid line) and $\pi/4$ (dashed line) radians.

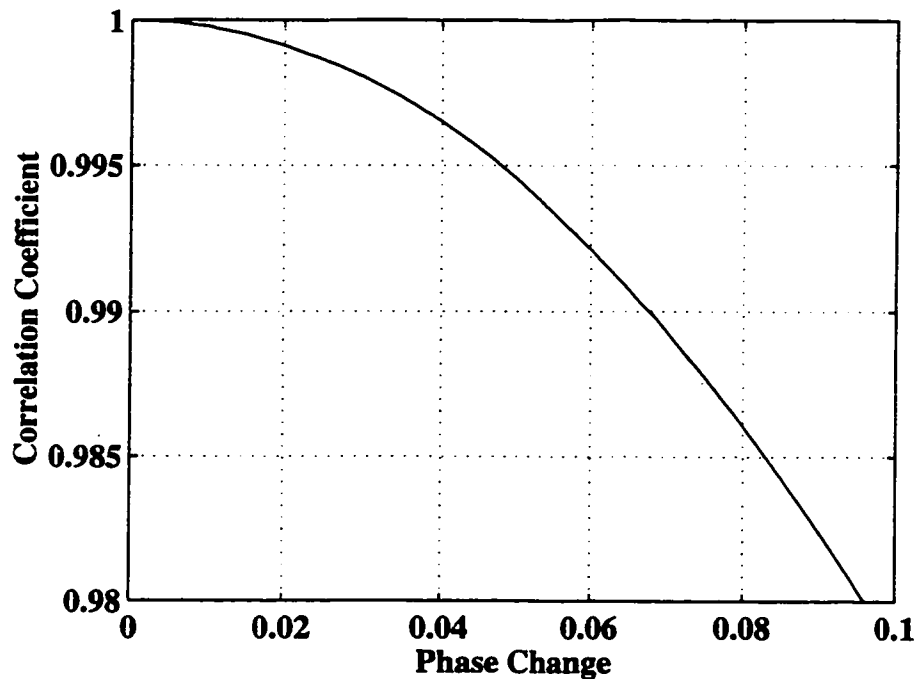


Figure 5.15: Variation of zeroth-lag correlation with phase shift.

Calculation of Phase Spectra

The maximum phase change observed in the data can also be estimated by comparing the phase spectrum of the mean record with the phase spectrum of the least correlated record. I begin by calculating the discrete Fourier transform (DFT) of the mean record and of least correlated record (day 182.9 for the Km-16U fixed site). The phase spectrum is calculated as the arctangent of the ratio of the imaginary part of the DFT to the real part (*Karl, 1989*). The results for Km-16U fixed site for frequencies 0:5 MHz are given in Figure 5.16 and show that the phase change for those frequencies is less than 0.05 radians. The phase shift of the center frequency of ~ 2 MHz is less than 0.01 radians. These values are consistent with the previous subsection which limited the change to less than 0.06 radians. Results from the other fixed site (Km-14) are similar.

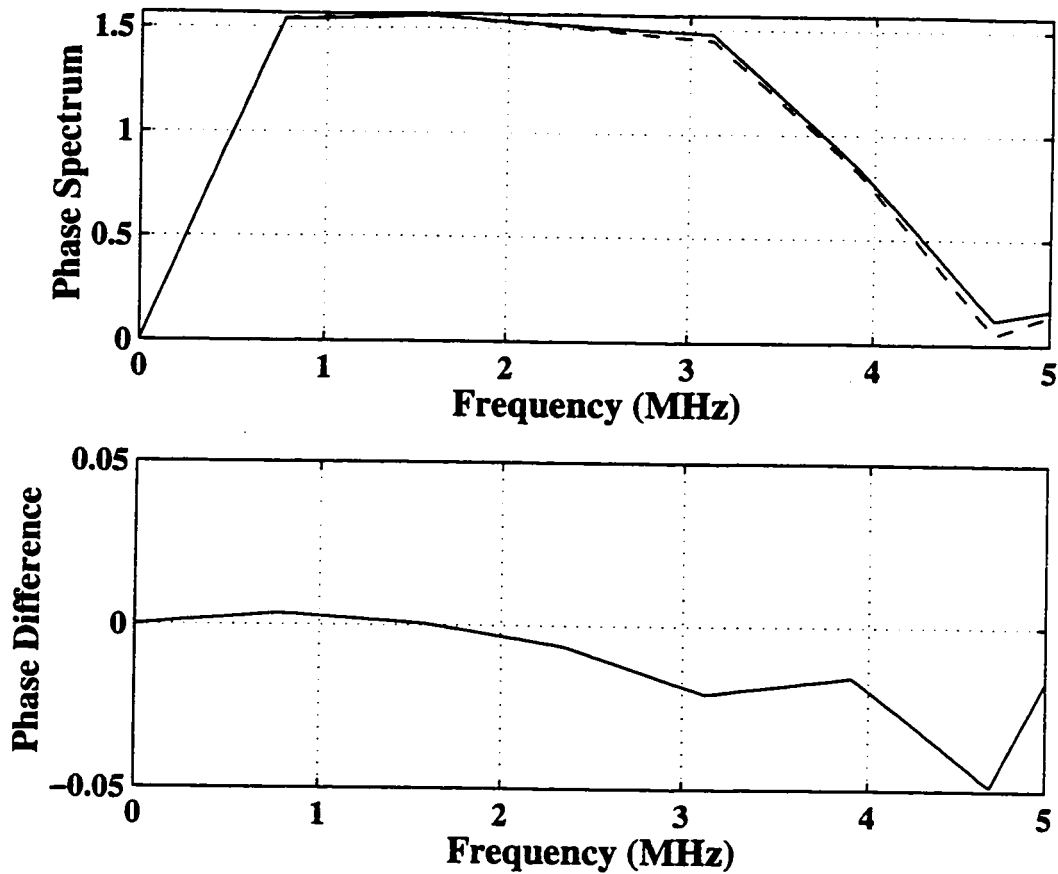


Figure 5.16: Upper Panel: phase spectra in radians of mean record (solid curve) and least correlated record (day 182.8, dashed curve) from Km-16U fixed site. Lower Panel: phase difference (radians) between the mean record and record from day 182.8.

5.5 Repeated RES Profiles

5.5.1 Methods

RES profiles were repeated along marked paths on the glacier surface. Waveforms (individual RES measurements) were acquired at fixed distance intervals using a bike-wheel odometer. Along these paths, waveforms were also acquired with the system stationary at several locations (marked by poles). One profile ran approximately longitudinally along glacier flow, the other three profiles ran approximately perpendicular to flow at 14, 16 and 18 km from the glacier head (Chapter 4, Figures 4.1).

The RES system used for profiling was the Tektronix 2432 receiver, MK-I transmitter, antennae with center frequency ~ 5 MHz, and a pre-amplifier (Chapter 2). Power was supplied by a gasoline powered generator. The z-scope image of each of the three cross profile lines (Km-14, 16, 18) is shown Chapter 4, Figures 4.2, 4.3, and 4.4.

5.5.2 Determination of Bed Reflection Power

Bed reflection characteristics from these repeated profiles are calculated in the following manner. An auto-picker routine was devised to determine the bed reflection travel time and peak-to-peak amplitude of the bed echo at each waveform along all profiles. The data quality from profiling is not as high as from the fixed sites, and comparison of repeat profiles is not simple. Data from profiling do not contain as many averages, and the averaging is done while the system is in motion so that an individual record is composed of signals averaged over a specific distance (15 or 30 m). Calculating the power of the bed reflection using Equation 5.1, defining the width of the pulse in terms of the maximum and minimum (Figure 5.5), and determining any phase change is not possible because the bed reflection pulse is often not well-defined. On occasion the bed reflection in an individual record can only be determined in the context of the surrounding records. Further, co-registration problems dominate the apparent measured changes in bed reflectivity when trying to simultaneously compare records from entire profiles.

To minimize these problems I have done the following. First, I adopt the convention of calculating the bed reflection power as the square of the peak-to-peak amplitude of the bed reflection pulse, and assume that this quantity is linearly related to the BRP calculated using Equation 5.1 over the width of the pulse. A comparison using the Km-16U data (where consistency of the bottom pulse permits use of Equation 5.1) verifies that this assumption is valid. Second, to minimize co-registration problems, I have limited the analysis of the repeated profiles to records made at pole locations while the system was stationary - in effect these measurements are similar

to the fixed site measurements described in the previous section. These repeated measurements are affected by variations of surface conditions, but are of sufficient quality to calculate the first principal component of the interior region.

5.5.3 *The Residual Bed Reflection Power*

The effects of varying transmission of energy must first be removed from the measured BRP at the pole locations along the repeated profiles to determine the residual BRP (BRP_R). For each of the pole locations I define the internal portion of the record to begin immediately after the direct wave and end just before the bed reflection - the length of this internal portion varies with ice thickness. I calculate the first principal component (E_1) and the amplitude of that component in each measurement C_1 . Then, as with the fixed sites, I remove the portion of the measured BRP that is linearly related to C_1 (Equation 5.2). The result of this analysis is a residual reflection power (BRP_R) whose variations are not related to changes in the amount of energy transmitted into the ice.

The uncertainty in the BRP_R is calculated as described above. The co-registration problems in these data are not entirely eliminated and the reflection time series resulting from the complex distribution of internal reflectors is not precisely duplicated at each measurement. As a result of the errors in co-registration the first principal component (E_1) of the internal region describes a smaller fraction of the total data variance (V_1) than for the fixed sites. In addition, because the ice thickness at most of the pole locations was less than at the fixed sites, the measurements provide a smaller interior region (smaller M). Therefore, as illustrated in Figure 5.10, because V_1 and M are lower for these measurements than for the fixed site data, the errors associated with the profile data are significantly higher.

The results of this analysis for all the 13 pole locations is shown in Figure 5.17. Locations along the Km-14 and Km-16 lines show that relative to errors there is little change in the bed reflection power in the center portion of the glacier. Changes

($\sim 25 - 50\%$) in BRP_R at the measurements on the north and south margins of the glacier occurred at Km-16 on day 166.5. Increases in BRP_R near the northern edge of Km-14 occurred on days 158.45 and 175.45. Since some increases occur on both sides of the glacier at the same time, and since the center portion of the profiles is relatively unchanged during those times, it is unlikely that some unconsidered effect is responsible for this change. It is likely that the observed changes in BRP_R toward the margins of the glacier on Km-14, Km-16 are caused by changes in reflectivity of the bed.

The results for Km-18 (Figure 5.17, top row) are not as clear. The changes in BRP_R are smaller than the calculated errors. The large errors arise because the first principal components of the interior section of the Km-18 data do not account for a large portion ($<40\%$) of total data variance. This is much less than the other two profiles ($>60\%$). The error increases as the total variance accounted for by the first principal component decreases (Figure 5.10). Possible reasons for this low variance are that there may have been fewer persistent internal reflectors in these locations or that co-registration was for some reason poorer at these locations than for the other two profiles. The large uncertainty prohibits confident evaluation of BRP_R changes at the poles on the Km-18 line.

Thus, of the locations along the repeated profiles that we consider, only five contain detected changes in the BRP_R : the northern location on Km-14 profile (1104.3 m), the northern two poles on the Km-16 profile (324.2, 514.4 m), and the southern two poles on the Km-16 profile (-663.3 m, -840.2 m). At the remainder of the measurement locations, uncertainty exceeds the calculated changes.

5.6 Summary and Conclusions

Repeated RES measurements on Black Rapids Glacier were made in 1993 during the time of an annually observed spring speedup. High time-resolution records were

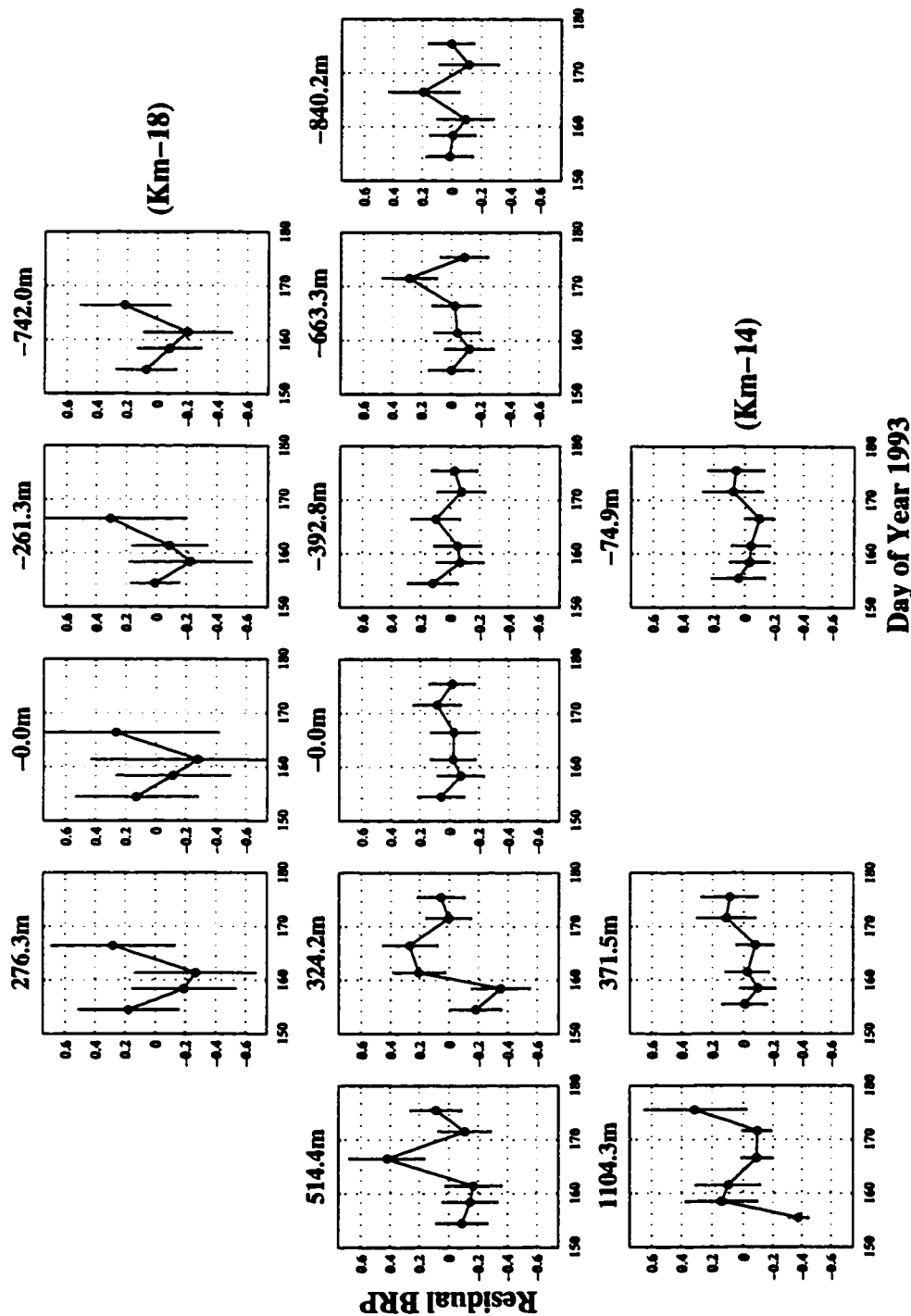


Figure 5.17: BRP_R (fraction of mean value) at the poles along profiles Km-18, Km-16, and Km-14 (from top to bottom) calculated using described PCA method to remove effect of varying energy transmission from the data. Measurement positions are given in meters north of glacier center. Km-14, Km-16 measurements were made on days 154.5, 158.45, 161.45, 166.5, 171.55, 175.45. Km-18 measurements were made on the first four of those days.

obtained with (\sim hourly) measurements collected at two fixed locations situated over the deepest part of the subglacial valley. Spatial sampling was obtained from profiles along fixed tracks and at fixed distance intervals spanning across the glacier surface every 3 to 4 days.

Analysis of these data shows the following:

- Varying surface conditions, such as the diurnal and seasonal variation of liquid water content of the snow and firn that occur in temperate environments, alter the coupling of the RES antennae to the dielectric interface. More surface water allows more energy to penetrate the sub-surface. This effect has been largely ignored in previous RES studies of temperate glaciers. A method using principal component analysis and persistent internal (in the ice) reflectors was devised to remove the effects of varying surface conditions from the bed reflection power signal. Although this discovery complicates the goal of detecting the time variation in basal properties it has the practical application that the optimal conditions for ground-based RES of ice occur when the surface is wet.
- Reduced data from high time-resolution repeated RES measurements at two fixed locations (Km-14, Km-16) over the deepest portion of the subglacial valley, indicate that the residual bed reflected power (BRP_R) varied less than 5% and reflected phase varied less than 0.05 radians during the period of observation in spring 1993.
- Repeated RES cross profiles at Km-14 and Km-16 are consistent with the conclusion that the bed reflection power varied less than uncertainties near the center of the glacier over the observation period.
- Repeated profiles at Km-14 and Km-16 indicate that some changes in bed reflectivity occurred toward the margins of the glacier during the time of the spring

speedup. Specifically the northern pole of Km-14, the northern two poles of Km-16, and the southern two poles of Km-16 show changes which exceed measurement uncertainties.

- Repeated profiling downstream of the fixed sites at Km-18 shows a different pattern from the two profiles up-glacier. Definite conclusions about the variation of bed reflection are not permitted because of large uncertainties.

In the following chapter concurrent geophysical measurements are introduced and the changes (or lack of changes) in power and/or phase reflected from the bed are analyzed to place limits on the physical changes of basal properties allowed by the data.

Chapter 6

RADIO ECHO-SOUNDING INVESTIGATION OF BASAL PROPERTIES, BLACK RAPIDS GLACIER, ALASKA II: INFERRED SUBGLACIAL STRUCTURE

6.1 *Summary*

The results of repeated radio echo-sounding measurements made from mid-May to mid-July, 1993 on Black Rapids Glacier (presented in Chapter 5) are reviewed together with other concurrent geophysical measurements. The center of the subglacial trough showed that the residual bed reflected power (BRP_R) varied less than 5% and reflected phase varied less than 0.05 radians during the period of observation. Some changes in bed reflectivity were observed toward the glacier margins. However, their timing in relation to other observed hydrological events is not clear. Models of the bed reflectivity are used to calculate the expected range of changes in basal dielectric properties for a hard and soft bed idealization of the subglacial system. Results show that little or no physical change occurred near the center of the glacier. Possible subglacial changes are therefore confined to those scenarios which do not transfer large quantities of water to and from the bed though they may allow for changes in basal water pressures. Toward the glacier margin, variations in the amount, distribution, or conductivity of basal water in a thin layer or distributed in a porous till layer could account for the measured variations in bed reflectivity. Such variations in marginal basal properties may contribute to, or be the result of the observed spring speedup. Longitudinal surface extension measured in the study region indicates that variations in speed down-glacier may be responsible for the locally-observed speedup.

These findings are not consistent with conventional views of spring hard bed glacier hydraulic system evolution and may indicate that changes in speed can be driven from changes in sensitive local areas rather than glacier-wide changes.

6.2 Introduction

We performed a series of repeated surface-based radio echo-sounding (*RES*) measurements to study the influence of subglacial hydrology on the flow of Black Rapids Glacier, AK (*BRG*), as part of a collaborative project with the University of Alaska Fairbanks. The intent of these measurements was to establish a remote sensing technique to investigate the changes in configuration of the subglacial drainage system from winter to spring as a result of changing melt water input, and to determine how these changes may give rise to the observed seasonal velocity variations. The *RES* repeated measurements and data analysis are presented in the previous chapter (Chapter 5). In this chapter, I review the current understanding of subglacial structure. I then use the findings of the *RES* measurements of reflected power and phase to place constraints on the possible changes in the hydrological system that occurred at the bed of *BRG* during the 1993 spring speedup event. These constraints are then compared with other geophysical measurements made during the speedup as well as other studies of glacier motion and hydrological structure to infer the kinds of structural change that occurred during the speedup event.

6.3 Expected Changes in Subglacial Hydrological Systems

6.3.1 General Descriptions of Subglacial Hydrology

Descriptions of glacial hydrology are generally segregated into two end member categories based on the morphology of the bed: hard bed and soft bed. The hard bed subglacial hydrology has been described in terms of three kinds of water passages: large channels (e.g., *Röthlisberger*, 1972; *Nye*, 1976), thin films at the basal interface

(e.g., *Weertman*, 1972), or distributed systems of linked cavities situated in the lee of bumps (e.g., *Walder*, 1986; *Kamb*, 1987). Each of these descriptions is characterized by differing relationships between melt-water input to the system and the resulting subglacial water pressure. In a tunnel-dominated drainage system, steady state water pressure and water flux are inversely related; water pressure is predicted to be lowest at times of high discharge (*Röthlisberger*, 1972). On the other hand, the pressure-flux relationship for a linked cavity system is direct; water pressure is highest at high discharge (*Walder*, 1986; *Kamb*, 1987). With increasing water flux, it is thought that a hard bed system evolves from a system of thin water films (e.g., *Weertman*, 1972, 1986) to a network of interconnected cavities (e.g., *Walder*, 1986), to a network of large channels either cut upwards into the ice (*Röthlisberger*, 1972), or downward into the bedrock (*Nye*, 1973).

Descriptions of soft bed hydrology are more complex. *Walder and Fowler* (1994) assert that flow can occur in channels incised upward into the ice or in a network of *canals* in the upper surface of the till layer. The pressure relationships of the channels and canals for a soft glacier bed is somewhat analogous to the relationships for channels and cavity systems for a hard bed. With increasing water flux the soft bed may evolve from a system of thin water films (*Weertman*, 1983), or flow through the porous till (e.g., *Engelhardt et al.*, 1978) to a network of interconnected spaces in the lee of boulders in the till (*Kamb*, 1987) to a network of channels incised upward into the ice and/or downward into the till (*Boulton and Hindmarsh*, 1987; *Walder and Fowler*, 1994, e.g.,).

It is likely that the hydrology of most temperate glaciers will involve a complex combination of all these types of passageways in a combination of hard and soft bed regimes. Ice flow, sliding at the bed, and variations of water input will work together to constantly alter the importance of the various components. The results of recent bore hole drilling at Black Rapids Glacier along a transverse line at Km-16 show that a thick (6 ± 1 m) till layer was present at those locations (*M. Truffer*, pers. comm.

1997). This suggests that soft bed models may be more relevant in this vicinity of Black Rapids Glacier.

In both hard and soft bed descriptions, the component with highest flux capacity is referred to as channelized flow, and it is characterized by an inverse relationship between water flux and water pressure. A result of this inverse relationship is the tendency for consolidation of flow in fewer channels as the larger channels (with larger fluxes and lower pressures) capture the smaller channels. Channelized flow is generally thought to become more dominant with increasing water flux. Flow in thin films or in cavities is referred to as a distributed system, and can be generally characterized by a direct relationship between water pressure and flux. The prevalence of distributed systems is thought to increase during times of decreased water flux. An important feature of a distributed system is that a larger fraction of the bed is covered by water than for a channelized system (*Willis*, 1995). It is clear that both distributed and channelized systems must coexist - even in times of sustained high subglacial water flux, since a distributed system must drain portions of the bed not accessed by channels. These generalizations likely capture the essence of subglacial systems and are useful in discussing the results of our measurements on Black Rapids Glacier.

6.3.2 *Expected Seasonal Evolution*

Given the framework outlined above, a typical evolution of a hard bed subglacial system in response to seasonal variations in meltwater input is suggested by several authors (e.g., *Willis*, 1995; *Paterson*, 1994; *Röthlisberger and Lang*, 1987). If the total amount of water at the bed is small and the water flux is low, water can flow in a thin film (\sim mm) distributed over a large portion of the glacier bed with steady state water pressures nearly equal to the ice overburden pressure. In the spring, when meltwater from the surface flows to the glacier bed, the increased water flux will increase the film thickness. *Walder* (1982) has shown that when the thickness of the film exceeds \sim 4 mm, film flow becomes unstable, and linked cavities should form as a result

of low pressure zones in the lee of protrusions. Small orifices link the cavities and the competition between melting and closure (due to ice overburden) of the orifices and cavity roofs is thought to control the stability of such a system (*Walder*, 1986; *Kamb*, 1987). If water flux increases and causes melt in the orifices to exceed closure, unstable orifice growth can occur and a system of linked cavities may be converted to a system of channels incised upward into the ice (*Kamb*, 1987). Sliding at the bed will carry the tunnels downslope and will tend to orient the channels parallel to the direction of sliding (*Kamb*, 1987). Thus at high water flux, most of the discharge out of the glacier is thought to occur through a channelized system. The reverse evolution is expected when the flux of meltwater decreases. *Willis* (1995) points out that a major difference between distributed and channelized systems is that water in a distributed system occupies a larger fraction of the glacier bed than a channelized system. This will tend to promote glacier sliding and will increase the response of glacier sliding to a rapid increase in water pressure. These ideas are consistent with observations that the rapid introduction of large quantities of water to the glacier bed has a large effect on glacier motion early in the melt season.

6.3.3 General Categories of Subglacial System Change

Given these basic descriptions of hard and soft bed subglacial systems and an outline of the sorts of expected changes that must occur during the melt season, the expected changes in the hydrological system might be summarized by the following:

- Total or partial conversion of a thin film to a linked cavity system
- Total or partial conversion of a linked cavity system to a channelized system
- Total or partial conversion of a channelized system to a linked cavity system
- Reduction or increase in the number or size of channels in a channelized system
- Reduction or increase in the connectivity of cavities in a cavity system
- Changes in till porosity

- Changes in water storage
- Isolation of, or connection to additional basal cavities (*Iken and Truffer, 1997*)
- Changes in the overall proportion of bed separation (*Iken and Truffer, 1997*)

Each of these changes may have effects on glacier sliding, but will also alter the power reflectivity for the radio waves we use to investigate these changes. Distinguishable among these changes are only those that change the dielectric structure of the basal interface. Several of these changes, such as the conversion of one drainage system to another, will likely cause a change in the distribution of water at the bed, and should therefore change the amount of reflected power. In general an increase in the spatial distribution or amount of water at the bed should increase the amount of power reflected. Consolidation (e.g. channelization) of water flow or a decrease in the amount of water at the bed should decrease the amount of power reflected from the bed.

Among these possibilities, only a few will tend to increase basal sliding which is necessary to explain the observed pattern in BRG speed during the period of observation. The physical interpretations of the RES measurements serve to eliminate some of these possibilities and help define which scenarios are most likely.

6.4 Constraints on Basal Property Changes from Repeated RES Measurements

Three steps are required to constrain the changes in basal conditions at Black Rapids Glacier based on repeated RES measurements: First, I make reference calculations of basal reflectivity and phase based on expectations of general conditions and basal properties at the bed. Second, I calculate the changes in basal properties from the reference conditions necessary to accommodate the RES-measured changes in reflected power and phase. Third, I eliminate changes that are not physically plausible.

6.4.1 Reference Calculations of Reflectivity and Phase

The expected range of reflectivities is calculated for two general cases: (1) a hard bed with a millimeters thick water layer and (2) a soft bed with a meters thick water saturated till layer. The methods used to calculate RES reflectivities and phase angles as well as effective dielectric properties are given in Chapter 3. For either model of subglacial structure, the dielectric properties of the underlying bedrock, the basal layer, and the layer thickness need to be specified.

Hard Bed

For an idealized hard bed (pictured as a water layer between ice and underlying bedrock), the primary unknowns for calculating RES reflectivity are the water layer conductivity and thickness. Ranges of experimental findings for these properties are discussed in Chapter 3. The subglacial water conductivity can be estimated from samples collected from boreholes on BRG: $\sim 3 \times 10^{-3} \text{ S m}^{-1}$ (Ian Willis, pers. comm. 1997), and from measurements of conductivity in the BRG outflow stream: average $\sim 3 \times 10^{-3} \text{ S m}^{-1}$ with a maximum $\sim 8 \times 10^{-3} \text{ S m}^{-1}$ *Raymond et al.* (1995). I therefore assume that the basal water conductivity at BRG ranges from $1 - 8 \times 10^{-3} \text{ S m}^{-1}$. The dielectric permittivity of the underlying bedrock should range between 7 and 11; the values for solid limestone and solid basalt (e.g., *Jones*, 1987). I assume the underlying bedrock to have intermediate permittivity 8.

Using the outlined range of values, I calculate the reflectivity and phase for the two frequencies used in this study using the three layer model given by *Born and Wolf* (1980), and outlined in Chapter 3. Figures 6.1 and 6.2 show the calculated reflectivity (solid lines) for the range of conductivities and water layer thicknesses for 2 and 5 MHz. The reflected phase (dashed lines, Figure 6.1) is also calculated for 2 MHz. A useful constraint is that the reflected power and reflected phase (Fig. 6.1) do not vary in the same manner as a function of thickness or conductivity.

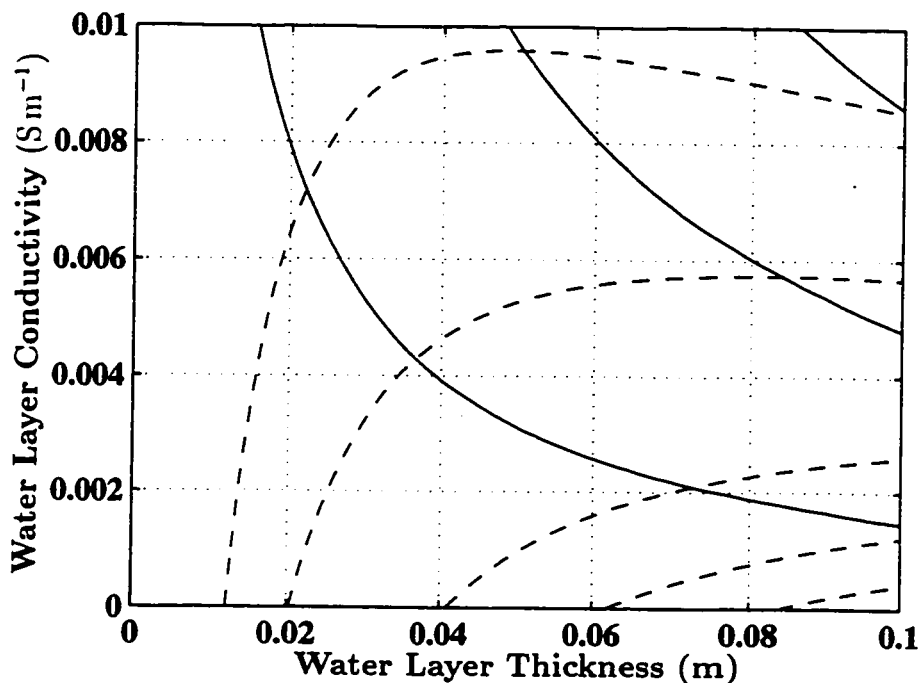


Figure 6.1: **Hard Bed:** Contours of reflectivity (solid lines, interval 0.1) and phase radians (dashed lines, interval 0.1) for 2 MHz wave impinging on a water layer of given thickness and conductivity situated between ice and rock, calculated using the three-layer reflectivity model outlined in Chapter 3.

Soft Bed

For a soft bed (pictured as a water-saturated till layer between ice and underlying bedrock), the primary unknowns to calculating reflectivity are till layer thickness, till porosity, the pore water conductivity and the underlying bedrock dielectric properties. The expected range of till layer thickness can be estimated from bore hole experiments done during 1996 and 1997 on BRG. Bore holes drilled approximately along the Km-16 line (Chapter 4, Figure 4.1), showed a meters thick till layer (M. Truffer, pers. comm. 1997). Porosities of a till layer can be expected to range from 20% (well-consolidated) to 40% (fully dilated) (e.g., *Alley et al.*, 1987; *Blankenship et al.*, 1987a). Assumptions of water conductivity and underlying bedrock properties are the same as for the hard bed case.

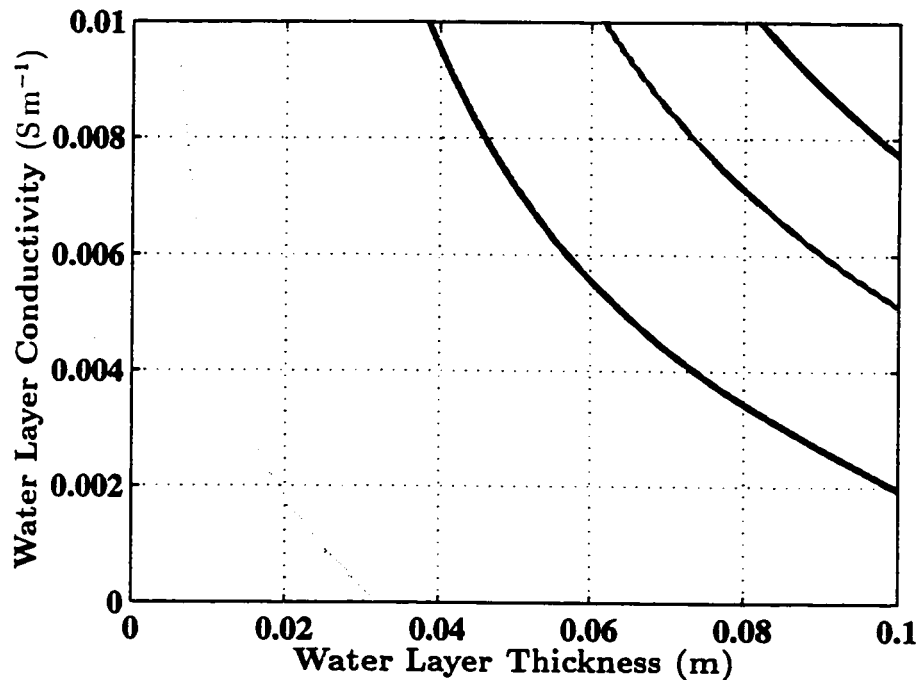


Figure 6.2: **Hard Bed:** Contours of constant reflectivity (interval 0.05) for 5 MHz wave impinging on a water layer of given thickness and conductivity situated between ice and rock, calculated using the the three-layer reflectivity model outlined in chapter 3.

Assuming a porosity range of 25-40% and pore water conductivity range of $1 - 8 \times 10^{-3} S m^{-1}$ yields an effective conductivity range of $0.2 - 2.6 \times 10^{-3} S m^{-1}$ (using the empirical relation given by *Keller and Frischknecht* (1966) and discussed in Chapter 3). The range of effective dielectric permittivities for the rock/water till layer of porosity 25-40% is 18-26 (using Looyenga's mixing model outlined Chapter 3). For the reference calculation I assume the till layer to have permittivity of 20 (the value for porosity of $\sim 30\%$). Figure 6.3 shows the calculated reflectivity (solid lines) and reflected phase (dashed lines) for the range of conductivities and till layer thicknesses for 2 MHz. Again, as with the hard bed assumptions, the reflected power and reflected phase from a till layer each varies in a different manner as a function of thickness and conductivity. Figure 6.4 shows the calculated reflectivity (solid lines)

for 5 MHz.

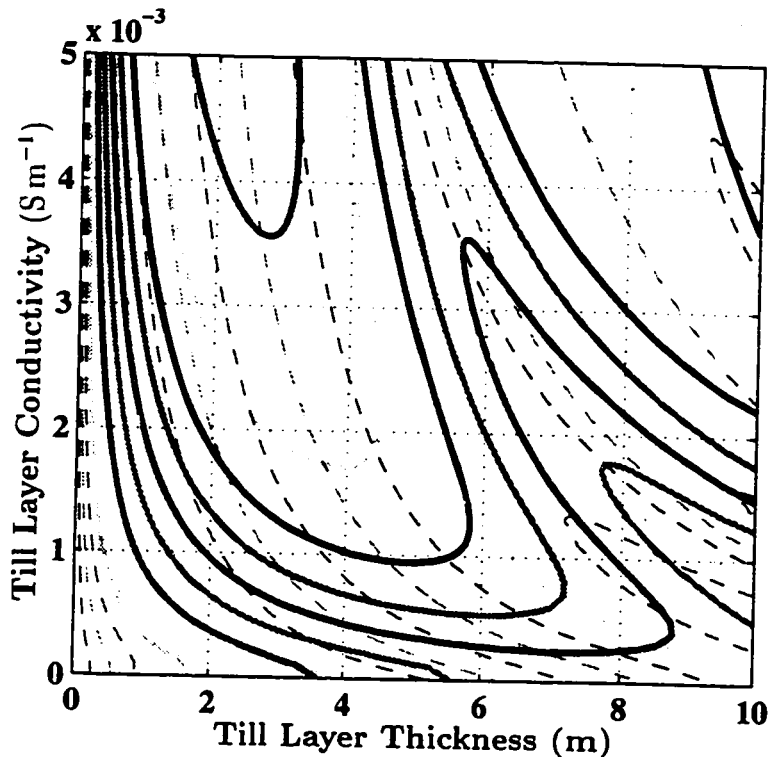


Figure 6.3: **Soft Bed:** Contours of reflectivity (dark solid lines, interval 0.1) and phase (dashed lines, interval 0.1) for 2 MHz wave impinging on a till layer (porosity 30%) of given thickness and conductivity situated between ice and rock, calculated using the effective conductivity, dielectric mixing and three-layer reflectivity models outlined in chapter 3.

6.4.2 Implications RES Fixed Site Measurements

RES measurements indicate that, over the period of observation, the bed reflection power changed by at most 5% and reflected phase by at most 0.06 radians at the two fixed sites at the center of the glacier. For the hard bed case it is possible (though not likely) that the thickness and the conductivity of the water layer could vary in a coordinated manner (approximately inversely) and still yield a constant reflectivity (Figure 6.1, solid lines). However, the measurements indicate that the phase of the

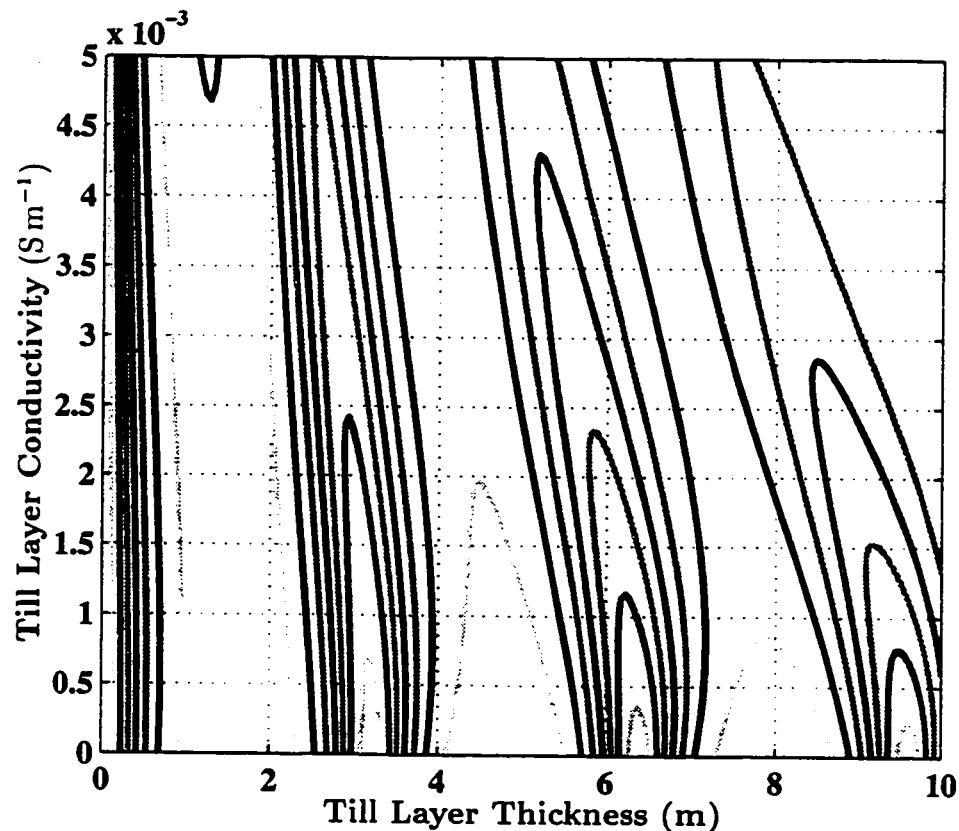


Figure 6.4: **Soft Bed:** Contours of constant reflectivity (interval 0.1) for 5 MHz wave impinging on a till layer (porosity 30%) of given thickness and conductivity situated between ice and rock, calculated using the effective conductivity, dielectric mixing and three-layer reflectivity models outlined in Chapter 3.

reflected pulse also remained constant. Figures 6.1 (hard bed, 2 MHz) and 6.3 (soft bed, 2 MHz) show that reflected power and reflected phase are distinct functions of layer thickness and conductivity. That is, the reflectivity and reflected phase do not vary in precisely the same manner. Because the data cannot limit the changes in reflected power and phase to zero, a range of physical changes is allowed. Figure 6.5 (filled region) illustrates an example of the possible range of layer thickness and conductivities allowed by the data, given an assumed initial water layer of 3 cm and conductivity of $5 \times 10^{-3} \text{ Sm}^{-1}$. The constraints are more severe for thinner and less

conductive layers.

The measurements strongly suggest that the electrical structure and there physical properties remained nearly unchanged at the glacier center during th speedup.

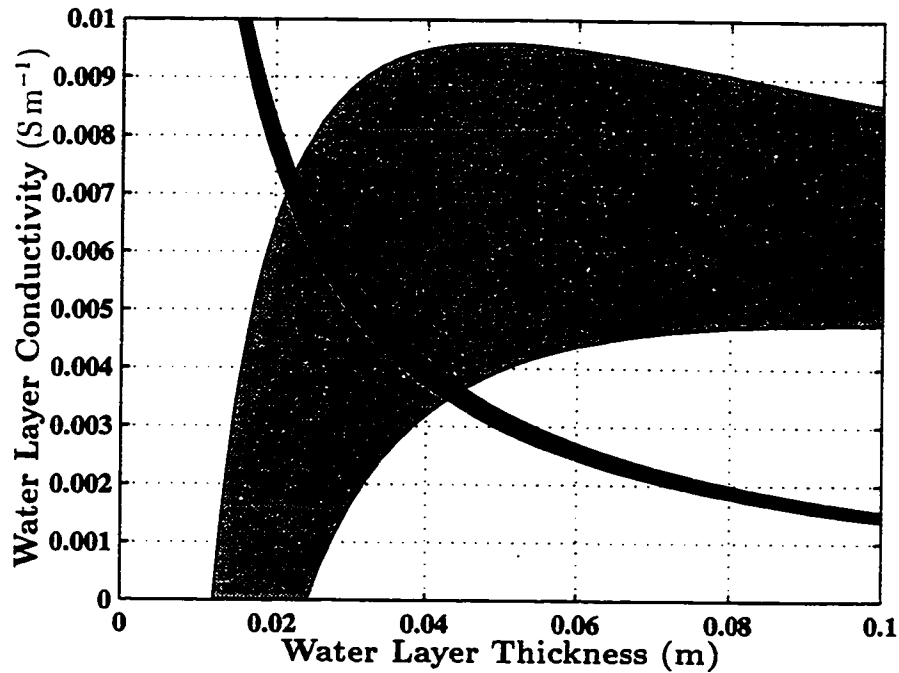


Figure 6.5: **Hard Bed:** Contour of reflectivity= 0.1 ± 0.05 (thick black line phase= -0.075 ± 0.05 radians (gray region) for 2 MHz wave impinging on a water of given thickness and conductivity situated between ice and rock, calculated the the three-layer reflectivity model outlined in Chapter 3. The area in cor between the black and gray regions is the allowable variation in water layer thic and conductivity for a given set of initial conditions.

6.4.3 Implications of Repeated RES Profiles

Interpretation of the repeated RES profile measurements is more difficult t the fixed sites. Large uncertainties allow for only a small portion of the da repeated profiles to be interpreted in terms of time variation of bed reflectio (Chapter 5). Further, phase information could not be reliably extracted f:

repeat profile data. I restrict the following discussion to the data collected at four poles along the Km-16 line (the northern two and southern two poles) and one pole on the Km-14 line (the northern most pole). Only data from these poles (which are toward the glacier margin) contain evidence for changes in reflected power that exceed the associated errors. The reflected power from these locations, plotted as percent differences from the mean, are summarized in Figure 6.6. The observed changes are approximately grouped as either 25 or 50% increases, or 25 or 50% decreases in reflected power. The remaining poles on the Km-14 and Km-16 line are near the center and indicate no change occurred. Below, I use the three layer reflectivity model with effective layer models (Chapter 3) to invert the reflected power for the perturbations (to assumed initial conditions) that might cause the observed changes in reflected power. Each reflectivity model parameter is considered individually though it is clear that changes in some parameters would be accompanied by changes in others. The hard and soft bed cases are considered separately.

Hard Bed

Under hard bed assumptions, a change in bed reflection power may occur due to change in amount, distribution or conductivity of the water layer (e.g. Fig. 6.2). Though changes in these individual quantities may not occur in isolation, I place limits on the changes by separately calculating the amount of change in each parameter that could account for the ~25-50% increases or decreases in reflected power. I begin by assuming that there is an initial thin water layer (2 mm) with conductivity $\sim 3 \times 10^{-3} S m^{-1}$ (as measured for water beneath Black Rapids).

A change in water layer thickness or conductivity could account for the observed changes in reflected power at the bed. Using the three layer model (*Born and Wolf*, 1980, Chapter 3), I calculate that an increase (decrease) of 25-50% in reflected power could be accommodated by an increase in layer thickness of 0.8-1.6 mm (decrease of 0.8-1.5 mm). An increase (decrease) of 25-50% in reflected power would also occur

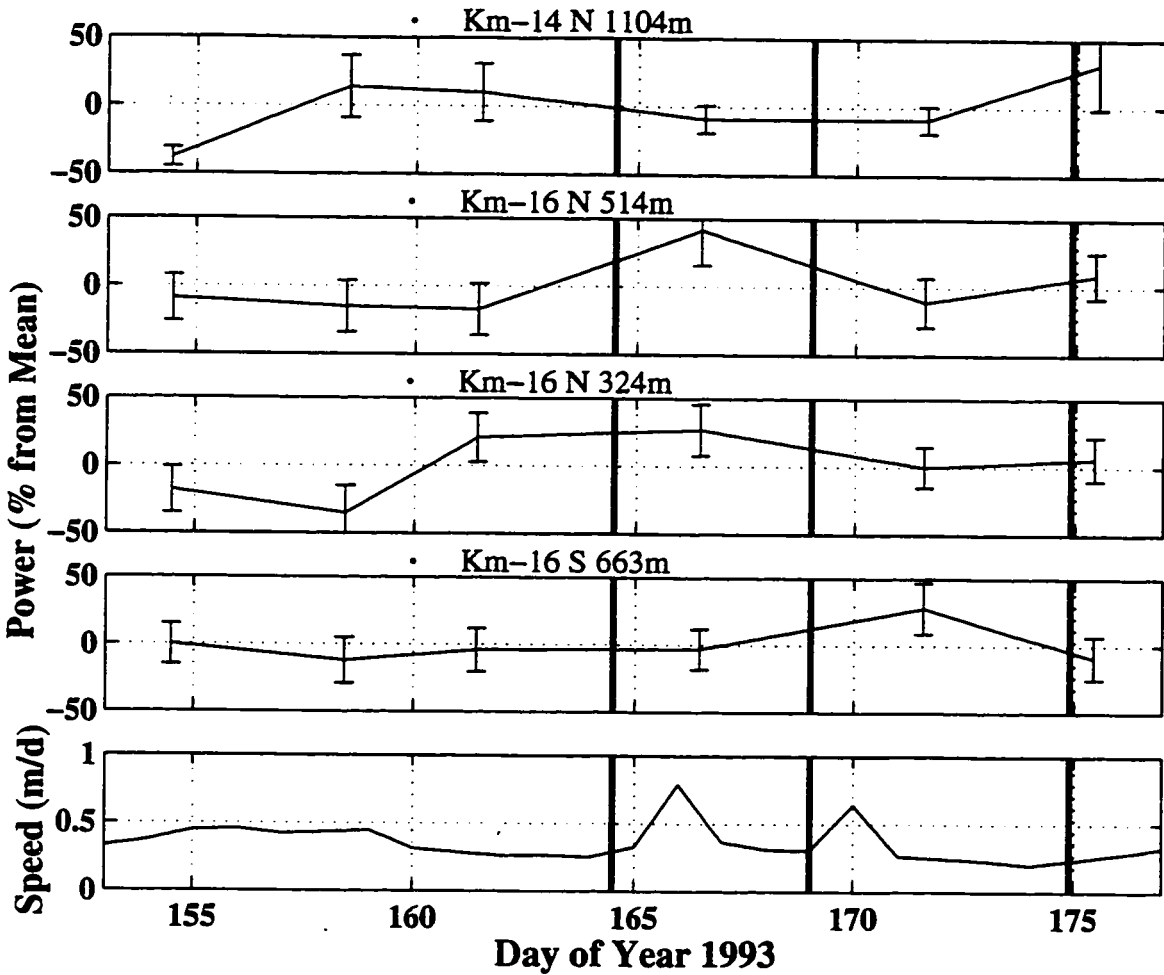


Figure 6.6: Reflected power (percent difference from mean value) at the northern pole of Km-14 (top panel), the northern two poles of Km-16 (panels 2 and 3 from top), a southern poles on Km-16 (panel 4 from top), and daily averaged surveyed glacier speed at Km-15 (bottom panel). Vertical lines indicated the onset of the three lake drainage events. Pole locations are given as horizontal distances perpendicular to flow relative to the center of the subglacial trough.

if the layer conductivity increased by $1.3 - 2.6 \times 10^{-3} S m^{-1}$ (decreased $1.7 - 2.6 \times 10^{-3} S m^{-1}$). Assuming thinner (thicker) or more (less) conductive initial conditions would require smaller (larger) changes in thickness and smaller (larger) changes in conductivity.

Changes in the spatial distribution of basal properties could also change the

reflected power. We first assume that the bed is initially 50% water covered, and the remainder of the bed is in direct contact with the ice. The reflectivity of such a surface can be determined by calculating the approximate effective dielectric permittivity of the heterogeneous surface (*Chan and Marton, 1974a*), then using that value in the three layer reflectivity model (*Born and Wolf, 1980, Chapter 3*). This gives an estimate of the dependence of the reflectivity on the fractional water coverage at the bed. We find that an increase (decrease) of reflected power of 25-50% requires an increase in coverage of 8-14% (decrease of 10-25%). Assuming a smaller (larger) initial fractional water coverage of the bed requires larger (smaller) increases because of the nonlinear relationship between fractional coverage and effective dielectric permittivity.

Thus, if we assume hard bed initial conditions, rather small changes in an initial water layer (~ 1 mm thickness, $\sim 1 \times 10^{-3} S m^{-1}$ conductivity, or $\sim 10\%$ change in fractional coverage) could cause the observed changes in reflectivity. None of these individual changes can be ruled out for obvious physical reasons.

Soft Bed

A change in the reflected power for soft bed assumptions of the subglacial structure may occur due to change in till porosity, till layer thickness, or change in the electrical conductivity of the pore water. Some of these quantities are inter-related (e.g. a change in porosity would likely result in a change of layer thickness), but for now I consider the effects of each of these separately. I assume the initial conditions of a till layer with porosity 30% and thickness 5 m and pore water conductivity $3 \times 10^{-3} S m^{-1}$. Using the mixing models outlined in Chapter 3, the effective conductivity of this till layer is $6.6 \times 10^{-4} S m^{-1}$, and the effective dielectric permittivity 20.

Using the three layer reflectivity model (Chapter 3), a 25-50% change in reflected power requires a change in till layer thickness of 0.35-0.65 m. The results are nearly symmetric for an increase or decrease in reflectivity given the initial thickness of 5 m.

It is important to note that the results will vary as the initial thickness of the till layer approaches multiples of one quarter of the wavelength (~ 3 m for 5 MHz) as discussed in Chapter 3 (see Figure 6.4). A decrease in porosity to 24-13% (increase to 35-40%) would also account for the decrease (increase) of reflected power of 25-50%. Finally, an increase (decrease) in reflected power of 25% and 50% would result from an increase (decrease) in pore water conductivity of $1.4 - 2.8 \times 10^{-3} S m^{-1}$.

Thus if we assume soft bed initial conditions, fairly large physical changes are required to account for the observed changes in reflectivity (porosity changes $\sim 10\%$, thickness changes ~ 0.3 m, or changes in pore water conductivity $\sim 1 \times 10^{-3} S m^{-1}$). Individually, none of these changes in the subglacial structure seem physically plausible.

We rule out the possibility of large changes in till porosity. The till is expected to be partly consolidated, the expected ranges of till porosity are $\sim 20-30\%$. The increase (decrease) in porosity necessary to account for a 50% increase (decrease) in reflected power would cause the till layer porosity to lie outside the range of expected values. The smaller changes in porosity needed to change reflectivity by 25% may also be larger than could occur on the time scale of days. *Clarke* (1987) showed that only the porosity in the upper half meter of till was affected by a change in deformation after 50 hours. Further, *Boulton and Hindmarsh* (1987) show, using time-dependent analysis, that changes in till porosity of $\sim 10\%$ to depths of meters due to perturbations in the subglacial system are predicted to take $\sim 10^2 - 10^3$ years - apparently because perturbations initially only affect the upper and middle portions of a meters-thick till layer.

Large changes in till layer thickness also seem prohibitive. Such changes in till layer thickness could have been revealed by detailed surveying of surface elevation in the vicinity of the locations considered on Km-14 and Km-16, but those measurements were not been made. The mechanism for such rapid (\sim days) and large (~ 0.3 m) increases or decreases in till layer thickness is unclear and would require unrealistically

large production or removal of till material.

Rapid changes in pore water conductivity are not expected because the mechanism would likely require the rapid flux of surface meltwater into the till. The movement of water in a till layer (discussed in Appendix F) as the result of changing water pressure can only affect a small thickness on the time scale of days (e.g., *Paterson, 1994*). Therefore, if the soft bed idealization is correct, the physical changes at the bed required to account for the measured changes in reflectivity toward the glacier margin, must be due either to simultaneous changes in the considered parameters, or to factors not considered.

Simultaneous changes in the till layer parameters are likely. For example, if till porosity changes, pore water volume, till layer thickness, effective conductivity (even if pore water conductivity remains constant), and the effective dielectric permittivity will all change. Starting with the same initial till properties as above, changing the till porosity from 30% to ~ 26.6 - 33.4% and ~ 22 - 38% , and accounting for the associated changes in conductivity, permittivity and thickness, will yield changes in reflected power of $\mp 25\%$ and $\mp 50\%$. The change in porosity needed to alter the reflected power by 25% may be possible, but the porosity change needed for a 50% change in reflected power is not likely to occur on the time scale of days.

It is probable that the soft bed idealization is not realistic. Several studies indicate that if a meters-thick till layer exists under a glacier, only the top portion of the till may be actively involved in deformation (e.g., *Clarke, 1987; Engelhardt and Kamb, 1997*) and therefore the only portion of the layer that may experience significant changes in physical properties. Also, the soft bed hydraulic system of canals described by *Walder and Fowler (1994)*, suggests that the canals should be $10^{-3} - 10^0$ m deep with likely thicknesses $\sim 10^{-2}$ cm. This also implies that changes in physical structure, associated with a changing subglacial hydraulic system, would likely be limited to the top portion of the till layer. Together these suggest that, with respect to calculating the power reflected from the basal layer, a better conceptual

model of the soft bed would be to consider the top $\sim 0.5 - 1$ m as the deformable till layer with potentially changing properties, and the underlying till as having constant properties. This conceptual model would be somewhat similar to the hard bed model, and the kinds of physical changes in a stratified till layer that could produce changes in reflected power may be similar in magnitude to those considered for the hard bed. Changes in porosity, thickness, water conductivity, and spatial distribution water for this upper portion of the till could all vary sufficiently to account for the 50% changes in reflected power. Therefore, it may be more realistic to get significant reflectivity changes as the result of large physical changes within a thin active till layer rather than from changes within a thick till layer.

Though the results are dependent on assumed initial conditions, we can conclude that if the soft bed assumptions are correct, the smaller observed changes in reflected power ($\sim 25\%$) may be the result of small changes in till porosity and associated changes in till thickness and bulk electrical properties. A different model of the soft bed is required to account for the larger observed changes in reflected power ($\sim 50\%$) where the necessary changes in porosity of a homogeneous till layer are too large. Such a model may involve a stratified till layer in which the upper portion (~ 1 m) may have changing physical properties and the bottom portion may be remain relatively unchanged during the period of observation. Regardless of the precise configuration, it is likely that the changes in reflectivity can be generalized as resulting from changes in the amount or distribution of water - either within the till, or at the surface of the basal layer.

Timing of Reflectivity Changes

The timing of reflectivity changes relative to surveyed glacier speed and the onset of lake drainage events is shown in Figure 6.6. No consistent pattern emerges. Each of the poles considered shows a distinct pattern of increasing and decreasing reflectivity. The northern pole on Km-14 shows a 50% increase at the beginning of the season

and an additional 50% increase at the end. The final increase occurs just after the third lake drainage even though the third lake drained well down-glacier ~ 1 km from this location. The northern-most and southern-most location along the Km-16 line appear to show a similar pattern of increasing and decreasing reflected power though the uncertainties in data from the southern pole prevent definite conclusions. There are only four changes in reflected power along the Km-16 line that exceed uncertainty: an increase at S 663 m on day 171.5, a decrease at N 324 m on day 158.5 then an increase on day 161.5 through 166.5, and an increase in power at N 514 m on day 166.5. Both southern poles on Km-16 show reflected power exceeded the average by more than 25% on day 166.5 - two days after the first lake drainage event.

6.5 *Synthesis of RES Results with Other Observations*

During the 1993 field season other observations included weather (Appendix D), surveying of surface speed and elevation (Appendix C), outflow stream turbidity, stage and electrical conductivity (*Cochran*, 1995), drainage of marginal lakes (Appendix E) and repeated active seismic measurements (*Nolan*, 1998).

6.5.1 *Comparison of RES with Seismic Measurements*

Seismic reflectivity measurements repeated daily during the 1993 field season by UAF investigators are described in detail in *Nolan* (1998), and here I highlight the main results.

In summary, *Nolan* (1998) finds that seismic anomalies occurred after each of the lake drainage events - one of these transitions from normal to anomalous state occurred in less than one hour. These anomalies are considered in terms of hard bed and soft bed descriptions of the basal interface. The hard bed description is ruled out because it requires 7 m of water to match the measured seismic velocities. *Nolan* (1998) concludes that the soft bed model is most consistent with the seismic

reflectivity data and predicts the existence of a till layer at least 5 m thick. He notes that the soft bed description is also motivated by the results from recent bore hole samples on BRG which reveal a thick (6 ± 1 m) till layer (M. Truffer, pers. comm., 1997). The seismic anomalies following lake drainages require either a decrease in till saturation or an increase in effective pressure. The favored explanation is a decrease in till saturation from 100% to 97% (by increasing pore space). *Nolan* (1998) suggests that the mechanism for rapidly lowering till saturation is hydraulic jacking by overpressurized channels during lake drainage events. In areas of decreased overburden, the pore-water pressures decrease allowing gas to come out of solution, thereby filling till void space and decreasing its saturation. The jacking and degassing processes can occur quickly and reversibly as is required by observations. On the basis of results from saturated soils literature, *Nolan* (1998) suggests that a decrease in till saturation may weaken the till, allow more deformation, and accommodate the observed increase in sliding velocity.

The Km-16U RES fixed site discussed in Chapter 5 was located over the same region where seismic reflections were measured by *Nolan* (1998). RES measurements at this site concurrent with the seismic measurements showed no detectable change in reflected power or phase. However, as is shown below, RES measurements would not likely detect the change in saturation suggested by the analysis of the seismic experiments.

To calculate the change in reflected power and phase measured by RES resulting from a change in saturation, we first calculate the power reflection coefficient and reflected phase assuming the initial conditions as in *Nolan* (1998); a 5 m thick till layer with 25% porosity and 100% saturation. In addition, we specify the pore water conductivity to be $3 \times 10^{-3} \text{ S m}^{-1}$, consistent with bore hole measurements at BRG in 1997. Using the dielectric mixing model and the effective conductivity model (Chapter 3, *Born and Wolf*, 1980), the effective dielectric coefficient for the till layer is $\bar{\epsilon} = 17.8$, and effective conductivity of the layer is $5 \times 10^{-4} \text{ S m}^{-1}$. Hence, for the

initial state the power reflection coefficient is then $R=0.207$, and the reflected phase $\delta_r = 0.384$.

A drop in saturation from 100% to 97% is taken to mean that the till layer with 25% porosity was initially 100% water-filled increased porosity (to 25.8%) to become 97% water and 3% gas filled. The resulting till layer will have increased in thickness from 5 m to 5.04 m. The effect of this small decrease in till saturation on the effective electrical conductivity of the till layer is not clear, though the effect is likely to be small since the connectivity of the interstitial water will not change significantly. The change in effective dielectric coefficient will be similarly small. The effective dielectric permittivity of a mixture of 97% water and 3% gas is $\epsilon_{water,gas} = 86$, and the effective dielectric permittivity of the 25.8% porosity till layer is $\epsilon_{till} = 25.8$. The reflectivity for the 5.04 m till layer is $R=0.208$ and phase $\delta_r = 0.382$. Thus, both reflectivity and phase would change less than 1%. Repeating the calculation for higher initial porosities gives similarly small results. Therefore, the RES repeated measurements at fixed sites, which show reflected power changes $<5\%$ and phase changes < 0.05 radians, are consistent with seismic measurements and interpretation. However, the RES measurements are unable to confirm the hypothesis given by *Nolan* (1998).

6.5.2 Importance of Glacier Margins

Since our RES measurements suggest that changes in basal conditions occurred toward the margin of the glacier, it is important to explore the role of glacier margins with respect to glacier motion.

Resistance to Sliding

The resistance to sliding provided by the glacier margins has been demonstrated in field measurements. For example, in a study of Athabasca Glacier, Alberta Canada, *Raymond* (1971) made flow measurements by surveying and by using tilt meters

in boreholes. The marginal sliding velocity of this temperate mountain glacier was much less than the sliding velocity at the center and the marginal shear strain rate was correspondingly larger than the basal strain rates near the center. This indicated that a significant portion of the resistance to sliding occurred toward the margins of the glacier. These results are somewhat analogous to those found for Ice Stream B, where the margins and bed were found to have nearly equal resistive drag - despite the very large width to depth ratio (*Echelmeyer et al.*, 1994). The motion of poles in a transverse section along Km-16 on BRG was surveyed between 18 May and 15 June (Appendix C, Figure C.1). The transverse velocity profile implies that the distribution of sliding velocity on BRG is qualitatively similar to that found by *Raymond* (1971) for Athabasca Glacier and is typical of many temperate mountain glaciers. These results are consistent with the subglacial hydraulic potential of Black Rapids Glacier for this region shown in Figure 6.7, which implies that the center of the glacier will be the location of the main drainage system for the glacier (Chapter 4).

Distribution of Water and Water Pressure

A possible explanation for the distribution of sliding at the bed comes from considering the distribution of the ratio of overburden pressure to the water pressure at the bed. We assume that the water table is laterally horizontal at a depth δ beneath an assumed laterally horizontal ice surface and that the average normal stress at the bed is equal to the ice overburden. Figure 6.8 shows the ratio of the overburden pressure to the water pressure at the bed, and illustrates that the difference between ice overburden and water pressure is greater away from the center of the glacier; a change in water table level may be expected to have a greater effect toward the margins. An increase (decrease) in the water table will have the additional effect of flooding a larger area of the glacier bed and may be consistent with variations in bed reflected power toward the edges of Km-14, Km-16 which suggest that changes in the amount or distribution of water occurred near the margin.

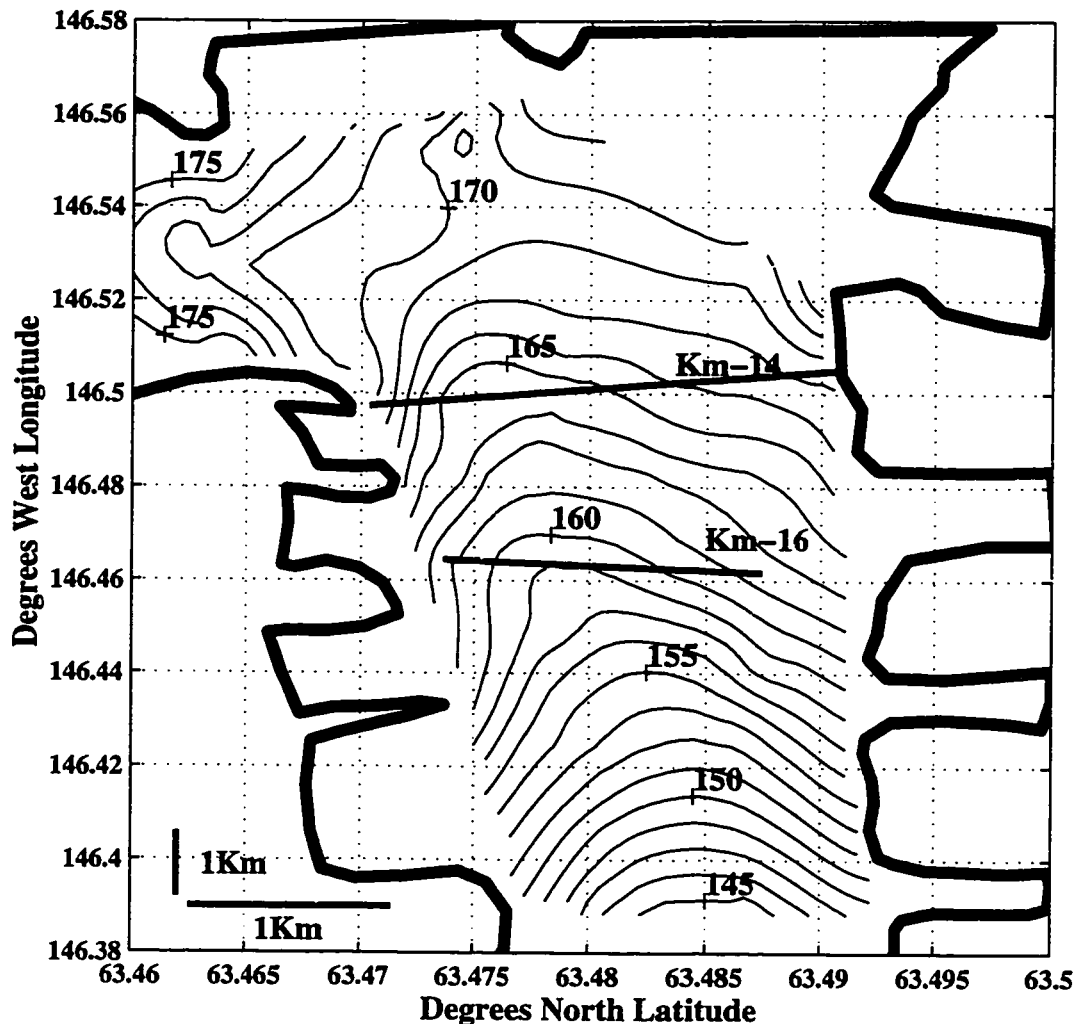


Figure 6.7: 1.25 bar contours of the subglacial hydraulic potential of Black Rapids Glacier. Calculation of hydraulic potential is given in Chapter 4. The Km-14, Km-16 profile lines are also shown.

Routing of Marginal Meltwater Sources

Black Rapids Glacier, like many temperate glaciers, is flanked by high mountain valley walls. The total glacier area including the tributaries is 246 km² while the total drainage basin area is 473 km² (Heinrichs *et al.*, 1995). Much of the water routed through the glacier drainage system originates from snow-melt on these valley

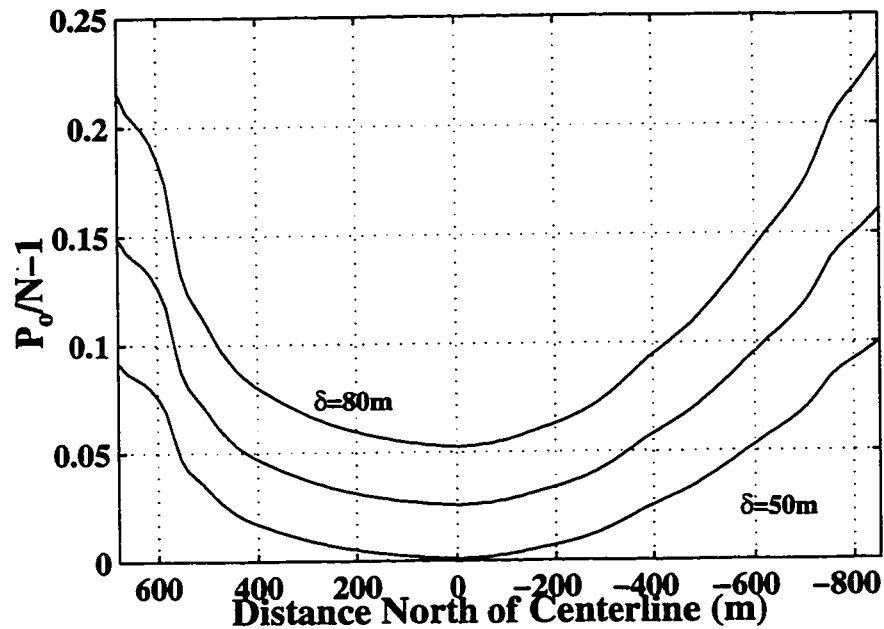


Figure 6.8: The ratio of overburden pressure to subglacial water pressure for Km-16 cross section of Black Rapids Glacier assuming a laterally horizontal water table. The bottom curve is for a level determined by hydrostatic equilibrium at the center, and the upper two curves are determined for levels up to 5% less than equilibrium, indicated by the depth (δ) of the water table below the ice surface.

walls. In addition, many large tributary glaciers enter BRG on both sides along its length. The size of these tributaries varies, but in total the surface area is comparable to the surface area of the glacier itself.

Hence, A large portion of the total water flux originates outside the main glacier and will be routed into the BRG subglacial system through passageways at the margin - an idea that has long been recognized (e.g. *Röthlisberger*, 1972). The lack of evidence of physical changes predicted by RES at the center of the glacier together with evidence of changes toward the margins of the glacier and the knowledge that much of the total water flux must enter at the margins suggests the possibility that glacier-wide speed is driven by changes in basal properties toward the glacier margin.

6.5.3 Longitudinal Coupling

It is also possible that the inferred changes in basal conditions toward the margin are not the cause of observed glacier speedup but are instead *caused by* the speedup. Survey measurements suggest that the spring speedup in the study region may be driven by changes in speed further down-glacier. Measurements of strain were made between poles on the centerline of Km-14 and Km-16 relative to the surveying monument at Km-15 (Appendix C). The cumulative strain between these locations is shown in Figure 6.9, and show that horizontal extension occurred between the up-glacier location at Km-14 and the survey monument at Km-15. Extension also occurred between the down-glacier location at Km-16 and Km-15. The values further indicate that extension down-glacier (between Km-15 and Km-16) exceeded that up-glacier (between Km-14 and Km-15). Photogrammetric measurements of surface velocity have shown that greatest spring speedup occurs down-glacier (near Km-20) of the study region (near Km-15) (*Heinrichs et al.*, 1995). Greater speeds down-glacier could pull the up-glacier ice along flow giving rise to the measured horizontal extension in this area.

Kamb and Echelmeyer (1986) suggest longitudinal coupling length (λ , Equation 6.1) for typical temperate glaciers of 1-3 times the ice thickness.

$$\lambda = \sqrt{\frac{4nf\bar{u}_o h \bar{\eta}}{\tau_o}} \quad (6.1)$$

where n is the flow-law exponent (*Nye*, 1952), f is the channel-shape factor (taken to be ~ 0.5 for a typical temperate valley), \bar{u}_o is velocity, h is the ice thickness, $\bar{\eta}$ is the average effective viscosity, and τ_o is the shear stress. Coupling length λ can increase with increased sliding u_o , and a value up to 12 times the ice thickness was found for a glacier in surge. Values for λ depend on estimates of the parameters of Equation 6.1, but we can estimate that the coupling length for Black Rapids Glacier during the spring would lie somewhere between the extreme values for a surging glacier and the upper bounds for a typical temperate glacier. Taking h to be 600 m, the horizontal

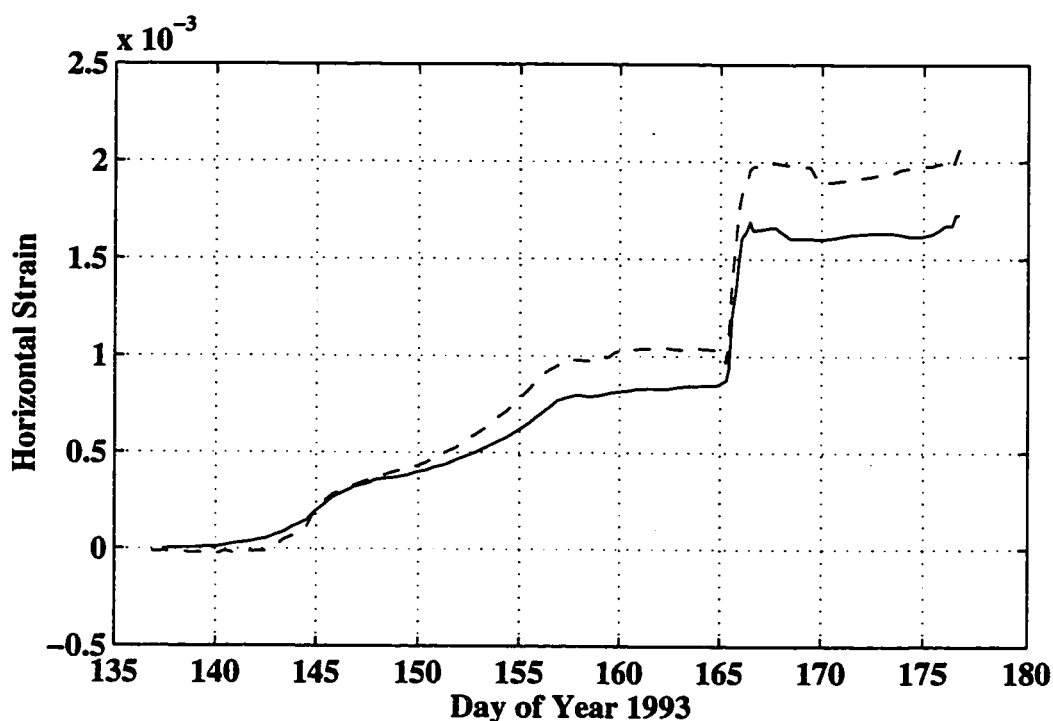


Figure 6.9: Cumulative horizontal strain between the survey monument at Km-15 and Km-14 (solid line) and between Km-15 and Km-16 (dashed line). Positive values indicate horizontal extension. Large strain on day 165 was the result of the first lake drainage event (Appendix E).

coupling length would then be $\sim 2-7$ km. It is therefore, not unreasonable that faster speeds down-glacier (near Km-20) may be exerting influence on the speed in the study region (near Km-14, Km-16).

These measurements, together with a lack of change in basal conditions detected at the center of the glacier in the study region raise the possibility that the spring speedup in this region is caused by changes occurring down-glacier. Changes in basal properties toward the glacier margin may result from the speedup rather than cause it.

6.5.4 Comparison With Expected Seasonal Evolution

Current theories to explain the seasonal evolution of the subglacial system all involve changes in the quantity and configuration of subglacial water. In Section 6.3.2, I review an expected evolution of a hard-bed subglacial system in response to seasonal changes in meltwater input. With increasing meltwater input, the drainage system is expected to become increasingly consolidated - starting out as a pervasive thin sheet and evolving to a channelized system. In addition, observations of vertical displacement during the time of spring speedup (presumably while the subglacial system is evolving from low-flux capacity to high), together with measurements of velocity and water pressure through bore holes have been interpreted as being the consequence of variable water storage at the bed (*Iken et al.*, 1983; *Iken and Bindshadler*, 1986). Variable water storage during this spring evolution has also been suggested on a theoretical basis (for the case of a sinusoidally varying hard bed) to be responsible for the measured vertical uplift as well as increased sliding velocities (*Iken*, 1981).

These models of subglacial system evolution may not be applicable at the center of BRG because physical changes of this sort should result in changes in bed reflectivity that were not observed. These results imply that hard bed models are not fully applicable to BRG and that large changes in basal water storage probably did not occur in the study region.

6.6 Summary and Conclusions

During the field season in spring 1993, Black Rapids Glacier experienced a large general trend of speedup and slowdown over the two month observation period. Glacier surface speed at Km-15 temporarily increased from winter speeds of $\sim 0.18 \text{ m d}^{-1}$ to levels approximately twice that over the period of approximately 40 days (Chapter 5, Figure 5.2). Superimposed on this trend are three nearly symmetric pulses in speed (maximum $\sim 1 \text{ m d}^{-1}$) following the drainage of large ice marginal lakes. These

drainage events were observed to affect the speed over the entire width of the glacier - though the point of water injection was different for the three events.

Repeated RES measurements at the center of the glacier show very little change in reflected power ($\sim < 5\%$) or phase ($\sim < 0.05$ radians) which places heavy constraints on the possible changes in physical structure of the basal interface that may have occurred during the period of measurement. Any physical process that changes the amount or electrical conductivity of the water would have resulted in reflected phase or power changes greater than those measured. Since the whole width of the glacier sped up during this time, the implication is that the water pressure changed over large areas of the bed and altered the basal mechanical characteristics in a manner which did not transfer water mass or change the subglacial electrical structure at the center of the glacier. This conclusion is somewhat consistent with the concurrent findings of the repeated seismic reflection measurements in this region (*Nolan, 1998*). These results suggest that the evolution of the subglacial hydrological system does not take the form of a large-scale re-organization or change in subglacial water storage near the center of the subglacial valley.

Repeated RES measurements from locations away from the center of the glacier show changes in reflected power that allow for changes in basal properties. Increased reflected power may be interpreted as more water at the bed or in the basal layer - though the configuration cannot be resolved. This gives rise to the possibility that the changes in glacier-wide speed may have been driven by changes in basal properties toward the margins of the glacier. RES measurements toward the margin could be accommodated by relatively small changes in water layer thickness or conductivity over a hard bed. The measurements could also be explained by changes in porosity of a meters-thick till layer (such as has been measured to exist), but models show that the required changes would take far too long to have occurred during the observation period. Instead, the RES measurements could be explained by changes in porosity and/or water conductivity in just the upper portion of a stratified till layer is allowed

to experience large changes of porosity or water organization on the time scale of days. The soft-bed explanation is preferred in view of recent borehole measurements which reveal a thick till layer in this region of BRG. The cause/effect relationship between spring speedup and the implied physical changes toward the margin is not clear.

Measurements of strain during this time show that the study area experienced horizontal extension (parallel to flow), with larger extension down-glacier. This implies that the glacier was increasing in speed more rapidly down-glacier. Past photogrammetric surface speed measurements concur with these measurements, and show that the largest increases in speed are down-glacier about 4 km from the study site. It is therefore quite possible that much of the increase in speed at the study site was driven by changes associated with speed increases down-glacier. If true, the changes in basal conditions toward the glacier margin implied by the RES measurements could again be a result of the local speedup rather than its cause.

The results suggest that changes in glacier speed during the spring evolution of the subglacial system in response to seasonal changes in meltwater input may in fact be driven by local changes at sensitive areas of the glacier (either at the margins or down glacier) rather than pervasive glacier-wide changes.

Chapter 7

RADIO ECHO-SOUNDING INVESTIGATION OF BASAL PROPERTIES, SIPLE DOME WEST ANTARCTICA

7.1 *Abstract*

Ground-based radio echo-sounding profiles across Siple Dome, West Antarctica are analyzed to reveal the spatial pattern of reflected power from within the ice and from the underlying basal interface. The radio-echo power returned from within the ice remains nearly constant across the dome except near the margins where the profile crosses topographic *scar features* visible in satellite imagery. The internal reflecting horizons, which persist for ~ 100 km across the dome, are abruptly terminated or strongly deformed at these locations. The scar features are interpreted to be margins of paleo-ice streams where the internal layering was disrupted by shearing between fast and slow moving ice. Following shutdown of an ice stream, continuous layers are expected to be deposited over the previously active shear margin; the age of the deepest continuous layer should indicate the time since the ice stream shut down. Although continuous layers were not detected across the paleo-margins surrounding Siple Dome, they may exist in the top 80 m which could not be imaged with the instrumentation. This would imply that shutdown occurred less than 400 - 650 years BP. Recent (1998) high-frequency radar revises this to 50 m (230 - 350 years BP).

The bed reflection power (BRP), corrected for the effects of instrumentation and ice thickness variation, is nearly constant across Siple Dome suggesting homogeneous basal properties. The measured change in basal reflectivity across the Siple Ice Stream margin allows constraints to be placed on the basal composition beneath Siple Dome.

The factor of 4 increase in returned power observed across the Siple Ice Stream margin limits the basal power reflection coefficient under Siple Dome to be 0.25 or less. This limit indicates that Siple Dome ice must be underlain by solid bedrock or at most a thin (less than ~ 1 m) frozen till layer.

Heat flow models and recent measurements suggest that the temperature at the base of Siple Dome is below freezing and measurements indicate that the ice is likely frozen directly to the solid underlying bedrock. Using typical bedrock dielectric properties, we calculate that the power reflection coefficient of the bed under Siple Dome (for 3 MHz radio waves) is ~ 0.04 - 0.08 . The reflected power increases across the Siple Ice Stream margin by a factor of ~ 4 which cannot be modeled using realistic contrasts in the properties of the basal rock. The reflectivity increase may be explained if Siple Ice Stream is underlain by ~ 30 - 60 mm of liquid water (conductivity 2.5×10^{-2} S). More water is required if it is distributed within the pore space of a till layer or if it is less conductive. The reflected power increase may also be explained if Siple Ice Stream is underlain by a meters-thick frozen till layer. A similar increase in reflected power is measured across the Ice Stream C margin, but a precise calculation is not possible with the data available. However, it is likely that a similar transition in basal composition occurs at this boundary.

The presence of a thick till layer beneath the Siple Ice Stream provides further evidence of its past activity and the possibility that the till is still thawed suggests that streaming motion ceased before the basal layer was frozen. The absence of a thick till layer beneath Siple Dome is consistent with its apparent stability as an inter-ice stream ridge in the past and may suggest that it will remain as a stable ice stream boundary in the future.

Using estimates for the current conditions in

7.2 Introduction

The dynamics and mass balance of the West Antarctic Ice Sheet (WAIS) depend critically on the motion of ice streams. Despite the low driving stresses (10^{-1} bar), these streams move at velocities of two to three orders of magnitude greater than the surrounding ice sheet. Given the mean thickness (10^3 m) and slope (10^{-3}) of these ice streams, it is not possible to accommodate this fast motion by ice deformation (e.g., Bentley, 1987; Echelmeyer *et al.*, 1994). Seismic experiments demonstrate that there is a dilated till layer with average thickness ~ 6 m (Blankenship *et al.*, 1987b) beneath locations observed on Ice Stream B. The results of bore-hole drilling support this conclusion (Engelhardt *et al.*, 1990a). It is thought that this dilated till layer or a thin water layer between the ice and till allows the ice to partially decouple from the underlying bedrock and to slide rapidly at low basal shear stresses (e.g., Alley *et al.*, 1987).

An important finding from measurements in the vicinity of the Siple Coast Ice Streams has been the discovery of rapid changes in ice stream activity (Alley and Whillans, 1991). The first indication of this was the discovery of dormant Ice Stream C (Rose, 1979). University of Wisconsin investigators have since used high frequency radio echo-sounding (RES) to map the depth of buried crevasses at the margins of Ice Stream C, and using an estimate of the accumulation rate, concluded that Ice Stream C stagnated about 130 years ago (Retzlaff and Bentley, 1993). The lack of spatial variation in the depths of buried crevasses indicates that a large area in the lower portion of the ice stream shut down nearly simultaneously. It has been suggested that the lower portion of Ice Stream C stagnated when its water supply was cut off by changing ice thickness distributions which altered the hydrological potential of the source area and diverted water toward Ice Stream B (Anandkrishnan and Alley, 1997). The head of Ice Stream C appears to continue to be active (Whillans and van der Veen, 1993).

Satellite imagery has revealed several curvilinear topographic scars which may be evidence of other zones of formerly active ice stream flow (e.g., *Bindschadler and Vornberger, 1990; Stephenson and Bindschadler, 1990; Scambos and Bindschadler, 1991*). Investigations of these scar features are motivated by the possibility of improving understanding of the mechanisms of ice stream flow and shutdown.

The history of ice stream flow surrounding Siple Dome, and the basal conditions that allowed that flow are of great interest for understanding the stability of the Siple Coast ice streams, the conditions which allow streaming motion, and the conditions under which streaming ceases. This chapter focuses on RES investigations (from the 1994-95 and 1996-97 field seasons) of Siple Dome, West Antarctica and the scar features on both of its flanks. We examine RES records which span Siple Dome and the scar features on its flanks. From these records, the depth of continuous internal reflecting horizons are used to estimate the time since shutdown of the now stagnant ice streams. We also use the pattern of reflected power in the RES records to infer the distribution of basal properties across the dome and show that the bed beneath the paleo-ice streams is likely either a thawed or frozen till >1 m thick, and that the bed beneath Siple Dome is either a hard bed or may contain a <1 m layer of frozen till.

7.3 Siple Dome Site Description

Siple Dome is situated on a bedrock plateau between ice streams C and D (Figure 7.1). Siple Dome is the largest of the inter ice stream ridges, and was selected as a site for a deep ice core because of its potential to yield information about the history of adjacent ice streams and past West Antarctic climate.

RES traverses done by University of Washington, St. Olaf College, and University of Colorado investigated curvilinear topographic scar features on the northeast and southwest flanks of Siple Dome visible in satellite imagery. Figure 7.2 is an AVHRR

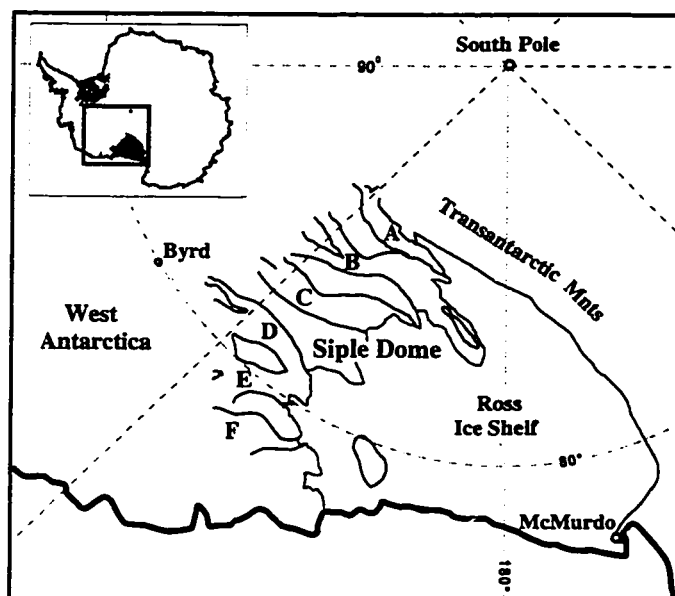


Figure 7.1: Map view of the Siple Coast Region of West Antarctica. The inset panel shows the position of the region relative to the Antarctic continent. Figure courtesy of Nadine Nereson.

(Advanced Very High Resolution Radiometry) image of Siple Dome which shows the scar features of interest.

We traversed Siple Dome and the scar on the north east side of the dome with the University of Washington *MK-II* mono-pulse RES system (Chapter 2) during the 1994-95 field season. Some of these traverses were repeated during the 1996-97 Antarctic field season by R. Jacobel and C. Raymond and were extended to include the southern flank of the dome. The focus of this chapter is a composite RES profile across Siple Dome. The profile (shown in Figure 7.3, upper panel) spans from 90 km south of the summit, crossing a paleo-margin of Ice Stream C (and several other topographic features), Siple Dome, and continues 71 km north across the relict Siple Ice Stream margin (Jacobel *et al.*, 1996). The profile is shown approximately by the continuous white line segments in Figure 7.2. The surface topography was obtained using the barometric pressure recorded with each RES measurement to interpolate

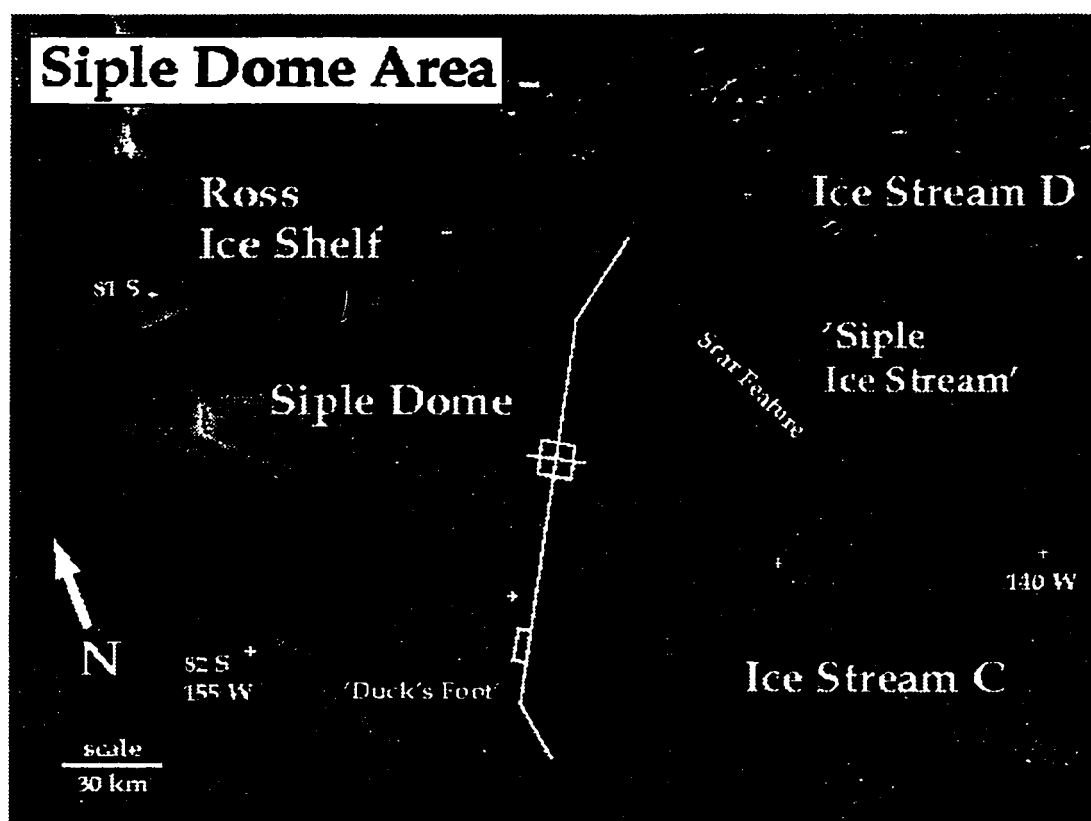


Figure 7.2: AVHRR satellite image of Siple Dome showing ice streams C and D. White lines display the paths of RES traverses performed during the 1994-95 and 1996-97 field seasons. Relict ice stream margins can be seen near both ends of the RES traverse (*Scar Feature* and *Duck's Foot*). Image courtesy of Ted Scambos, National Snow and Ice Data Center, University of Colorado.

between GPS-measured elevations (*Scambos and Nereson, 1995*).

7.4 Radio Echo-Sounding Data

Spatial variations of the bed reflection power (BRP) can be interpreted to determine variations in conditions at the base of an ice sheet. Variations in the BRP can be caused both by variations in the thickness and dielectric properties of the overlying ice as well as by variations in the bed dielectric properties. The effects of varying ice thickness and properties must be removed to isolate variations in the BRP caused by

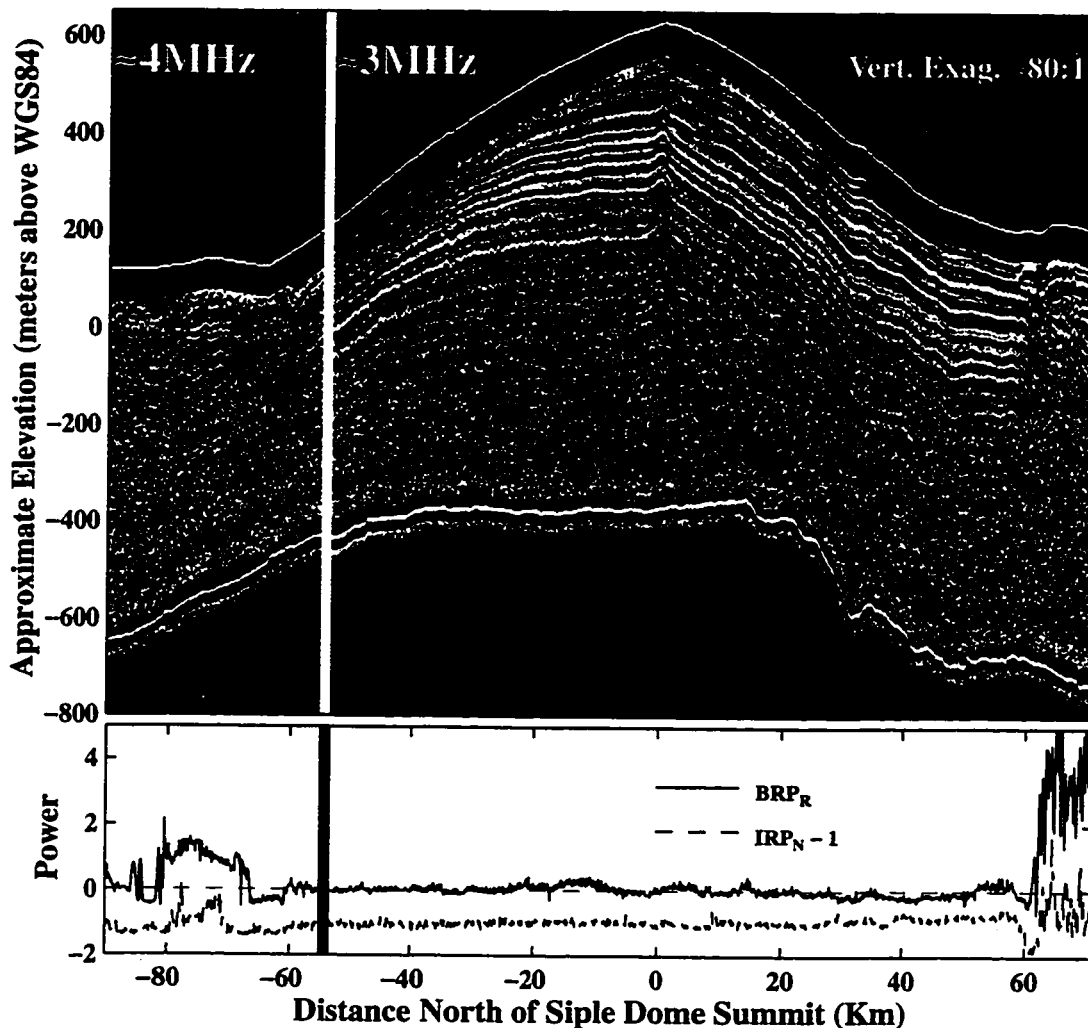


Figure 7.3: The upper panel displays a composite of 4 and 3 MHz RES data obtained by R. Jacobel, and C. Raymond in 1996. The first $0.75 \mu\text{s}$ (80 m) of data (clipped by the direct wave) are shown in black. Surface topography was obtained primarily by GPS surveying (*Scambos and Nereson, 1995*). The lower panel displays the BRP_R (Equation 7.2), and the IRP_N (Equation 7.3) shifted by -1 for display purposes and is discussed in subsequent sections. The vertical line in both panels marks the frequency transition in the data. Ice Stream D is to the north (right), and Ice Stream C is to the south (left).

changes in bed reflectivity.

7.4.1 *Removal of Instrumentation Effects*

The direct wave, which travels from transmitter to receiver along the snow surface, arrives at the receiver with an amplitude several orders of magnitude larger than the reflection signals from within the ice. Small reflections from shallow reflectors are superimposed on top of this large signal. The receiver gain must be set high enough to resolve small reflection signals and as a result the large signal from the direct wave is heavily clipped. Most of the reflection information at the beginning of each record is lost for the duration of the direct wave ($\sim 0.75 \mu\text{s} = 80 \text{ m}$). The surface conditions in these polar regions are likely to be spatially constant, and therefore the direct wave has a distinct and consistent signature. Some near-surface reflection information can be retrieved by removing this signature.

The direct wave signature is contained in the average of the records in a profile. We cannot simply remove the average from each individual record because that would also remove *any* signal from reflectors parallel to the surface such as reflecting horizons at constant depth. Therefore, a low-pass filter is first applied to the mean record from the time beyond the end of the direct wave to the end of the record. This produces a *filtered mean* record that contains the direct wave signature, but is smoothed beyond that point. This filtered mean record is subtracted from each individual record in the section and the process is repeated for each of the sections of the profile. The *demeaned* data are then bandpass filtered with a zero-phase forward and reverse digital filtering routine with a fourth-order Butterworth filter (corner frequencies 1:10 MHz) to remove high frequency environmental and system noise and low frequency system noise.

7.4.2 *Selection of Basal Reflection*

The filtered data are plotted and an automated bed reflection picking routine is used to determine the precise travel time and amplitude of the bed reflection from within

a hand-selected time window which is chosen to bracket the bed. Figure 7.4 displays the bed reflection portion of a typical record with the picked features labeled.

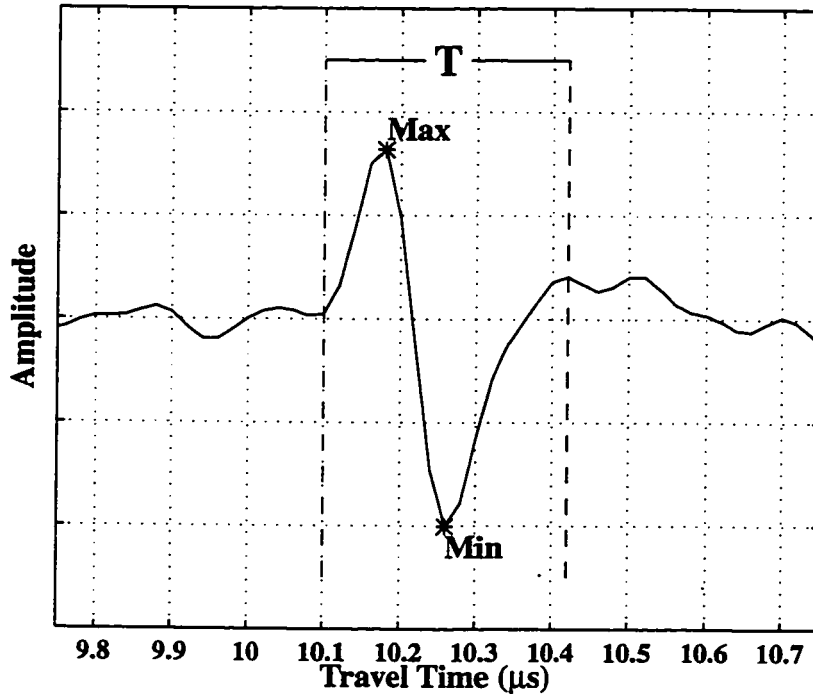


Figure 7.4: The bed reflection from a typical RES record from Siple Dome plotted as returned amplitude vs two-way travel time. The travel time and amplitude of the maximum and minimum are labeled, and the period of the pulse T is shown as the window of time between the dashed vertical lines.

The shape of the bed reflection is uniform across Siple Dome which allows for a simple definition of the duration of the reflection (bed reflection window). The period of the bed reflection T is defined to be twice the time interval between the maximum and minimum value (Figure 7.4), consistent with the results of Fourier analysis in defining the center frequency of the bed reflection.

7.4.3 Calculation of Power

I define the returned power P from within time window $t_1:t_2$ as one-half the sum-of-squared amplitudes (A_i) divided by the number of samples in the window:

$$P \equiv \frac{1}{2(t_2 - t_1 + 1)} \sum_{i=t_1}^{t_2} A_i^2. \quad (7.1)$$

This definition is consistent with the definition of the energy of a monochromatic sinusoidal wave train, which is simply half the amplitude squared and integrated over a full period. Normalizing by the number of samples allows a comparison of the power without distorting the results by the width of the window.

The window of time over which power calculations are made is defined as time length T centered on the reflected pulse (Figure 7.4). For each record the bed reflection power is calculated over a window using Equation 7.1. This quantity is referred to as the *bed reflection power* (BRP).

As a measure of radio wave reflection and attenuation properties within the ice, the normalized power (Equation 7.1) for a fixed window from ($2 \leq t \leq 6 \mu s$) is calculated. This time window begins immediately after the clipped direct wave and ends just before the bed reflection for the shallowest portion of the profile. This quantity is referred to as the *internal reflection power* (IRP). The IRP is a measure of the amount of energy being reflected from within the ice column and is assumed to be an index of the power attenuated/scattered in the ice. Calculating the IRP is motivated by the fact that variations in the BRP may be caused by variations in the IRP. An increase (decrease) in the BRP may be caused by a decrease (increase) in the IRP. On the other hand, an increase (decrease) in both the IRP and BRP might indicate that either the attenuation in the ice decreased (increased), or that the amount of energy propagating from the transmitter into the sub-surface ice increased (decreased). For example, the presence of buried crevasses is expected to scatter and reflect energy reducing energy propagation to the ice interior and bed. This would decrease both the BRP and IRP. Such an effect is likely responsible for the

simultaneous decrease in IRP and BRP near -70 km and at 60 km shown in Figure 7.5, where buried crevasses are believed to exist.

The RES system records $\sim 1 \mu\text{s}$ of pre-trigger signal with each record which enables us to determine the level of background noise. The noise power (calculated using Equation 7.1) provides a reference for interpreting the signal to noise ratio.

Figure 7.5 displays a semi-log plot of the BRP, IRP, and noise (all calculated by Equation 7.1). The noise level is more than an order of magnitude less than the IRP and BRP. The decrease in noise level near the dome summit (-5 to +10 km) corresponds to a reduced traverse speed across the surface while profiling (C. Raymond, pers. comm.) and the corresponding increase in data averaging. The IRP is relatively constant across the dome, but the variability increases across the scar features at either end of the profile. The large decrease in the BRP between -60 km and the summit is primarily related to the increase in ice thickness and is discussed in detail in section 7.4.4.

7.4.4 Correction for Ice Thickness Variation

The attenuation of signal with path length (travel time or ice thickness) is a first-order effect. The greater the path length, the greater the attenuation due to geometric spreading of the wavefront and absorption/reflection within the ice. Changes of ice thickness across Siple Dome cause the BRP to vary by nearly two orders of magnitude (Figure 7.5). Therefore, the BRP must be corrected for varying ice thickness. Because knowledge of the instrumentation and ice properties is insufficient, a physically-based correction is not possible. However the data span a sufficient ice thickness range to make an empirical correction.

An empirical relationship between travel time (ice thickness) and BRP is formulated using a section of the RES profile where the relationship is smooth and single-valued. The section from -54 km to +57 km is chosen because the ice and bed properties are expected to be homogeneous and variations in BRP should be caused

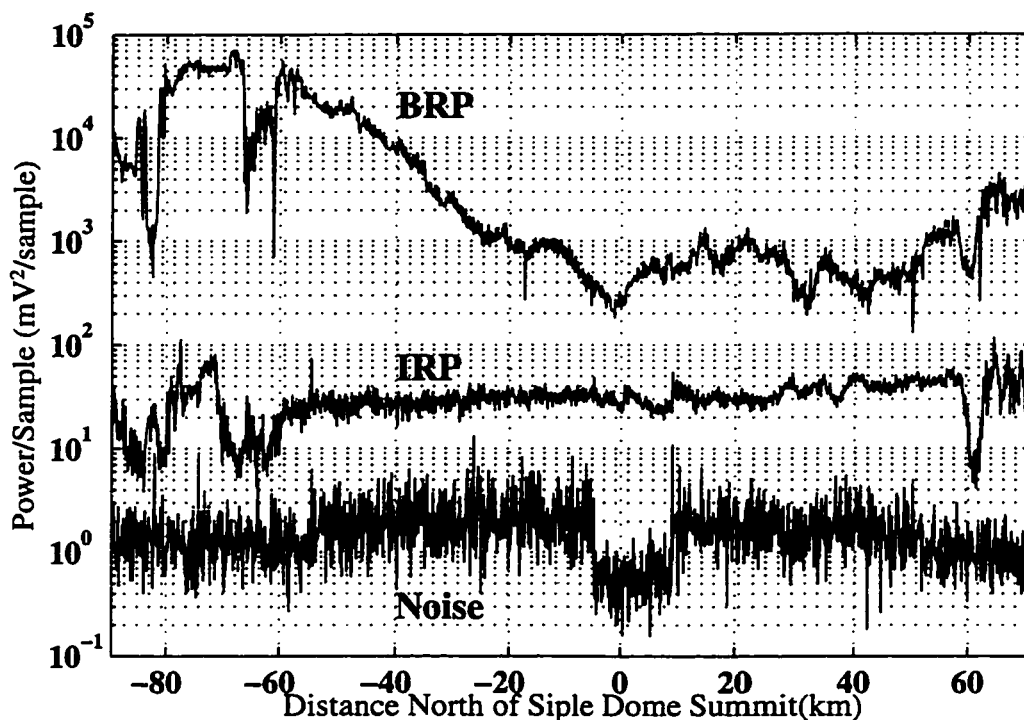


Figure 7.5: Relative power levels of (from top to bottom) bed reflection power (BRP), internal reflection power (IRP), and noise. The BRP varies with IRP, noise, ice thickness and dielectric properties at the bed. The large scale variation in BRP is due to varying ice thickness across the profile which is discussed in section 7.4.4.

primarily by variations in travel time. Data from regions where obvious contrasts in ice or bed properties occur (e.g., across the scar features) are excluded. In this section, the IRP is nearly constant which suggests that the ice properties are relatively homogeneous.

A third-degree polynomial fit characterizes the BRP/thickness relationship ($r^2 = 0.97$, $rms = 0.04 \times 10^4 \text{ mV}^2 \text{ sample}^{-1}$), and the residuals are evenly distributed about the function - though the fractional uncertainty in the fit is slightly higher for larger values of travel time (Figure 7.6, inset panel). The goodness of fit and pattern of the residuals suggests that the data chosen for this empirical relationship are not significantly affected by variations in bed reflectivity or ice properties. An alternative

explanation is that the ice properties and/or bed reflectivity vary smoothly as a function of ice thickness which is not physically reasonable.

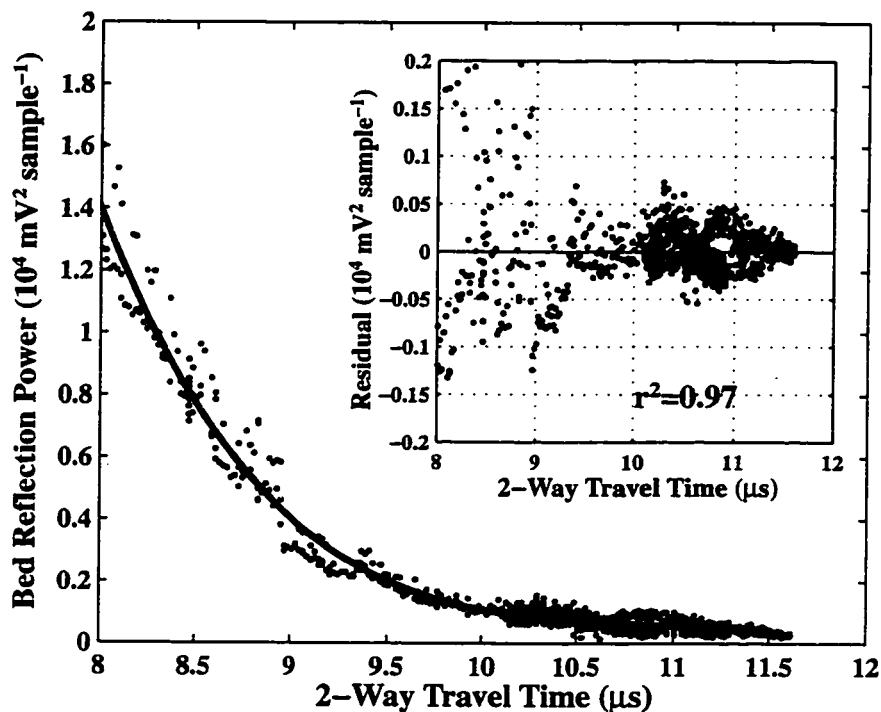


Figure 7.6: Main panel: BRP versus travel time relation. The data are displayed as points. The solid line displays the best (least-squares) third-degree polynomial fit to the data. Inset panel: residuals from fit.

7.4.5 Correction for Frequency Differences

The main profile across Siple Dome is a composite of data collected at 3 MHz center frequency and a small portion collected at 4 MHz. The first (southern) section of the profile was measured with center frequency ~ 4 MHz, the remaining section was measured with center frequency ~ 3 MHz. Center frequencies of these data were determined by a Fourier power spectrum analysis of the bed reflection pulse of 100 records in each section. The precise results of the analysis yield 3.9 ± 0.3 MHz for the 4 MHz section and 3.1 ± 0.3 MHz for the 3 MHz section. The system response, the ice atten-

uation and basal reflectivity are all frequency dependent. A small (10 km) section was repeated at both frequencies, but the overlapping region covers an insufficient ice thickness range to derive an empirical relationship between the two frequencies. The 4 MHz portion of the data are simply multiplied by a constant value to match the 3 MHz portion such that the results are continuous across the transition. Results from the 4 MHz data in this composite profile are therefore qualitatively correct, but absolute values are not directly comparable to the 3 MHz data.

7.5 *The Residual Bed Reflection Power of Siple Dome*

The residual bed reflection power (BRP_R) is BRP remaining after applying the depth correction. I define the BRP_R as the fractional difference of the measured BRP from the BRP calculated from the empirical fit:

$$BRP_R = \frac{\text{measured } BRP}{\text{calculated } BRP} - 1. \quad (7.2)$$

The BRP_R is the portion of the BRP that is not explained by the ice thickness variation. For comparison, the normalized internal reflection power (IRP_N) is defined as the fractional difference of the measured values from the mean value:

$$IRP_N = \frac{\text{measured } IRP}{\text{mean } IRP} - 1. \quad (7.3)$$

Both BRP_R and IRP_N are plotted in Figure 7.7. They are also shown in Figure 7.3, where the variation of BRP_R and IRP_N can be seen in relation to the topographic and stratigraphic features of the dome. The BRP_R is relatively constant across the Dome but both the variability and the power increase significantly across the scar features at either end of the profile. These corrected data are discussed further in sections below.

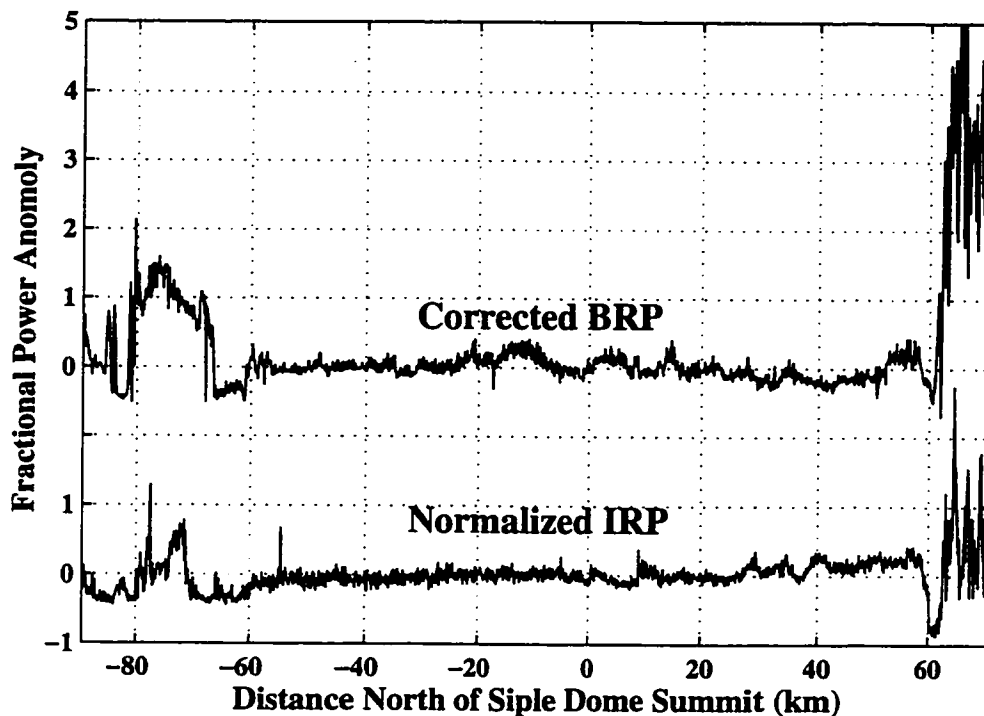


Figure 7.7: The BRP_R is calculated from Equation 7.2, and the IRP_N from Equation 7.3.

7.6 Discussion

7.6.1 Buried Stratigraphy Across the “Siple Ice Stream” Margin

Figure 7.8 displays a high-resolution (4 MHz) traverse across the north scar of Siple Dome. The abrupt termination of well defined internal layering at \sim Km 55 (Figure 7.8) established that the *scar* feature on the northeast flank of Siple Dome is likely a relict ice stream margin (Jacobel *et al.*, 1996). The assumption is that shearing associated with the formerly-active margin disrupted the internal stratigraphy. The termination of internal layering is clearly visible in both Figures 7.3 and 7.8 near 60 km where internal reflecting horizons below 200 m¹, persistent for tens of kilometers across Siple Dome make a slight down-turn and then vanish. This disappearance

¹ A calculation of radio wave velocity at Siple Dome can be found in Appendix G.

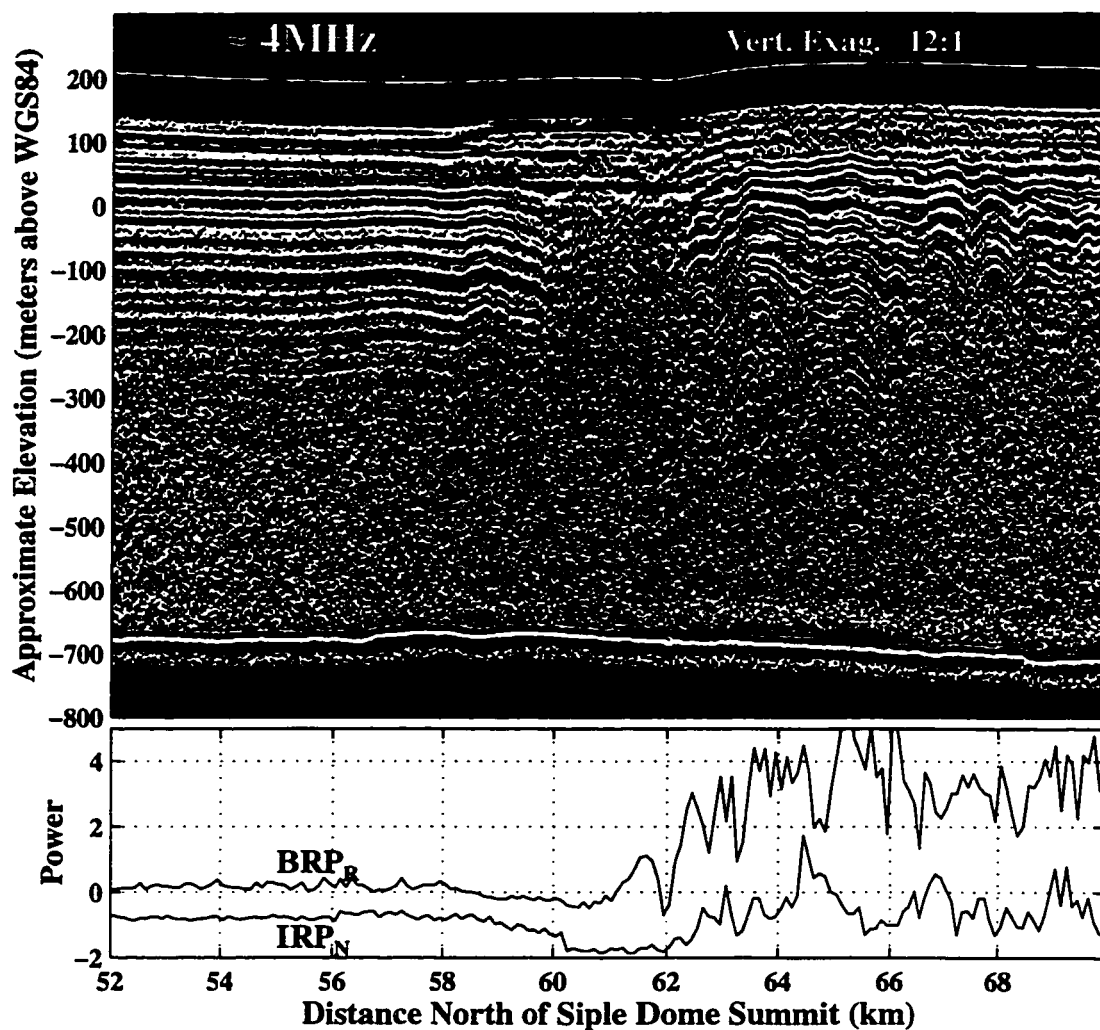


Figure 7.8: A composite of the 1996 ~ 3 MHz RES traverse across the north scar of Siple Dome. The first $0.75 \mu\text{s}$ (80 m) of data are clipped by the direct wave and are shown in black. The horizontal axis is consistent with Figure 7.3. Evidence of buried crevasses is seen as faint point diffractors (visible as hyperbolae) between 60 and 65 km in the top $2 \mu\text{s}$ (200 m) of the profile. The BRP_R (Equation 7.2) and IRP_N (Equation 7.3) (shown in lower panel) are the same as in Figure 7.3.

of the internal layers is coincident with the scar feature seen in AVHRR imagery (Figure 7.2). This scar extends from the upper part of Ice Stream C to the Ross Ice shelf parallel to the active margin of Ice Stream D. The internal stratigraphy visible beyond the scar further along the profile (beyond 62 km) has a folded character

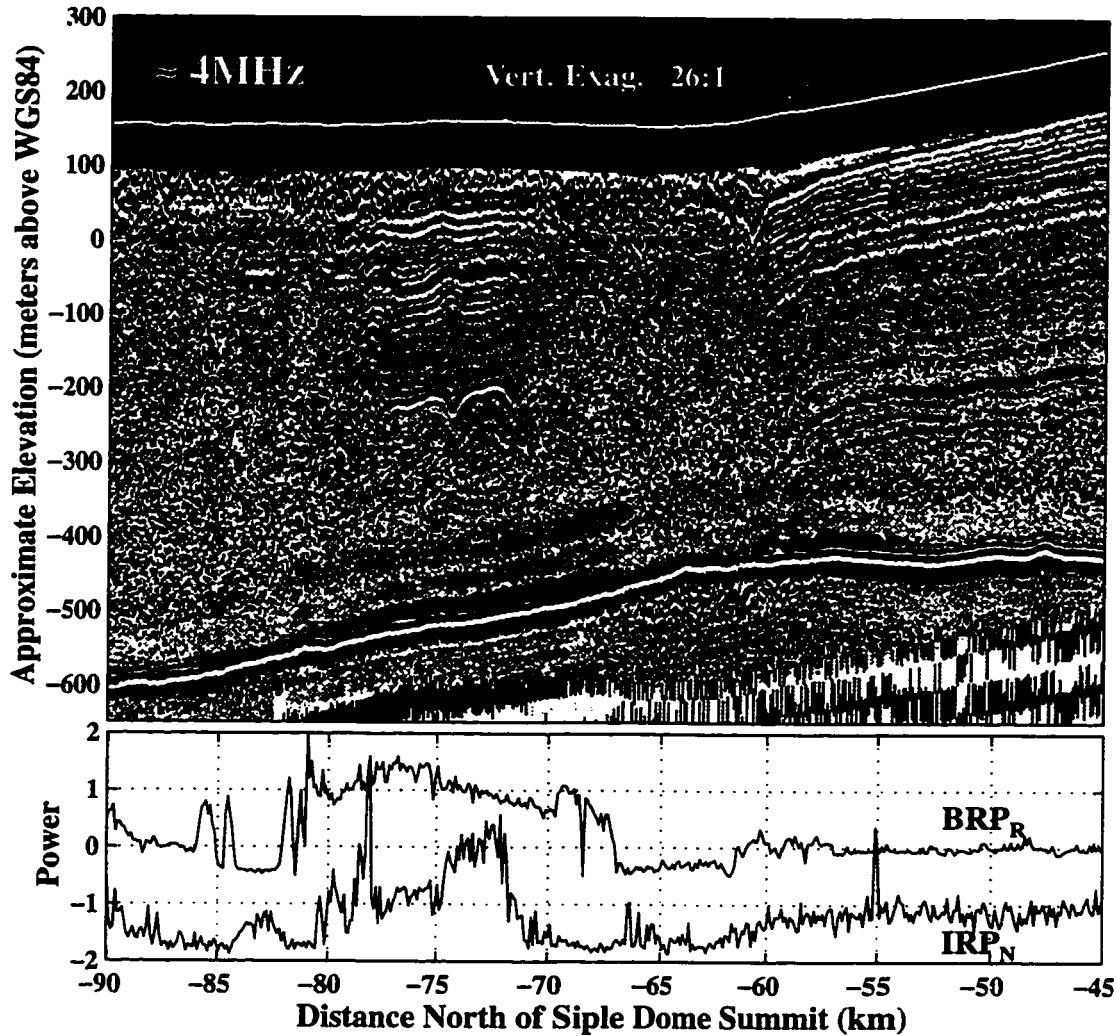


Figure 7.9: A composite of the 1996 4 MHz RES traverse across the ice stream C margin. Data are reduced by the methods described above. The first 80 m of data are clipped by the direct wave and are shown in black. The horizontal axis is consistent with Figure 7.3. The BRP_R (Equation 7.2) and IRP_N (Equation 7.3) (shown in lower panel) are the same as in Figure 7.3.

similar to that found in RES traverses within active ice streams (e.g., *Jacobel et al.*, 1993).

The age of ice stream stagnation can be estimated if we assume that the previous activity prevented continuous layer formation and that new continuous layers form

across the previously active margin after shutdown. Under these assumptions, the age of shutdown corresponds to the age of the deepest continuous layer. In an earlier interpretation using data from the 1994 field season, we believed we had identified a continuous layer between 1.5 and 2.2 μs which corresponds to a depth of ~ 200 m and an age of 1300-1700 years BP (*Jacobel et al.*, 1996). However, a continuous layer is not visible in the higher-resolution RES data collected during the 1996 field season (Figure 7.8) and it is likely that our earlier estimate of the stagnation age is too old. If a continuous layer exists, it must be within the portion of data obscured by the direct wave (the upper 0.75 μs ~ 80 m shown in black in Figure 7.8). If we assume that a continuous layer exists at the maximum depth obscured by the direct wave (~ 80 m), we can place an upper limit on the age of shutdown. At the Siple Dome summit, 80 m depth corresponds to an age of 650 years *Mayewski et al.* (1995). Assuming that the accumulation rate is 1-1.5 times higher at the Siple Ice Stream margin (N. Nereson, pers. comm.), the upper limit of the age of shutdown is 400-650 years BP. The actual age of shutdown will be less if the deepest continuous layer is shallower than 80 m.

However, it is possible that post-shutdown shearing might still be sufficient to disrupt layers and prevent the formation of continuous layers across the paleo-margin. Results from velocity measurements indicate the higher sloped dome ice is flowing more rapidly than the lower sloped and relatively stagnant Siple Ice Stream (N. Nereson, pers. comm.). It is possible that the current shearing along this margin may prevent the development of any clear continuous layers. On the other hand, it is possible that moderate shearing may not disturb a continuous layer as seen by low-frequency RES (wavelength $\sim 10^1 - 10^2$ m). If layers are visualized as continuous sheets deposited across the margin (as is generally assumed in the common practice of interpreting these layers as isochrones), we can imagine that in conditions of shearing, the sheet may be simply torn along this margin and realigned; the up-flow portion of the sheet on one side of the margin would line up with the down-flow portion of the other. In this case, a small discontinuity may be formed and might not be detected

by RES profiles taken at a low spatial density. Therefore, the age of layers continuous across the margin may not yield an accurate age of the cessation of rapid shearing. A better estimate could be determined from measurements of the minimum depth of buried crevasses as was done using high-frequency RES by *Retzlaff and Bentley* (1993) on Ice Stream C. Since crevassing indicates rapid shearing, the shallowest buried crevasse provides both evidence of rapid shear and the time when rapid shearing ceased. Crevasses shallower than ~ 80 m can not be detected in these data, but during the 1997-98 field season, crevasse burial depth at the Siple Ice Stream margin near its junction with Ice Stream C was found to be ~ 50 m using a high frequency (80 MHz) RES system (N. Lord, pers. comm. 1998). This depth is consistent with the prediction made above (that the depth is less than 80 m), and revises the timing of shutdown (under the same assumptions of local accumulation rate relative to Siple Dome summit) to 230-350 years BP. This age is consistent with a recent estimate based on the evolution of margin topography which predicts that the Siple Ice Stream shut down <500 years ago (*Nereson*, 1998).

7.6.2 *Bed Reflection Power Variations Across the Siple Ice Stream Margin*

The BRP_R is nearly constant across Siple Dome but increases by a factor of ~ 4 and becomes more variable across the margin of the Siple Ice stream (Figure 7.3), (since the BRP_R is defined to be the fractional difference from the empirical travel time vs power relation, the value of ~ 3 as shown in Figure 7.7 lower panel beyond 60 km means that the reflected power actually increased by a factor of ~ 4). This increase in BRP_R implies that the physical conditions at the bed changed across the transition and can be used to estimate the current basal conditions of the Siple Ice Stream and beneath Siple Dome.

7.6.3 *Inferred Basal Composition of Siple Dome*

Based on a one-dimensional heat flow calculation (*Nereson et al.*, 1996), and on direct measurements through bore-holes (H. Engelhardt, pers. comm. 1998), it is likely that Siple Dome is frozen at its bed. The increase in BRP_R measured across the paleo-ice stream margin allows us to directly place limits on the basal composition beneath Siple Dome.

The largest reflectivity of any interface can be at most $\mathcal{R}=1.0$, but realistically, the highest reflectivity from a range of expected basal layers is $\sim \mathcal{R}=0.8$ (e.g., *Jiracek*, 1967; *Bogorodsky et al.*, 1985). Since the BRP_R beneath Siple Dome is a factor of 4 less than under the Siple Ice Stream, we can infer that the reflectivity under Siple Dome is at most $\mathcal{R}=0.25$, but is more likely less than $\mathcal{R}=0.20$. Calculations of the reflectivity for measured properties of frozen permafrost materials (Chapter 3, *Jiracek*, 1967), show that the reflectivity for these materials is generally greater than $\mathcal{R}=0.2$, so we can therefore conclude that there cannot be a thick (>1 m) frozen till layer beneath Siple Dome - though a layer less than the skin depth of the radio wave (<1 m) is possible.

7.6.4 *Inferred Basal Composition of Siple Ice Stream*

We cannot directly conclude that Siple Dome ice is frozen to the underlying bedrock from our RES measurements. Attempts to drill into the basal material under Siple Dome were prevented by the presence of a solid material which bent the drill, which indicates that Siple Dome is underlain by solid bedrock rather than a frozen till layer (H. Engelhardt, pers. comm. 1998). I proceed under the assumption that the indications from drilling attempts are correct.

To calculate the reflectivity of the bed beneath Siple Ice Stream, I first calculate the reflectivity for Siple dome using estimates of the electrical properties of bedrock. The range of dielectric permittivities for bedrock is relatively narrow, and most rock

should have a value between 7 (limestone), 10 (sandstone) and 11 (basalt) (e.g., Jones, 1987; Bogorodsky *et al.*, 1985). Electrical conductivities for the frozen bedrock should range $10^{-4} - 10^{-5} \text{ Sm}^{-1}$ (Jiracek, 1967). Thus, bedrock underlying Siple Dome will likely have dielectric permittivity $\epsilon_{rock} = 7 : 11$, and electrical conductivity $\sigma_{rock} = 10^{-5} - 10^{-4} \text{ Sm}^{-1}$. Under the assumption that Siple Dome ice is frozen directly to the underlying bedrock, we can calculate that the power reflection coefficient for ice frozen to this range of rock types using a two-layer reflectivity model (Chapter 3, Born and Wolf, 1980) would be $\mathcal{R}=0.04:0.08$. The increase in reflected power by a factor of ~ 4 across the Siple Ice Stream margin implies that the reflectivity increases from $\mathcal{R}=0.04:0.08$ under Siple Dome to $\mathcal{R}=0.16:0.32$ under Siple Ice Stream. The large reflectivities under Siple Ice stream cannot be the result of ice frozen to solid bedrock because it requires permittivities and/or conductivities for the rock that are well-beyond the expected range. The large reflectivities under Siple Ice stream more likely are due to ice overlying a thawed bed or a frozen till layer - both possibilities are considered separately below.

Siple Ice Stream: Thawed Bed

The suggested range of Siple Ice Stream basal reflectivities ($\mathcal{R}=0.16-0.32$) could be due to the existence of liquid water at the bed. For example, a water layer $\sim 30-60$ mm thick and electrical conductivity in the range of that measured in the basal layer under Ice Stream B ($2.5 \times 10^{-2} \text{ Sm}^{-1}$) (Engelhardt *et al.*, 1990a) would yield $\mathcal{R}=0.16-0.32$. It is unlikely that such a large thickness of water could exist as a distributed layer over a hard bed because it would be unstable and evolve into a channelized network (Walder, 1982). Since the large reflectivity occurs beneath a paleo-ice stream margin, the water would more likely be distributed in the pores of a till layer several meters thick, similar to that found beneath active Ice Stream B (Blankenship *et al.*, 1987b) and consistent with the view that the bed of an ice stream consists of a dilated till layer saturated with pressurized water. Using a three-

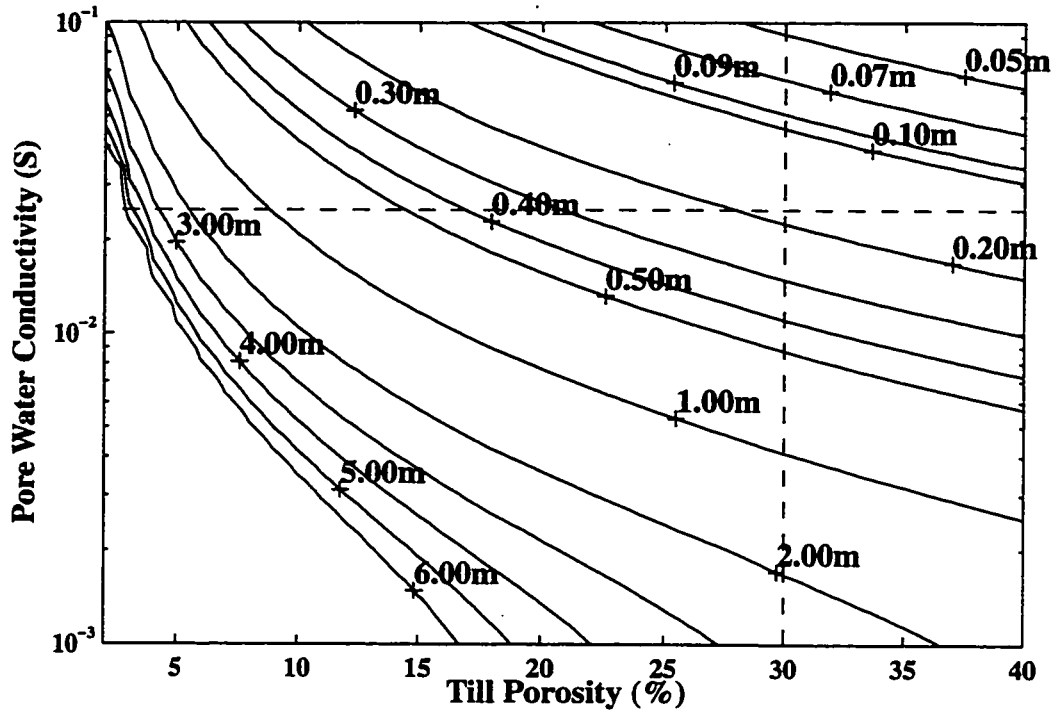


Figure 7.10: Contours (in meters) of water saturated till layer thickness given till porosity and water conductivity that produce $\mathcal{R}=0.20$ for a frequency of 3 MHz. The dashed horizontal line indicates the conductivity measured under Ice Stream B by *Engelhardt et al.* (1990a). The dashed vertical line indicates porosity of 30% as is expected for saturated consolidated till. Layers thicker than 6 m are not calculated.

layer (ice, basal layer, rock) reflectivity model (Chapter 3, *Born and Wolf*, 1980), the Looyenga dielectric mixing model described in *Glen and Paren* (1975), and an effective conductivity model (*Keller and Frischknecht*, 1966), I calculate thickness contours of a saturated till layer as a function of till porosity and interstitial water conductivity, that would produce a constant reflectivity. An example of the results of this calculation assuming a 3 MHz frequency and reflectivity $\mathcal{R}=0.20$ (in the range given above) are shown in Figure 7.10.

If we interpret the RES to imply that water is still present beneath the Siple Ice Stream, the total amount of water that must have existed when the stream was active can be estimated. Using a range of values for the geothermal flux ($55\text{-}65\text{ mW m}^{-2}$)

and a measurement of the conductive flux for a melting bed (80 mW m^{-2} , *Engelhardt et al.*, 1990b) through 1 km ice thickness under conditions (such as surface temperature) typical to West Antarctica, the rate of freezing of liquid water beneath a 1 km thick stagnant ice column (no frictional heating) is $\sim 1\text{-}3 \text{ mm a}^{-1}$. If liquid water is still present at the bed, shutdown of the ice stream about 300 years ago implies that at least 0.3-0.9 m of water must have existed when the ice stream was active. However, if the basal layer in this region has experienced a net positive (negative) horizontal divergence of water since ice stream activity ceased, the calculated thickness will be an underestimate (overestimate) since the water would remove (contribute) additional energy toward maintaining thawed bed conditions.

Siple Ice Stream: Frozen Till

The range of Siple Ice Stream basal reflectivities ($\mathcal{R}=0.16\text{-}0.32$) could also be explained by the existence of frozen till layer at the bed. The dielectric permittivity for a frozen till layer composed of the rock types mentioned above and having a well-consolidated till porosity of 20% would range between $\sim 6\text{-}8$. The conductivity of a frozen till layer is poorly constrained and few measurements of electrical properties of frozen composite materials have apparently been made. Conductivities for a variety of synthetic permafrosts given in (*Jiracek*, 1967) range from 8×10^{-4} to $2 \times 10^{-2} \text{ Sm}^{-1}$. Measurements by (*Hoekstra and Delaney*, 1974) show that a water-saturated sand and gravel mixture had conductivity 10^{-3} Sm^{-1} when thawed but decreased abruptly by a factor of 30 to $\sim 3 \times 10^{-5} \text{ Sm}^{-1}$ when frozen at -3°C . Composites with finer grains show less abrupt decreases in conductivity when frozen. The conductivity of finer grained water saturated materials decreases smoothly with temperature, and for some materials may not decrease significantly until temperatures are well-below freezing. If we the assume that the results given by (*Hoekstra and Delaney*, 1974) for the water-saturated sand and gravel mixture are somewhat typical of rock-water composites, a frozen till layer similar in composition to the layer beneath Ice Stream B

would decrease from $2.5 \times 10^{-2} \text{ Sm}^{-1}$ as measured when thawed to $\sim 8 \times 10^{-4} \text{ Sm}^{-1}$ when it freezes. Based on the range of experimental results for the conductivity of frozen rock/water composite materials (e.g., Keller, 1987; Hoekstra and Delaney, 1974; Jiracek, 1967), the estimate above represents a lower limit on the frozen till conductivity and the actual conductivity is likely to be significantly higher.

If a frozen till layer underlain by solid bedrock exists beneath Siple Ice Stream and we assume it has conductivity $8 \times 10^{-4} \text{ Sm}^{-1}$, permittivity 7, the reflectivity model shows that the layer would need to be at least 1.1 m thick (for $\mathcal{R}=0.16$) or 2.5 m thick (for $\mathcal{R}=0.32$). Since the estimated conductivity for the frozen till is likely a lower limit, the frozen till layer could be even thinner. These calculated till layer thicknesses are in the range of thicknesses thought to exist beneath active ice streams and therefore cannot be ruled out as a possible explanation of the predicted reflectivity under the Siple Ice stream.

7.6.5 Pattern of Reflected Power Variation

The small-scale variability of the BRP_R beyond the Siple Ice Stream margin could be caused by increased variability of the IRP_N and/or small-scale (less than one ice thickness) variations in properties at the bed. Figure 7.8 shows increased variability in the IRP_N across the scar feature which is likely caused by changes in scattering from buried crevasses. Variability in the basal layer properties is also indicated by the point diffractors (appearing as inverted hyperbolae) at the bed in Figure 7.8. Such diffractors would be expected if the basal till layer geometry is spatially variable so that the ice-till interface is in places rough on the scale of a wavelength (~ 50 m). If the bed is everywhere a non-diffuse reflector (specular), a laterally heterogeneous layer would have variable reflectivity, but would not give rise to the point diffractors seen in the record. The variation in reflected power and the presence of diffractors therefore indicate heterogeneity in the basal conditions beneath the Siple Ice Stream.

Figure 7.8 shows the outer boundary of the paleo-shear margin at ~ 60 km, and

yet the BRP_R does not increase significantly until ~ 62 km. The returned signal from this 2 km portion of the profile is affected by increased attenuation because both BRP_R and IRP_N decrease. This makes it difficult to accurately locate the transition in reflected power. It is possible that the boundary currently occurs on the ice stream side of the outer boundary of the paleo-ice stream. If true, (and if the reflectivity increase is interpreted as being a transition to a thawed bed) it may indicate migration of the frozen boundary into the former ice stream and away from its presumed initial position at the paleo-ice stream margin.

7.6.6 Basal Reflection Power Variations: Duck's Foot

RES data gathered from 55 to 90 km south of the summit used a slightly different center frequency than the rest of the profile (Figure 7.9). This section of the profile crosses a relict margin feature of Ice Stream C that has been called the *Duck's Foot* by Scambos and Jacobel, (1996)². The effect of varying ice thickness was removed from the BRP using the relation described in section 7.4.4 to produce the BRP_R .

Large BRP_R variations are also visible in this region (Figure 7.9). While the amplitude of these variations can not be determined precisely (because of the reasons discussed in Section 7.4.5), a pattern of higher values and larger variability similar to those observed on the north scar is evident. It is likely that this pattern is similarly caused by liquid water or frozen till at the bed. Since Ice Stream C stagnated ~ 130 years b.p. (Retzlaff and Bentley, 1993), if liquid water is still present, following the arguments of the previous section, a layer of water at least ~ 0.3 m thick must have been present at the bed when the ice stream was active. However, since the ice is thinner here, the freezing rate would be larger and therefore this would be an underestimate of the past liquid water content. A net horizontal divergence of water in the basal layer will again affect the results of the heat flow calculation and will in

² Presentation at the 1996 West Antarctic Ice Sheet Initiative workshop.

turn affect the prediction of the amount of water which existed when Ice Stream C was active.

7.7 Conclusions

RES traverses across curvilinear scar features visible in AVHRR imagery on the flanks of Siple Dome support the idea that these scars are artifacts of former ice stream margins. Our earlier interpretation of the continuity of internal layers across the northern scar is not correct; the age of shutdown of the former ice stream is more recent than the 1300 years BP suggested by *Jacobel et al.* (1996). Reanalysis using the new higher-resolution data does not show continuous layers, and recent high-frequency data imply that shutdown occurred less than 230 - 350 years BP.

The RES profiles show a large contrast in the BRP_R across the margins, suggesting that either liquid water or a meters-thick frozen till layer is still present beneath the now stagnant ice streams surrounding Siple Dome. While it is generally thought that fast ice stream motion occurs when liquid water is present at the bed, the possibility of liquid water currently beneath the paleo-ice streams may indicate that it is not a sufficient condition. The variability of the BRP_R and the presence of point diffractors at the bed imply small length scale contrasts in basal properties beneath Siple Ice Stream. The large increase in reflected power across the margin also allows the conclusion that a thick (greater than ~ 1 m) frozen till layer must not exist beneath Siple Dome - though a thin layer (less than ~ 1 m) may be permitted by the data. The nearly constant BRP_R across the dome implies that no layer exists beneath the dome. The absence of a thick till layer beneath Siple Dome is consistent with its apparent stability as an inter-ice stream ridge in the past (*Nereson, 1998*) and may suggest that it will remain as a stable limitation of ice stream width in the future.

If we interpret the BRP_R variation to indicate liquid water is present at the base of these paleo-ice streams, several conclusions are possible. The current presence of

liquid water, a simple energy balance calculation for the bed and the estimated timing of ice stream shutdown place limits on the amount of water expected at the bed of the ice streams when they were active. Under these assumptions, these calculations indicate that at least a ~ 1 m layer of water must have been present beneath the Siple Ice Stream when it was active. Corresponding observations, assumptions and calculations show that at least ~ 0.5 m of water would have been present beneath Ice Stream C when it was active. Although the actual amount of water remaining depends on whether water has been advected to or from the basal layer since shutdown, it is clear that shutdown must have occurred before the basal layer was completely frozen. If the heat balance at the bed became negative allowing freezing at the bed the water pressure in the basal material would decrease as water is drawn from the till layer to the freezing interface (*Jacobson and Raymond, 1998*). Following this scenario, ice stream shutdown would have occurred when the water pressure at the bed decreased causing partial consolidation of the till layer.

Chapter 8

SUMMARY AND CONCLUSIONS

In this chapter I summarize the conclusions drawn in the previous chapters resulting from radio echo-sounding (RES) measurements and analyses. These measurements and analyses were done to investigate the evolution of basal properties of Black Rapids Glacier, Alaska during the time of spring speed-up, and to examine the distribution of internal ice and basal properties at Siple Dome, West Antarctica.

8.1 *Black Rapids Glacier, Alaska*

New RES data collection and analysis techniques developed here have been useful for examining changes in the basal structure of a temperate glacier. Measurements were made during the time of spring speed up on Black Rapids Glacier (BRG) in 1993, with stationary RES systems, oriented over the center of the glacier. The data from the stationary systems provide high quality bed reflection power and phase information. The bed reflection power at these stationary sites varied in a predictable diurnal manner. By examining the total amount of power reflected from water bodies within the ice, I determined that the diurnal variation in returned power was related to the daily variation in the liquid water content of the snow. The variations in surface properties apparently alters the coupling of the antennae to the interface such that the energy transmitted into the ice subsurface varies with the amount of liquid water. This result was not anticipated. To remove the effect of varying transmission of energy from the returned signal, I developed a method of calibration which uses the amplitude of the persistent features within the ice (determined by principal

component analysis). The assumption underlying the use of this calibration is that some of the internal reflectors/scatterers do not vary with time. The RES records from fixed sites give some justification for this assumption because they show that the timing and form of many internal reflections is stable, indicating that many returns are produced by persistent englacial structures. I use principal component analysis to quantify the commonality in the signal returned from interior reflectors/scatterers, and use the changes in amplitude of that common signal as a reference to remove the effects of varying energy transmission from the measured bed reflection power to produce the residual bed reflection power (BRP_R) - the portion of the reflected power variation due to changes in bed properties.

The BRP_R from measurements at the center of the glacier place strong limits on the possible changes in physical properties at the bed because they show very small changes in BRP_R ($4 \pm 4\%$) and reflected phase (< 0.06 radians) during the period of observation. The small changes imply that any physical changes which may have occurred in the subglacial system at the center of the glacier were of a nature that was not detectable by RES. I therefore conclude that the possible changes in the subglacial system at the center of the glacier are limited to scenarios in which the water pressure may have changed (to accommodate the observed speedup) in such a manner that altered the basal mechanical characteristics but did not change the total water mass. These results suggest that the response of the subglacial hydrological system to seasonal variations in meltwater input did not appear to take the form of a large-scale reorganization near the center of the glacier, but may have been driven by changes elsewhere (e.g. toward the margin, up or down glacier).

Repeated RES measurements made along marked cross-profile lines were also affected by variations in surface conditions. The calibration method I developed for the fixed site data was not applicable to these repeated profiles except at fixed points where we collected records while the system was stationary. The original large data set of repeated profiles was therefore reduced to measurements at 13 pole locations.

Measurements from locations near the center of the glacier showed no detectable change in reflected power over the observation period - consistent with the results of from the RES fixed sites. Of the 13 pole locations only the BRP_R at 5 locations - all toward the glacier margin - showed evidence of changes in reflection power which exceed the uncertainties. The changes in BRP_R at these 5 locations can be interpreted as changes in basal properties. For example, the changes in BRP_R can be explained by slight changes in the thickness, conductivity or spatial distribution of a thin water layer over solid bedrock. However, since boreholes recently drilled on BRG near the study region show that there is a meters-thick till layer underlying the width of the glacier, we are motivated to explore explanations for the measured reflectivity changes in the context of a soft bed. To explain the reflectivity measurements by changes in a 5 m-thick till layer requires changes in till porosity of 3-9% (with associated changes in layer thickness, effective dielectric permittivity and conductivity). However, since modeling indicates that changes in till porosity through a meters-thick till layer to take far longer (years) (*Boulton and Hindmarsh, 1987*) than the interval over which the reflection changes occurred (days). Therefore such changes in till porosity of a thick till layer are not likely the cause of the observed changes in BRP_R . Instead, the RES measurements may suggest that a stratified basal till layer, with an active upper section and a relatively stagnant lower section, may be a more appropriate idealization. Such a stratified till layer is consistent with results which show that the upper tens of centimeters are most actively involved in deformation and most susceptible to changes in porosity on short time scales (e.g., *Clarke, 1987; Boulton and Hindmarsh, 1987*). Changes in the amount or conductivity of water in tens of centimeters of a till layer (similar in nature to those calculated for the hard bed) would explain the measured reflectivity changes and are physically possible on the time scale of days.

In all of the models considered, a measured increase in reflected power would likely be associated with an increase in water - either as a layer or distributed in a

till. Since changes in BRP_R only occurred toward the margins of the glacier, the glacier-wide speedup may have been driven by changes in basal properties in that region. However, measurements of longitudinal extension in the study region suggest the additional possibility that the broad trend of glacier speed up may be driven by longitudinal coupling with changes in speed occurring down-glacier from the study site. The results suggest that changes in glacier speed during the spring evolution of the subglacial system in response to seasonal changes in meltwater input may in fact be driven by local changes to sensitive areas of the glacier (either at the margins or downglacier) rather than pervasive glacier-wide changes.

Given these conclusions, future studies using repeated RES measurements to look for temporal and spatial changes in sub-ice structure should do several things differently. First, because the data from the RES sites whose antennae were left completely undisturbed provided far better and more continuous data, a future study should employ as many such fixed sites as possible. Several RES fixed sites should be positioned along two transverse lines across the glacier. The two transverse lines should be separated by a distance comparable to the estimated longitudinal coupling length (~ 5 km in this case). This configuration would allow a closer investigation of the basal changes occurring across the glacier width as well as those occurring at a significantly different location along the glaciers length. If limitations on the amount of available equipment prevent sufficient spatial coverage, then repeated profiles should be done at approximately the same time (or times) of day along densely marked transverse pole lines in such a manner that records are always collected with the system stationary at the marked locations. An extensive concurrent motion surveying campaign should also be done to measure horizontal strain and also to investigate the velocity profile along the transverse line on which the RES fixed sites are placed. High-time resolution is now possible for such a survey by using new automated theodolites/electronic distance meters. Finally, concurrent measurements of basal water pressure and electrical conductivity through bore holes in the study region (if possible without interfering

with the RES systems) would provide valuable information useful for both ground truth to be used in the radar interpretation and for analysis together with the motion surveys.

8.2 Siple Dome, Antarctica

RES profiles from Siple Dome revealed strong evidence of large changes in internal and basal reflection characteristics across surface lineations visible in satellite imagery. Internal reflecting horizons, that were persistent across the dome, vanish across the margins. The power reflected from the bed, which varied simply as a function of ice thickness across the dome, increased significantly across the margins.

The disappearance of layers across the margins has been interpreted to indicate that these surface lineations mark paleo-ice stream margins - where the shear between slow moving and rapid moving ice causes the layers to disappear. In previous work (*Jacobel et al.*, 1996), we estimated the time since Siple Ice stream shut down by assuming that all previous layers were disturbed by the shearing at the active ice stream boundary and that undisturbed layers would begin to form across the margin immediately after the ice stream shuts down. I now believe that such a layer does not exist and that our assumptions may not have been correct. Instead, I suggest that determining the depth to buried crevasses is a more reliable method to date the shut-down. Using crevasse burial depths recently determined at the Siple Ice Stream margin near its junction with Ice Stream C during 1997-98 field season, we estimate the timing of shutdown to be ~420 years BP.

From the experience gained with the Black Rapids Glacier RES data, we knew that the increase in bed reflection power across the paleo-margins could not be simply interpreted without considering other factors which may affect the returned signal power. For example, we expect that the thermal regime may have been different across the margin and we also expect buried crevasses on the margin itself - both

of which would affect the power returns from the bed. However, since the reflected power from within the ice was nearly constant across the paleo-ice stream margin, we have evidence that the bulk electrical properties of the ice column on either side of the margin are similar. The analysis of internal reflection power also showed a decrease in the immediate vicinity of the margin which suggested that buried crevassing must exist in the upper portion of the ice column. Subsequent RES measurements have shown this to be true.

After removing the effect of varying ice thickness to produce a residual bed reflection power (BRP_R), we find that the BRP_R is nearly constant across the dome but increases by a factor of 4 across the Siple Ice stream margin. This change in BRP_R is used to place limits on both the composition beneath Siple Dome and beneath the ice stream. We conclude that Siple Dome is likely either frozen to solid bedrock or a thin < 1 m thick frozen till layer. However, since the reflection power across the dome is nearly constant, it is unlikely that a till layer is present because its electrical properties and thickness would have to be spatially constant over the entire width of the dome. Recent drilling at Siple Dome supports the assertion of a hard bed under Siple Dome, and I proceed under the assumption that Siple Dome is frozen to solid bedrock. In this case, the increase in BRP_R is interpreted as a transition from ice frozen to bedrock (Dome) to either ice over a thawed bed or a frozen till layer of thickness > 1 m. The data imply similar conclusions for the Duck's Foot margin toward Ice Stream C as for the Siple Ice Stream Margin. The absence of a thick till layer beneath Siple Dome is consistent with its apparent stability as an inter-ice stream ridge in the past and suggests that it may remain as a stable limiter of ice stream width in the future.

The possibility that thawed conditions exist under relict ice streams is important to the understanding of ice stream dynamics. If true, it shows that shutdown must have occurred before the basal layer was completely frozen. This implies that the existence of water is not sufficient for ice stream activity and may suggest that instead

water pressure sufficient to dilate the till is required for ice streams to slide at the bed.

From the results at Siple Dome, I also conclude that several methods would be useful in future RES studies. First, many additional conclusions are possible from RES studies if ground truth from bore holes in the region are available. Such information would be useful in aiding in distinguishing between conductive frozen till layers and thawed bed conditions. Second, by repeating profiles at a wide range of frequencies, more information is potentially available because the basal layers are very dispersive. Thus, potential information about basal layer thickness may be possible from a multi-frequency approach. Alternatively, the use of a pulse-modulated RES system in which absolute returned phase could be measured, could further constrain the basal interface properties.

8.3 The Potential and Limitations of Radio Echo-Sounding

The results presented in this dissertation give rise to several points related to the use of RES for determining sub-ice structure - some suggestions relevant to the particular projects have already been listed.

The use of RES to detect temporal or spatial variations of subsurface properties relies on the assumption that the surface and intermediate properties remain equal, and where that assumption fails, relies on the ability to properly account for the intermediate properties that are variable. The Black Rapids Glacier study clearly illustrates the importance of properly accounting for the variation of energy transmitted into the ice sub-surface which was likely caused by variations in liquid water at the surface. These considerations are important for future studies which use RES to detect temporal reflectivity changes in temperate settings. Though we were ultimately able to interpret the Siple Dome RES data without correcting for varying ice properties, BRG studies illustrate the potential hazard of doing so. It is again

important for future studies of variations in basal properties to consider the possible variations in either surface reflections (e.g., crevasses) or ice properties (e.g., temperature, conductivity).

A lack of knowledge of system characteristics leads to uncertainty when calculating absolute basal reflectivity and hence basal properties. Unknowns for our RES systems include: 1) transmitted power, 2) transmitted pulse shape, 3) transmitting/receiving antennae gain, 4) absolute signal to noise distinguishing capabilities, and 5) effective “footprint” of the system. In studies involving repeated measurements or when looking for spatial variations, many of these unknowns cancel (e.g. 1, 2, and 3 above). However, these unknowns prevent direct calculations of absolute reflection coefficients and necessitate the reliance on other measurements or assumptions about basal composition. For example, at Black Rapids Glacier, the estimates of “baseline” reflectivities were necessary because they could not be directly calculated. Similarly, estimations of the reflectivity beneath Siple Dome had to be made based on expectations of the basal composition and conditions rather than being calculated directly. If absolute reflectivities could be determined, RES measurements could be directly used as an independent estimate of the actual physical conditions at the bed.

By working within the limitations outlined above (and in several of the Chapters), I have shown that in addition to the standard use of determining ice thickness, RES provides a powerful tool for making rapid large-scale non-invasive investigations of sub-ice properties. No other geophysical tool is realistically capable of doing such detailed large-scale and low-cost studies as were performed on Siple Dome. Similarly, the non-invasive fully-automated high-time resolution studies done on Black Rapids Glacier were only possible with RES. Improvements to RES equipment such as increasing transmitted power, receiver sensitivity and digitization rates will certainly further the usefulness of the technique.

BIBLIOGRAPHY

- Alley, R. B., and I. M. Whillans, Changes in the West Antarctic Ice Sheet, *Science*, 254(5034), 959–963, 1991.
- Alley, R. B., D. D. Blankenship, C. R. Bentley, and S. T. Rooney, Till Beneath Ice Stream B 3. Till Deformation: Evidence and Implications, *Journal of Geophysical Research*, 92(B9), 8921–8929, 1987.
- Anandakrishnan, S., and R. B. Alley, Stagnation of Ice Stream C, West Antarctica by water piracy, *Geophysical Research Letters*, 24(3), 265–268, 1997.
- Arcone, S. A., and A. J. Delaney, Dielectric Properties of Thawed Active Layers Overlying Permafrost Using Radar at VHF, *Radio Science*, 17(3), 618, 1982.
- Bentley, C. R., Antarctic Ice Streams: A Review, *Journal of Geophysical Research*, 92(B9), 8843–8868, 1987.
- Berry, M. V., On deducing the form of surfaces from their diffracted echoes, *Journal of Physics A: General Physics*, 5(2), 272–291, 1972.
- Berry, M. V., The statistical properties of echoes diffracted from rough surfaces, *Philosophical Transactions of the Royal Society of London, Ser. A*, 273(1237), 611–654, 1973.
- Berry, M. V., Theory of Radio Echoes From Glacier Beds, *Journal of Glaciology*, 15(73), 65–74, 1975.
- Bindschadler, R. A., and P. L. Vornberger, AVHRR imagery reveals Antarctic ice dynamics, *EOS*, 71(23), 1990.

- Blankenship, D. D., C. R. Bentley, S. T. Rooney, and R. B. Alley, Seismic measurements reveal a saturated porous layer beneath an active Antarctic ice stream, *Nature*, *322* (6074), 54–57, 1986.
- Blankenship, D. D., S. Anandkrishnan, J. L. Kempf, and C. R. Bentley, Microearthquakes under and alongside Ice Stream B, Antarctica, detected by a new passive seismic array, *Annals of Glaciology*, *9*, 30–34, 1987a.
- Blankenship, D. D., C. R. Bentley, S. T. Rooney, and R. B. Alley, Till Beneath Ice Stream B 1. Properties Derived from Seismic Travel Times, *Journal of Geophysical Research*, *92*(B9), 8903–8912, 1987b.
- Blindow, N., and F. Thyssen, Ice Thickness and Inner Structure of the Vernagtferner (Oetztal Alps): Results of Electromagnetic Reflection Measurements, *Zeitschrift für Gletscherkunde und Glazialgeologie*, *22*(1), 43–60, 1986.
- Bogorodsky, V. V., C. R. Bentley, and P. E. Gudmandsen, *Radioglaciology*, D. Reidel Publishing Company, 1st edn., 1985.
- Born, M., and E. Wolf, *Principles of Optics*, Oxford; New York: Pergamon Press, 6th edn., 1980.
- Boulton, G. S., and R. C. A. Hindmarsh, Sediment deformation beneath glaciers: Rheology and geological consequences, *Journal of Geophysical Research*, *92*(B9), 9059–9082, 1987.
- Chan, E. C., and J. P. Marton, Generalized Maxwell Garnett equations for rough surfaces, *Journal of Applied Physics*, *45*(11), 5004–5007, 1974a.
- Chan, E. C., and J. P. Marton, Surface roughness interpretation of ellipsometer measurements using the generalized Maxwell Garnett theory, *Journal of Applied Physics*, *45*(11), 5008–5014, 1974b.

- Claerbout, J. F., *Imaging the earth's interior*, chap. 5, p. 398, Blackwell Scientific Publications, 1985.
- Clarke, G. K. C., Subglacial till: A physical framework for its properties and processes., *Journal of Geophysical Research*, 92(B9), 9023–9036, 1987.
- Cochran, O., The subglacial hydraulics of the surge-type Black Rapids Glacier, Alaska: a schematic model., Master's thesis, University of Alaska, Fairbanks, 1995.
- Collins, D. N., Seasonal Variations of Solute Concentration in Melt Waters Draining From an Alpine Glacier, *Annals of Glaciology*, 2, 11–16, 1981.
- Dillon, W. R., and M. Goldstein, *Multivariate Analysis Methods and Application*, John Wiley and Sons, Inc., 1st edn., 1984.
- Drewry, D. J., Antarctica: Glaciological and Geophysical Folio, Tech. rep., Scott Polar Research Institute, Cambridge, 1983.
- Echelmeyer, K. A., W. D. Harrison, C. Larsen, and J. E. Mitchell, The role of the margins in the dynamics of an active ice stream, *Journal of Glaciology*, 40(136), 527–538, 1994.
- Engelhardt, H., and B. Kamb, Basal hydraulic system of West Antarctic ice stream: constraints from borehole observations, *Journal of Glaciology*, 43(144), 207–231, 1997.
- Engelhardt, H., W. Harrison, and B. Kamb, Basal sliding and conditions at the glacier bed as revealed by bore-hole photography, *Journal of Glaciology*, 20, 469–508, 1978.
- Engelhardt, H., N. Humphrey, and B. Kamb, Borehole geophysical observations on Ice Stream B, Antarctica, *Antarctic Journal of the U.S.*, 25(5), 80–82, 1990a.

- Engelhardt, H., N. Humphrey, B. Kamb, and M. Fahnestock, Physical conditions at the base of a fast moving Antarctic ice stream, *Science*, 248, 57–59, 1990b.
- Glen, J., and J. Paren, The electrical properties of snow and ice, *Journal of Glaciology*, 15(73), 15–38, 1975.
- Griffiths, D. J., *Introduction to Electrodynamics*, Prentice-Hall, Inc, Englewood Cliffs, New Jersey 07632, 2nd edn., 1989.
- Harrison, W. D., L. R. Mayo, and D. C. Trabant, Temperature measurements of Black Rapids Glacier, Alaska, 1973., in *Climate of the Arctic. Proceedings of the 24th Alaska Science Conference.*, edited by G. Weller, and S. A. Bowling, pp. 350–352, Fairbanks, AK, University of Alaska, 1973.
- Heavens, O. S., *Optical Properties of Thin Solid Films*, Academic Press Inc., 1955.
- Heinrichs, T. A., L. R. Mayo, D. C. Trabant, and R. S. March, Observation of the Surge-Type Black Rapids Glacier, Alaska, During a Quiescent Period, 1970-92, Tech. Rep. Open File Report 94-512, U. S. Geological Survey, Fairbanks, Alaska, 1995.
- Heinrichs, T. A., L. R. Mayo, K. A. Echelmeyer, and W. D. Harrison, Quiescent-phase evolution of a surge-type glacier: Black Rapids Glacier, Alaska, U.S.A., *Journal of Glaciology*, 42(140), 110–122, 1996.
- Hodge, S. M., D. L. Wright, J. A. Bradley, R. W. Jacobel, N. Skou, and B. Vaughn, Determination of the surface and bed topography in central Greenland, *Journal of Glaciology*, 36(122), 17–30, 1990.
- Hoekstra, P., and A. J. Delaney, Dielectric Properties of Soils at UHF and Microwave Frequencies, *Journal of Geophysical Research*, 79(11), 1699–1708, 1974.

- Hooke, R., T. Laumann, and J. Kohler, Subglacial water pressures and the shape of subglacial conduits, *Journal of Glaciology*, 36(122), 67 – 71, 1990.
- Hubbard, B. P., M. J. Sharp, I. C. Willis, M. K. Nielsen, and C. C. Smart, Borehole water-level variations and the structure of the subglacial hydrological system of Haut Glacier d’Arolla, Valais, Switzerland, *Journal of Glaciology*, 41(139), 572–583, 1995.
- Hunderi, O., Optics of Rough Surfaces, Discontinuous Films and Heterogeneous Materials, *Surface Science*, 96(1-3), 1–31, 1980, Proceedings of the Fourth International Conference on Ellipsometry.
- Iken, A., The effect of the subglacial water pressure on the sliding velocity of a glacier in an idealized numerical model, *Journal of Glaciology*, 27(97), 407–421, 1981.
- Iken, A., and A. Bindschadler, Combined measurements of subglacial water pressure and surface velocity of Findelengletscher, Switzerland: Conclusions about drainage system and sliding mechanism, *Journal of Glaciology*, 32(110), 101–119, 1986.
- Iken, A., and M. Truffer, The relationship between subglacial water pressure and velocity of Findelengletscher, Switzerland, during its advance and retreat, *Journal of Glaciology*, 43(144), 328–338, 1997.
- Iken, A., H. Röthlisberger, A. Flotron, and W. Haeberli, The uplift of the Unteraargletscher at the beginning of the melt season – a consequence of water storage at the bed?, *Journal of Glaciology*, 29(101), 28–47, 1983.
- Jackson, J. D., *Classical Electrodynamics*, John Wiley & Sons, Inc., 2nd edn., 1975.
- Jacobel, R., and S. Anderson, Interpretation of radio echo returns from internal water bodies in Variegated Glacier., *Journal of Glaciology*, 33(115), 319–323, 1987.

- Jacobel, R., and C. Raymond, Radio echo-sounding studies of englacial water movement in Variegated Glacier, Alaska, *Journal of Glaciology*, 30(104), 22–29, 1984.
- Jacobel, R., T. Scambos, C. Raymond, and A. Gades, Changes in the configuration of Ice Stream flow from the West Antarctic Ice Sheet, *Journal of Geophysical Research*, 101(B3), 5499–5504, 1996.
- Jacobel, R. W., A. M. Gades, D. L. Gottschling, S. M. Hodge, and D. L. Wright, Interpretation of radar-detected internal layer folding in West Antarctic Ice Streams, *Journal of Glaciology*, 39(133), 528–537, 1993.
- Jacobson, H. P., and C. F. Raymond, Location of ice stream margins, thermal effects, *Journal of Geophysical Research*, 1998, in press.
- Jiracek, G. R., Radio Sounding of Antarctic Ice, Tech. Rep. 67-1, University of Wisconsin Geophysical & Polar Research Center, 6021 South Highland Road Madison, Wisconsin 53706, 1967.
- Jones, F. H. M., Digital Impulse Radar For Glaciology: Instrumentation, Modelling, and Field Studies, Master's thesis, University of British Columbia, 1987.
- Kamb, B., Glacier surge mechanism based on linked cavity configuration of the basal water conduit system, *Journal of Geophysical Research*, 92(B9), 9083–9100, 1987.
- Kamb, B., and K. A. Echelmeyer, Stress-gradient coupling in glacier flow: I. longitudinal averaging of the influence of ice thickness and surface slope, *Journal of Glaciology*, 32(111), 267–284, 1986.
- Kamb, B., C. Raymond, W. Harrison, H. Engelhardt, K. Echelmeyer, N. Humphrey, M. Brugman, and T. Pfeffer, Glacier surge mechanism: 1982-1983 surge of Variegated Glacier, Alaska, *Science*, 227, 469–479, 1985.

- Karl, J. H., *An Introduction to Digital Signal Processing*, chap. 5. The Discrete Fourier Transform, pp. 79–93, Academic Press, Inc., San Diego, California 92101, 1989.
- Keller, G. V., *Electromagnetic Methods in Applied Geophysics*, chap. 2: Rock and Mineral Properties, pp. 13–52, Investigations in Geophysics, Volume 3, Society of Exploration Geophysics, 1987.
- Keller, G. V., and F. C. Frischknecht, *Electrical methods in geophysical prospecting*, Pergamon Press, Oxford, New York, 1st edn., 1966.
- Mayewski, P. A., M. S. Twickler, and S. Whitlow, The Siple Dome ice core - reconnaissance glaciochemistry, *Antarctic Journal of the U.S.*, *30*, 85–87, 1995.
- Nayfeh, M. H., and M. K. Brussel, *Electricity and Magnetism*, John Wiley & Sons, Inc., 1985.
- Neal, C. S., Radio-echo power profiling, *Journal of Glaciology*, *17*(77), 527–530, 1976.
- Nereson, N. A., The flow history of Siple Dome and Ice Streams C and D, West Antarctica: Inferences from geophysical measurements and ice flow models, Ph.D. thesis, University of Washington, 1998.
- Nereson, N. A., E. D. Waddington, C. F. Raymond, and H. P. Jacobson, Predicted age-depth scales for Siple Dome and inland WAIS ice cores in West Antarctica, *Geophysical Research Letters*, *23*(22), 3163–3166, 1996.
- Nienow, P., M. Sharp, and I. Willis, Temporal Switching Between Englacial and Subglacial Drainage Pathways: Dye Tracer Evidence From the Haut Glacier D'Arolla, Switzerland, *Geografiska Annaler*, *78 A*, 51–59, 1996.
- Nolan, M. A., Seismic Detection of Transient Changes Beneath Black Rapids Glacier, Alaska, Ph.D. thesis, University of Alaska Fairbanks, 1998.

- Nye, J., Water at the bed of a glacier, in *Proceedings of the Cambridge Symposium*, pp. 189–194, IAHS, 1973, Nr.95.
- Nye, J. F., Reply to Mr. Joel E. Fisher's comments, *Journal of Glaciology*, 2(11), 52–53, 1952.
- Nye, J. F., Water flow in glaciers: jökulhlaups, tunnels and veins, *Journal of Glaciology*, 17, 181–207, 1976.
- Oswald, G., Investigation of sub-ice bedrock characteristics by radio echo sounding., *Journal of Glaciology*, 15(73), 75–88, 1975.
- Oswald, G., and G. Robin, Lakes beneath the Antarctic ice sheet, *Nature*, 275(5423), 251–254, 1973.
- Paren, J., and G. Robin, Internal reflections in polar ice sheets, *Journal of Glaciology*, 21(85), 251–259, 1975.
- Paterson, W. S. B., *The Physics of Glaciers*, Pergamon Press, Oxford, 3rd edn., 1994.
- Post, A., The exceptional advances of the Muldrow, Black Rapids, and Susitna glaciers, *JGR*, 65(11), 3703–3712, 1960.
- Rasmussen, L. A., Refraction correction for radio-echo soundings of ice overlain by firn, *Journal of Glaciology*, 32(111), 192–194, 1986.
- Raymond, C. F., Flow in a transverse section of Athabasca Glacier, Alberta, Canada, *Journal of Glaciology*, 10(58), 55–69, 1971.
- Raymond, C. F., and W. D. Harrison, Evolution of Variegate Glacier, Alaska, U.S.A., prior to its surge., *Journal of Glaciology*, 34(117), 154–169, 1988.
- Raymond, C. F., R. J. Benedict, W. D. Harrison, K. A. Echelmeyer, and M. Sturm, Hydrological discharges and motion of Fels and Black Rapids Glaciers, Alaska,

- U.S.A.: implications for the structure of their drainage systems., *Journal of Glaciology*, 41(138), 290–304, 1995.
- Retzlaff, R., and C. R. Bentley, Timing of stagnation of Ice Stream C, West Antarctica, from short-pulse radar studies of buried surface crevasses, *Journal of Glaciology*, 39(133), 553–561, 1993.
- Richards, K., et al., An Integrated Approach to Modelling Hydrology and Water Quality in Glacierized Catchments, *Hydrological Processes*, 10, 479–508, 1996.
- Robinson, E. A., and S. Treitel, *Geophysical Signal Analysis*, chap. 3, p. 466, Prentice-Hall, 1980.
- Rose, K. E., Characteristics of ice flow in Marie Byrd Land, Antarctica, *Journal of Glaciology*, 24(90), 63–75, 1979.
- Röthlisberger, H., Water pressure in intra- and subglacial channels, *Journal of Glaciology*, 11(62), 177–203, 1972.
- Röthlisberger, H., and H. Lang, Glacial Hydrology, in *A.M. Gurnell and M.J. Clark (Ed.), Glacio-Fluvial Sediment Transfer - An Alpine Perspective*, pp. 207–284, John Wiley and Sons, Chichester, New York, Toronto, Singapore, 1987.
- Scambos, T., and N. Nereson, Satellite image and GPS study of the morphology of Siple Dome, Antarctica, *Antarct. J. U.S., 1995 Review*, 30(5), 87–89, 1995.
- Scambos, T. A., and R. A. Bindschadler, Feature maps of Ice Streams C, D, E, West Antarctica, *Antarctic Journal of the U.S.*, 26(5), 312–314, 1991.
- Sharp, M., K. Richards, I. Willis, N. Arnold, P. Nienow, W. Lawson, and J.-L. Tison, Geometry, Bed Topography and Drainage System Structure of the Haut Glacier D’Arolla, Switzerland, *Earth Surface Processes and Landforms*, 18, 557–571, 1993.

- Shreve, R. L., Movement of Water in Glaciers, *Journal of Glaciology*, 11(62), 205–214, 1972.
- Smith, B. E., and S. Evans, Radio echo sounding: Absorption and scattering by water inclusion and ice lenses, *Journal of Glaciology*, 11(61), 133–146, 1972.
- Stephenson, S. N., and R. A. Bindschadler, Is ice-stream evolution revealed by satellite imagery?, *Annals of Glaciology*, 14, 273–277, 1990.
- Sturm, M., and D. M. Cosgrove, An unusual jökulhlaups involving potholes on Black Rapids Glacier, Alaska Range, Alaska, U.S.A., *Journal of Glaciology*, Correspondence, 1990, Vol. 36, No. 122, pp 125–126.
- Turcotte, D. L., and G. Schubert, *Geodynamics Applications of Continuum Physics to Geological Problems*, chap. 9. Flow in Porous Media, pp. 381–417, John Wiley and Sons, 1982.
- van Beek, L., *Progress in Dielectrics*, vol. 7, chap. Dielectric behaviour of heterogeneous system, pp. 69–114, London, Heywood Books, 1967.
- Walder, J., and A. Fowler, Channelized subglacial drainage over a deformable bed, *Journal of Glaciology*, 40(134), 3–15, 1994.
- Walder, J., and B. Hallet, Geometry of former subglacial water channels and cavities, *Journal of Glaciology*, 23, 335–346, 1979.
- Walder, J. S., Stability of sheet flow of water beneath temperate glaciers and implications for glacier surging, *Journal of Glaciology*, 28(99), 273–293, 1982.
- Walder, J. S., Hydraulics of subglacial cavities, *Journal of Glaciology*, 32(112), 439–445, 1986.
- Walford, M., and M. Harper, The detailed study of glacier beds using radio-echo techniques, *Geophys. J. R. Astr. Soc.*, 67, 487–514, 1981.

- Walford, M., and M. Kennett, A synthetic-aperture radio echo experiment at Storglaciaren, Sweden, *Journal of Glaciology*, 35(119), 43–47, 1989.
- Walford, M. E. R., M. I. Kennett, and P. Holmlund, Interpretation of radio echoes from Storglaciaren., *Journal of Glaciology*, 32(110), 39–49, 1986.
- Watts, R. D., and A. E. England, Radio Echo Sounding of Temperate Glaciers: Ice Properties and Sounder Design Criteria, *Journal of Glaciology*, 17(75), 39–48, 1976.
- Watts, R. D., and D. L. Wright, Systems for measuring thickness of temperate and polar ice from the ground or from the air, *Journal of Glaciology*, 27(97), 459–469, 1981.
- Weertman, B. R., Interpretation of ice sheet stratigraphy: A radar-echo sounding study of the Dyer Plateau, Antarctica, Ph.D. thesis, University of Washington, 1993.
- Weertman, B. R., C. F. Raymond, and J. Chin, A light-weight impulse ice radar for profiling of ice depth and internal layering of ice sheets., *EOS*, 43(71), 1308, 1990.
- Weertman, J., General theory of water flow at the base of a glacier or ice sheet, *Reviews of Geophysics and Space Physics*, 10(1), 287–333, 1972.
- Weertman, J., Basal water film, basal water pressure, and velocity of traveling waves on glaciers, *Journal of Glaciology*, 29(101), 20–27, 1983.
- Weertman, J., Basal water pressure and high pressure basal ice, *Journal of Glaciology*, 32(112), 455–463, 1986.
- Wessel, P., and W. H. F. Smith, New version of the Generic Mapping Tools released, *EOS*, 76, 329, 1995.

- Whillans, I. M., and C. J. van der Veen, New and improved determinations of velocity of Ice Streams B and C, West Antarctica, *Journal of Glaciology*, 39(133), 483–490, 1993.
- Willis, I. C., Intra-annual variations in glacier motion: a review, *Progress in Physical Geography*, 19(1), 61–106, 1995.
- Wu, T. T., and W. P. King, The cylindrical antenna with nonreflecting resistive loading, *IEEE Trans. Antennas Propagat.*, AP-13, 369–373, 1965.

Appendix A

ELECTROMAGNETIC WAVES IN DIELECTRIC MEDIA.

A.1 *Electromagnetic Waves in Non-Conducting Media*

The derivations in this appendix are based on Maxwell's equations. Each of the sections in this appendix is merely a building block leading to a conducting three-layer reflectivity model. The approach I outline first goes through the derivation of the reflectivity for a two-layer non-conducting and three-layer non-conducting configurations. The results from these derivations form the basis for the relations of the three-layer conducting model introduced in chapter 3.

A.1.1 *Maxwell's Equations in Free-Space*

Where there is no charge or current, Maxwell's equations are (following *Griffiths* (1989) and *Nayfeh and Brussel* (1985)):

$$\left. \begin{array}{ll} (a) \nabla \cdot \mathbf{E} = 0 & (c) \nabla \times \mathbf{E} = -\frac{\partial \mathbf{B}}{\partial t} \\ (b) \nabla \cdot \mathbf{B} = 0 & (d) \nabla \times \mathbf{B} = \mu_o \epsilon_o \frac{\partial \mathbf{E}}{\partial t} \end{array} \right\} \quad (\text{A.1})$$

These form a set of coupled, first-order, partial differential equations for \mathbf{E} and \mathbf{B} . By applying the curl to (c) and (d) above:

$$\begin{aligned} \nabla \times (\nabla \times \mathbf{E}) &= \nabla(\nabla \cdot \mathbf{E}) - \nabla^2 \mathbf{E} = \nabla \times \left(-\frac{\partial \mathbf{B}}{\partial t} \right) \\ &= -\frac{\partial}{\partial t} (\nabla \times \mathbf{B}) = -\mu_o \epsilon_o \frac{\partial^2 \mathbf{E}}{\partial t^2} \\ \nabla \times (\nabla \times \mathbf{B}) &= \nabla(\nabla \cdot \mathbf{B}) - \nabla^2 \mathbf{B} = \nabla \times \left(-\mu_o \epsilon_o \frac{\partial \mathbf{E}}{\partial t} \right) \end{aligned}$$

$$= \mu_0 \epsilon_0 \frac{\partial}{\partial t} (\nabla \times \mathbf{E}) = -\mu_0 \epsilon_0 \frac{\partial^2 \mathbf{B}}{\partial t^2}$$

We know that $\nabla \cdot \mathbf{B} = 0$ and $\nabla \cdot \mathbf{E} = 0$. Thus:

$$\nabla^2 \mathbf{E} = \mu_0 \epsilon_0 \frac{\partial^2 \mathbf{E}}{\partial t^2}, \quad \nabla^2 \mathbf{B} = \mu_0 \epsilon_0 \frac{\partial^2 \mathbf{B}}{\partial t^2} \quad (\text{A.2})$$

In a free space, the components of \mathbf{E} and \mathbf{B} satisfy the classical wave equation:

$$\nabla^2 f = \frac{1}{v^2} \frac{\partial^2 f}{\partial t^2} \quad (\text{A.3})$$

A.1.2 Maxwell's Equations in Non-Conducting Matter

Inside matter, but still in regions with no free charge or free current, Maxwell's equations are modified by material constants.

$$\left. \begin{array}{ll} (a) \nabla \cdot \mathbf{D} = 0 & (c) \nabla \times \mathbf{E} = -\frac{\partial \mathbf{B}}{\partial t} \\ (b) \nabla \cdot \mathbf{B} = 0 & (d) \nabla \times \mathbf{H} = \mu_0 \epsilon_0 \frac{\partial \mathbf{D}}{\partial t} \end{array} \right\} \quad (\text{A.4})$$

$$\mathbf{D} = \epsilon \mathbf{E}, \quad \mathbf{H} = \frac{1}{\mu} \mathbf{B} \quad (\text{A.5})$$

If the medium is linear and homogeneous in μ and ϵ , then equations A.4 simplify to:

$$\left. \begin{array}{ll} (a) \nabla \cdot \mathbf{E} = 0 & (c) \nabla \times \mathbf{E} = -\frac{\partial \mathbf{B}}{\partial t} \\ (b) \nabla \cdot \mathbf{B} = 0 & (d) \nabla \times \mathbf{B} = \mu \epsilon \frac{\partial \mathbf{E}}{\partial t} \end{array} \right\} \quad (\text{A.6})$$

A.1.3 Plane Waves in Free Space

\mathbf{E} and \mathbf{B} in empty space, satisfy the three-dimensional wave equation.

$$\nabla^2 \mathbf{E} = \frac{1}{c^2} \frac{\partial^2 \mathbf{E}}{\partial t^2}, \quad \nabla^2 \mathbf{B} = \frac{1}{c^2} \frac{\partial^2 \mathbf{B}}{\partial t^2} \quad (\text{A.7})$$

$c = 1/\sqrt{\epsilon_0 \mu_0}$ is the speed of light in free space. If we consider a monochromatic plane wave that is traveling in the x-direction, that is a wave with single frequency

and has no y or z-dependence.

$$\hat{\mathbf{E}}(x, t) = \hat{\mathbf{E}}_0 e^{i(kx - \omega t)}, \quad \hat{\mathbf{B}}(x, t) = \hat{\mathbf{B}}_0 e^{i(kx - \omega t)} \quad (\text{A.8})$$

$\hat{\mathbf{E}}$ and $\hat{\mathbf{B}}$ are the complex amplitudes (denoted with a “^”) of the electric and magnetic fields.

Since $\nabla \cdot \mathbf{E} = 0$ and $\nabla \cdot \mathbf{B} = 0$, we can write

$$(\hat{E}_0)_x = (\hat{B}_0)_x = 0. \quad (\text{A.9})$$

This means that electromagnetic waves only have components transverse to the direction of propagation. Also, Faraday’s law, $\nabla \times \mathbf{E} = -\frac{\partial \mathbf{B}}{\partial t}$, gives the following relation between electric and magnetic amplitudes:

$$\begin{aligned} -k(\hat{E}_0)_z &= \omega(\hat{B}_0)_y, \quad k(\hat{E}_0)_y = \omega(\hat{B}_0)_z \\ B_0 &= \frac{k}{\omega} E_0 = \frac{1}{c} E_0 \end{aligned} \quad (\text{A.10})$$

By introducing the wave vector κ , which points in the direction of propagation \mathbf{r} with amplitude equal to the wave number κ , we can re-write equations A.8 in the general form:

$$\hat{\mathbf{E}}(\mathbf{r}, t) = \hat{E}_0 e^{i(\kappa \cdot \mathbf{r} - \omega t)} \hat{\mathbf{n}} \quad (\text{A.11})$$

$$\hat{\mathbf{B}}(\mathbf{r}, t) = \frac{1}{c} \hat{E}_0 e^{i(\kappa \cdot \mathbf{r} - \omega t)} (\hat{\mathbf{k}} \times \hat{\mathbf{n}}) = \frac{1}{c} \hat{\kappa} \times \hat{\mathbf{E}} \quad (\text{A.12})$$

A.1.4 Reflection and Transmission Coefficients I: 2-layer, Non-Conducting Media

If we apply the necessary boundary conditions to electromagnetic fields incident on the interface between two linear media, we can derive the reflection and transmission coefficients for that interface. The boundary conditions are:

$$\left. \begin{aligned} (a) \quad \epsilon_1 E_{1\perp} &= \epsilon_2 E_{2\perp} & (c) \quad \mathbf{E}_{1\parallel} &= \mathbf{E}_{2\parallel} \\ (b) \quad B_{1\perp} &= B_{2\perp} & (d) \quad \frac{1}{\mu_1} \mathbf{B}_{1\parallel} &= \frac{1}{\mu_2} \mathbf{B}_{2\parallel} \end{aligned} \right\} \quad (\text{A.13})$$

Consider a monochromatic plane wave with frequency ω traveling in the x direction and that the yz plane at $x = 0$ forms a boundary between two non-conducting dielectric media. The incident wave is given by:

$$\left. \begin{aligned} \hat{\mathbf{E}}_I(x, t) &= \hat{E}_{0I} e^{i(k_1 x - \omega t)} \hat{j} \\ \hat{\mathbf{B}}_I(x, t) &= \frac{1}{v_1} \hat{E}_{0I} e^{i(k_1 x - \omega t)} \hat{k} \end{aligned} \right\} \quad (\text{A.14})$$

The resulting reflected wave is:

$$\left. \begin{aligned} \hat{\mathbf{E}}_R(x, t) &= \hat{E}_{0R} e^{i(-k_1 x - \omega t)} \hat{j} \\ \hat{\mathbf{B}}_R(x, t) &= -\frac{1}{v_1} \hat{E}_{0R} e^{i(-k_1 x - \omega t)} \hat{k} \end{aligned} \right\} \quad (\text{A.15})$$

The transmitted wave:

$$\left. \begin{aligned} \hat{\mathbf{E}}_T(x, t) &= \hat{E}_{0T} e^{i(-k_2 x - \omega t)} \hat{j} \\ \hat{\mathbf{B}}_T(x, t) &= -\frac{1}{v_2} \hat{E}_{0T} e^{i(-k_2 x - \omega t)} \hat{k} \end{aligned} \right\} \quad (\text{A.16})$$

At $x = 0$, the fields on both sides of the boundary must conform to the boundary conditions in equations A.13. Equation A.13 (c) requires:

$$\hat{E}_{0I} + \hat{E}_{0R} = \hat{E}_{0T} \quad (\text{A.17})$$

Equation A.13 (d) requires:

$$\frac{1}{\mu_1} \left(\frac{1}{v_1} \hat{E}_{0I} - \frac{1}{v_1} \hat{E}_{0R} \right) = \frac{1}{\mu_2} \left(\frac{1}{v_2} \hat{E}_{0T} \right)$$

or

$$\hat{E}_{0I} + \hat{E}_{0R} = \beta \hat{E}_{0T} \quad (\text{A.18})$$

where

$$\beta = \frac{\mu_1 v_1}{\mu_2 v_2} \quad (\text{A.19})$$

Solving equations A.17 and A.18 yields the reflected and transmitted amplitudes relative to the incident amplitude:

$$\hat{E}_{0R} = \left(\frac{1 - \beta}{1 + \beta} \right) \hat{E}_{0I}, \quad \hat{E}_{0T} = \left(\frac{2}{1 + \beta} \right) \hat{E}_{0I} \quad (\text{A.20})$$

The amount of reflected energy is given by the ratio of reflected energy to the incident energy:

$$R = \left(\frac{\hat{E}_{0R}}{\hat{E}_{0I}} \right)^2 = \left(\frac{n_1 - n_2}{n_1 + n_2} \right)^2 \quad (\text{A.21})$$

The transmitted energy is given by:

$$T = \frac{\epsilon_2 v_2}{\epsilon_1 v_1} \left(\frac{\hat{E}_{0T}}{\hat{E}_{0I}} \right)^2 = \frac{n_2}{n_1} \left(\frac{2n_1}{n_1 + n_2} \right)^2 \quad (\text{A.22})$$

Where

$$n_1 = \sqrt{\frac{\epsilon_1 \mu_1}{\epsilon_0 \mu_0}}, \quad n_2 = \sqrt{\frac{\epsilon_2 \mu_2}{\epsilon_0 \mu_0}}$$

are the indices of refraction for the two media.

A.1.5 Two-Layer, Non-Conducting, Oblique incidence, *p* Polarization

For oblique incidence and electric field polarized parallel to the plane of incidence (*p* polarization), the expressions for reflected and transmitted amplitudes are (*Griffiths*, 1989):

$$\hat{E}_{0R} = \left(\frac{\alpha - \beta}{\alpha + \beta} \right) \hat{E}_{0I}, \quad \hat{E}_{0T} = \left(\frac{2}{\alpha + \beta} \right) \hat{E}_{0I} \quad (\text{A.23})$$

Where:

$$\beta = \frac{\mu_1 v_1}{\mu_2 v_2} = \frac{\mu_1 n_2}{\mu_2 n_1}, \quad \alpha = \frac{\cos \theta_T}{\cos \theta_I}$$

Similarly, the reflection and transmission coefficients are given by the **Fresnel formulae**:

$$R_{\parallel} = \left(\frac{E_{0R}}{E_{0I}} \right)^2 = \frac{n_2 \cos \theta_I - n_1 \cos \theta_T}{n_2 \cos \theta_I + n_1 \cos \theta_T} \quad (\text{A.24})$$

$$T_{\parallel} = \frac{\epsilon_2 v_2}{\epsilon_1 v_1} \left(\frac{E_{0T}}{E_{0I}} \right)^2 \frac{\cos \theta_T}{\cos \theta_I} = \frac{2n_1 \cos \theta_I \sin \theta_T}{n_2 \cos \theta_I + n_1 \cos \theta_T} \quad (\text{A.25})$$

A.1.6 Two-Layer, Non-Conducting, Oblique incidence, *s* Polarization

For oblique incidence and electric field polarized normal to the plane of incidence (*s* polarization), we arrive at the **Fresnel formulae**:

$$R_{\perp} = \frac{n_1 \cos \theta_I - n_2 \cos \theta_T}{n_1 \cos \theta_I + n_2 \cos \theta_T} \quad (\text{A.26})$$

$$T_1 = \frac{2n_1 \cos \theta_I}{n_2 \cos \theta_I + n_1 \cos \theta_T} \quad (\text{A.27})$$

A.1.7 Three-layer, Non-Conducting, Oblique Incidence, *s* Polarization

Consider a homogeneous dielectric layer between two homogeneous media. I denote the layers 1, 2, and 3 for the top layer, the layer and the bottom layer respectively. I also introduce h as the layer thickness.

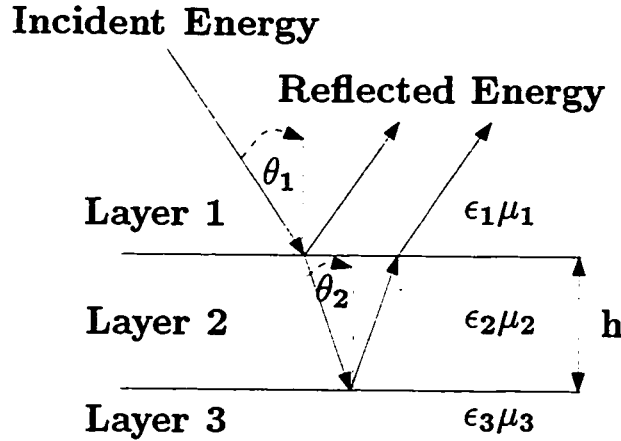


Figure A.1: Schematic diagram of 3-layer reflectivity model.

First define:

$$\beta = \frac{2\pi}{\lambda_0} n_2 h \cos \theta_2, \text{ and } p_j = n_j \cos \theta_j \quad (\text{A.28})$$

According to the Fresnel formulae for interface 1-2, we have for the electric vector parallel to the interface:

$$r_{12} = \frac{n_1 \cos \theta_1 - n_2 \cos \theta_2}{n_1 \cos \theta_1 + n_2 \cos \theta_2} = \frac{p_1 - p_2}{p_1 + p_2} \quad (\text{A.29})$$

$$t_{12} = \frac{2n_1 \cos \theta_1}{n_1 \cos \theta_1 + n_2 \cos \theta_2} = \frac{2p_1}{p_1 + p_2} \quad (\text{A.30})$$

There are analogous expressions for the coefficients at the interface 2-3. The formulae for r and t are:

$$r = \frac{r_{12} + r_{23} e^{2i\beta}}{1 + r_{12} r_{23} e^{2i\beta}} \quad (\text{A.31})$$

$$t = \frac{t_{12}t_{23} e^{2i\beta}}{1 + r_{12}r_{23} e^{2i\beta}} \quad (\text{A.32})$$

Reflectivity and transmissivity are given by:

$$\mathcal{R} = |r|^2 = \frac{r_{12}^2 + r_{23}^2 + 2r_{12}r_{23} \cos 2\beta}{1 + r_{12}^2 r_{23}^2 + 2r_{12}r_{23} \cos 2\beta} \quad (\text{A.33})$$

$$\mathcal{T} = \frac{p_3}{p_1} |t|^2 = \frac{n_3 \cos \theta_3}{n_1 \cos \theta_1} \frac{t_{12}^2 t_{23}^2}{1 + r_{12}^2 r_{23}^2 + 2r_{12}r_{23} \cos 2\beta} \quad (\text{A.34})$$

A.2 Electromagnetic Waves in Conducting Media

To consider the propagation of electromagnetic waves in conducting media, we must account for Joule heat production and the resulting attenuation of electromagnetic energy. In addition to being highly attenuating, good conductors are also strong reflectors. The conductivity of a material may be accounted for by simply introducing a complex dielectric constant in place of the real constant used in the non-conducting case. However, the assumptions in the previous section (no free charge or current) no longer apply.

A.2.1 Maxwell's Equations in Conducting Media

Inside conducting matter with dielectric constant ϵ , permeability μ , and conductivity σ . Maxwell's equations are modified by material constants (equations A.5)¹. That is: $\mathbf{D} = \epsilon\mathbf{E}$, $\mathbf{B} = \mu\mathbf{H}$, and also we add Ohm's law: $j = \sigma\mathbf{E}$.

$$\left. \begin{aligned} (a) \nabla \times \mathbf{H} - \frac{\epsilon}{c} \frac{\partial \mathbf{E}}{\partial t} &= \frac{4\pi}{c} \sigma \mathbf{E} & (b) \nabla \times \mathbf{E} + \frac{\mu}{c} \frac{\partial \mathbf{B}}{\partial t} &= 0 \\ (c) \nabla \cdot \mathbf{E} &= \frac{4\pi}{\epsilon} \rho_f & (d) \nabla \cdot \mathbf{H} &= 0 \end{aligned} \right\} \quad (\text{A.35})$$

¹ I follow the approach of (*Jackson, 1975*) and (*Born and Wolf, 1980*), and adopt the use of cgs system electrostatic units. More complete treatments of this theory can be found in these texts or in (*Heavens, 1955; Griffiths, 1989, e.g.*).

Take the divergence of equation A.35 (a) and use equation A.35 (c):

$$-\frac{\epsilon}{c} \nabla \cdot \frac{\partial \mathbf{E}}{\partial t} = \frac{4\pi\sigma}{c} \frac{4\pi}{\epsilon} \rho_f \quad (\text{A.36})$$

Differentiating equation A.35 (c) with respect to time yields:

$$\nabla \cdot \frac{\partial \mathbf{E}}{\partial t} = \frac{4\pi}{\epsilon} \frac{\partial \rho_f}{\partial t} \quad (\text{A.37})$$

Equations A.36 and A.37 combine to eliminate $\nabla \cdot \frac{\partial \mathbf{E}}{\partial t}$:

$$\frac{\partial \rho_f}{\partial t} + \frac{4\pi\sigma}{\epsilon} \rho_f = 0 \quad (\text{A.38})$$

Integrating yields:

$$\rho_f(t) = \rho_f(0) e^{-(t/\tau)} \quad \text{where} \quad \tau = \frac{\epsilon}{4\pi\sigma} \quad (\text{A.39})$$

This means that free charge dissipates with a characteristic time τ . If we are interested in time scales longer than this, we can neglect the ρ_f term in equation A.35 (c).

If we take the curl of equation A.35 (a) and (b), we arrive at the wave equation for \mathbf{E} :

$$\nabla^2 \mathbf{E} = \frac{\mu\epsilon}{c^2} \frac{\partial^2 \mathbf{E}}{\partial t^2} + \frac{4\pi\mu\sigma}{c^2} \frac{\partial \mathbf{E}}{\partial t} \quad (\text{A.40})$$

Assuming that the wave is monochromatic with angular frequency ω , \mathbf{E} is of the form $\mathbf{E} = \mathbf{E}_0 e^{-i\omega t}$, then A.35 (a) and (b) become:

$$\nabla \times \mathbf{H} + \frac{i\omega}{c} \left(\epsilon + i \frac{4\pi\sigma}{\omega} \right) \mathbf{E} = 0 \quad (\text{A.41})$$

$$\nabla \times \mathbf{E} - \frac{i\omega\mu}{c} \mathbf{H} = 0 \quad (\text{A.42})$$

and A.40 is:

$$\nabla^2 \mathbf{E} + \hat{k}^2 \mathbf{E} = 0 \quad \text{where} \quad \hat{k}^2 = \frac{\omega^2 \mu}{c^2} \left(\epsilon + i \frac{4\pi\sigma}{\omega} \right). \quad (\text{A.43})$$

These equations are same as the non-conducting case, but now the dielectric constant is complex:

$$\hat{\epsilon} = \epsilon + i \frac{4\pi\sigma}{\omega} \quad (\text{A.44})$$

and also the refractive index:

$$\hat{n} = n(1 + i\kappa) \quad (\text{A.45})$$

The constants n and κ (referred to as the *attenuation index* or *extinction coefficient*) can be expressed in terms of the material constants.

$$\hat{n}^2 = n^2(1 + 2i\kappa - \kappa^2) \quad \text{and} \quad \hat{n}^2 = \mu\hat{\epsilon} = \mu \left(\epsilon + i\frac{4\pi\sigma}{\omega} \right) \quad (\text{A.46})$$

Equating real and imaginary parts of these two expressions:

$$n^2(1 - \kappa^2) = \mu\epsilon \quad (\text{A.47})$$

$$n^2\kappa = \frac{2\pi\mu\sigma}{\omega} = \frac{\mu\sigma}{\nu} \quad (\text{A.48})$$

From these:

$$n^2 = \frac{1}{2} \left\{ \sqrt{\mu^2\epsilon^2 + \frac{4\mu^2\epsilon^2}{\nu^2}} + \mu\epsilon \right\}, \quad (\text{A.49})$$

$$n^2\kappa^2 = \frac{1}{2} \left\{ \sqrt{\mu^2\epsilon^2 + \frac{4\mu^2\epsilon^2}{\nu^2}} - \mu\epsilon \right\} \quad (\text{A.50})$$

The most simple solution to equation A.43 is a plane, time harmonic wave:

$$\hat{\mathbf{E}}(x, t) = \hat{\mathbf{E}}_0 e^{i(kx - \omega t)}, \quad (\text{A.51})$$

Substituting $\hat{k} = \omega\hat{n}/c = \omega n(1 + i\kappa)/c$, this becomes:

$$\mathbf{E} = \mathbf{E}_0 e^{-\frac{\omega}{c}n\kappa x} e^{i\omega \left(\frac{n}{c}x - t \right)} \quad (\text{A.52})$$

The real portion of equation A.52 is a plane wave with length $\lambda = 2\pi/\omega n$ and attenuation given by the exponential term

$$\mathbf{E} = \mathbf{E}_0 e^{-\frac{\omega}{c}n\kappa x} \cos \left\{ \omega \left[\frac{n}{c}x - t \right] \right\} \quad (\text{A.53})$$

From this we get the characteristic attenuation distance referred to as the *skin depth*:

$$d_{skin} = \left(\frac{\lambda}{4\pi\kappa_i} \right). \quad (\text{A.54})$$

A quick check of the skin depth for typical ice properties, $\epsilon_{ice} = 3.17$, $\sigma_{ice@0C} = 10^{-6}(\Omega^{-1}m^{-1})$, at 5MHz: $d_{skin} \approx 300m$.

The equations for the three-layer reflectivity model can now be derived using the relations outlined.

A.2.2 Three-layer, Conducting, Oblique Incidence

Equations A.29 - A.32, give the reflection and transmission coefficients for a dielectric film situated between two dielectric media. In this section the three-layer model is developed, allowing the intermediate layer to be conductive. To do so requires replacing the index of refraction n_2 in the non-conducting equations (given in Appendix A, § A.1.7) with a complex index $\hat{n}_2(1 + i\kappa_2)$. A schematic diagram is shown in Figure A.2. Following *Born and Wolf* (1980) to simplify notation we introduce variables u_2 and v_2 such that:

$$\hat{n}_2 \cos \theta_2 = u_2 + iv_2 \quad \text{where } u_2, v_2 \text{ are } \Re \quad (\text{A.55})$$

Squaring equation A.55 and using the law of refraction $\hat{n}_2 \sin \theta_2 = n_1 \sin \theta_1$, we find:

$$(u_2 + iv_2)^2 = \hat{n}_2^2 - n_2^2 - n_1^2 \sin^2 \theta_1. \quad (\text{A.56})$$

Equate the real and imaginary parts:

$$\left. \begin{aligned} u_2^2 - v_2^2 &= n_2^2(1 - \kappa_2^2) - n_1^2 \sin^2 \theta_1 \\ u_2 v_2 &= n_2^2 \kappa_2 \end{aligned} \right\} \quad (\text{A.57})$$

Solving A.57 for u_2 and v_2 yields:

$$\left. \begin{aligned} 2u_2^2 &= n_2^2(1 - \kappa_2^2) - n_1^2 \sin^2 \theta_1 + \sqrt{[n_2^2(1 - \kappa_2^2) - n_1^2 \sin^2 \theta_1]^2 + 4n_2^4 \kappa_2^2}, \\ 2v_2^2 &= -[n_2^2(1 - \kappa_2^2) - n_1^2 \sin^2 \theta_1] + \sqrt{[n_2^2(1 - \kappa_2^2) - n_1^2 \sin^2 \theta_1]^2 + 4n_2^4 \kappa_2^2}. \end{aligned} \right\} \quad (\text{A.58})$$

These values will be used in calculating layer reflectivity.

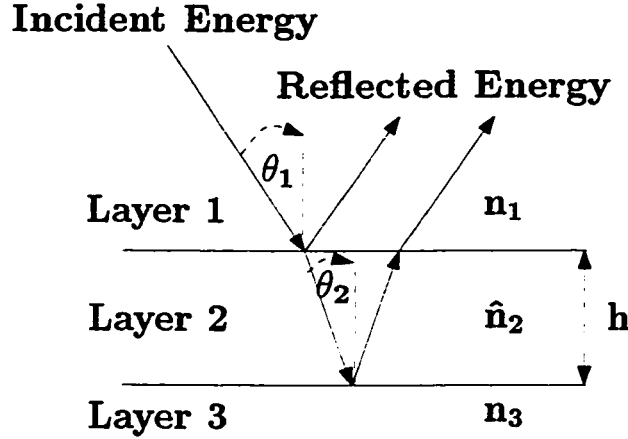


Figure A.2: Schematic diagram of 3-layer reflectivity model. Where n_1, n_3 are the real indices of refraction of layers 1 and 3 and \hat{n}_2 is the complex index refraction of conducting layer 2. h is the thickness of layer 2. θ_1 is the angle of incidence on the $n_1 - \hat{n}_2$ interface, and θ_2 is the angle of incidence on the $\hat{n}_2 - n_3$ interface.

Electric vector perpendicular to plane of incidence (p Polarization)

Making substitution A.55 in § A.1.7 equation A.29, we calculated the reflection at the 1-2 interface,

$$r_{12} = \rho_{12} e^{i\phi_{12}} = \frac{n_1 \cos \theta_1 - (u_2 + iv_2)}{n_1 \cos \theta_1 + (u_2 + iv_2)} \quad (\text{A.59})$$

From equation A.59, we get:

$$\rho_{12}^2 = \frac{(n_1 \cos \theta_1 - u_2)^2 + v_2^2}{(n_1 \cos \theta_1 + u_2)^2 + v_2^2}, \quad \tan \phi_{12} = \frac{2v_2 n_1 \cos \theta_1}{u_2^2 + v_2^2 - n_1^2 \cos^2 \theta_1}. \quad (\text{A.60})$$

For transmission at the first interface (following § A.1.7):

$$t_{12} = \tau_{12} e^{i\chi_{12}} = \frac{2n_1 \cos \theta_1}{n_1 \cos \theta_1 + u_2 + iv_2}, \quad (\text{A.61})$$

yields:

$$\tau_{12}^2 = \frac{(2n_1 \cos \theta_1)^2}{(n_1 \cos \theta_1 + u_2)^2 + v_2^2}, \quad \tan \chi_{12} = -\frac{v_2}{n_1 \cos \theta_1 + u_2}. \quad (\text{A.62})$$

Also, we can get the analogous relations for reflection and transmission at interface two:

$$\rho_{12}^2 = \frac{(n_3 \cos \theta_3 - u_2)^2 + v_2^2}{(n_3 \cos \theta_3 + u_2)^2 + v_2^2}, \quad \tan \phi_{23} = \frac{2v_2 n_3 \cos \theta_3}{u_2^2 + v_2^2 - n_3^2 \cos^2 \theta_3}. \quad (\text{A.63})$$

$$\tau_{23}^2 = \frac{4(u_2^2 + v_2^2)}{(n_3 \cos \theta_3 + u_2)^2 + v_2^2}, \quad \tan \chi_{23} = -\frac{v_2 n_3 \cos \theta_3}{u_2^2 + v_2^2 + u_2 n_3 \cos \theta_3}. \quad (\text{A.64})$$

The angle θ_3 can be determined from θ_1 by use of the law of refraction.

$$n_1 \sin \theta_1 = \hat{n}_2 \sin \theta_2, \quad \hat{n}_2 \sin \theta_2 = n_3 \sin \theta_3 \Rightarrow n_3 \sin \theta_3 = n_1 \sin \theta_1 \quad (\text{A.65})$$

Electric Vector parallel to plane of incidence s Polarization

Finally, we obtain the relationships for the transmission and reflection coefficients for the case of the electric vector parallel to the plane of incidence by replacing the quantities $p_j = n_j \cos \theta_j$ with $q_j = \cos \theta_j / n_j$.

$$r_{12} = \rho_{12} e^{i\phi_{12}} = \left. \begin{aligned} &= \frac{\frac{1}{n_1} \cos \theta_1 - \frac{1}{\hat{n}_2} \cos \theta_2}{\frac{1}{n_1} \cos \theta_1 + \frac{1}{\hat{n}_2} \cos \theta_2} = \frac{\hat{n}_2^2 \cos \theta_1 - n_1 \hat{n}_2 \cos \theta_2}{\hat{n}_2^2 \cos \theta_1 + n_1 \hat{n}_2 \cos \theta_2} \\ &= \frac{[n_2^2(1 - \kappa_2^2) + 2in_2^2\kappa_2] \cos \theta_1 - n_1(u_2 + iv_2)}{[n_2^2(1 - \kappa_2^2) + 2in_2^2\kappa_2] \cos \theta_1 + n_1(u_2 + iv_2)} \end{aligned} \right\} \quad (\text{A.66})$$

Which yields:

$$\left. \begin{aligned} \rho_{12}^2 &= \frac{[n_2^2(1 - \kappa_2^2) \cos \theta_1 - n_1 u_2]^2 + [2n_2^2 \kappa_2 \cos \theta_1 - n_1 v_2]^2}{[n_2^2(1 - \kappa_2^2) \cos \theta_1 + n_1 u_2]^2 + [2n_2^2 \kappa_2 \cos \theta_1 + n_1 v_2]^2}, \\ \tan \phi_{12} &= 2n_1 n_2^2 \cos \theta_1 \frac{2\kappa_2 u_2 - (1 - \kappa_2^2)v_2}{n_2^4(1 + \kappa_2^2)^2 \cos^2 \theta_1 - n_1^2(u_2^2 + v_2^2)} \end{aligned} \right\} \quad (\text{A.67})$$

For transmission at the first interface, we use § A.1.7 (A.30) and replace $n_j \cos \theta_j$ by $\cos \theta_j / n_j$,

$$t_{12} = \tau_{12} e^{i\chi_{12}} = \left. \begin{aligned} &= \frac{\frac{2}{n_1} \cos \theta_1}{\frac{1}{n_1} \cos \theta_1 + \frac{1}{\hat{n}_2} \cos \theta_2} \\ &= \frac{2[n_2^2(1 - \kappa_2^2) + 2in_2^2\kappa_2] \cos \theta_1}{[n_2^2(1 - \kappa_2^2) + 2in_2^2\kappa_2] \cos \theta_1 + n_1(u_2 + iv_2)}. \end{aligned} \right\} \quad (\text{A.68})$$

From A.68:

$$\left. \begin{aligned} \tau_{12}^2 &= \frac{4n_2^4(1 + \kappa_2^2)^2 \cos^2 \theta_1}{[n_2^2(1 - \kappa_2^2) \cos \theta_1 + n_1 u_2]^2 + [2n_2^2 \kappa_2 \cos \theta_1 + n_1 v_2]^2}, \\ \tan \chi_{12} &= \frac{n_1[2\kappa_2 u_2 - (1 - \kappa_2^2)v_2]}{n_2^2(1 + \kappa_2^2)^2 \cos \theta_1 + n_1[(1 - \kappa_2^2)u_2 + 2\kappa_2 v_2]}. \end{aligned} \right\} \quad (\text{A.69})$$

The analogous relations for the second interface:

$$\left. \begin{aligned} \rho_{23}^2 &= \frac{[n_2^2(1 - \kappa_2^2) \cos \theta_3 - n_3 u_2]^2 + [2n_2^2 \kappa_2 \cos \theta_3 - n_3 v_2]^2}{[n_2^2(1 - \kappa_2^2) \cos \theta_3 + n_3 u_2]^2 + [2n_2^2 \kappa_2 \cos \theta_3 + n_3 v_2]^2}, \\ \tan \phi_{23} &= 2n_3 n_2^2 \cos \theta_3 \frac{2\kappa_2 u_2 - (1 - \kappa_2^2)v_2}{n_2^4(1 + \kappa_2^2)^2 \cos^2 \theta_3 - n_3^2(u_2^2 + v_2^2)} \end{aligned} \right\} \quad (\text{A.70})$$

and

$$\left. \begin{aligned} \tau_{23}^2 &= \frac{4n_3^2(u_2^2 + v_2^2)}{[n_3 u_2 + n_2 2(1 - \kappa_2^2 \cos \theta_3)]^2 + [n_3 v_2 + 2n_2^2 \kappa_2 \cos \theta_3]^2}, \\ \tan \chi_{23} &= \frac{n_2^2[(1 - \kappa_2^2)v_2 - 2\kappa_2 u_2] \cos \theta_3}{n_3[u_2^2 + v_2^2] + n_2^2[(1 - \kappa_2^2)u_2 + 2\kappa_2 v_2] \cos \theta_3}. \end{aligned} \right\} \quad (\text{A.71})$$

Now, from ρ_{ij} , ϕ_{ij} , χ_{ij} , τ_{ij} , the transmission and reflection coefficients can be evaluated as in § A.1.7. To simplify the equations, define η :

$$\eta = \frac{2\pi}{\lambda_0} h, \quad (\text{A.72})$$

where λ_0 is the wavelength of the radiation in free space and h is the layer thickness. This reduces to

$$\beta = \frac{2\pi}{\lambda_0} \hat{n}_2 h \cos \theta_2 = (u_2 + iv_2)\eta. \quad (\text{A.73})$$

The reflection and transmission coefficients from § A.1.7 (A.31)-(A.32) are now:

$$r = \rho e^{i\delta_r} = \frac{\rho_{12} e^{i\phi_{12}} + \rho_{23} e^{-2v_2\eta} e^{i(\phi_{23} + 2u_2\eta)}}{1 + \rho_{12}\rho_{23} e^{-2v_2\eta} e^{i(\phi_{12} + \phi_{23} + 2u_2\eta)}} \quad (\text{A.74})$$

$$t = \tau e^{i\delta_t} = \frac{\tau_{12}\tau_{23} e^{v_2\eta} e^{i(\chi_{12} + \chi_{23} + u_2\eta)}}{1 + \rho_{12}\rho_{23} e^{-2v_2\eta} e^{i(\phi_{12} + \phi_{23} + 2u_2\eta)}} \quad (\text{A.75})$$

From (A.74) the reflectivity \mathcal{R} (commonly referred to as the *power reflection coefficient*) \mathcal{R} , and phase of the reflected wave δ_r are:

$$\mathcal{R} = |r|^2 = \frac{\rho_{12}^2 e^{2v_2\eta} + \rho_{23}^2 e^{-2v_2\eta} + 2\rho_{12}\rho_{23} \cos[\phi_{23} - \phi_{12} + 2u_2\eta]}{e^{2v_2\eta} + \phi_{12}^2 \phi_{23}^2 e^{-2v_2\eta} + 2\rho_{12}\rho_{23} \cos[\phi_{12} + \phi_{23} + 2u_2\eta]}, \quad (\text{A.76})$$

$$\tan \delta_r = \frac{\rho_{23}(1 - \rho_{12}^2) \sin(2u_2\eta + \phi_{23}) + \rho_{12}[e^{2v_2\eta} - \rho_{23}^2 e^{-2v_2\eta}] \sin \phi_{12}}{\rho_{23}(1 - \rho_{12}^2) \cos(2u_2\eta + \phi_{23}) + \rho_{12}[e^{2v_2\eta} + \rho_{23}^2 e^{-2v_2\eta}] \cos \phi_{12}} \quad (\text{A.77})$$

These relations hold for both p and s polarizations of the electric vector when the ρ and ϕ appropriate to the polarization are used.

From (A.74) we get:

$$\mathcal{T} = \frac{n_3 \cos \theta_3}{n_1 \cos \theta_1} |t|^2 = \frac{n_3 \cos \theta_3}{n_1 \cos \theta_1} \frac{\tau_{12}^2 \tau_{23}^2 e^{-2v_2\eta}}{1 + \rho_{12}^2 \rho_{23}^2 e^{-4v_2\eta} + 2\rho_{12}\rho_{23} e^{-2v_2\eta} \cos[\phi_{12} + \phi_{23} + 2u_2\eta]}, \quad (\text{A.78})$$

$$\tan[\delta_t - \chi_{12} - \chi_{23} + u_2\eta] = \frac{e^{2v_2\eta} \sin 2u_2\eta - \rho_{12}\rho_{23} \sin(\phi_{12} + \phi_{23})}{e^{2v_2\eta} \cos 2u_2\eta + \rho_{12}\rho_{23} \cos(\phi_{12} + \phi_{23})} \quad (\text{A.79})$$

From equations (A.76)-(A.79) we can calculate the reflection and transmission power and phase for a layer of known thickness (h), conductivity (σ) and permittivity (ϵ_2).

Appendix B

PRINCIPAL COMPONENT ANALYSIS

Principal component analysis (PCA) is used in Chapter 5 to identify features in the ice which are persistent in all repeated measurements at a particular location. The residual bed reflection power (BRP_R) is calculated by removing the linear relationship between magnitude of these constant features and the measured BRP. In this appendix, I briefly describe the theory of PCA and how I use it in reducing the measured BRP data.

B.1 Principal Component Analysis in 2-D

First, to understand how PCA works in general, consider a hypothetical set of data consisting of repeated measurements of two quantities A and B . We could plot these hypothetical 2-D data as shown in Figure B.1, where the axes OX_1 and OX_2 represent A and B , respectively.

If we are interested in the configuration of these data, and if there were some advantage, we could rotate the axes and relate the data to new axes. One possible advantage of rotating the axes is that the new axes may carry some meaning. In this example, we could rotate the axes $\alpha = 45^\circ$ to the new position OY_1, OY_2 . The Y_1 component of the data would then represent how much the BRP and IRP vary in the same sense and is given by:

$$Y_1 = x_1 \cos \alpha + x_2 \sin \alpha = \frac{\sqrt{2}}{2}(x_1 + x_2).$$

The Y_2 component of the data represents how much A and B vary in the opposite

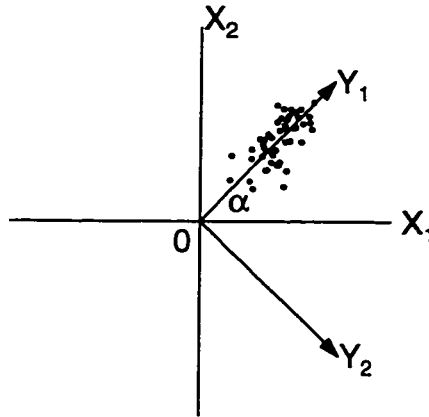


Figure B.1: Example data shown plotted on their measured axes OX_1 , OX_2 , and with another set of axes OY_1 , OY_2 rotated an angle α from these measured axes.

sense and is given by:

$$Y_2 = -x_1 \sin \alpha + x_2 \cos \alpha = \frac{\sqrt{2}}{2}(-x_1 + x_2).$$

In the data in Figure B.1, the hypothetical A , B data primarily vary together (along OY_1).

A second possible advantage of rotating the axes is that it may be possible to more simply represent the variation of the data with a new set of axes. The data above (Fig. B.1) have an obvious grouping, and as I've chosen OY_1 there is a wide spread of the data (i.e. projection of the data) on the Y_1 axis, while the spread of the data on the Y_2 axis is relatively small. If the spread of the data on the Y_2 axis were sufficiently small, we could represent the data by just its Y_1 component, and we would then effectively replace the two original variables (A and B) by the derived variable Y_1 that is a linear combination of the two. This representation would serve to reduce the dimensionality of the data from two to one.

Different rotations of the axes (different values of α) will produce differing projections on to the resulting Y_1 and Y_2 axes, and among all of these rotations we can define one of these as being the "best". There are two main definitions commonly

used to determine the “best” projection.

1. The value of α that results in the largest possible sum of the squared inner products of the data and Y_1 .
2. The value of α that results in the largest possible variance of the projections of the data on to Y_1 . (largest spread of the Y_1 components of the data).

Either of these two definitions may have advantages depending on the application. It can be shown that if the average of all of the data have been subtracted from the data (i.e. the data are *mean centered*), then the two definitions are equivalent, and are further equivalent to minimizing the sum of the squares of the perpendicular distances of the data from OY_1 .

By the first definition (maximizing the squared inner product), the first PC will be more sensitive to the position in space of the data than the shape of the data. The different data configurations shown in Figure B.2) would all have the same first PC, since the maximization of the dot product would be dominated by the position of the mean of the data.

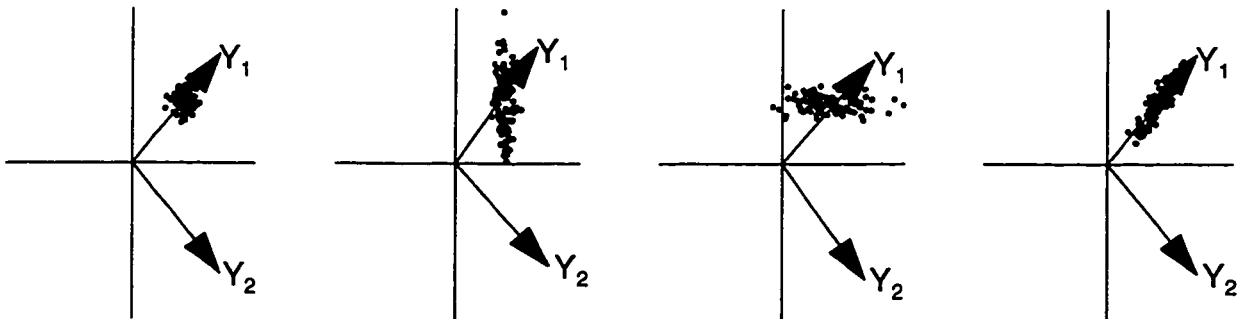


Figure B.2: Four groups of data plotted on their original axes. The principal components of each are shown to be the same in each case using the first definition.

By the second definition (maximizing the variance of the projection of the data), the first PC will be sensitive to the shape of the data, and not to its position. The different data configurations (Fig. B.3) would have different first PCs. I adopt this

definition primarily because it gives a result that is independent of the original axes. In addition, by calculating the principal components using the second definition, the variance accounted for by each principal component is automatically calculated.

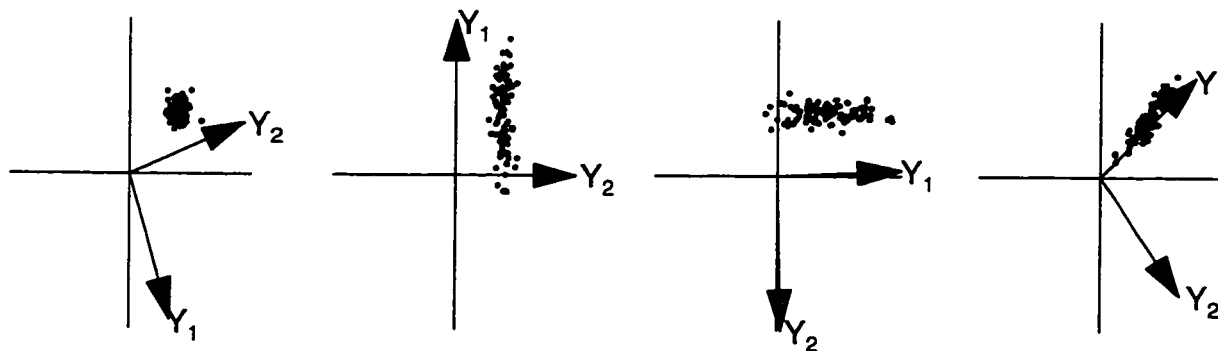


Figure B.3: Four groups of data plotted on their original axes. The principal components of each are shown to be the different in each case using the second definition above.

B.2 Principal Component Analysis in M -Dimensions

In the previous section hypothetical data of 2-dimensions and the resulting 2 principal components were considered. In general, data are of M dimensions. The steps for determining all M of the PCs is as follows (adopting the second definition of “best” above):

1. Model the (mean-centered) data as a swarm of N points in M -dimensions; each dimension corresponding to a measured variable. For repeated RES measurements, M corresponds to the number of samples considered in each waveform and N corresponds to the number of waveforms (records).
2. Search for the line $0Y_1$ in this space such that the spread of the data, when projected on to this line is a maximum. The normalized vector in this direction is the first principal component which I will call \mathbf{E}_1 . The projection of the i^{th} measurement onto \mathbf{E}_1 is C_1 , and represents the magnitude of the first principal component present in the i^{th} measurement.

3. To calculate the second principal component, consider the $(M-1)$ dimensional subspace orthogonal to $0Y_1$, and look for a line $0Y_2$ such that the spread of the points when projected onto $0Y_2$ is maximized. The normalized vector in this direction is the second principal component (E_2). Note that this spread is necessarily less than that for $0Y_1$.
4. Continue this process for all M dimensions to determine E_1, E_2, \dots, E_M .

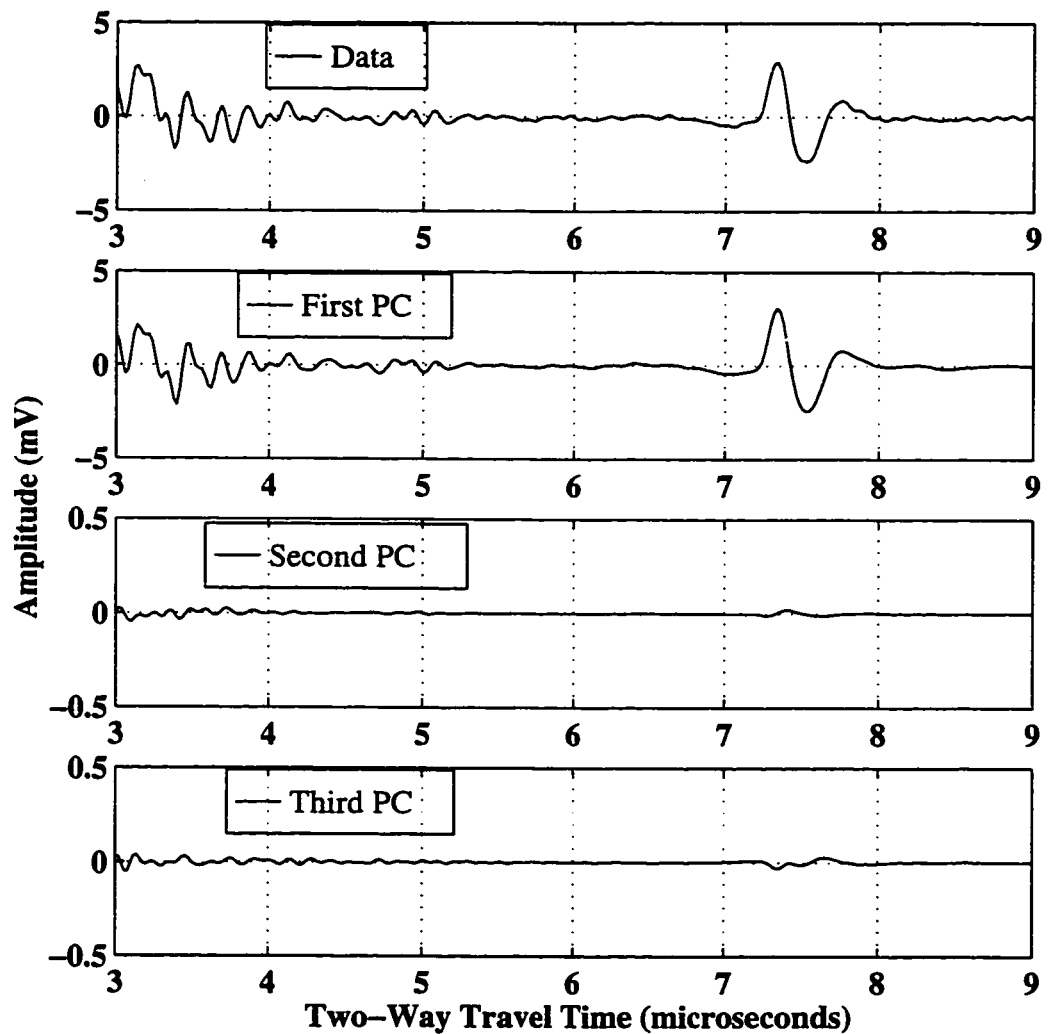


Figure B.4: Example record from Km-16U, day 158.6 (top panel), and the first three principal components E_1, E_2, E_3 scaled by their coefficients C_1, C_2, C_3 .

B.3 Application of PCA to Repeated RES Measurements

For RES repeat measurement data, the first principal component \mathbf{E}_1 is calculated for a section of the waveforms which contains energy reflected from within the ice. \mathbf{E}_1 then represents the shape of the waveform that is most common throughout the measurements, and will contain the signal from reflectors which are constant and will exclude those which are variable (the variable reflectors will be recorded in subsequent principal components). Figure B.4 shows a typical record (top panel) and the first three principal components, calculated from $3\mu\text{S}$ to the end of the record. The fraction of the total data variance accounted for by the first ten principal components is shown in Figure B.5 and is somewhat typical of the results from the analysis of repeated RES measurements. The break in slope in the fraction of total variance accounted for between the first principal component and the second through tenth components indicates by the so-called *scree test* (e.g., *Dillon and Goldstein, 1984*) that in this case only the first component is significant - though this is not always the case. C_{1i} is calculated by projecting the i^{th} measurement onto the normalized vector \mathbf{E}_1 . C_{1i} represents the magnitude of \mathbf{E}_1 contained in the i^{th} measurement, and therefore represents the magnitude of the persistent reflectors present in the waveform. The linear relationship between the C_{1i} and measured bed reflection power is interpreted as being caused by varying amounts of power reaching the ice subsurface (because of instrumentation and/or ice surface property variations).

Once the principal component \mathbf{E}_1 of the interior portion of the data and the amplitude of that component present in each measurement C_{1i} are determined, I subtract the portion of the measured BRP that is linearly related to the C_{1i} . This relation (dropping the subscripts) is given by:

$$BRP_r = BRP - (A + BC_1), \quad (\text{B.1})$$

where A , B are coefficients determined by the best (least squares) linear fit between C_1 and BRP (the measured bed reflection power). Power variations that remain

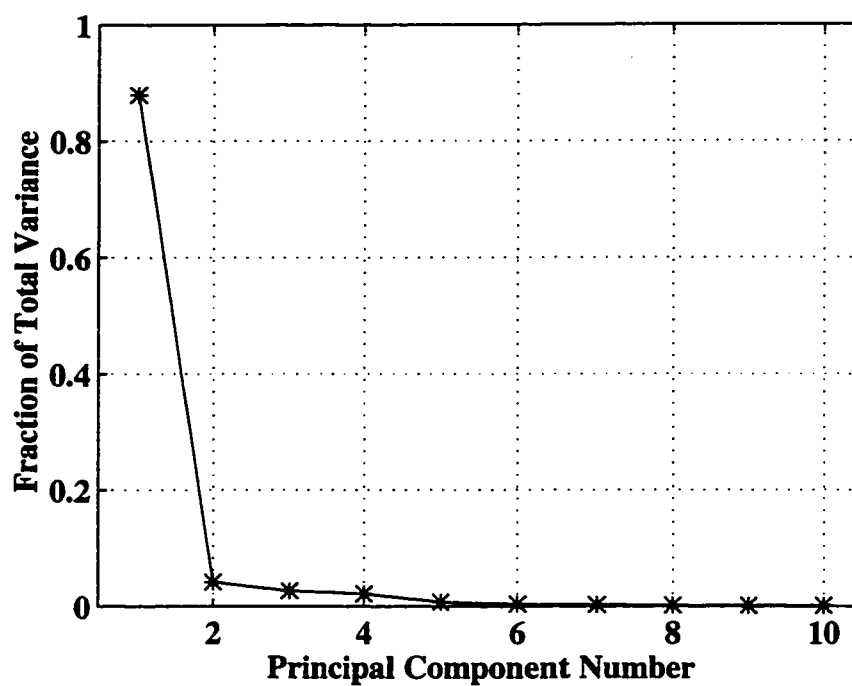


Figure B.5: Fraction of total data variance accounted for by the first ten principal components.

(BRP_r) are not due to power transmission variations, but are presumably due to variations in the physical conditions at the base of the glacier.

Appendix C

SURVEY MEASUREMENTS, BLACK RAPIDS GLACIER, AK

During the 1993 field season at Black Rapids Glacier, the velocity and vertical position of a point near the glacier center at approximately Km-15 was established using conventional optical surveying techniques employing theodolite (to determine horizontal and vertical angles) and electronic distance measuring devices (EDM) (to measure distance from the instrument to a corner reflector)¹. The horizontal position of the top of a wooden stake driven into the ice was determined relative to two fixed base stations, No Return (NR) and Bee (B) on the glacier margin. The displacement between two measurements was calculated as the square root of the sum of squares of the changes in the two horizontal components divided by the measurement interval. The relative vertical position of the Km-15 marker was measured relative to the nearer pole, NR, and was calculated as the product of the slope distance and cosine of the vertical angle minus the height of the instrument above the marker. These survey measurements were made at least twice daily, and when possible more frequently during times of glacier speed up. Distance measurements were reproducible to 0.002-0.005m, theodolite measurements were reproducible to 1-3 seconds. The resulting horizontal speeds had errors of at most 0.008m day⁻¹, and vertical positions had errors of at most 0.02m.

¹ These measurements were organized by Keith Echelmeyer who also made most of the measurements during the first half of the field season. All field party members contributed by making some these measurements during the season.

Measurements were also made to determine the strain between the survey site and poles at locations up (Km-12, Km-14) and down-glacier (Km-16, Km-17). Strain rates were calculated as the change in distance between the marker and the Km-15 survey point divided by the initial length and the time interval of the measurement.

The results of these measurements are summarized in Figure C.1. Measurements to the Km-12 survey marker are omitted because the measurements were inaccurate and often not done because of light refraction at the snow surface, and due to a lack of ranging power of the EDM. The anomalously high strain shown in Figure C.1, bottom panel after day 175 was due to a tipping motion of the survey markers. Measurements to those markers were not continued beyond this point.

The motion of a transverse line of poles along Km-16 were also surveyed at four intervals during the field season (18, 23 May and 2, 10, 15 June 1993). The averaged daily speed was then calculated for each interval. Pole S4 was not measured on 15 June. The results of these measurements are summarized in Figure C.2.

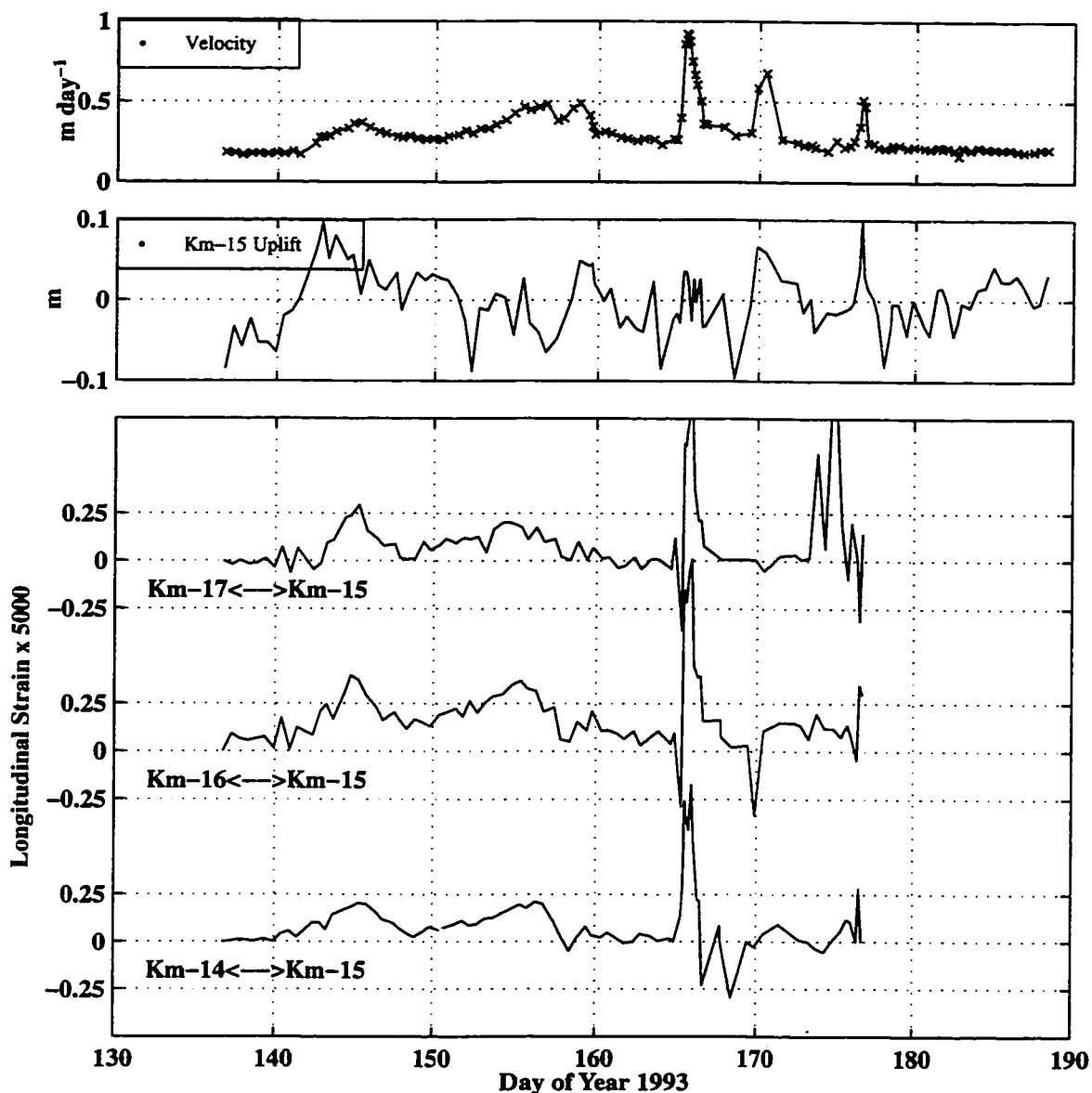


Figure C.1: Summary of twice-daily survey measurements from Km-15.5. The panels from top to bottom display: down glacier speed (m d^{-1}), vertical displacement (m), strain rates between labeled poles (d^{-1}). Cross marks on the top panel indicate the time when survey measurements were made. In the second panel, the linear trend due to the downward motion of the location from down glacier flow, has been removed.

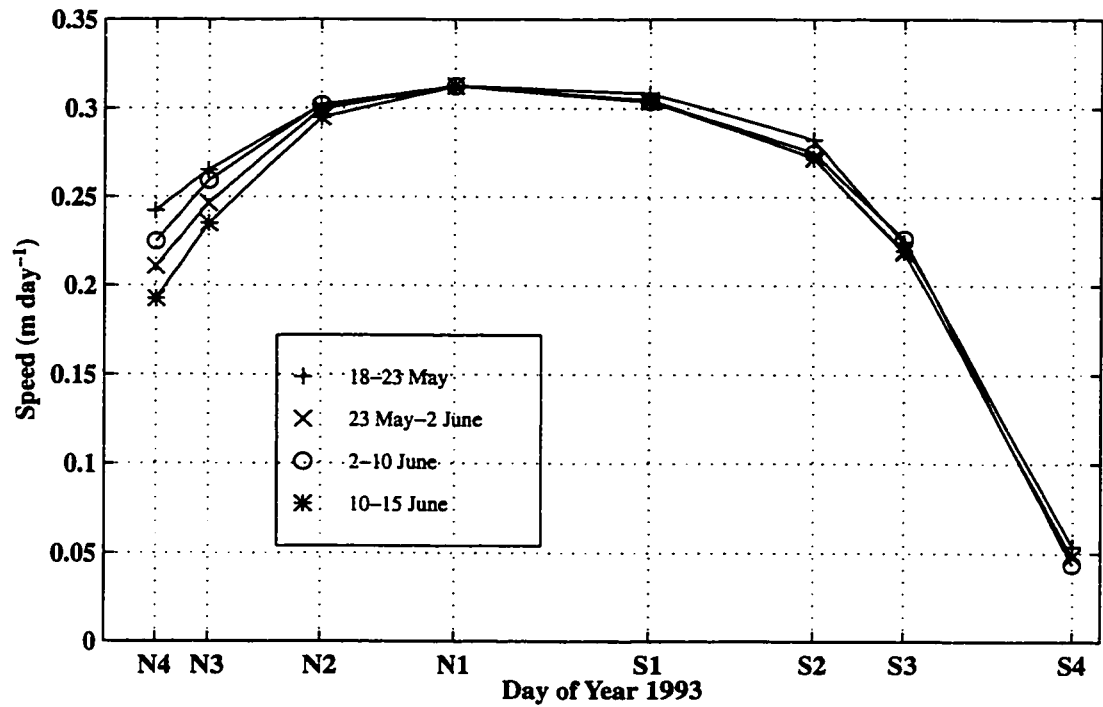


Figure C.2: Transverse velocity profile at Km-16. Speeds shown are the averaged daily values within the time spans indicated in the legend. The view shown is looking down-glacier.

Appendix D

WEATHER OBSERVATIONS, BLACK RAPIDS GLACIER, AK

A weather station was positioned at *Will's Ear*, which is located on the north glacier margin near the Km-15 line ($63^{\circ} 29' 41.1598'' N$, $146^{\circ} 30' 20.7080'' W$). Precipitation, temperature, and broadband incoming solar radiation was measured and was recorded hourly by a Cambell CR-10 data logger. The code and instrumentation were set up by H. Conway. A summary of the measurements is shown in Figure D.1. The weather could be characterized as clear and stable with only two significant precipitation events during the measurement period.

Ablation was measured twice daily at a pole 2m from the Km-15 surveying station. Figure D.2 displays the water equivalent ablation. Survey notes indicate that the ablation at the pole was down to bare ice on day 170. I used an approximate snow density ($\rho_{snow} = 400 \text{ kg m}^{-3}$) to convert days 137-170 to water equivalent, and an approximate ice density ($\rho_{ice} = 917 \text{ kg m}^{-3}$) thereafter.

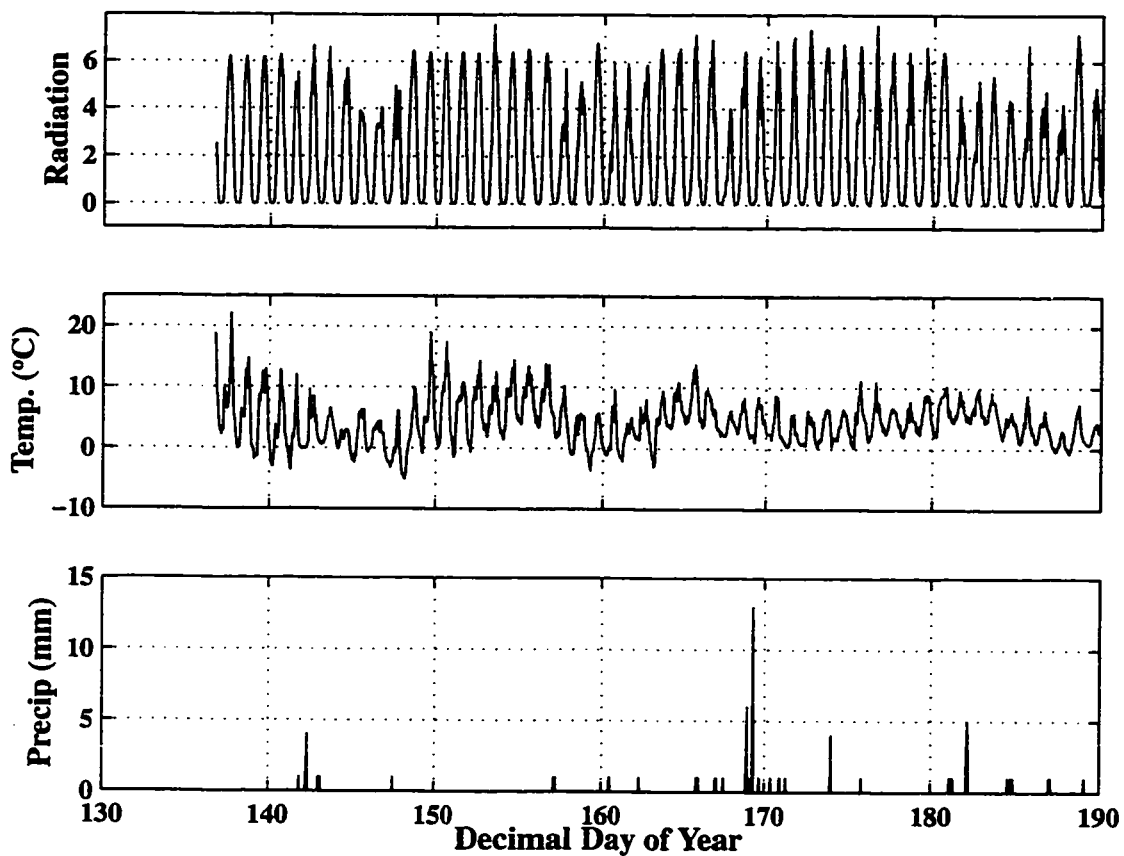


Figure D.1: Summary of hourly weather observations recorded by the weather station located at the north margin of BRG, Km-15, showing temperature ($^{\circ}\text{C}$), precipitation (mm of water), and incoming solar radiation (uncalibrated units).

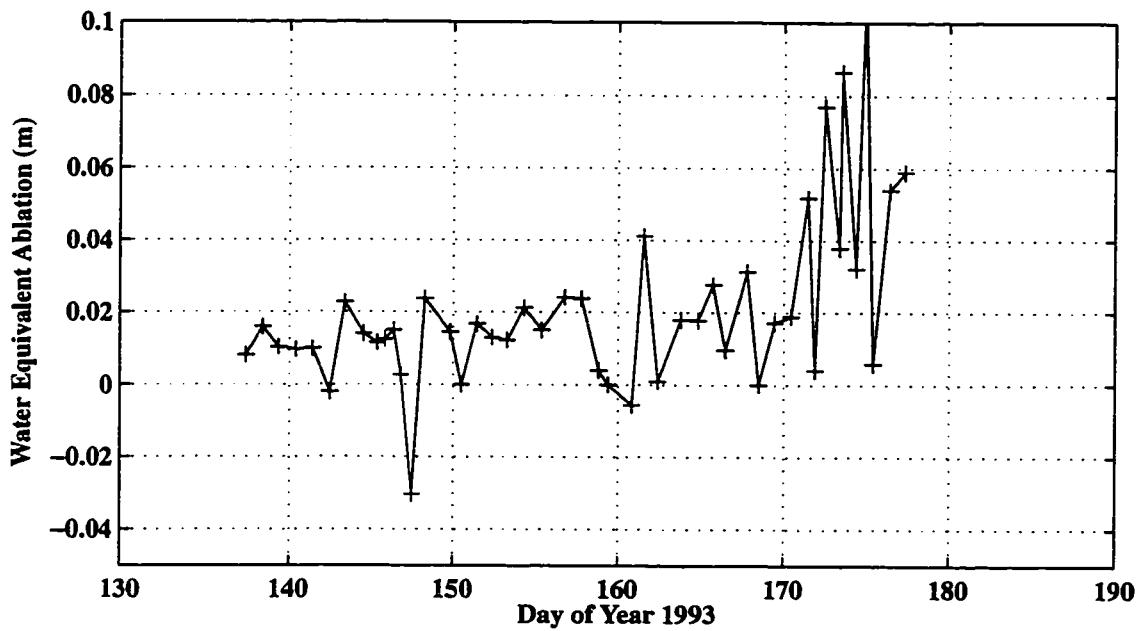


Figure D.2: Ablation as measured near the Km-15 survey site. Because a density profile was not measured, the values are calculated assuming $\rho_{snow} = 400 \text{ kg m}^{-3}$ for days prior to 171, and $\rho_{ice} = 917 \text{ kg m}^{-3}$ thereafter.

Appendix E

MARGINAL LAKE DRAINAGE EVENTS

Observations of three lake drainage events were noted during the 1993 field season. Several large lakes formed as depressions filled with melt water at the margins of BRG. These lakes apparently fill annually. *Sturm and Cosgrove* (1990) report a previous drainage of one of these lakes and mention previous observations of lake drainages.

The first lake drainage ($\sim 10^6 m^3$) began slightly after noon on day 164 (13 June, 1993). This is known from direct observations just prior and slightly after the drainage began. This lake drainage follows the pattern described in *Sturm and Cosgrove* (1990). The lake broke through its ice dam in the south east corner, and flowed supra-glacially through an incised channel (~ 5 m wide; up to 20 m deep). This channel is presumably the residual of previous drainage events; its initial location likely determined by fractures or weaknesses in the surrounding ice. The water flowed approximately 1 km in this incised canyon and progressively disappeared down moulins. The time series of water flux from this lake is not known. The approximate maximum flow likely occurred early on day 165, but large flows continued for about 24 hours. Rhodamine B Dye was injected in the largest moulin draining the lake outflow at about Km-13.5, north of the centerline. Dye appeared in the outflow stream approximately 12 hours later, and continued at an approximately constant mean level for the following 14 days *Cochran* (1995). The second lake drainage ($\sim 10^5 m^3$) was not directly observed at the time of drainage. Though a large pothole nearby was observed to have been drained the following day (*Nolan*, 1998). This lake drainage event is estimated to have occurred very near to the start of day 169, and the injection point would have been directly up-glacier from the center of the Km-14 line.

The third lake ($\sim 10^6 m^3$) drainage occurred at the north glacier margin near Km-15 and was well-observed as it drained through a tunnel at the bottom of the lake. This drainage began at the beginning of day 175, and the injection point was at the north glacier margin and about 2 km downstream from the injection points of the other two drainages.

The approximate onset of the lake drainage events are shown as vertical lines in figure 5.2. Each of the drainage events resulted in a nearly symmetric peak in glacier velocity, and a peak in seismicity. The rapid injection of water from these events, despite the differing points of injection had a glacier-wide effect on motion. These events suggest a high-degree of connectivity of the hydrological system.

Appendix F

DIFFUSION OF WATER IN TILL LAYERS

The steady state flow of water through porous till is often assumed to occur according to Darcy's law; that the flow is linearly proportional to the applied pressure gradient and inversely proportional to the fluid viscosity (e.g., *Turcotte and Schubert, 1982*). Under this assumption changes in water pressure propagate into the till layer by diffusion (*Paterson, 1994*):

$$D \left(\frac{\partial^2 p}{\partial z^2} \right) = \frac{\partial p}{\partial t} \quad (\text{F.1})$$

where D is the hydraulic diffusivity (function of till and water properties), p is water pressure, z is depth, and t is time. D ranges from $4 \times 10^{-4} - 6 \times 10^{-7} \text{ m}^2 \text{ s}^{-1}$ (*Paterson, 1994*) with larger values relating to more coarse materials. The amplitude of a sinusoidal variation of period T decreases as:

$$P(z) \approx e^{-z\sqrt{\pi/(DT)}} \quad (\text{F.2})$$

so the characteristic depth of penetration is: $\sqrt{DT/\pi}$. Figure F.1 shows that the characteristic depth for diurnal variations ($T \approx 10^5 \text{ s}$) is $\sim 10^{-1} \text{ m}$.

It is clear that rapid (\sim hourly) variations in basal conditions must occur by processes other than the transport of water through the till.

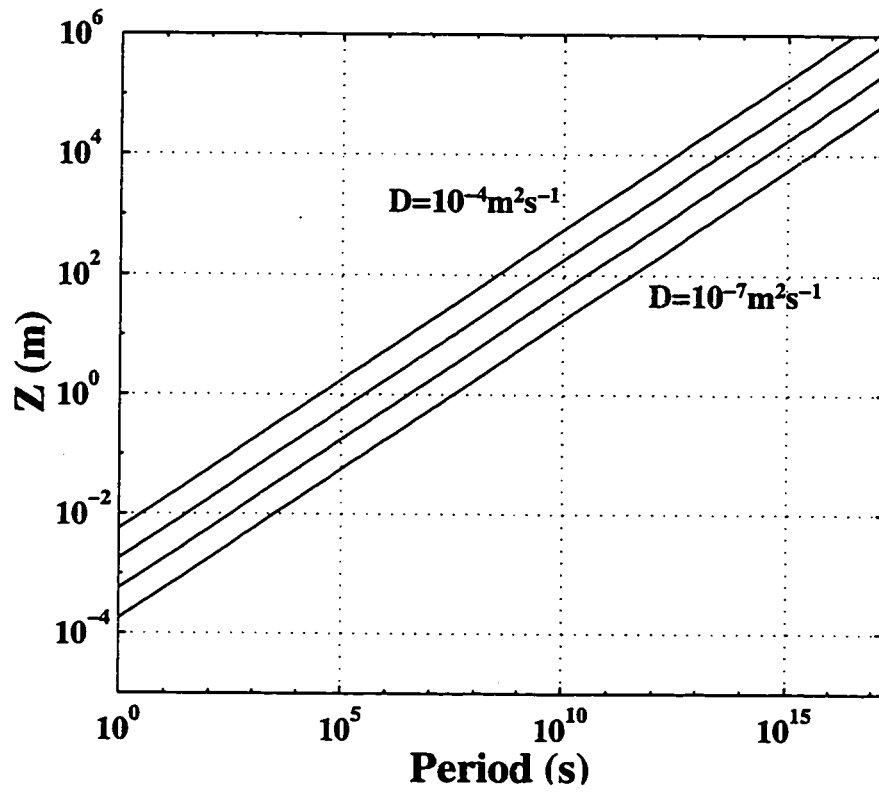


Figure F.1: Characteristic depth for a range of hydraulic diffusivities D for periods of one second to one year.

Appendix G

CALCULATION OF RADIO WAVE PROPAGATION VELOCITY AT SIPLE DOME.

A *constant midpoint profile* (CMP) or *move out* is a common measurement made in reflection seismology (e.g., *Robinson and Treitel, 1980; Claerbout, 1985*) as well as in radio echo-sounding (e.g., *Blindow and Thyssen, 1986*). The purpose of such an experiment is to obtain the integrated average propagation velocity to a reflector, and to accurately determine its depth.

With ice-penetrating RES, a CMP experiment is done with the transmitter and receiver placed a measured distance apart centered over a fixed location on the ice surface (the constant midpoint). The transmitting and receiving antennae are arranged in the *broadside parallel* configuration (*Watts and Wright, 1981*). Measurements are made over a range of separation distances, and the resulting data are a series of travel-times versus separation distances. From a simple geometric calculation to account for the angle and separation from the midpoint, one arrives at a simple relationship between travel time and separation distance:

$$-H^2 + \left(0.5\tau_i + \frac{S_i}{2C_{air}}\right)^2 c_{ice}^2 = + \left(\frac{S_i}{2}\right)^2. \quad (G.1)$$

Where τ_i is the i^{th} two-way travel time measured in micro-seconds, S_i is the i^{th} separation distance measured in meters, and C_{air} is the velocity of radio waves in air $300 \text{ m } \mu\text{S}^{-1}$. The resulting constant H is the depth (in meters) beneath the constant midpoint, and the c_{ice} is the integrated average velocity (in $\text{m } \mu \text{ s}^{-1}$) for the ice column to depth H .

During the 1994 field season Robert Jacobel (St. Olaf College) and I performed

a constant midpoint profile measurement at Siple Dome near local grid S40, E40 (south and east 4 km from the summit). Using the measurements and Equation G.1, the depth of the location was found to be $H = 996 \pm 2$ m, and the velocity was $c_{ice} = 170.4 \pm 0.8$ m μ S⁻¹. We had anticipated that some of the internal reflecting horizons may produce reflections strong enough to be seen in multiple records of the CMP experiment. If a sequence of layers were seen, one could repeat this calculation for each layer and establish a velocity profile for the ice column. However, since the internal layers are in fact very weak reflectors (typically 20-40 dB below the bed reflection), we were not able to do such an analysis.

The velocity found by this method is useful for calculating the ice thicknesses near 1 km in this region. However, for reflectors shallower than 1 km, the travel velocity will be progressively dominated by the faster wave velocity in the firn. Thus, one must exercise caution when using this CMP-determined velocity for calculating depths to shallow reflectors as it will tend to underestimate the actual depth. In this case, the wave velocity through the firn has to be calculated based on a firn density profile (e.g., *Rasmussen*, 1986).

VITA

Name: Anthony M. Gades

Date: June 10, 1998

Education

B. A.: Physics, St. Olaf College, 1991

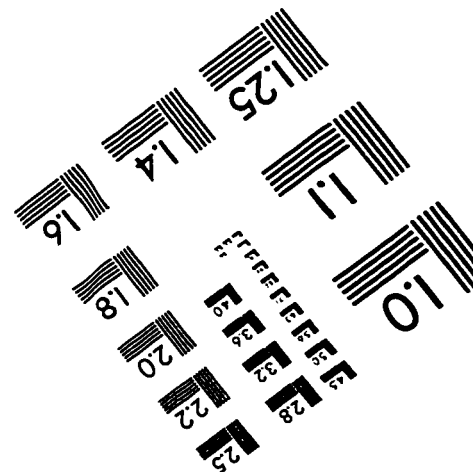
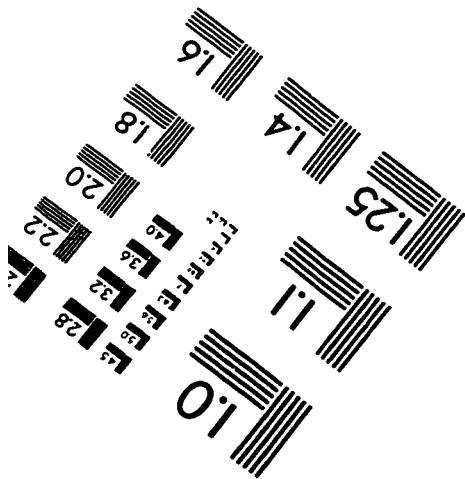
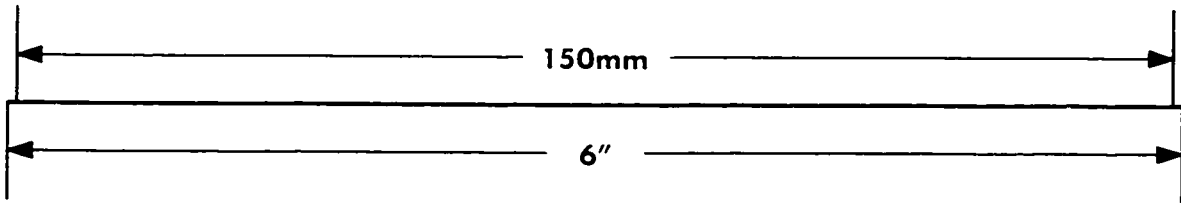
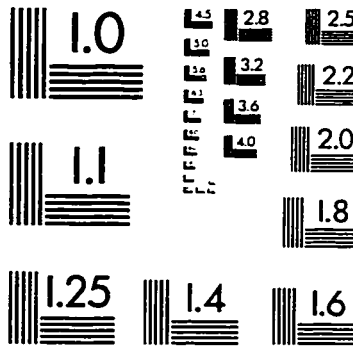
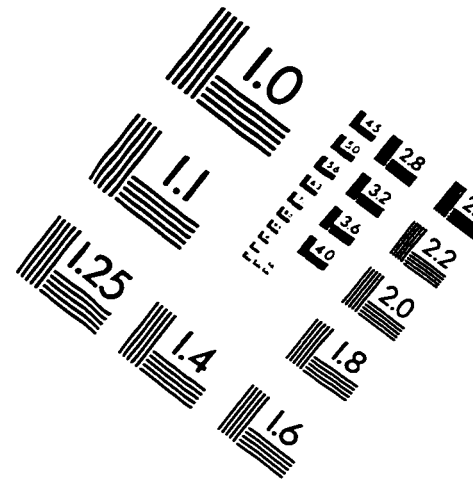
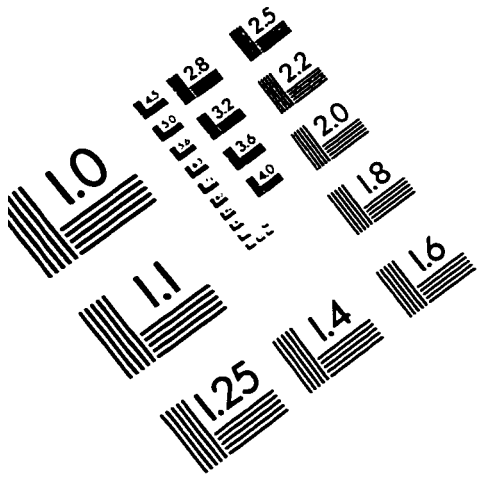
B. A.: Mathematics, St. Olaf College, 1991

Ph. D.: Geophysics, University of Washington, 1998

Thesis Titles

Ph. D.: Spatial and Temporal Variations of Basal Conditions Beneath Glaciers and Ice Sheets Inferred From Radio Echo-Sounding Measurements

IMAGE EVALUATION TEST TARGET (QA-3)



APPLIED IMAGE, Inc
1653 East Main Street
Rochester, NY 14609 USA
Phone: 716/482-0300
Fax: 716/288-5989

© 1993, Applied Image, Inc.. All Rights Reserved